# Solid-Supported Lipid Membranes: Formation, Stability and Applications

by

Haw Zan Goh

Submitted in partial fulfilment of the
requirements for the degree of
Doctor of Philosophy
at
Carnegie Mellon University
Department of Physics
Pittsburgh, Pennsylvania

**Thesis Committee Member:**
Professor Mathias Lösche (Chair)
Professor Markus Deserno
Professor Alex Evilevitch
Professor Lynn Walker

January 2013

**Abstract**

This thesis presents a comprehensive investigation of the formation of supported lipid membranes with vesicle hemifusion, their stability under detergents and organic solvents and their applications in molecular biology.

In Chapter 3, we describe how isolated patches of DOPC bilayers supported on glass surfaces are dissolved by various detergents (decyl maltoside, dodecyl maltoside, CHAPS, CTAB, SDS, TritonX-100 and Tween20) at their CMC, as investigated by fluorescence video microscopy. In general, detergents partition into distal leaflets of bilayers and lead to the expansion of the bilayers through a rolling motion of the distal over the proximal leaflets, in agreement with the first stage of the established 3-stage model of lipid vesicle solubilization by detergents. However, solubilization pathways are different for different detergents. For decyl/dodecyl maltoside, CHAPS and SDS, dissolution of bilayers starts only once the bilayers reach a critical lipid:detergent ratio in the bilayers, whereas for CTAB, TritonX and Tween20, dissolution starts once detergents partition into the bilayers. From the expansion dynamics of bilayers, we conclude that the energy loss due to the partitioning of detergents is balanced by the released heat and the increment of the planar bilayer's curvature energy. Moreover, in contrast to a previous view that detergents need to be present on both leaflets of bilayers to initiate solubilization, we find that detergents in the distal leaflets of bilayers are sufficient to induce micellization. Lastly, we estimate the energy barrier for detergents to partition into lipid bilayers and find it is on the order of 3 to 7 kT.

Subsequently, we study the partitioning of organic solvents (methanol, ethanol, isopropanol, propanol, acetone and chloroform) into isolated bilayer patches on glass in Chapter 4 with fluorescence microscopy. The area expansion of bilayers due to the partitioning of organic solvents is measured. From the titration of organic solvents, we measured the rate of area expansion as a function of the volume fraction of organic solvents, which is proposed to be a measure of strength of interactions between solvents and membranes. From the same experiments, we also measure the maximum expansion of bilayers (or the maximum binding stoichiometry between organic solvents and lipids) before structural breakdown, which depends on the depth of penetration of solvents to the membranes. From the partitioning dynamics, it is observed that bilayers expand the area through the same rolling motion as described for detergent partitioning in

Chapter 3. The energy loss due to the partitioning of organic solvents was balanced by the released heat and the increment of planar bilayer's curvature energy. Upon desorption of organic solvents, the bilayers shrink the area through the edges and by forming pores within the bilayers, concomitantly increase the contour length of bilayer edges, indicating self-healing is impossible for this system.

In Chapter 5, we investigate the formation of sparsely-tethered bilayer lipid membranes (stBLMs) with vesicle hemifusion. In vesicle hemifusion, lipid vesicles in contact with a hydrophobic alkyl-terminated self-assembled monolayer (SAM) deposit a lipid monolayer to the SAM surface, thus completing the bilayer. Electrical Impedance Spectroscopy and Neutron Reflectivity are used to probe the integrity of stBLMs in terms of their insulating and structural properties. Preparation conditions are screened for those that are optimal for stBLM formation. Concentrations of lipid vesicles, hydrophobicity of SAMs, the presence of calcium and high concentrations of salt are identified as the key parameters. We show that stBLMs can be formed with vesicles of different compositions. Vesicle hemifusion opens up a new route in preserving the chemical compositions of stBLMs and facilitating membrane proteins incorporation.

In Chapter 6, we visualize the hemifusion pathway of giant unilamellar vesicles (GUVs) with planar hydrophobic surfaces at the single vesicle level with fluorescence video microscopy. When a GUV hemifuses to a surface, its outer leaflet breaks apart and remains connected to the surface presumably through a hemifusion diaphragm. Lipids from the outer leaflet are transferred to the surface as a lipid monolayer that expands radially outward from the hemifusion diaphragm, thereby forming the loosely packed outer hemifusion zone. The tension of the outer leaflet rises as lipids are transported to the outer hemifusion zone until it is large enough to rupture the GUV. Therefore, a pore forms near the hemifusion diaphragm through which the water encapsulated within the GUV is expelled. Additionally, lipids flipped from the inner to outer leaflet via the pore and are transferred to the surface. The hemifusion of lipids from both leaflets to the surface leads to the formation of the inner hemifusion zone densely packed with lipids. The inner and outer hemifusion zones expand radially as concentric discs with a rate of about 1000 $\mu m^2/s$, suggesting the expansion is driven by surface hydrophobicity. The spreading dynamics of the lipid monolayer is consistent with a model where the energy dissipated by friction between the monolayer and the surface is equal to the difference of surface energy when the surface is covered by a lipid

monolayer. The mechanism revealed in this work provides insights into membrane reorganization and improves the understanding of vesicle-surface interactions.

The tethering of membranes is a common process regulating membrane fusion throughout the secretory pathway. The Prof. Linstedt laboratory at the CMU Department of Biological Sciences has been focusing on the elucidation of the mechanism of Golgi membrane tethers, GRASP (Golgi Reassembly And Stacking Proteins), which are essential for the formation of the characteristic ribbon structure of the Golgi apparatus. Typically, such work involves *in vivo* expression of these proteins which tracks how specific mutations affect organelle morphology. However, it remains unclear in such investigations, whether a certain active protein is sufficient to trigger the formation of the characteristic structure or if other factors, for example auxiliary proteins, are involved. Therefore, in Chapter 7, we develop an *in vitro* assay employing stBLMs and lipid vesicles to examine the functionality of GRASP in membrane tethering. Membrane-bound GRASP on opposing membranes dimerizes and tethers fluorescently-labeled vesicles to stBLMs. The fluorescence intensity of images taken at stBLM surfaces is used to quantify the tethering activity. Both wild type and mutant proteins were studied to shed light on the molecular mechanism of tethering. We show that the GRASP domain is sufficient and necessary for membrane tethering. In addition, the tethering capability of GRASP is impaired when the internal ligands and the binding pockets participating in dimerization are deleted and mutated. Membrane anchors, sizes of vesicles and membrane compositions are explored for their influence on the outcomes of the assay. Furthermore, preliminary analysis from neutron reflectivity measurements shows that both the internal ligands and binding pockets are exposed instead of buried toward the membrane surface. In summary, we establish a functional assay for studying GRASP activity *in vitro*. This assay may also be used for studies of similar supramolecular structure formation processes in molecular biology.

# Acknowledgments

I would like to express my profound gratitude to my advisor, Prof. Mathias Lösche. Without his help and guidance, this thesis will not be possible. I particularly appreciate the degree of freedom he has given to me during the course of this thesis research. I would also like to thank former group members who have helped me in my research. They are Dr. Prabhanshu Shekhar, who taught me how to use a Mac operating system and the neutron reflectivity fitting software, Dr. Sidd Shenoy, who showed me how to use the fluorescence microscope and the Surface Plasmon Resonance spectrometer, Dr. Radu Moldovan, who showed me how to remove a needle from a syringe by using the cap of the needle, Dr. Markus Wiegand and Dr. Peter Yaron, who taught me everything I know about a vacuum system, Dr. Frank Heinrich, who helped me in taking neutron reflectivity data and analyzed the reflectivity data in Chapter 7, Dr. Matteo Brocio, who contributed some of the data I included in Chapter 5, Dr. Hirsh Nanda and Marilia Cabral, who helped in neutron reflectivity experiments, and Dr. Agnieszka Kalinowski, who taught me how to perform a SDS-PAGE experiment.

Furthermore, I would like to acknowledge the assistance from Prof. Markus Deserno, Prof. Adam Linstedt, Collin Bachert, Prof. Fred Lanni, Dr. Joseph Mindell and his group members, Dr. Cheemeng Tan and Dr. ZhiXia Zhong. Without their collaborations and research inputs, a lot of the results in this thesis would not be possible.

In Physics Department, I am very indebted to Mrs. Donna Thomas, Mrs. Hilary Homer, Mrs. Mary Jane Hutchinson, Mr. Albert Brunk, Mr. Montel Rudolph, Mr. Gary Wilkin, Prof. Manfred Paulini and Mr. Chuck Gitzen, who I always bugged for the ordering of materials. A lot of things would not go smoothly without their helps. I am also very grateful to the committee members of my thesis, namely Prof. Markus Deserno, Prof. Alex Evilevitch and Prof. Lynn Walker. I appreciate the time they have spent in my annual review and their advices on my research progress.

Finally, I would like to thank my family in Malaysia for their unconditional love and supports.

# Contents

# List of Tables

# List of Figures

# Chapter 1

# Introduction

The first chapter of this thesis introduces the system of interest, namely solid supported lipid membranes. The motivation for developing supported lipid membranes as models of biological membranes is addressed. Additionally, the advantages of using supported membranes in biomedical research and their potential in technological applications are discussed.

## 1.1 Biological Membranes

Biological membranes define the boundary of cells, cell nuclei and organelles in the cytosol. They control the entry and egress of molecules for the corresponding membrane-bounded compartments, the signalling and the communication of cells, and provide a distinct biochemical environment from the outside world. Diseases are found to be membrane-mediated, too [4]. Consequently, the importance of biological membranes in living systems cannot be overestimated.

The basic structure of biological membranes is that of a lipid bilayer embedded with proteins. Lipids are amphiphilic molecules with hydrophilic headgroups and hydrophobic tails. They self-assemble into a bilayer structure in water, with their hydrophobic tails facing each other and their hydrophilic headgroups facing the aqueous phase, shielding the hydrophobic tails from a direct contact with water (Figure 1.1). The thickness of lipid bilayers is about 5 nm, with a hydrophobic core of about 3 nm formed by the hydrophobic tails. These lipid bilayers incorporate membrane proteins to carry out biological functions. There are two major classes of membrane proteins: integral membrane proteins, in which some domains of the proteins span across the

5 nm thick lipid bilayers, and peripheral membrane proteins, in which the proteins are only bound to one side of lipid membranes, either by binding to other proteins in membranes or by absorbing directly to lipid headgroups.

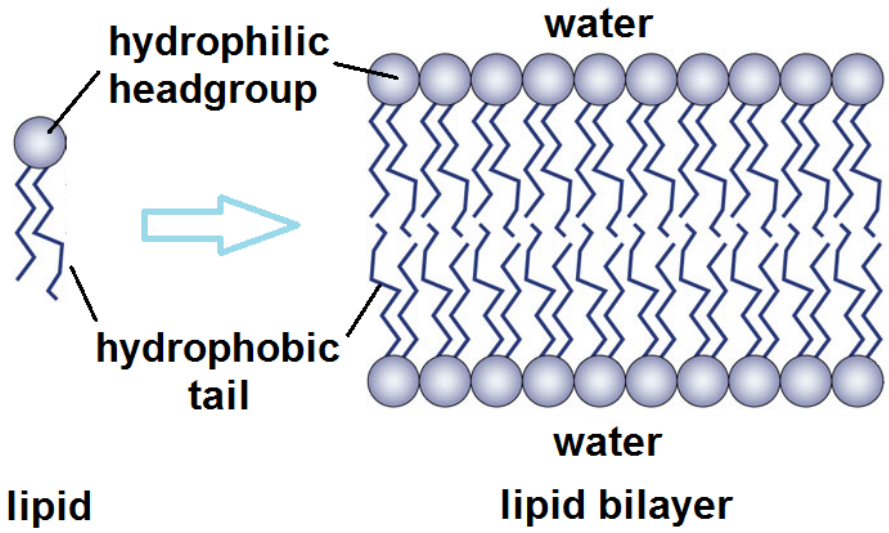


Figure 1.1: *The amphiphilic nature of lipids determines their self-assembly. In aqueous environment, lipids assemble into a lipid bilayer (on the right), with their headgroups facing the aqueous phase and their hydrophobic tails facing each other, to minimize the contact between the tails and water.*

The schematic diagram of a biological membrane is shown in Figure 1.2. Major components of biomembranes including phospholipids, which have a phosphate in their headgroups, glycolipids, which have a carbohydrate attached to the headgroups, cholesterol, sphingomyelin, integral membrane proteins and peripheral membrane proteins. The compositions of biological membranes are tightly regulated by cellular machinery for performing vital biological processes.

## 1.2 Models of Biomembranes and Solid-Supported Lipid Membranes

The chemical compositions of biological membranes are inherently complex and diverse. For example, headgroups of different chemical structures are associated with phospholipids, one of the major constituents of biomembranes. These headgroups include phosphatidylcholine (PC), phosphatidic acid (PA), phosphatidylethanolamine

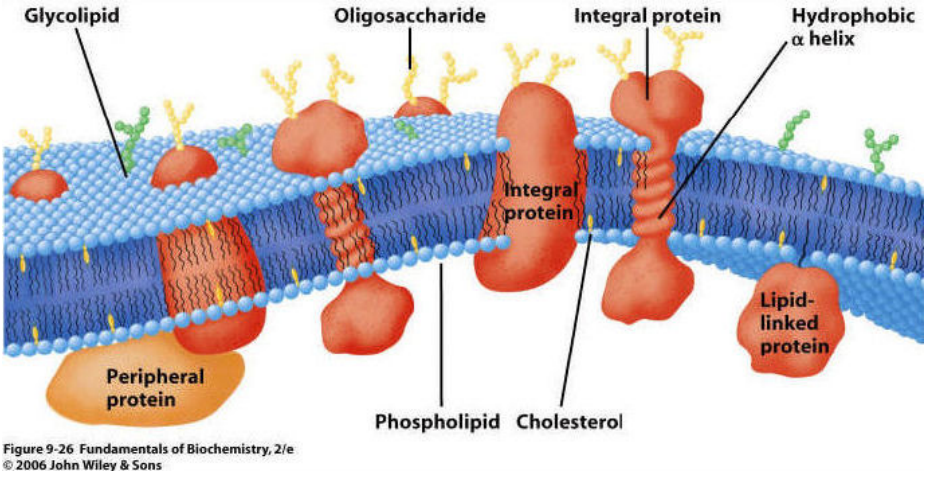


Figure 1.2: *A schematic diagram of a biological membrane. The biological membrane is a complex fluid that is composed of a wide variety of biomolecules.*

(PE), phosphatidylserine (PS), phosphatidylglycerol (PG) and phosphatidylinositol (PI). Out of these headgroups, PC and PE are zwitterionic whereas the rest are anionic at physiological pH. Furthermore, hydrocarbon chains of phospholipids have distinct chain lengths and degrees of saturation. The dissimilarity of phospholipids' chemical structures are associated with distinct physio-chemical properties.

Due to the extreme complexity of membrane compositions, it is not straightforward to pinpoint chemical species that are responsible for certain effects from experimental results involving biomembranes. To circumvent this problem, experiments are often carried out with models of biomembranes. A model biomembrane is a reductionist system, which mimics characteristic properties of biomembranes while reducing the parameters in an experiment to a minimal level by controlling the chemical compositions of the model membranes. For instance, one can systematically increase molar ratio of anionic lipids in model membranes to investigate electrostatic regulated effects. Therefore, models of biomembranes allow scientists to pinpoint the parameters that are responsible for particular phenomena uniquely.

Since the 1960s and 1970s, the most widely employed model biomembranes are black lipid membranes (BLMs) [5, 6]. BLMs are free-standing planar lipid bilayers suspended over apertures of about 100 $\mu$m in diameter. They are formed either by painting the lipids dissolved in organic solvents directly on the apertures with a brush or by fusion of two Langmuir monolayers at the air-water interface while apertures are pushed through lipid-covered water surfaces. BLMs allow electrical measurements

right across the membranes through the aqueous phase. Electrical properties of lipid bilayers such as capacitances and resistances are thus obtained. Additionally, molecular biologists reconstitute ion channels into BLMs to study functionality of the channels with single channel recording due to high resistances of BLMs (a few $M\Omega\,cm^2$). However, BLMs are not stable mechanically and only last for a few hours after their formation.

Another model biomembranes are lipid vesicles or liposomes [7]. Lipid vesicles are closed shell lipid bilayers dispersed in water. Depending on preparation protocols, their sizes can range from tens of nanometers to tens of microns. Giant unilamellar vesicles (GUVs) of a few tens of microns can be visualized directly with an optical microscope. On the other hand, large unilamellar vesicles (LUVs) of about 100 nm are often utilized to study the interactions of proteins with membranes. The permeation of molecules across lipid bilayers is also investigated with vesicles. Finally, vesicles have been studied as a drug delivery system taking advantage of their encapsulation capability and biocompability.

Langmuir monolayers at the air-water interface are yet another model membranes [8, 9]. The interfaces between their headgroups with buffer surfaces are models of biomembrane surfaces. The adsorption of proteins to them can be probed with film balance experiments and by x-ray or neutron reflectivity measurements, while the phase separation of lipids into domains is studied by optical microscopy. Nevertheless, since they are only monolayers, incorporation of integral membrane proteins which span both leaflets of biomembranes, is impossible.

The last model membranes are solid-supported lipid membranes [10–17]. There are generally two types of supported membranes: supported lipid bilayers on hydrophilic surfaces and supported lipid monolayers on hydrophobic surfaces. Both supported bilayers and monolayers were introduced in the early 1980s [10–12]. Since the inception, they have gained a widespread acceptance as models of biomembranes. They have been used extensively in both biomedical research and technological applications. There are at least two major advantages of using supported membranes: stability and uses of surface sensitive techniques. Due to the coupling with underlying solid substrates, they are mechanically more stable than BLMs and can last for days once they are formed. This is particularly crucial for practical applications that require a long term stability of devices. With a planar geometry on solid surfaces, one can use surface sensitive techniques [18] such as atomic force microscopy (AFM), surface

plasmon resonance (SPR), quartz crystal microbalance (QCM), x-ray and neutron reflectometry to study their interactions with DNA, proteins, or even living cells, which are otherwise hard if not impossible to apply to vesicles or BLMs. In term of technological applications, once incorporated with sensing or receptor proteins, they serve as a platform for biosensing, chemical separations and pharmaceutical screenings. Therefore, a combination of these advantages makes solid supported lipid membranes very attractive systems for various purposes.

Different architectures of supported membranes have been reported in the literature, such as (sparsely) tethered bilayer lipid membranes [19–25], hybrid bilayer membranes [26, 27], polymer-supported/tethered membranes [28, 29] and lipid bilayers directly supported on hydrophilic surfaces [12]. These membranes can be coupled to different substrates, such as gold, glass or silicon dioxide, as surface supports. Depending on the desired purposes, different architectures fulfill the requirements for some tasks, but not all the aspects mentioned previously. For instance, lipid bilayers directly supported on hydrophilic surfaces are prepared easily by incubating solid surfaces with lipid vesicles. However, there are only a few Angstroms of thin water gaps between supports and membranes, which make transmembrane proteins incorporation difficult. One would use polymer-supported lipid bilayers for transmembrane proteins incorporation because there are relatively thick hydrated layers (larger than 3 nm) between supports and membranes. However, these systems are usually not electrically insulating and are not suitable for electrical measurements. Consequently, the choice of a particular supported membrane system depends highly on the desired functions of the experiments or applications.

Among supported membranes, the most widely used model membranes are lipid bilayers directly supported on hydrophilic surfaces [30]. Typical substrates are glass, mica and silicon oxide. The preparation of such supported lipid bilayers does not require any special surface chemistry or grafting/tethering molecules for forming self-assembled monolayers (SAMs) as proximal leaflets (leaflets closer to solid surfaces). Supported lipid bilayers are formed on surfaces either by vesicle fusion [31] or Langmuir-Blodgett transfer [12]. In vesicle fusion, surfaces are incubated with vesicles. Vesicles adhere to surfaces and rupture to form continuous planar bilayers [32–34]. In Langmuir-Blodgett transfer, bilayers are transferred to solid substrates from Langmuir monolayers at the air-water interface in a two steps process.

As the most widely used supported membrane systems, it is imperative to under-

stand the fundamental properties of supported lipid bilayers to improve their design, patterning and fabrication. Therefore, in this thesis, we investigated the interactions of supported lipid bilayers on glass with detergents (Chapter 3) and organic solvents (Chapter 4), as these two agents are widely used to solubilize lipid bilayers. Isolated supported lipid bilayers with the area of a few thousand square microns were deposited on glass surfaces through rupturing of GUVs. These bilayer patches were labeled with fluorophores for visualization under a fluorescence microscope. They were incubated with detergents or organic solvents and the area expansion of bilayers due to partitioning of these molecules was captured by the microscope. From the partitioning dynamics of detergents, we constructed solubilization pathways of membranes by detergents and proved that a critical lipid:detergent ratio in membranes was not required to drive the dissolution for some detergents. From the titration of supported bilayers with organic solvents, we measured the increment of bilayers' area per volume fraction of organic solvents and the maximum area expansion of bilayers. For both cases, the stability of supported bilayers crucially relied on the curvature frustration of membranes and not the adhesion between solid surfaces and bilayers. The findings presented would help in designing mixed bilayers with different properties and understanding their stability under distinct environments.

However, from the studies above, it was discovered that proximal leaflets which face solid surfaces are immobile. Therefore, incorporation of integral membrane proteins into supported lipid bilayers is most probably meaningless since it will certainly impede functions of proteins. Consequently, to circumvent this problem, other supported membranes could be used. For this purpose, sparsely-tethered bilayer lipid membranes (stBLMs) are a very attractive candidate [23, 24].

A schematic diagram of a stBLM is shown in Figure 1.3. In stBLMs, some of the lipids in proximal leaflets are thiolated and are covalently attached to underlying gold surfaces through thiol-gold bonds (tethering lipids). The surface density of tethering lipids is controlled by co-adsorption of small spacer molecules, $\beta$-mercaptoethanol ($\beta$ME). Because tethering lipids have 6 or 9 units of hydrophilic ethylene glycerol in between the thiols and glycerol backbones and they are spaced out laterally by $\beta$ME, there are 1.5 to 2 nm thick hydrated submembrane spaces between gold surfaces and lipid membranes. The volume fraction of water in submembrane spaces can be higher than 60% depending on the lateral spacing of tethering lipids. The existence of submembrane spaces is advantageous for membrane protein incorporation since they

prevent a direct contact of proteins with solid surfaces. In fact, membrane proteins such as $\alpha$-hemolysin have been incorporated into stBLMs in a high density [35].

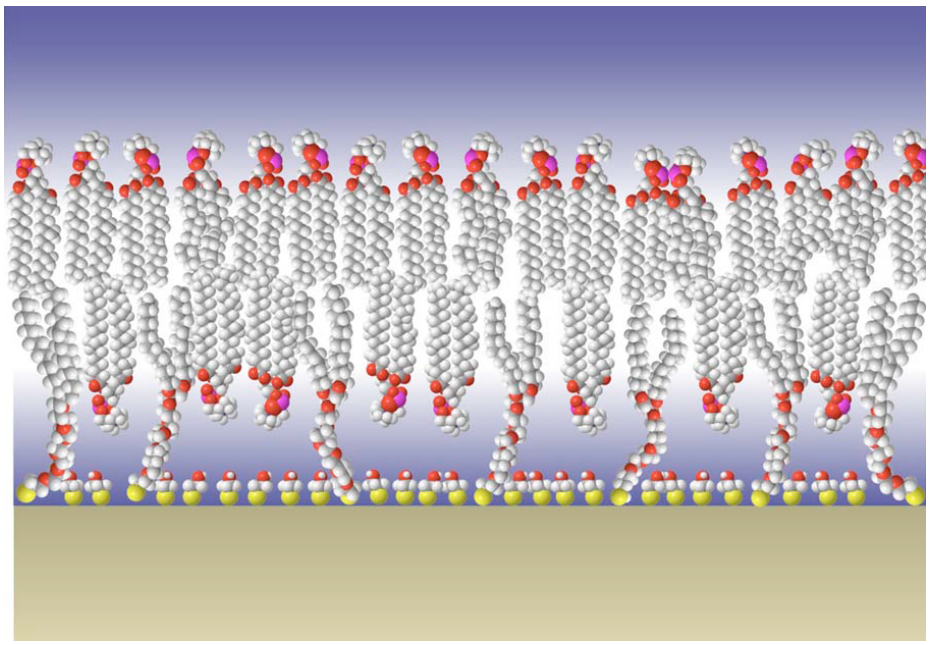

Figure 1.3: *A schematic diagram of a sparsely-tethered bilayer lipid membrane (stBLM). Some of the lipids in proximal leaflet are covalently attached to the underlying gold surface. Surface density of tethering lipids is controlled with co-adsorption of small spacer molecules, $\beta$ME. The surface chemistry of tethering lipids and spacer molecules decouples the lipid membrane from the gold surface with a nanometers thick hydrated submembrane space.*

There are three kinds of tethering lipids for the formation of stBLMs: WC14, FC16 and HC18. Both WC14 and HC18 have 6 units of ethylene glycerol whereas FC16 has 9 units of ethylene glycerol. The hydrocarbon chains for WC14, FC16 and HC18 are myristoyl, palmitoyl and oleoyl respectively. These tethering lipids have been tested to form well insulating stBLMs with different lipids.

Apart from the hydrated submembrane spaces that facilitate incorporation of membrane proteins, the underlying gold surfaces are also a strength for developing stBLMs into biosensors. With electrically conducting gold surfaces, Surface Plasmon Resonance (SPR) is utilized to quantify the binding of molecules to membranes and Electrical Impedance Spectroscopy (EIS) is used to probe the electrical properties. With the versatility of stBLMs, we used EIS to screen the quality of stBLMs formed with vesicle hemifusion in Chapter 5 and utilized SPR to examine the binding of

proteins to stBLMs in Chapter 7.

A traditional method to form stBLMs is through rapid solvent exchange (RSE) [20]. In this method, lipids of desired compositions are mixed in organic solvents (usually ethanol). Mixed SAMs that consist of tethering lipids and $\beta$ME are incubated with ethanolic solutions of lipids. These solutions are then flushed with aqueous solutions and lipids precipitate on mixed SAM surfaces to complete the bilayers. RSE is a reliable way in forming stBLMs on mixed SAMs of low hydrophobicity. Nevertheless, RSE renders the integral membrane protein incorporation impossible since proteins denature in organic solvents.

An alternative route to form stBLMs is through vesicle hemifusion [36] (see the Discussion of Chapter 6 for the explanation of the word 'hemifusion'). Lipid vesicles encountering hydrophobic surfaces reorganize and deposit lipid monolayers to the surfaces. Therefore, proteins incorporated in vesicles (proteoliposomes) are transported to stBLMs during hemifusion. Driven by this benefit, in Chapter 5, we optimized the vesicle hemifusion protocol for forming stBLMs. In addition, we revealed the mechanism of this process at a single vesicle level in Chapter 6.

Last but not least, we extended the application of stBLMs in molecular biology by developing a stBLM and lipid vesicles based *in vitro* assay to investigate functionality of GRASP (Golgi Reassembly And Stacking Protein) in membrane tethering. The assay relied on the ability of GRASP in tethering fluorescently-labeled vesicles to stBLMs and the results were quantified by the fluorescence intensity of images taken at stBLM surfaces. In addition, we performed neutron reflectivity measurements on GRASP bound on stBLMs to determine its orientation. The results are presented in Chapter 7 and the assay developed here could be broaden to study other membrane proteins on supported membranes.

# Chapter 2

# Experimental Techniques

A few important experimental techniques are introduced in this chapter. These techniques were used extensively to study the properties of solid-supported lipid membranes. They are Fluorescence Microscopy, Electrical Impedance Spectroscopy (EIS), Neutron Reflectivity (NR) and Surface Plasmon Resonance (SPR). Fluorescence Microscopy is employed to probe the lateral organization and the spreading of lipids on planar surfaces. Furthermore, diffusion of lipids is measured with Fluorescence Recovery After Photobleaching (FRAP). EIS investigates electrical properties of supported membranes whereas NR examines the stratified nature of samples structurally. Finally, SPR is sensitive to deposition of molecules on supported membranes. Since these methods complement each other, a combination of them thus provides a coherent picture of the samples under scrutiny.

## 2.1 Fluorescence Microscopy

Fluorescence is a phenomenon in which a fluorophore emits a photon after it absorbs another photon at the other wavelength. The absorption/excitation and the corresponding emission spectrum are the unique properties of a particular fluorophore. The emission is Stokes-shifted if the emitted photon is longer in wavelength compared with the absorbed photon. It is the Stokes shift between the excitation and the emission that makes fluorescence so useful, since it enables one to selectively detect the fluorophores of interest. For instance, in a typical fluorescence experiment, one excites the fluorophores at the excitation wavelengths and detects at the emission wavelengths by using appropriate filters, and hence filters out the exciting light without

blocking the emission fluorescence. With the filtering scheme, one could differentiate the fluorescing objects from the background environment in a specific way. To put in the other word, fluorescence imaging is almost equivalent to chemical imaging since it only detects the desired molecules.

Fluorescence Microscopy [37, 38] has become a standard and powerful technique in both biomedical and materials science research. This trend is accelerated by the rapid development in the field of fluorescent proteins and organic dyes, which could be easily tagged to molecules of interest. As a result, with the labeling, the samples are visualized under a fluorescence microscope. Spatial distributions of fluorophore-tagged molecules are reflected by the intensity in fluorescence images. Additionally, if images are taken as a function of time, spatio-temporal dynamics of samples is revealed by fluorescence imaging.

Solid-supported lipid membranes are well-suited to be studied by fluorescence microscopy. As the membranes are only nanometers thick and are confined in a planar geometry by solid supports, fluorescence imaging can be carried out without invoking the scanning in the axial direction. In a typical case, membranes are doped with small amounts of fluorescently-labeled lipids. As long as the doping level is low, the fluorescently-labeled lipids are expected to follow the bulk properties of the membranes. For instance, membrane lateral organization is probed with fluorescence microscopy. This includes phase separation of membranes into different domains [39, 40] and presence of defects in membranes. A fluorescence image of a DOPC hybrid bilayer membrane, with an OTS SAM (see Chapter 6) as the underlying substrate, is displayed in Figure 2.1. DOPC was doped with 0.125 mol% of LR-PE, a fluorescently-labeled lipid, in this example. Apart from the edge of a field stop, which shows up on the upper right and upper left corner of the image, the image is featureless and has uniform fluorescence intensity across the entire image. It implies that LR-PE (or DOPC) was homogeneously distributed across the entire field of view and the membrane was defect-free down to the optical resolution (features below the optical resolution can be investigated with AFM). In addition, time-lapsed fluorescence microscopy is used to visualize the spreading of lipid membranes on solid surfaces [41–45]. Consequently, in this thesis, fluorescence microscopy was utilized to study the hemifusion of lipid vesicles with planar hydrophobic surfaces and the spreading of lipid mono/bilayers on the corresponding surfaces.

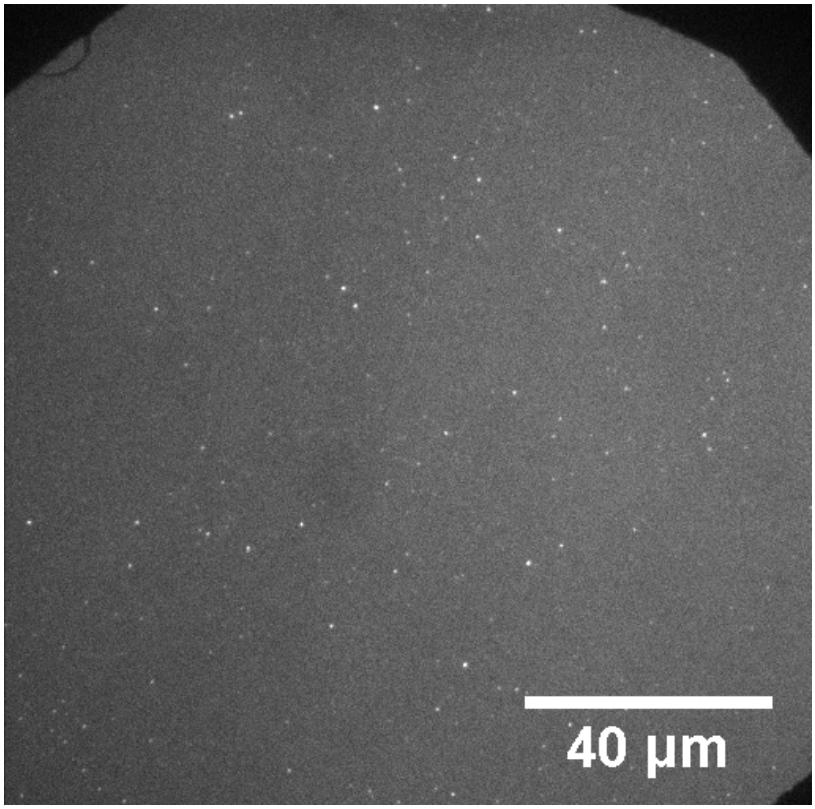


Figure 2.1: *A fluorescence image of a DOPC hybrid bilayer membrane.*

Apart from membranes, fluorescence microscopy is used to investigate biomolecules such as proteins [46], DNA, and lipid vesicles [47–50], which are absorbed on membranes. To image these objects, they need to be fluorescently labeled. Their behavior and binding stoichiometry on membranes are studied with single particle tracking [46, 51]. Moreover, their binding to membranes is quantified by measuring the intensity of recorded fluorescence images, because the fluorescence intensity of the images is directly proportional to the amount of fluorescing objects bound to membranes. This implementation opens up a new window in biosensing. For example, by incorporating suitable receptors into supported membranes, corresponding binding of fluorescently-labeled ligands to the receptors is detected with a fluorescence microscope. Following this setup, we developed a fluorescence microscopy based *in vitro* assay to examine functionality of GRASP in tethering fluorescently-labeled lipid vesicles to supported membranes. The ability of GRASP in tethering vesicles to membrane surfaces is quantified by measuring the fluorescence intensity of the images taken at membranes interfaces (see chapter 7 for details). This example demonstrates the strength of

fluorescence imaging in exploring supported membranes related phenomena.

### 2.1.1 Instrumentation of Fluorescence Microscopy

In our experiments, fluorescence microscopy imaging was performed by using an inverted Carl Zeiss Axiovert 200M microscope. Fluorescence images were recorded with a Hamamatsu C9100-12 EM-CCD camera (Hamamatsu, Bridgewater, NJ), controlled with IPLab (Biovision Technologies, Exton, PA). The excitation source was a 100 W HBO103W/2 mercury lamp (Osram, Munich, Germany). Both excitation and emission light were focused by a Carl Zeiss oil-immersion, Plan-Apochromat objective, which has a numerical aperture (NA) of 1.4.

Supported lipid membranes were assembled on #1.5 thickness glass coverslips which were purchased from Electron Microscopy Science (Hatfield, PA), with or without extra gold layers or self-assembled monolayers (SAMs) coating. The glass coverslips were assembled in Skyes-Moore chambers for imaging. Two fluorescently labeled lipids were used throughout the experiments in this thesis, 1,2-dioleoyl-sn-glycero-3-phosphoethanolamine-N-(lissamine rhodamine B sulfonyl) (ammonium salt) (LR-PE) and 1,2-dipalmitoyl-sn-glycero-3-phosphoethanolamine-N-(7-nitro-2-1,3-benzoxadiazol-4-yl) (ammonium salt) (NBD-PE). Both fluorophores were purchased from Avanti Polar Lipids (Alabaster, AL) and the fluorescing moieties, lissamine rhodamine and nitrobenzoxadiazole (NBD), are located on the lipid' headgroups. Lissamine rhodamine is bulkier than NBD albeit has an advantage that it is more photostable. In chloroform, the excitation maximum for lissamine rhodamine is at 560 nm while the emission maximum is at 583 nm. For NBD, it is 460 nm and 535 nm. Accordingly, to detect LR-PE, a combination of Carl Zeiss filter set BP546/12:FT560:BP665/20 was used. While for NBD-PE, a BP450-490:FT510:BP515-565 filter set was used. For pre-focusing on glass-water interfaces without any fluorophores bound on surfaces, we also set up a filter set to detect the reflection of light from the glass-water interfaces. To achieve this, dichroic mirrors are replaced by 50:50 beam splitters and no emission filters are placed between samples and the camera. With this combination of filter, one could focus exclusively on glass surfaces without the help of fluorescence emitted from supported membranes.

The detection scheme in a standard epi-fluorescence widefield microscope is schematically shown in Figure 2.2. White light from a mercury lamp, represented by arrows

in 3 colors (red, green and blue), travels from the left to the right. An excitation filter, mounted on a filter cube, only allows light of selected wavelengths to pass through it (blue light in this case). Upon entering the filter cube, the blue light is reflected 90° upward by a dichroic mirror inclined 45° with respect to the filter cube. The blue light is then focused by a microscope objective to a supported membrane and excites fluorophores. Fluorescence emission from the fluorophores, represented by red light to show the emission is Stokes-shifted with respect to the excitation, is collected by the same objective and passes through the dichroic mirror again. Any light other than the emission is blocked by the emission filter. Finally, the emitted light travels to a camera and forms an image.

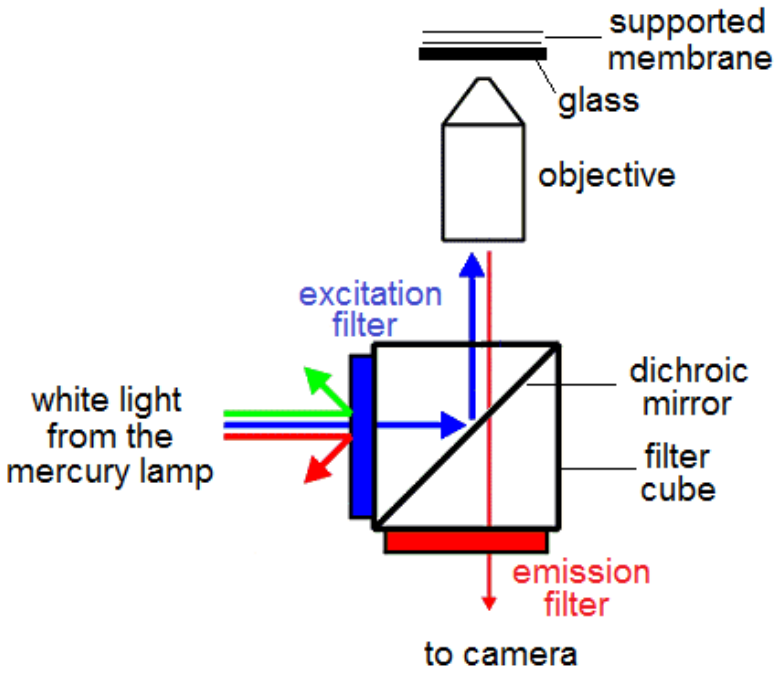


Figure 2.2: *The schematic diagram of the excitation and the emission scheme in an epi-fluorescence wildfield microscope.*

In our case, a high NA objective of 1.4 was used. It is advantageous to use a high NA objective because it has a small depth of field. Depth of field [38] is defined as the axial distance between the nearest and the farthest objects in an image plane that appears sharp. Its value, arbitrarily defined as the first minimum in the axial position of the point spread function, is given by the formula $2n\lambda/NA^2$, in which $n$ is the refractive index of water at 1.33 and $\lambda$ is the wavelength of the emitted light.

For LR-PE, the emitted wavelength is 665 nm as controlled by the emission filter. Consequently, the depth of field is about 900 nm. Any object that is farther away from the focus plane by this distance will appear blur on the image since fluorescence emitted by it is defocused. Although fluorescence originated outside of this depth of field is not blocked by a pinhole as in confocal microscopy, a high NA objective improves the optical sectioning in the axial direction significantly for a widefield microscope. This is crucial as we need to focus on two distinct focal planes when we studied the hemifusion of microns size Giant Unilamellar Vesicles (GUV) with planar hydrophobic surfaces (see chapter 6 for details). High NA objective supplies the optical sectioning in the emission volume and enables a sharp focusing at desired planes with a minimal disturbance from other planes.

### 2.1.2 Fluorescence Recovery After Photobleaching (FRAP)

Fluorescence microscopy could be easily adapted to perform Fluorescence Recovery After Photobleaching (FRAP) experiments. FRAP is used extensively to study the diffusion of lipids within planar membranes, the mobility of absorbed objects and the binding reaction on membrane surfaces [52–56]. In a typical FRAP experiment, planar membranes are mixed with a low concentration of fluorophores and a small spot on the membranes is illuminated by high intensity excitation light. This excitation light photobleaches some fluorophores in this small spot and lowers the fluorescence intensity of the spot compared with its surrounding. The intensity of the excitation light is then lowered to a level that does not further photobleach fluorophores. The bleached fluorophores diffuse out of the spot whereas unbleached fluorophores outside the spot diffuse into the spot. Correspondingly, the fluorescence intensity of the bleached spot recovers. By monitoring the recovery of the spot's fluorescence intensity, diffusion coefficients of the fluorophores are measured. In comparison with Fluorescence Correlation Spectroscopy (FCS) [57, 58] or single particle tracking [51, 59], FRAP has the advantages that it is technically simpler than the other two methods and does not require a super low concentration of fluorophores (a few fluorophores within a diffraction limited spot).

For our fluorescence microscope, a small circular spot of about 26 $\mu$m in diameter, confined by a field stop, is illuminated by a mercury lamp at its highest intensity for about 10 s. As a result, we create a uniformly bleached circular spot. After this, the

intensity of the excitation light is reduced to its minimum setting and the fluorescence images of the bleached spot are taken for the next 1 or 2 minutes. The fluorescence intensity recovery of the bleached spot is then obtained directly from the images taken. To quantitatively evaluate the recovery, recovery curves are fitted to an equation describing the recovery of a uniformly bleached circular spot [55],

$$I(t) = I(0) + [I(\infty) - I(0)] * exp(-2\tau/t) * [I_0(2\tau/t) + I_1(2\tau/t)] \qquad (2.1)$$

$I(0)$ is the fluorescence intensity of the bleached spot at $t = 0$ of the recovery and $I(\infty)$ is the intensity at $t = \infty$, $\tau$ is the characteristic recovery time, $I_0$ and $I_1$ are the modified Bessel function of the first kind of zeroth and first order. For a bleached spot with a radius $r$, the diffusion coefficient, $D = r^2/4\tau$, is thus obtained. Any deviations of the recovery curves from the fitting equation indicate the bleached spots are not uniformly bleached circularly, for example when the bleaching time is comparable to the characteristic recovery time. For fluid membranes supported on solid surfaces, the typical diffusion coefficients of lipids are on the order of a few $\mu m^2/s$ [60, 61]. Strictly speaking, it is the diffusion coefficients of fluorophores, which may have distinct chemical structures than the rest of lipids in the membranes, that are being measured. Nevertheless, these diffusion coefficients are often cited to represent the diffusion coefficients of the remaining lipids. Besides, in practice, when fluorescence images of supported membranes are taken, it is imperative to do the FRAP experiments to verify the objects in the images are indeed supported membranes and are not due to reflection from solid surfaces.

An exemplary fluorescence recovery curve is shown in Figure 2.3, where the fluorescence intensity is plotted as a function of time. An isolated DOPC bilayer supported on glass, which was used as the sample in Chapter 3 and 4, was mixed with 0.3 mol% of LR-PE. A circular spot of about 13 $\mu$m was bleached and the fluorescence intensity of that spot was monitored for the next 1 minute. The recovery trace was fitted to Eq. (2.1) and the resulting diffusion coefficient was $2.31 \pm 0.09\,\mu m^2/s$, which is reasonable. It illustrates the usefulness of FRAP in probing the property of supported membranes.

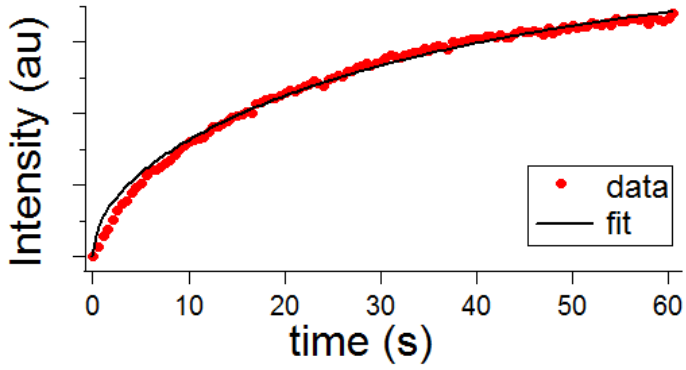


Figure 2.3: *An example of a fluorescence recovery curve in a FRAP experiment.*

## 2.2 Electrical Impedance Spectroscopy (EIS)

Electrical Impedance Spectroscopy (EIS) [62] is used to investigate electrical properties of solid-supported lipid membranes. In a typical impedance measurement, a sinusoidal voltage of amplitude $V_\circ$ and angular frequency $\omega$ (or frequency $f$, in which $\omega = 2\pi f$), $V(\omega) = V_\circ \exp(i\omega t)$, is applied across a sample. Provided the applied voltage, $V(\omega)$, is small enough and only perturbs the sample slightly from its equilibrium condition, the response will be linear. A current, $I(\omega) = I_o \exp(i(\omega t - \theta))$, which has a real amplitude $I_o$, an angular frequency $\omega$ (because the response is linear), and a phase shift between the voltage and current, $\theta$, is produced. As a result, the impedance of the system at the angular frequency $\omega$, $Z(\omega)$, is given by $Z(\omega) = V(\omega)/I(\omega) = (V_o/I_o)\exp(i\theta)$. Since $Z(\omega)$ is a complex number, it has both a magnitude $\mid Z \mid$ and a phase of $\theta$, where $Z(\omega) =\mid Z \mid \exp(i\theta)$. The impedance is measured as a function of frequency. Its magnitude, $\mid Z \mid$, and phase, $\theta$, are plotted against frequency in a Bode plot and form a corresponding impedance spectrum.

EIS can unravel electrical properties of layered structures in a relatively straightforward manner. In our measurements, the frequency of the applied voltage is from 0.1 Hz to 100 kHz. In this range of frequency, since supported lipid membranes are non-magnetic, the dispersion of the impedance is due to the interfacial polarization (accumulation of charges on layer interfaces) [63] and the transport of charges across the layers. Therefore, each layer in the layered structures could be modeled as a resistor having a resistance, $R$, in parallel with a capacitor having a capacitance, $C$. The capacitance in this parallel $RC$ accounts for the accumulation of charges at the interfaces whereas the resistance accounts for the charge transport across the layers.

As a consequence, if a sample has N such layers, electrically it is equivalent to N parallel $RC$ that are arranged in series, as shown in Figure 2.4 [64–67]. Modeling the impedance response of a system with this approach is termed equivalent circuit modeling. Routinely, upon performing an impedance measurement, the resulting impedance spectrum is fitted to an equivalent circuit in Figure 2.4 to extract the resistance and capacitance of each layer.

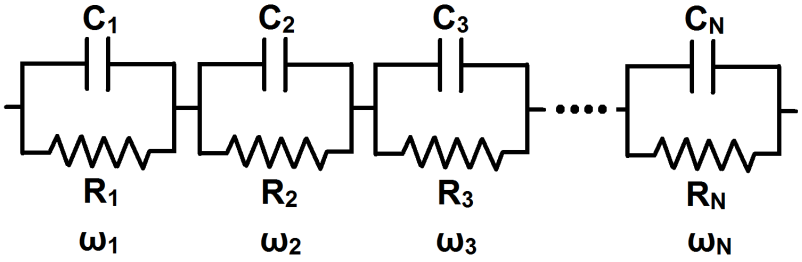


Figure 2.4: The equivalent circuit used to to model the impedance spectrum of a layered structure.

Mathematically, the impedance of a capacitor with a capacitance $C$ is $1/i\omega C$, with a phase of $-90°$. For a resistor with a resistance $R$, the impedance is $R$ and the phase is zero. Similarly, the total impedance of a parallel $RC$ is given by

$$Z = \frac{R}{1 + (i\omega/\omega_{RC})} \tag{2.2}$$

$\omega_{RC} = 1/RC$ is the characteristic frequency of the parallel $RC$. For elements in parallel, the total impedance at a particular frequency is dominated by the element that has a much smaller magnitude of impedance compared with the rest of the elements. So for a parallel RC, at high frequency ($\omega >> \omega_{RC}$), $\mid Z \mid \rightarrow 1/i\omega C$ and the phase approaches $-90^o$. The phase is $-45^o$ when $\omega = \omega_{RC}$. As the frequency decreases to $\omega << \omega_{RC}$, the resistance dominates the total impedance with $\mid Z \mid \rightarrow R$ and the phase $\rightarrow 0$.

For N parallel $RC$ that are in series, the total impedance is

$$Z = \sum_{i=1}^{N} \left[ \frac{R_i}{1 + (i\omega/\omega_i)} \right] \tag{2.3}$$

It is obvious that if $\omega_h = \omega_k$, the denominator of the $h$-th term in the sum is equal to the denominator of the $k$-th term, these 2 terms could be combined into a single term. This implies that 2 parallel $RC$, which have an identical $\omega_{RC}$ and in series, may not be resolved electrically by frequency domain impedance measurements even if they have distinct $R$ and $C$. Instead, the impedance spectrum of a series combination of parallel $(R_1C_1)$ and $(R_2C_2)$ with the same $\omega_{RC}$ is identical to the impedance spectrum of a single parallel $RC$ with $R = R_1 + R_2$ and $C = \omega_{RC}/(R_1 + R_2)$. This phenomenon directly points to a fact that the equivalent circuit modeling is not unique and there might be more than one equivalent circuit that could explain the impedance spectrum. Similarly, for elements in series, the total impedance is dominated by the element that possesses a much larger magnitude of impedance compared with the rest. Hence, for a series combination of parallel $RC$, if each parallel $RC$ has a $\omega_{RC}$ differs from the other $\omega_{RC}$ by orders of magnitude, one can see the phase of the impedance oscillates between $\sim -90^o$ and $\sim 0^o$ in the impedance spectrum, since the impedance is dominated by different $R$ and $C$ at different frequency range. To illustrate this, we produced an impedance spectrum of 3 parallel $RC$ arranged in series. The simulated spectrum is shown in Figure 2.5, with the magnitude and the phase of the impedance plotted as a function of frequency. In this combination, $R_1 = 10\,\Omega$, $C_1 = 10^{-9}\,\mathrm{F}$, so $\omega_1 = 10^8\,\mathrm{rad/s}$, $R_2 = 10000\,\Omega$, $C_1 = 10^{-7}\,\mathrm{F}$, so $\omega_2 = 10^3\,\mathrm{rad/s}$, and finally $R_3 = 10^7\,\Omega$, $C_3 = 10^{-5}\,\mathrm{F}$, so $\omega_3 = 10^{-2}\,\mathrm{rad/s}$. The $\omega_{R_iC_i}$ in this example differs from each other by 5 or 10 orders of magnitude. At the highest frequency of this spectrum ($f$ from $10^8$ to $10^6$ Hz), the total impedance is dominated by the parallel $R_1C_1$, so $Z_{total} \sim Z_{R_1C_1}$. At this frequency range, the phase of the impedance increases from $\sim -90^\circ$ to $\sim 0^\circ$ as the frequency decreases because the impedance that is dominated by $C_1$ at high frequency is taken over by $R_1$ as the frequency goes down. $\mid Z_{total} \mid \sim 1/\omega C_1$ when the phase $\sim -90^\circ$ and $\sim R_1$ when the phase $\sim 0^\circ$. According, $\mid Z \mid$ show a plateau when the total impedance is dominated by $R_1$ since its value is frequency independent around that frequency. The phase is $\sim -45^\circ$ when $\omega = \omega_1$ and the $\omega_1$ is labeled in Figure 2.5. When the frequency is lower than $10^6$ Hz, $R_2C_2$ starts to play a role in the impedance spectrum. As $\omega$ is still much larger than $\omega_2$, the impedance of the parallel $R_2C_2$ is dominated by $C_2$. It is the competition between $C_2$ and $R_1$ (they are in series in this frequency range since the other elements in the circuit are not crucial in determining the impedance) that brings the phase of the impedance from $\sim 0^\circ$ (phase of $R_1$) at $f \sim 10^6$ Hz to a phase

of $\sim -90°$ (phase of $C_2$) again at $f \sim 10^4$ Hz. The impedance from $f \sim 10^4$ to 10 Hz is totally dominated by the parallel $R_2C_2$. Therefore, the phase of the impedance increases from $\sim -90°$ to $\sim 0°$ in this range with a phase of $\sim -45°$ at $\omega = \omega_2$. Following the same argument, the parallel $R_3C_3$ will finally compete with the parallel $R_2C_2$ and bring the phase down to $\sim -90°$ and up to $\sim 0°$ in the end.

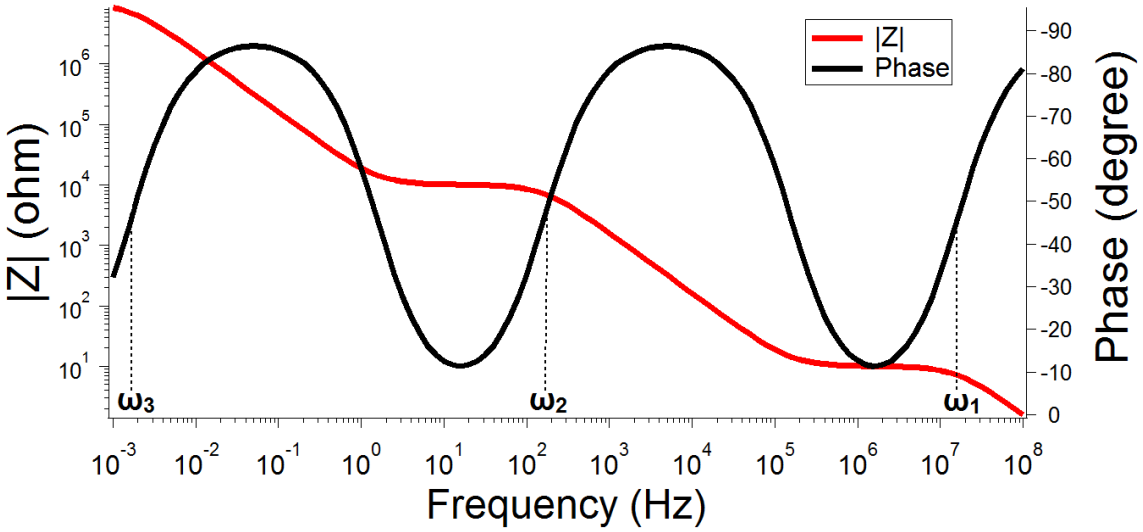


Figure 2.5: *The impedance spectrum modeled with 3 parallel RC that are in series. The magnitude of the impedance, | Z |, is colored in red while the phase is colored in black.*

In a nutshell, we have shown how an equivalent circuit is related to the corresponding impedance spectrum. From the impedance spectrum, one can derive an equivalent circuit and estimate good starting values for $R$ and $C$ for the equivalent circuit fitting based on the physical principles discussed. Lastly, it is also critical to notice that the frequency range in a particular measurement decides which element can be uncovered by the impedance spectrum. For instance, in Figure 2.5, if the measurement is performed beyond 10 Hz or $\omega >> \omega_3$, there is no way one could unravel the exact values of $R_3$ and $C_3$.

### 2.2.1 stBLM and EIS

A typical impedance spectrum of a DPhyPC stBLM is shown in Figure 2.6. To extract the pertinent electrical parameters such as the capacitance and the resistance

of the stBLM, the spectrum is fitted to an equivalent circuit as shown in Figure 2.7. The equivalent circuit is conceived by considering the stratified nature of stBLMs. It consists of a parallel $RC$ ($R_{solution}$ and $C_{stray}$) that accounts for the electrical properties of buffer solutions. In series with this parallel $RC$, gold-submembrane space interfaces are modeled with a capacitor of capacitance $C_{gold}$. Gold surfaces are polarizable electrodes in these measurements, namely charges accumulate at gold surfaces to form Helmholtz and Gouy-Chapman layer, leading to a capacitive behavior [68]. No charges are transferred across gold-submembrane space interfaces within the frequency of measurements. Therefore, a capacitor is sufficient to capture the feature of gold surfaces instead of a parallel $RC$. Finally, a $R_{stBLM}$ in parallel with a $CPE_{stBLM}$ are used to represent lipid membranes. $CPE$ stands for constant phase element and its impedance is $Z = 1/[CPE(i\omega)^{\alpha}]$ [62]. CPE is equal to capacitance if $\alpha = 1$. $CPE$ is widely employed in equivalent circuit modeling in place of a capacitor to model the behavior that deviates from a capacitor. There are a lot of physical effects that lead to $CPE$, such as surface roughness and distribution of relaxation time [62, 64]. In this equivalent circuit, $CPE$ significant improves the fitting at a frequency range when the phase increases from $\sim -90^{\circ}$ toward $0^{\circ}$ as the frequency decreases (from 100 to 10 Hz in Figure 2.6). The deviation from a capacitor happens when stBLMs start to conduct ions across them or when $R_{stBLM}$ begins to play a role in determining the total impedance of the systems. A highly possible reason for this deviation is that gold surfaces of stBLMs are not an ideal sink or source of ions as assumed by the gold capacitance [69, 70]. For example, the Deybe length of gold surfaces is comparable to the thickness of submembrane spaces so that the Gouy-Chapman layers of the gold surfaces penetrate into the lipid membranes [71]. Still, for stBLMs, usually $\alpha > 0.95 \sim 1$. As a result, one can equate the numerical values of $CPE$ to the numerical values of lipid membrane capacitances and the numerical values of $R_{stBLM}$ do not change significantly regardless of the choice of constant phase elements or capacitances in the equivalent circuit fittings.

In Figure 2.6, the fitting was performed from 10 Hz to 30 kHz. Depending on how insulating a particular stBLM is, sometimes even at the lowest frequency of the impedance measurements (0.1 Hz), the gold capacitance does not play a role in the impedance spectra. Consequently, to make our equivalent circuit fitting consistent, we ignored the gold capacitance in the equivalent circuit. For this reason, 10 Hz was chosen as the lower bound frequency of the fitting in Figure 2.6 because this

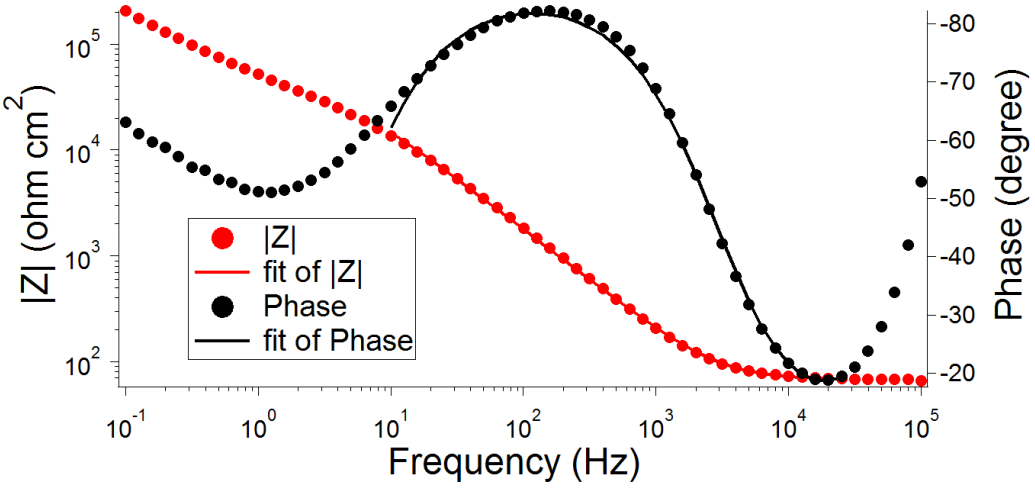


Figure 2.6: *The impedance spectrum of a DPhyPC stBLM and the corresponding equivalent circuit fitting. | Z | is colored in red while the phase is colored in black. The data points are in dots (•) whereas the corresponding fits are in continuous line (—).*

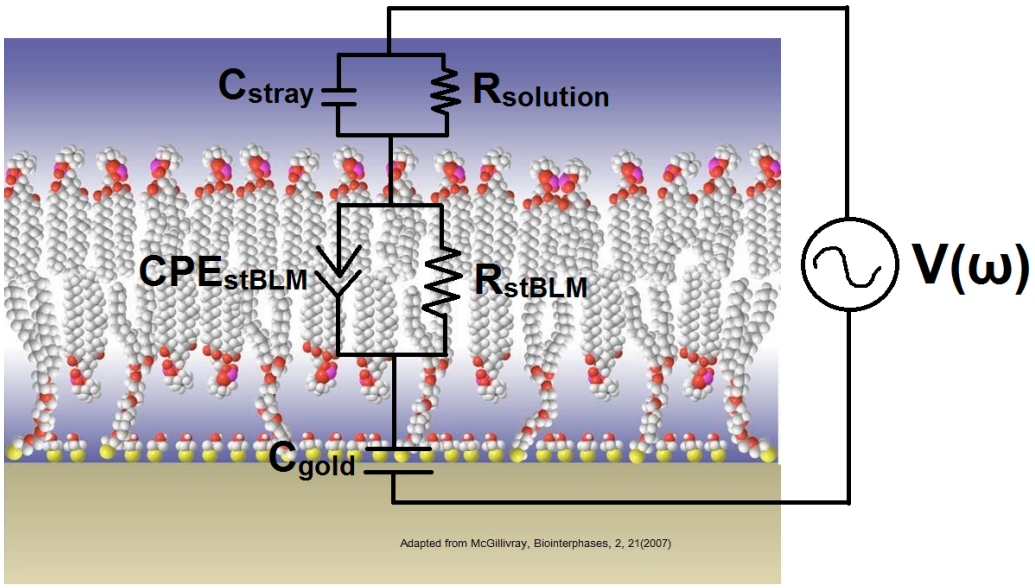


Figure 2.7: *A schematic diagram on how the impedance measurement is performed on a stBLM and the equivalent circuit of the stBLM. A sinusoidal voltage $V(\omega)$ is applied across the stBLM as shown and the impedance is recorded at different $\omega$. The impedance spectrum is then fitted to an equivalent circuit that mimics the behavior of the stBLM electrically.*

$\omega \sim \omega_{R_{stBLM}C_{stBLM}} \sim \omega_{R_{stBLM}CPE_{stBLM}}$. Accordingly, within this fitting range, the impedance spectrum was only minimally influenced by the gold capacitance while we were able to reveal the value of $R_{stBLM}$ and $CPE_{stBLM}$ accurately. In this example, the DPhyPC stBLM has a $R_{stBLM}$ of $35 \pm 1\,\mathrm{k\Omega cm^2}$, $CPE = 1.13 \pm 0.18\,\mu\mathrm{Fcm^{-2}s^{\alpha-1}}$ and $\alpha = 0.936 \pm 0.002$. As discussed previously, since $\alpha \sim 1$, numerical values of $CPE_{stBLM}$ are close to numerical values of $C_{stBLM} = \epsilon_o \epsilon_{CH} d$. $\epsilon_o$ and $\epsilon_{CH}$ are the permittivity of free space and the dielectric constant of hydrocarbon chains of membranes respectively, and $d$ is the thickness of membranes at $\sim 3$ nm. $CPE_{stBLM}$ is close to the capacitance of lipid bilayers or cellular membranes [72], verifying the robustness of stBLMs in mimicking the electrical properties of biological membranes. As a concluding remark, it is intriguing to notice that $R_{stBLM}$ and $C_{stBLM}$ are both very sensitive to water-filled pores in membranes. Electrically, water-filled pores are modeled as a parallel $R_{pore}C_{pore}$, which is in parallel with $R_{stBLM}C_{stBLM}$. Therefore, $R_{pore}C_{pore}$ combines with $R_{stBLM}C_{stBLM}$ to give an effective parallel $R_{effective}C_{effective}$ with

$$R_{effective} = \frac{R_{pore}R_{stBLM}}{R_{pore} + R_{stBLM}} \tag{2.4}$$

and

$$C_{effective} = C_{pore} + C_{stBLM} \tag{2.5}$$

Provided the area fraction of water-filled pores is large (> a few percents), it follows that $R_{effective} \sim R_{pore}$ since $R_{stBLM} \gg R_{pore}$ [23] and $C_{effective}$ increases significantly by a factor of 2 to 4. As a result, the impedance spectrum of a stBLM with a few percents of water-filled pores resembles the impedance spectrum of a SAM because the impedance of the stBLM is no longer much larger than the impedance of gold and aqueous phase to be resolved uniquely. It also demonstrates that beyond a certain threshold value of pore coverage (> 5% for example), EIS is no longer suitable to characterize the properties of stBLMs. Therefore, EIS measurements can be used as the quality control experiments in assessing the completeness of stBLMs.

### 2.2.2 Instrumentation of EIS

Impedance measurements [23] were performed by using a Solartron (Farnborough, UK) system, with a combination of a model 1286 potentiostat and a model 1250 frequency response analyzer, controlled with Zplot (Scribner Associates, Southern Pines, NC). The schematic diagram of the setup is shown in Figure 2.7. A voltage, $V(\omega)$, of amplitude 10 to 30 mV was applied across stBLMs and the measurements were carried out from 100000 to 0.1 Hz. Gold surfaces of stBLMs were used as the working electrodes. The reference voltages across stBLMs were measured with a saturated silver-silver chloride microelectrode (Microelectrodes, Bedford, NH) and the current was injected by a platinum wire (Sigma Aldrich, St. Louis, MO). All measurements were performed at 0 V bias against the open circuit potential of the samples. Lastly, the equivalent circuit fitting was performed by using ZView (Scribner Associates, Southern Pines, NC) with the equivalent circuit as shown in Figure 2.7.

## 2.3 Neutron Reflectivity (NR)

Neutron Reflectivity (NR) is a standard method for probing structures of solid-supported lipid membranes at an Angstrom level [2, 8, 9, 73–75]. In NR experiments, neutrons are specularly reflected by a set of interfaces in a stratified medium. This is shown schematically in Figure 2.8. The incident neutron beam of intensity $I_o$, directed at an incident angle $\theta$, impinges on the medium. In this stratified structure, each layer $i$ has a thickness $d_i$ and a neutron scattering length density (nSLD) $\rho_i$. Due to the wave-particle duality, neutrons with a momentum $p$, are described as a plane wave having a de Broglie wavelength of $\lambda = h/p$. At the same time, the neutron scattering length density, $\rho_i$, could be related to the "refractive index" of the layer, $n_i$, through the relationship $n_i = 1 - \frac{\lambda^2}{2\pi}\rho_i$. Therefore, it is clear that reflection of neutrons from an interface is similar in nature to reflection of light as seen in daily life.

If neutrons are specularly reflected with angles of incidence = angles of reflection $= \theta$, the momentum transfer, $Q_z$, is in the direction normal to these interfaces, with $Q_z = \frac{4\pi}{\lambda} sin\theta$. The intensity of reflected neutrons, $I_R$, is recorded as a function of the reflected angles or the momentum transfer, $Q_z$. This can be presented in a reflectivity curve where the reflectivity, $R = I_R/I_o$, is plotted as a function of momentum transfer, $Q_z$. The depth profile of the stratified medium is retrieved from the reflectivity curve

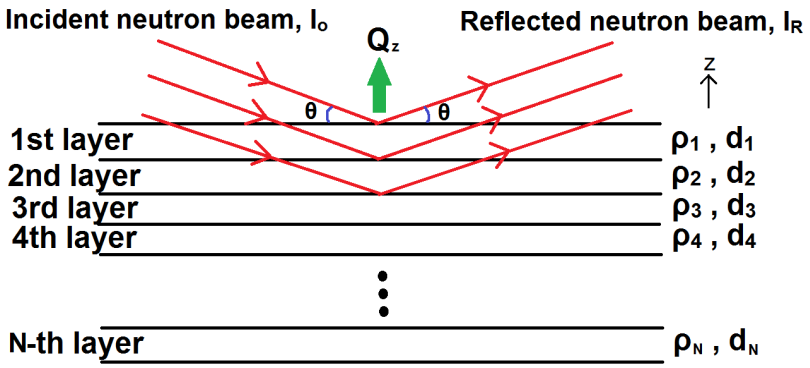


Figure 2.8: *The schematic diagram of a neutron reflectivity experiment performed on a stratified medium that has N layers. Each layer in the medium has a thickness $d_i$ and a neutron scattering length density $\rho_i$. The incident neutrons of intensity $I_o$ are reflected specularly (angle of incidence = angle of reflection = $\theta$) from each interface due to the difference in $\rho$. The intensity of reflected neutron, $I_R$, is recorded as a function of $\theta$ or $Q_z$.*

either by direct inversion of the reflectivity curve to a nSLD profile or through model fitting [76].

The interactions of neutrons with matter satisfy the Schrödinger equation and this equation can be reduced to Helmholtz equation. As a result, by matching the boundary conditions at each interface for a multilayer system as in Figure 2.8, the reflectivity from the interfaces can be calculated by the so-called transfer matrix method [73]. This transfer matrix method is exactly identical with the matrix method in light reflection, which is governed by the Maxwell equations. In this method, the $i^{th}$ layer is represented by a 2 x 2 transfer matrix, $M_i$,

$$M_i = \begin{pmatrix} cos(Q_z n_i d_i/2) & sin(Q_z n_i d_i/2)/n_i \\ -n_i sin(Q_z n_i d_i/2) & cos(Q_z n_i d_i/2) \end{pmatrix}$$

Consequently, for a N-layer system, the total transfer matrix, $M = M_N M_{N-1} ... M_2 M_1$. M is still a 2 x 2 matrix with $M = \begin{pmatrix} M_{11} & M_{12} \\ M_{21} & M_{22} \end{pmatrix}$. The reflectivity, $R$, for this system is then given by

$$R = \frac{(M_{11}^2 + M_{12}^2 + M_{21}^2 + M_{22}^2)/2 - 1}{(M_{11}^2 + M_{12}^2 + M_{21}^2 + M_{22}^2)/2 + 1} \tag{2.6}$$

For neutron reflectivity of stBLMs, the measurements are typically repeated on a

sample by using two or three solvent contrasts, namely $D_2O$ (with a $\rho \sim 6.4\times10^{-6}$ Å$^{-2}$), CM4 (contrast mixture of $H_2O$ and $D_2O$ with a $\rho \sim 4 \times 10^{-6}$ Å$^{-2}$), or $H_2O$ (with a $\rho \sim -0.56 \times 10^{-6}$ Å$^{-2}$). As a result, two or three reflectivity curves are generated for a physical sample. These curves are then fitted to a model to improve the confidence on the validity of the model and allows us in highlighting different layers in the sample. Reflectivity curves of a DPhyPC stBLM on a FC16:$\beta$ME = 1:1 SAM, which were obtained with three different solvents, are shown in Figure 2.9. The data points are shown in dots (•) while the corresponding box model fittings are represented by lines (—) (see next paragraph for the box model fitting). Oscillations are observed in the curves due to the interference of reflected neutrons. For a 3-layers system, which has 2 interfaces, in the limit of $R \ll 1$ where the kinematic approximation is true [73], the amplitude of oscillations is proportional to the difference of $\rho$ across the interfaces and the period of oscillations is inversely proportional to the distance between two interfaces.

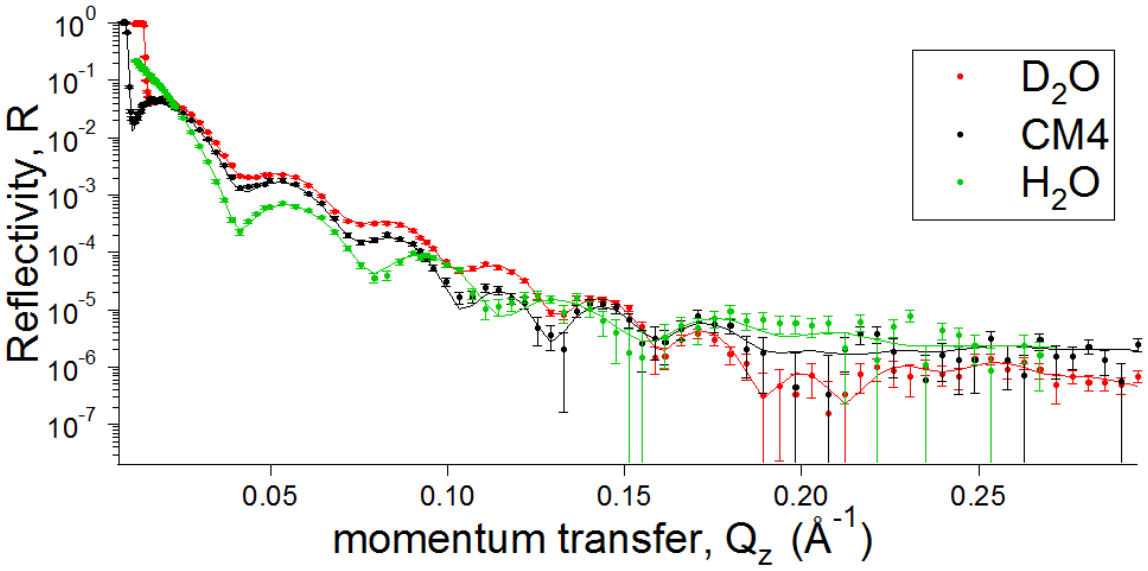


Figure 2.9: *The reflectivity curves of a DPhyPC stBLM on a FC16:$\beta$ME = 1:1 SAM. The reflectivity measurements were carried out by using 3 different solvents ($D_2O$, CM4 and $H_2O$) with a distinct $\rho$. The data of the curves is shown in dots (•) while the best-fits to the box model are shown in lines (—).*

### Box Model

The first method to extract structural information from reflectivity curves is through the box model fitting [23, 24]. In a box model, each layer in the stratified medium has a thickness $d_i$ and a neutron scattering length density $\rho_i$, as depicted in Figure 2.8. Furthermore, the interfaces between two adjacent layers are smoothed by error functions that are parsed into small boxes. The reflectivity from this model is calculated for each solvent contrast by using the transfer matrix method and is compared with experimental data. The best-fit model is the one with a set of $(d_i, \rho_i)$ that minimizes the $\chi^2$ between the experimental curves and the curves calculated from the models. For stBLMs, the box model typically consists of semi-infinite mediums of silicon, followed by thin layers of silicon oxide, bonding layers of chromium, gold layers, submembrane spaces between membranes and gold surfaces ($sub$), hydrocarbon core of lipid membranes ($core$), headgroup layers of distal lipid leaflets ($dhg$) and finally another semi-infinite mediums of solvents. For submembrane spaces, hydrocarbon core of lipid membranes and distal headgroup layers, their $\rho$ depend on volume fractions ($vf$) of solvents within the layers and $\rho$ of solvents. It is given by the following equation

$$\rho_{sub,core,dhg} = vf_{PEG,CH,hg} * \rho_{PEG,CH,hg} + vf_{solvent} * \rho_{solvent} \tag{2.7}$$

in which $PEG$ stands for polyethylene glycol and it is the tether of stBLMs, $CH$ stands for hydrocarbon chains of lipid membranes and $hg$ stands for lipid headgroups. Moreover, $vf_{PEG,CH,hg} + vf_{solvent} = 1$. Depending on the solvents, $\rho$ of these layers varies. In the box model, apart from $\rho_{solvent}$, the other parameters such as $\rho$, $d$ and $vf$ are constrained to be equal for the reflectivity curves obtained under distinct solvents.

The reflectivity curves in Figure 2.9 were fitted with the box model and the best-fits are shown in the same figure with lines (—). The resulting nSLD profiles from the fitting are shown in Figure 2.10 for each solvent. The nSLD profile for each contrast overlaps with each other at every region except the submembrane space, the headgroup layer and the bulk solvent. This was due to the existence of solvents in these regions and therefore their $\rho$ was changed. This is the strength of the contrast variation in revealing the structure of stBLMs. It is of special significance in unravelling the volume fraction of solvents/water in the submembrane space. Besides, the $\rho$ of the hydrocarbon core of the stBLM overlap for all the solvents used. It

directly corroborates the fact that the hydrocarbon core of the membrane was almost solvent-free ($\ll 1\%$ by volume fraction), otherwise the $\rho$ would be different in that region for different solvents.

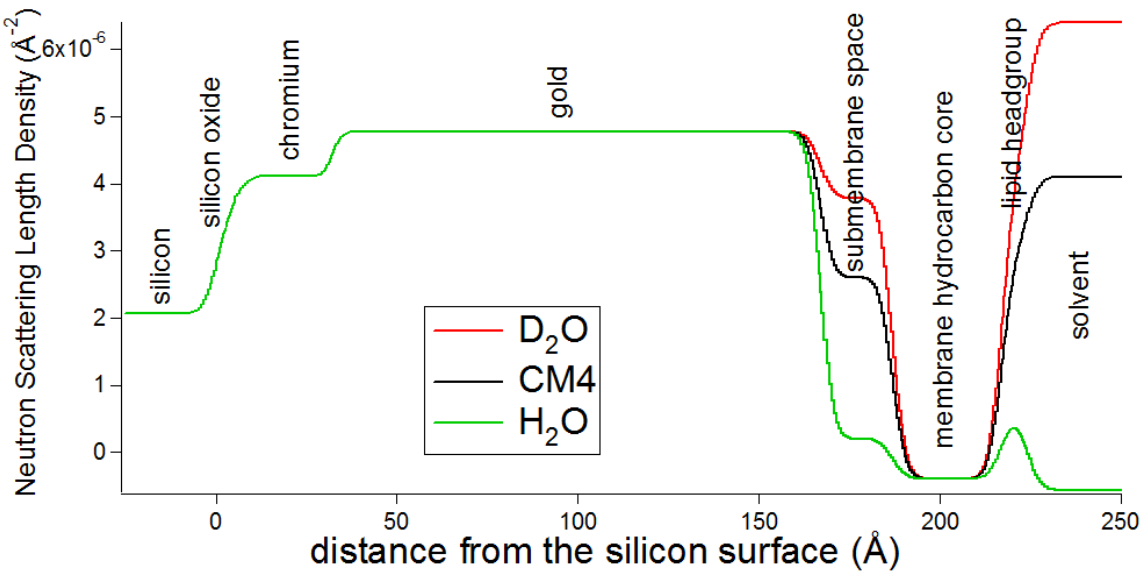


Figure 2.10: *The best-fit nSLD profiles for the DPhyPC stBLM in Figure 2.9. The identity of each layer is labeled on the graph.*

To further evaluate the uncertainty of the fitting parameters in the box model, we employ a Monte Carlo resampling approach [24]. In this approach, a large number of synthetic reflectivity curves, generally about 1000, are generated. These synthetic curves are created by considering the actual data points and the associated error bars, namely the points in each synthetic curve differs from the actual data points by a random normal deviate in which the width of the applied normal distributions is given by the standard deviation of the actual data. Each synthetic curve is fitted to the same box model and thus produces a set of distributions for te fitting parameters. The uncertainties of the fitting parameters are obtained from these distributions. Additionally, correlations between any two fitting parameters can be calculated from this resampling approach.

### Continuous Distribution (CD) Model

Even though the box model fitting is widely used to analyze NR data, it is not straightforward to interpret the resulting nSLD profiles at a molecular level. Alternatively,

the continuous distribution (CD) model fitting [2] can be performed in replacement for box model fitting.

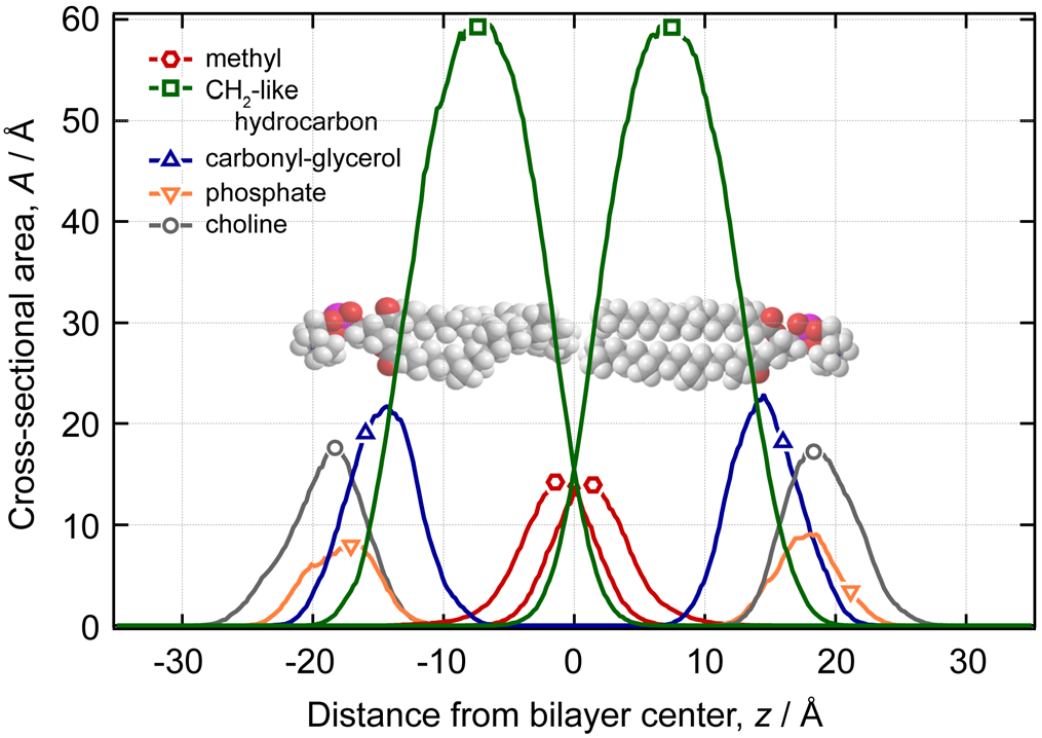


Figure 2.11: *The area profiles of submolecular components parsed from a DMPC bilayer along membrane normal are shown. The image is adapted from reference [2].*

In the CD model, a molecule or its submolecular components are represented by their area along membrane normal (or z-direction). For example, in Figure 2.11, a DMPC bilayer obtained from a molecular dynamics simulation is shown [77]. The DMPC was parsed into its submolecular components, which are the end methyl group of the hydrocarbon chain, the $CH_2$ hydrocarbon chain, the carbonyl-glycerol backbone, the phosphate group and the choline group. The area profile along the membrane normal for each submolecular component is presented in the figure. Each area profile resembles a Gaussian function. Therefore, in the CD model, the area profile of molecular or submolecular components is parameterized as a sum of two error functions which ensures ideal volume filling

$$A(z) = \frac{V}{2l}\left(erf\left(\frac{z - z_o + \frac{l}{2}}{\sqrt{2}\sigma_1}\right) - erf\left(\frac{z - z_o - \frac{l}{2}}{\sqrt{2}\sigma_2}\right)\right) \tag{2.8}$$

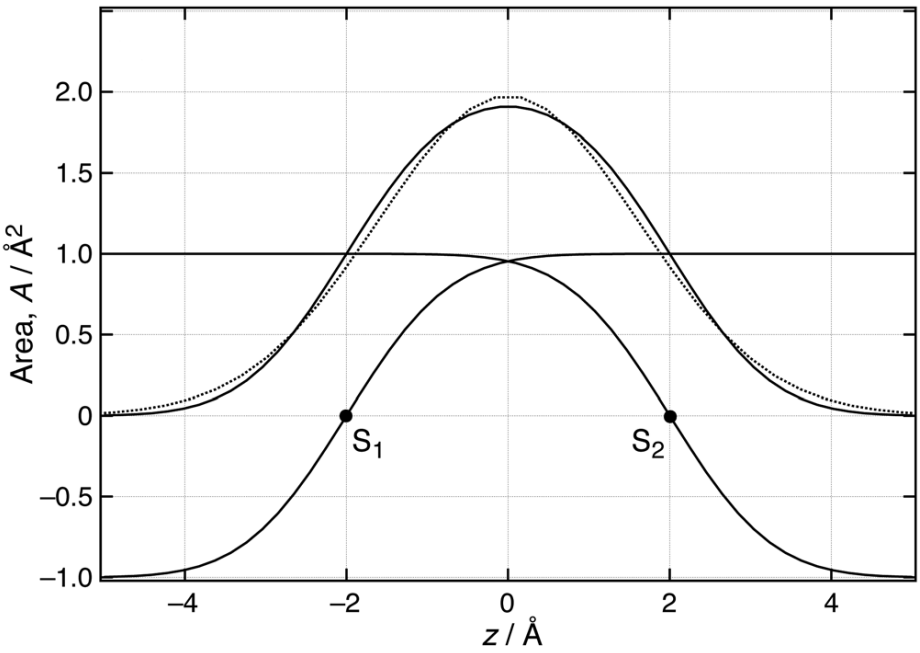


Figure 2.12: *An A(z) is described by the sum of 2 error function, $S_1$ and $S_2$. A Gaussian function in dashed line is also overlaid with $A(z)$ for comparison. The image is adapted from reference [2].*

where *erf* stands for an error function, $V$ is the volume of a particular (sub)molecular component, $z_o$ is the center location of the component, $\sigma$ is the width or roughness of the error function and $l$ is the projected length or thickness of the component along $z$. $z_o$, $\sigma$ and $l$ are the fitting parameters. It can be proved that $\int_{-\infty}^{+\infty} A(z)\,dz = V$, the volume of the component. An example of $A(z)$ obtained with this parameterization is illustrated in Figure 2.12 with $l = 4$ Å, $V = 8$ Å$^3$ and $\sigma_1 = \sigma_2 = 1$ Å. The sum of the two error functions, $S_1$ and $S_2$, gives rise to $A(z)$, which is also shown in lines (—). In the figure, a Gaussian function in dashed line is also overlaid with $A(z)$ for comparison.

Typically, for stBLMs, lipids are parsed into headgroups, alkyl chains and end methyl groups, whereas tethering lipids are parsed into PEG, glycerol backbone, alkyl chains and end methyl groups. Besides, $\beta$ME is also included as a component in submembrane spaces. The nSLD profile for a particular set of ($l$, $z_o$, $\sigma$) is calculated and is compared with experimental data. The fitting is improved by adjusting the values of ($l$, $z_o$, $\sigma$) for each component. With this fitting scheme, contributions of each (sub)molecular component to reflectivity are separated from the rest of the molecules.

They allow the interpretation of reflectivity at a molecular level. It is particularly crucial in Chapter 7 in which we need to isolate the contribution of proteins bound to stBLMs from the remaining molecules for determining their orientation.

## 2.4 Surface Plasmon Resonance (SPR)

Surface Plasmon Resonance (SPR) is a standard tool in the field of biosensing. It is used extensively in studying the binding of ligands or proteins to surface-immobilized receptors or solid-supported lipid membranes [78–80]. A typically employed excitation scheme, termed Kretschmann configuration, is shown in Figure 2.13. In this configuration, s-polarized incident light illuminates gold surfaces from the glass below at an angle larger than the critical angle, so that the incident light is totally reflected from the glass-gold-dielectric(water) interfaces. In this attentuated total reflection setup, evasnescent light at a particular resonance angle has a momentum that matches the momentum of surface plasmon at the gold-dielectric interfaces. The condition is described by the following equation [81]:

$$k_{parallel} = \frac{2\pi}{\lambda}\sqrt{\frac{\epsilon_{dielectric}\epsilon_{gold}}{\epsilon_{dielectric}+\epsilon_{gold}}} \tag{2.9}$$

in which $k_{parallel}$ is the wave vector of excitation light parallel to gold-dielectric interfaces that excites the surface plasmon, $\lambda$ is the wavelength of the excitation light in vacuum, $\epsilon_{dielectric}$ and $\epsilon_{gold}$ are the dielectric constant of dielectric mediums and gold respectively. When $\epsilon_{dielectric}$ and $\epsilon_{gold}$ are of opposite signs and $\epsilon_{gold} < -\epsilon_{dielectric}$, the condition of surface plasmon resonance is satisfied. As a result, surface plasmon resonance is excited by absorbing the energy of the photon. The intensity of reflected light or the reflectivity is measured as a function of the incident angles (or reflected angles, since the light is specularly reflected). Since the light that excites the surface plasmon resonance at this resonance angle loses its energy, the intensity of reflected light shows a minimum at the resonance angle, as shown in Figure 2.13. Again, as in the case of neutron reflectivity, the reflectivity curve of this particular configuration can be calculated by using the transfer matrix method by plugging in the appropriate optical parameters for each layer.

The exact value of the resonance angle is very sensitive to the refractive index of the dielectric layer beyond the gold surface as described in Eq. (2.9). Binding of

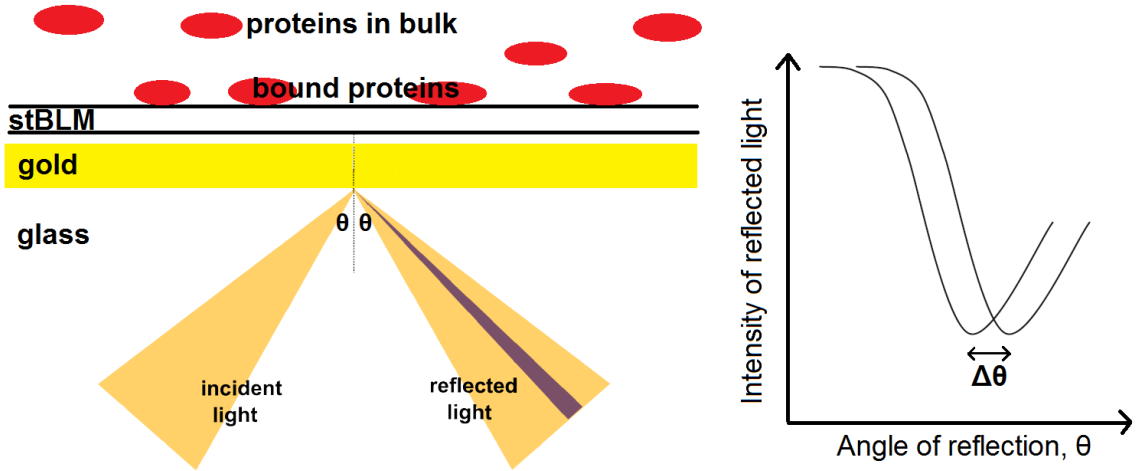


Figure 2.13: *The schematic diagram of a SPR measurement in a Kretschmann configuration. s-polarized incident light at different incident angles, $\theta$, illuminates the sample and is reflected. The intensity of reflected light is recorded by a camera and resembles the reflectivity curve as shown on the right. The shift in the resonance angle, $\triangle\theta$, is used to quantify the amount of absorbed proteins on stBLMs.*

proteins to surfaces of stBLMs changes the refractive index of the layers and shifts the resonance angles. It is the shifting of resonance angles, $\triangle\theta$, that is utilized to quantify the binding of proteins to stBLMs. It can be shown that when the thickness of absorbed layers is much smaller than the penetration depth of the evanescent waves into the dielectric mediums (a few hundred nanometers here), the shifting of resonance angles is directly proportional to the product of $(n_{layer} - n_{solution}) * d_{layer}$, in which $n_{layer}$ and $n_{solution}$ are the refractive index of the absorbed protein layers and the bulk solution respectively, and $d_{layer}$ is the thickness of the absorbed protein layers [82]. For dry proteins, $n_{protein} = 1.57$ [82] whereas for the bulk buffer solution, $n_{solution} = 1.33$. For the instrument employed here, SPR resonance curves are recorded on a CCD camera as a function of pixels instead of angles. A full conversion from pixels to angles is unnecessary provided $\triangle\theta$ is proportional to $\triangle pixel$ and we only need to quantify the thickness or the amount of bound proteins. To calibrate the SPR response of our particular SPR instrument, we used the known values of supported DOPC monolayers on HC18:$\beta$ME = 3:7 SAMs. For DOPC monolayers on HC18:$\beta$ME = 3:7 SAMs, their thickness, $d_{lipid}$, is $\sim 14$ Å and their refractive index, $n_{lipid}$, is 1.45 [83]. Supported DOPC monolayers induced a $\triangle pixel_{lipid}$ of 83.3 $\pm$ 14.4 pixels (average $\pm$ standard deviation for n = 10 samples) in SPR resonance angles. Therefore,

$$\frac{\triangle pixel_{protein}}{\triangle pixel_{lipid}} = \frac{(n_{protein} - n_{solution}) * d_{protein}}{(n_{lipid} - n_{solution}) * d_{lipid}} \tag{2.10}$$

By inserting the values into this equation, we find that

$$\frac{d_{protein}}{\triangle pixel_{protein}} = 0.084 \pm 0.015\,\text{Å} \tag{2.11}$$

per pixel change in resonance angles. With a protein density of 1.43 g/cm$^3$ [84], the mass of deposited proteins is 1.2 ± 0.2 ng/cm$^2$ per pixel change in resonance angles.

To quantify protein binding, stBLMs are titrated with proteins at increasing bulk concentrations. First, proteins are injected to a SPR cell and $\triangle pixel$ is recorded as a function of time. When the $\triangle pixel$ reaches a stable value, a higher concentration of proteins are injected. The process is repeated for a few concentrations of proteins. The final pixel change at each protein concentration, $\triangle pixel_{final}$, is plotted as a function of protein concentrations, $c$. The data are fitted to the Langmuir adsorption equation,

$$\triangle pixel_{final} = \triangle pixel_{max} \frac{c}{c + K_d} \tag{2.12}$$

which assumes binding sites on stBLMs are discrete and independent from each other. $\triangle pixel_{max}$ and $K_d$ are free parameters in the fitting and are the maximum $\triangle pixel$ with $c \to \infty$ and the binding constant.

### 2.4.1 Instrumentation of SPR

The SPR instrument was purchased from SPR Biosystems (Germantown, MD) [85]. About 45 nm of gold films are sputtered on microscope glass slides. stBLM-coated gold films are assembled on a SPR cell in a Kretschmann configuration for measurements. The light source is a superluminescent LED (EXS7510, Exalos AG, Switzerland) that emits light at a wavelength of 763.8 Å. The LED emission is focused on the sample by a hemicylindrical prism to cover a range of incident angles on the samples. Reflected light is collected by a Hamamatsu C10990 camera (Hamamatsu, Bridgewater, NJ). The SPR resonance curves are fitted to a series of polynomials to extract the values of resonance angles. The temperature of the SPR cell is controlled with a LFI-3751 temperature controller (Wavelength Electronics, Bozeman, MT) at 21°C.

# Chapter 3

# Solubilization of Supported Lipid Bilayers by Detergents

## 3.1 Introduction

Interactions of lipid bilayers or vesicles with detergents have been studied intensively due to their significance in the field of integral membrane protein purification or reconstitution, detergent resistance membrane fragments (lipid raft), medical applications of surfactants and the effect of biosurfactants on biomembranes [1, 86–97]. Methods that are used frequently to study the detergent-vesicle interactions include isothermal titration calorimetry [91] (measuring the enthalpy and the partition coefficient of detergents into lipid membranes), light scattering (measuring sizes of particles in lipid-detergent mixtures), cryo electron microscopy [90] (visualizing morphology of lipid-detergent aggregations at the nanoscale) and optical microscopy [98–100] (examine the shape transformation of giant unilamellar vesicles).

From such studies, a general consensus on dissolution of lipid vesicles by detergents is by the so-called 3 stage model [86]. In the first stage of this 3 stage model, detergent monomers partition into the bilayers and increase the sizes of vesicles. Partitioning continues up to a point at which the vesicles are saturated with the detergents. After this saturation is reached, any addition of detergents into the vesicles solubilizes the vesicles to mixed lipid-detergent micelles. This is the onset of the second stage in the 3 stage model where the vesicles and the mixed micelles coexist. Lastly, in the third stage, all the vesicles are dissolved and only the mixed micelles are left in the system.

In this work, we prepared fluorescently labeled, isolated DOPC bilayer patches supported on glass surfaces through rupturing of giant unilamellar vesicles (GUVs). We further incubated the bilayers with 7 commonly employed detergents, namely decyl and dodecyl maltoside, CHAPS, CTAB, SDS, TritonX-100 and Tween20 (see Figure 3.1), at their critical micelle concentrations (CMC). The solubilization process was monitored by a fluorescence microscope. From the time series of images taken, we measured the area of the bilayers while simultaneously utilized the fluorescence intensity of the images as the solubilization indicator. From the dynamics of expansion and dissolution of bilayers, we revealed the details of this solubilization process, both qualitatively and quantitatively. Moreover, some observations did not follow the conventional view of membrane solubilization, which would not otherwise be uncovered by the above mentioned methods employed to study the vesicle-detergent system.

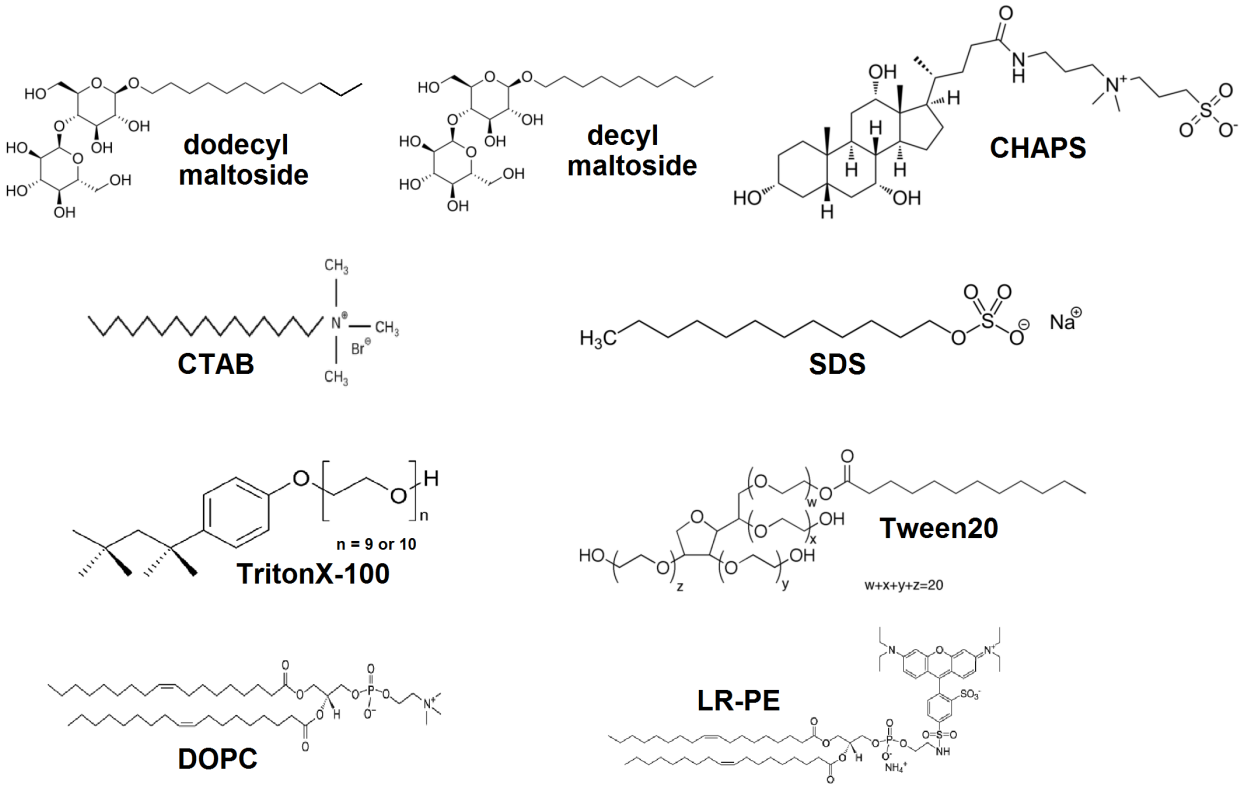


Figure 3.1: *The chemical structure of detergents used in the experiments. At pH ∼ 7, apart from CTAB and SDS, which are positively and negatively charged on the headgroups, the remaining are zwitterionic. Also shown at the bottom are the chemical structure of DOPC and fluorescently-labeled lipids, LR-PE.*

| Detergent | CMC (mM) | Charge | Free Energy | Maximum Expansion | Inner/Outer Zone |
|---|---|---|---|---|---|
| Decyl Maltoside | 1.8 | Zwitter-ionic | $-4 \times 10^{-21}$ J | $39 \pm 15$ % | Yes |
| Dodecyl Maltoside | 0.17 | Zwitter-ionic | $-5 \times 10^{-21}$ J | $30 \pm 14$ % | Yes |
| CHAPS | 9 | Zwitter-ionic | $-4 \times 10^{-21}$ J | $26 \pm 1$ % | Yes |
| CTAB | 1 | Positive | $-3 \times 10^{-21}$ J | Not Applicable | Yes |
| SDS | 9 | Negative | $-4 \times 10^{-21}$ J | $8 \pm 3$ % | Unclear |
| TritonX -100 | 0.24 | Zwitter-ionic | $-4 \times 10^{-21}$ J | Not Applicable | No |
| Tween20 | 0.059 | Zwitter-ionic | Unknown | Not Applicable | No |

Table 3.1: *The table summarizing the properties of detergents and the results of this work. Free energy of partitioning per molecule is obtained from reference [1]. The maximum expansion refers to the maximum area expansion of bilayers before the onset of solubilization and is thus not applicable to the detergents that do not require a critical lipid:detergent ratio to solubilize the bilayers. Lastly, the presence of the inner and outer zone is the indicator that detergents partition into the proximal leaflets during the expansion.*

## 3.2 Materials and Methods

### Materials

1,2-dioleoyl-sn-glycero-3-phosphocholine (DOPC) and 1,2-dioleoyl-sn-glycero-3-phosphoethanolamine-N-(lissamine rhodamine B sulfonyl) (ammonium salt) (LR-PE) were purchased from Avanti Polar Lipids (Alabaster, AL) and used as received. n-decyl-$\beta$-D-maltopyranoside (decyl-maltoside, CMC $\sim$ 1.8 mM), n-dodecyl-$\beta$-D- maltopyranoside (dodecyl-maltoside, CMC $\sim$ 0.17 mM) and polyoxyethylene(20)sorbitan monolaurate (Tween20, CMC $\sim$ 0.059 mM) were purchased from Anatrace (Maumee, OH). 3-[(3-cholamidopropyl) dimethylammonio]-1-propanesulfonate (CHAPS, CMC $\sim$ 9 mM) and cetyltrimethylammonium bromide (CTAB, CMC $\sim$ 1 mM) were purchased from Sigma Aldrich (St Louis, MO). Sodium dodecyl sulfate (SDS, CMC $\sim$ 9 mM) was purchased from Fisher Scientific (Pittsburgh, PA). Polyethylene glycol p-(1,1,3,3-tetramethylbutyl)-phenyl ether (TritonX-100, CMC $\sim$ 0.24 mM) was purchased from

JT Baker (Mansfield, MA). Number 1.5 thickness glass coverslips were purchased from Electron Microscopy Science (Hatfield, PA). All other chemicals were of HPLC grade and the ultrapure water was prepared in a Millipore (Billerica, MA) Milli-Q water purification device.

### Formation of GUVs and Supported Lipid Bilayers

GUVs were formed by the gentle hydration method [101, 102]. In brief, 1 mg/ml of DOPC was mixed with 1wt.% LR-PE (molar ratios of 160:1) in a chloroform:methanol = 1:1 mixture. 10 $\mu$l of this solution was spread on a microscope glass slide and evaporated under vacuum for $\sim$ 1 hour to remove any residual solvents. Dry lipid films were then resuspended in 200 mM sucrose and GUVs were formed within a few hours. To deposit patches of lipid bilayers on glass, number 1.5 thickness glass coverslips were rinsed with Hellmanex detergent and soaked in Nochromic solution for 15 minutes. The coverslips were then rinsed with copious amounts of water and ethanol, dried under nitrogen gas, before they were assembled into Sykes-Moore chambers. GUVs diluted with 95 mM NaCl + 10 mM HEPES, pH = 7 buffer, were injected into the chambers and the GUVs ruptured on glass surfaces [32, 34] to form patches of lipid bilayers. This process was interrupted after a few minutes by rinsing away the excess GUVs with buffer before the bilayers completely covered the glass surfaces. Supported bilayers were then transferred to a fluorescence microscope for imaging.

### Fluorescence Microscopy

Fluorescence imaging was performed with a Zeiss 63x Plan-Apochromat (NA = 1.4) objective lens and all other details are described in section (2.1.1). Video was recorded at 5 fps. The focus was on the glass-water interface. Detergent solutions (in 95 mM NaCl + 10 mM HEPES at pH = 7) were injected so that the chambers contained the detergents at their CMC and recording of images was started a few seconds before the injection.

### Fluorescence Recovery After Photobleaching (FRAP)

To verify that the fluorescence from the objects observed in the experiments was from fluid lipid bilayers, FRAP experiments were routinely performed as described in section (2.1.2) and the results were similar to the curve in Figure 2.3.

**Image Analysis**

ImageJ (National Institute of Health) was used for off-line image processing. To determine the area of bilayers, images recorded were converted to binary images by setting a threshold intensity halfway between the average background and the average object intensity.

## 3.3 Results

### 3.3.1 Decyl maltoside, dodecyl maltoside and CHAPS

The solubilization pathway of supported DOPC bilayers by these 3 detergents at their CMC was qualitatively identical and therefore the case discussed here also applies to them. In Figure 3.2 (the full movie M3-1 can be found at *http://www.youtube.com/watch?v=oZAUTvX1p84*), a DOPC bilayer, doped with fluorescently labeled lipids, LR-PE, was deposited on a glass surface through rupturing of GUVs and decyl maltoside at the CMC (1.8 mM) was injected into the chamber.

The initial size of the bilayer was $\sim 5500\ \mu m^2$ (image **a**). At $t > 20$ s, detergents started to partition into the bilayer and expanded the bilayer to the uncovered glass surface (image **b** and **c**). During the expansion, the edge of the bilayer was brighter (image **b**) as a result of LR-PE accumulation. As the expansion continued, the bilayer started to develop the inner and outer zone (image **d**). The outer zone was lower in fluorescence intensity and haloing the inner zone. The inner zone was the original area covered by the bilayer before the expansion (see below). Besides, in image **d**, the edge of the bilayer became smoother than the preceding images. The outer zone dissolved into mixed lipid-detergent micelles faster than the inner zone (image **e**) and the bilayer was completely solubilized in the end (image **f**).

The accumulation of LR-PE on the edge is the signature of the rolling motion (Figure 3.3) [43, 45]. In our case, only distal leaflets of bilayers (farther away from the glass surfaces and facing the aqueous phase) were exposed to detergents. Therefore, detergents can only partition into the distal leaflets. As a result, the distal leaflets expanded by rolling over the proximal leaflets (closer to glass). The proximal leaflets remained stationary and lipids and detergents from the distal leaflets flipped into the proximal leaflets through the edges of the bilayers. Due to a bulky and negatively charged headgroup that is hard to fit into a few Å thick water layer between supported

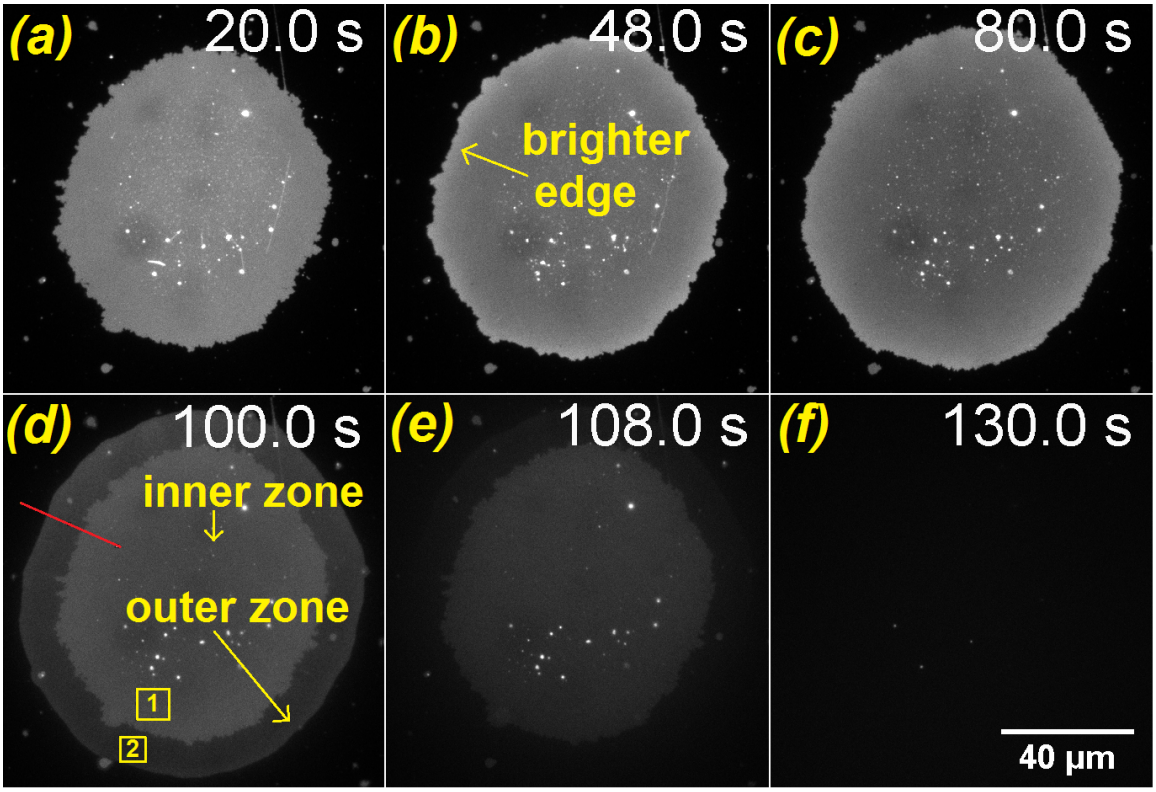


Figure 3.2: *The solubilization of a DOPC supported bilayer by 1.8 mM decyl maltoside and the time series images of the process. All images are on the same contrast. The bilayer expanded radially outward when detergents partitioned into its distal leaflet (image* ***a*** *to* ***c****). The expansion happened through the rolling motion of the distal leaflet over the proximal leaflet. As a result, LR-PE accumulated on the edge of the bilayer and caused a brighter bilayer edge (image* ***b****). 2 zones (with the outer zone haloing the inner zone) showed up in image* ***d*** *and the outer zone dissolved faster than the inner zone (image* ***e****). Finally all the lipids were dissolved (image* ***f****). The full movie M3-1 can be found here.*

bilayers and negatively charged glass surfaces [2], LR-PE did not flip into the proximal leaflets and accumulated on the edges of the distal leaflets. Diffusion of lipids was not able to completely eliminate the accumulation of LR-PE on the edge as the Péclet number is $\frac{R(dR/dt)}{D} = \frac{dA/dt}{2\pi D} > 1$ ($D$ is the diffusion coefficient of lipids and see the partitioning dynamics below for the explanation of other terms). The dyes still accumulated on edges even if we changed the fluorophores to lipids with NBD on their headgroups, in which NBD is zwitterionic and is much smaller than lissamine rhodamine (data not shown). To support the depletion of LR-PE in the proximal

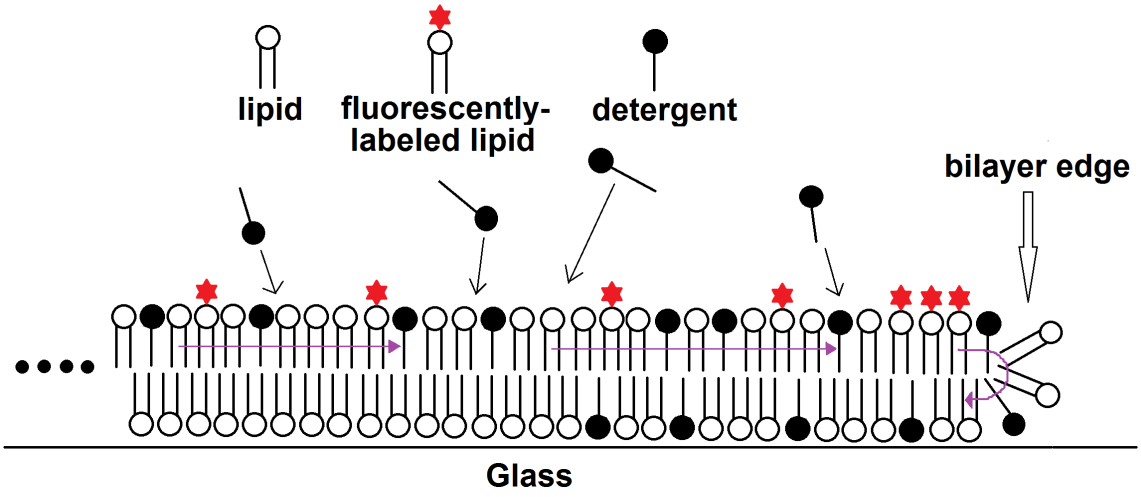


Figure 3.3: *The rolling motion of distal leaflets over proximal leaflets is the mode of expansion for bilayers. In this figure, detergents in the bulk solution partition into the distal leaflet and lipids in the distal leaflet move to the right toward the bilayer edge as indicated by purple arrows. Lipids in the proximal leaflet remain stationary and lipids flip from the distal to the proximal leaflet at the bilayer edge. Since fluorescently-labeled lipids, LR-PE, have a bulky fluorophore on the headgroup, they do not flip to the proximal leaflet and accumulate on the edge of the bilayer, as indicated by their higher density on the edge.*

leaflets, iodide quenching experiments were carried out to estimate the distribution of LR-PE in two leaflets. When we incubated neat bilayers with 1 M of sodium iodide to quench the LR-PE on the distal leaflets [103], the fluorescence intensity of the bilayers dropped to 12% of the original value. Assuming 1 M of iodide quenches all of the LR-PE on the distal leaflets, this result indicated that only $\sim$ 12% of the total LR-PE in the bilayers were in the proximal leaflets (1 M of iodide does not 100% quench LR-PE [43, 45, 103], therefore 12% is the upper bound). An uneven distribution of LR-PE across the leaflets promoted brighter edges during the expansion, and hence unmistakably supports the rolling motion as the mode of expansion for bilayers.

To quantify the expansion process, we plot the area of the bilayer and the average fluorescence intensity of the recorded images as a function of time in Figure 3.4. Also on the same graph, we plot the average fluorescence intensity of the inner zone as defined by the ROI (region of interest) labeled '1' in image **d** of Figure 3.2, and the average fluorescence intensity of the outer zone as defined by the ROI labeled '2'. Since we used a high NA objective for imaging, the fluorescence intensity of images was

used as an indicator for the bilayer's solubilization, since lipids dissolved into mixed micelles will quickly diffuse away from the field or depth of view of the objective. The intensity trace was approximately constant until $t \sim 95$ s, indicating that no lipids were dissolved before this. The solubilization started after $t > 95$ s, characterized by a sharp drop in the intensity. By that time, the bilayer had expanded from 5500 $\mu$m$^2$ to 8500 $\mu$m$^2$, with an average rate of $\frac{dA}{dt} = 37\,\mu\text{m}^2/\text{s}$ as determined from a linear fit. It had expanded by 55% before the initiation of dissolution (the average $\pm$ std is 39 $\pm$ 15 % for n = 4 samples), indicating a critical lipid:detergent ratio is needed to induce micellization. For detergents that form a micelles of 4 to 5 nm in diameter and with an aggregation number (the number of molecules that makes up a micelle) of 60 to 100, the headgroup area of the detergents is on the order of 0.5 to 0.8 nm$^2$. In this case, by assuming an area per molecule of 0.7 nm$^2$ for both lipids and detergents and they mixed homogeneously, the critical lipid:detergent ratio is 1:0.55. The expansion continued after the onset of solubilization, reaching a maximum area of $\sim 9000$ $\mu$m$^2$ at $t \sim 100$ s prior to its abrupt decline to $< 5000$ $\mu$m$^2$ at $t \sim 120$ s. The growth of the area after 120 s was due to the inaccuracy of image segmentation after the bilayer was solubilized. On the other hand, after the onset of solubilization, the intensity trace decreased smoothly until the background level when the bilayer was dissolved completely.

The inner and outer zone appeared right after the onset of solubilization at $t \sim 95$ s, when the outer zone dissolved faster than the inner zone, causing an outer zone with a lower fluorescence intensity. It was evident from the average intensity of the inner and outer zone in Figure 3.4. Initially, the outer zone (or ROI '1') was not covered by the bilayer. Its intensity rose when ROI '1' was covered by the bilayer progressively ($t$ from 40 to 90 s). Meanwhile, the intensity of the inner zone dropped as the fluorophores density decreased when the bilayer expanded. The intensity of the outer zone was higher than the inner zone at $t \sim 88$ s due to the brighter edge as described earlier. After the onset of solubilization at $t \sim 95$ s, because the outer zone dissolved faster than the inner zone, its intensity was lower than the inner zone again, and created the boundary of the inner-outer zone in image **d** of Figure 3.2. In the end, the intensity trace of both zones overlapped after $t > 120$ s with the background level when the whole bilayer was dissolved.

To demonstrate the existence of the brighter edge and the inner-outer zone quantitatively, the fluorescence intensity along the red line drawn in image **d** of Figure 3.2 is

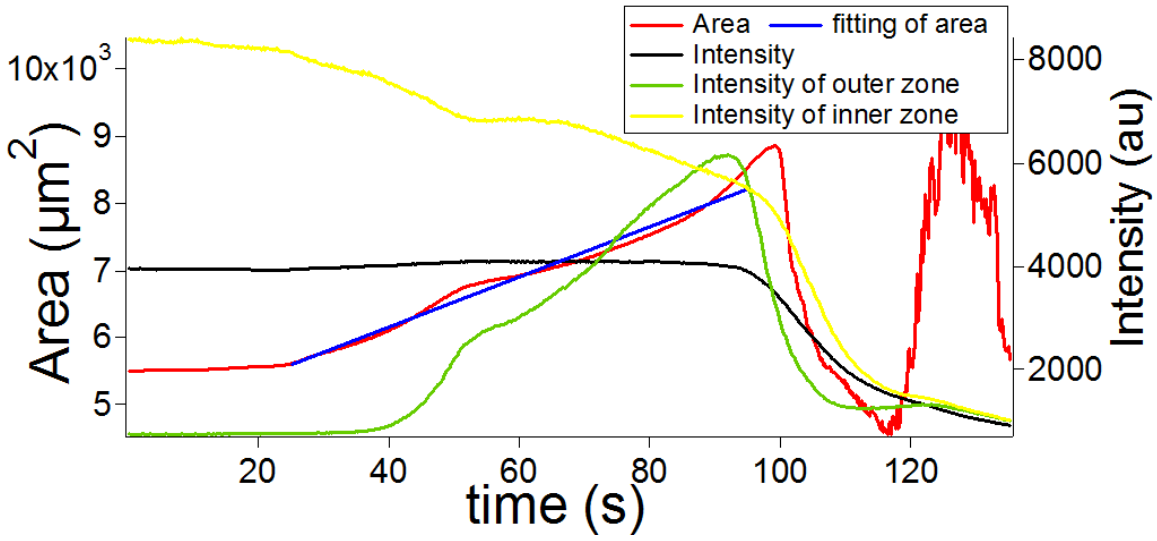


Figure 3.4: *The area of the bilayer, the mean fluorescence intensity of images, and the mean fluorescence intensity of the inner and outer zone are plotted as a function of time for the event in Figure 3.2. The intensity of the inner and outer zone is the intensity of the ROI labeled '1' and '2' in image* ***d*** *of Figure 3.2.*

plotted in Figure 3.5 for different times. At $t = 20$ s (image **a**), the intensity along the line resembled a step function. The intensity drop at $r \sim 12$ $\mu$m was due to the boundary of the bilayer and the uncovered glass. When the bilayer expanded radially outward at $t = 48$ s (image **b**), its edge was higher in intensity ($12$ $\mu m < r < 15$ $\mu$m) than its center ($r < 12$ $\mu$m). At $t = 100$ s (image **d**), apart from a drop in intensity at $r \sim 23$ $\mu$m, which was the bilayer-glass boundary, an extra drop caused by the inner-outer zone interface could be identified at $r \sim 12$ $\mu$m. It is also important to note that the boundary of the inner-outer zone exactly located at the bilayer-glass boundary at $t = 20$ s. Lastly, the intensity was roughly a constant along the line at $t = 130$ s (image **f**) after all the lipids were solubilized.

The boundary between the inner and outer zone was situated precisely on the boundary of the original bilayer before the expansion. To illustrate this, we produce an outline (in green) for the bilayer in image **a** with image segmentation. The green outline is then overlaid with image **d** and the resulting image is shown in Figure 3.6. The green outline contours the inner zone of image **d** closely and confirms that the inner zone was the area covered by the original bilayer. To explain this effect, we propose that the proximal leaflets of the inner zones were detergent-free. During the expansion, both lipids and detergents on the distal leaflets flipped to the proximal

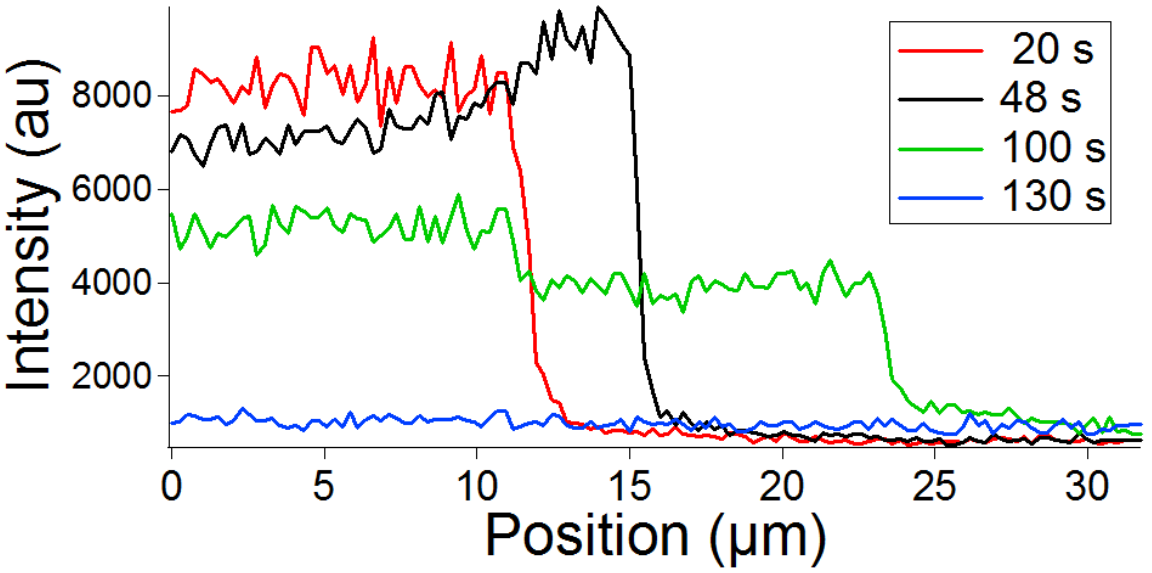


Figure 3.5: *The fluorescence intensity profiles along the red line drawn in image* ***d*** *of Figure 3.2 at different times to show the brighter edge during the expansion and the existence of the inner and outer zone.*

leaflets of the outer zones through the edges. Provided the lipids and detergents in the proximal leaflets were mobile, then the detergents on the outer zones and the lipids in the inner zones (both in the proximal leaflets) would diffuse into the other zones within the timescale of the expansion ($\sim$ 60 s here), and the inner-outer zone boundaries would not located on the boundaries of the original bilayers, but within them. Since this was not the case, we concluded that the lipids and detergents in the proximal leaflets were immobile, at least at a timescale of tens of seconds. Indeed, proximal leaflets of supported bilayers have a lower area per lipid [2] and most probably are in a gel-like phase. On the other hand, if the detergents within the inner zones or bilayer interiors were able to flip-flop from the distal to proximal leaflets considerably, they should expand the area of the inner zones and again the inner-outer zones boundaries would not overlap with the boundaries of original bilayers. Hence, the possibility of detergent flip-flop within the bilayer interiors can be safely excluded. In addition, since the proximal leaflets of the inner zones were detergent free, instead of a lipid:detergent ratio of 1:0.55, a lipid:detergent ratio of 1:1.1 initiated micellization of the outer zones, assuming the lipids and detergents flipped into the proximal leaflets at the same rate.

The outer zones with both lipids and detergents in their proximal and distal leaflets were dissolved faster than the inner zones. It is in agreement with the conventional

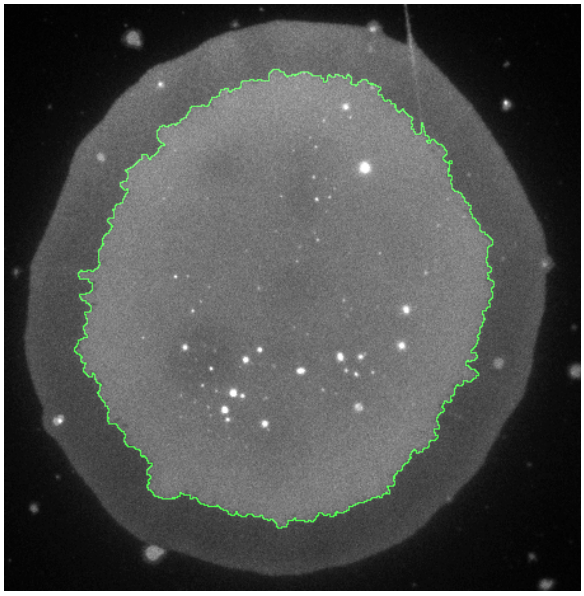

Figure 3.6: *To show the inner zone was the area covered by the original bilayer before the expansion, the bilayer in image* ***a*** *of Figure 3.2 is outlined in green contour. This green contour is overlaid with image* ***d****. The outline contours the inner zone of image* ***d*** *completely.*

view that detergents solubilize lipid membranes once they partition into both leaflets. However, detergents in distal leaflets alone are also sufficient to induce micellization of the inner zones as observed. Since bilayer patches were deposited through an adhesion-rupturing pathway [32, 34] of a single (or a few) GUV, the interior of bilayers were defect free down to nanoscale. As a result, no lipid bilayer edges could be found in the inner zones that would facilitate translocation of detergents from distal to proximal leaflets. A combination of immobile proximal leaflets and the lack of lipid bilayer edges excluded the possibility of detergent flipping into the proximal leaflets of the inner zones. Therefore, in our case, the curvature frustration of one of the leaflets was sufficient for membrane solubilization.

Besides, important information is associated with the expansion dynamics. During the expansion, the total energy of the system (bilayer + detergents + aqueous phase), $E_{total}$, must be conserved. This implies its time derivative,

$$\frac{dE_{total}}{dt} = 0 = \frac{dE_{adhe}}{dt} + \frac{dE_{fric}}{dt} + \frac{dE_{edge}}{dt} + \frac{dE_{part}}{dt} + \frac{dE_{curv}}{dt} + absorbed\,or\,released\,heat \tag{3.1}$$

$E_{adhe}$ is the adhesion energy between lipid bilayers with glass surfaces, so

$$\begin{aligned}\frac{dE_{adhe}}{dt} &= \gamma\frac{dA}{dt} \\ &= (-0.15\,\mathrm{mN/m}) \times (37\,\mu\mathrm{m}^2/\mathrm{s}) \\ &= -5.6 \times 10^{-15}\,\mathrm{J/s}\end{aligned} \tag{3.2}$$

in which $\gamma = -0.15\,\mathrm{mN/m}$ [104] is the adhesion energy per unit area between glass and lipid bilayers.

$E_{fric}$ is the work dissipated by frictional force due to the rolling motion. Friction exists between the hydrocarbon chains of 2 leaflets when distal leaflets slide along stationary proximal leaflets. This scenario is depicted in Figure 3.7 by assuming the bilayer is circular. In this figure, the surface is covered by a circular ring of a lipid monolayer from $r = 0$ to $R$. Lipids move radially outward as indicated by red arrows and at each radial distance $r$ from the origin, the radial velocity is $v(r)$. Therefore the friction per unit area experienced by the lipids at the radial distance $r$ is $bv(r)$, in which $b$ is the friction coefficient between 2 leaflets and $\sim 10^8\,\mathrm{Ns/m^3}$ [105–108]. As the lipids at $r$ move by a small distance $dr$ radially outward, the work done per unit area is

$$dE_{fric}^{unit\,area} = bv(r)dr \tag{3.3}$$

Accordingly,

$$\begin{aligned}\frac{dE_{fric}^{unit\,area}}{dt} &= bv(r)\frac{dr}{dt} \\ &= bv^2(r)\end{aligned} \tag{3.4}$$

By assuming the possibility that a detergent partitions into the circular bilayer is a constant across the entire area of the bilayer, then the probability that a detergent will partition into an area of $r < \epsilon$ $(0 < \epsilon < R)$ is $\dfrac{\epsilon^2}{R^2}$. It follows that the area expansion due to partitioning of detergents for the area of $r < \epsilon$ is

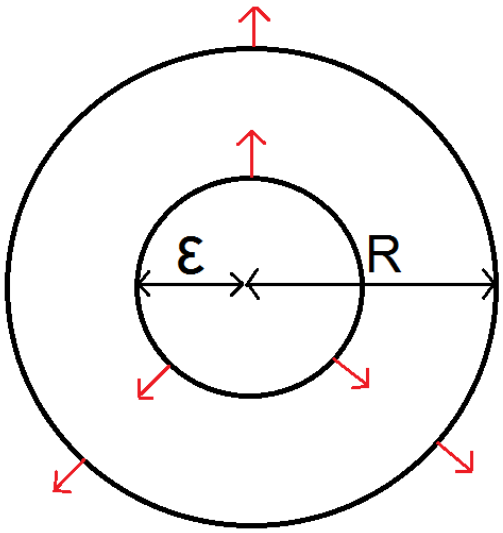


Figure 3.7: *The circular ring from $r = 0$ to $R$ is covered by a lipid monolayer and the lipids move radially outward as indicated by the arrows in red. The probability that a detergent will partition within the area of $r < \epsilon$ is* $\frac{\epsilon^2}{R^2}$.

$$\left.\frac{dA}{dt}\right|_{r<\epsilon} = \frac{dA}{dt}\frac{\epsilon^2}{R^2} \tag{3.5}$$

Accordingly, by using the fact that $A|_{r<\epsilon} = \pi\epsilon^2$, $A = \pi R^2$ and thus $\left.\frac{dA}{dt}\right|_{r<\epsilon} = 2\pi\epsilon \left.\frac{dr}{dt}\right|_{r=\epsilon}$ and $\frac{dA}{dt} = 2\pi R\frac{dR}{dt}$, the preceding relationship leads to

$$\left.\frac{dr}{dt}\right|_{r=\epsilon} = \frac{dR}{dt}\frac{\epsilon}{R} \quad \text{or} \quad v(r) = v(R)\frac{r}{R} \tag{3.6}$$

where we have set $v(r) = \frac{dr}{dt}$ and $v(R) = \frac{dR}{dt}$. By substituting $v(r)$ in the previous equation into $\frac{dE_{fric}^{unit\,area}}{dt}$,

$$\frac{dE_{fric}^{unit\,area}}{dt} = bv^2(R)\frac{r^2}{R^2} \tag{3.7}$$

By integrating the preceding equation across the entire area of the lipid monolayer from $r = 0$ to $R$,

$$\begin{aligned}\frac{dE_{fric}}{dt} &= \int_0^R bv^2(R)\frac{r^2}{R^2}\,2\pi r\,dr \\ &= \frac{1}{2}\pi bR^2\left(\frac{dR}{dt}\right)^2 \\ &= \frac{b}{8\pi}\left(\frac{dA}{dt}\right)^2 \\ &= (10^8\,\mathrm{Ns/m^3}/8\pi)(37\,\mu\mathrm{m^2/s})^2 \\ &= 0.55\times10^{-14}\,\mathrm{J/s}\end{aligned} \tag{3.8}$$

$E_{edge}$ is the energy of bilayer edges, so

$$\frac{dE_{edge}}{dt} = 2\pi T\left(\frac{dR}{dt}\right) \tag{3.9}$$

$T$ is the line tension of bilayer edges $\sim 10$ pN [109]. Strictly speaking, the perimeter of the bilayer obtained from image segmentation did not really change (not shown) because the rough edge of the bilayer became a smooth edge during the expansion. Nevertheless, assuming a circular bilayer grows from 5500 $\mu$m$^2$ to 8500 $\mu$m$^2$ in 60 s, then $\dfrac{dR}{dt} \sim 0.2\,\mu$m/s and

$$\begin{aligned}\frac{dE_{edge}}{dt} &= (10\,\mathrm{pN})(0.2\,\mu\mathrm{m/s}) \\ &= 2\times10^{-18}\,\mathrm{J/s}\end{aligned} \tag{3.10}$$

$E_{part}$ is the energy loss when detergents in the aqueous phase partition into bilayers. For decyl maltoside, the (free) energy change per molecule $E_{part}^{molecule}$ is $\sim -4\times10^{-20}$ J [1, 110] (all the detergents in this study have a $E_{part}^{molecule}$ about this value), then

$$\begin{aligned}\frac{dE_{part}}{dt} &= number\,of\,detergents\,partitioned\,per\,unit\,time\;\times\;E_{part}^{molecule} \\ &= \left(\frac{dA}{dt}\right)\div(area\,per\,detergent)\;\times\;E_{part}^{molecule} \\ &= (37\,\mu\mathrm{m^2/s})\div(0.7\,\mathrm{nm^2})\times(-4\times10^{-20}\,\mathrm{J}) \\ &= -2.1\times10^{-12}\,\mathrm{J/s}\end{aligned} \tag{3.11}$$

The curvature energy of planar bilayers,

$$E_{curv} = A \times \left( \left( \frac{1}{2} \right) \kappa (2C - 2C_o)^2 + \bar{\kappa} C^2 \right) \tag{3.12}$$

requires special attention. $\kappa$ is the bending modulus of DOPC bilayers $\sim 8.5 \times 10^{-20}$ J [111]. $\bar{\kappa}$ is the saddle splay modulus and $C$ is the curvature of planar bilayers $\sim 0$. The term involving $\bar{\kappa}$ could be ignored because membranes did not change the topology during the expansion. To a good approximation, the mean spontaneous curvature of lipid-detergent mixtures, $C_o$, is given by the area weighted spontaneous curvature of lipids and detergents [112, 113],

$$C_0 = \left( \frac{A_o}{A} \right) C_o^{lip} + \left( \frac{A - A_o}{A} \right) C_o^{det} \tag{3.13}$$

$A_o$ is the original area of bilayers. Assuming that the spontaneous curvature of DOPC, $C_o^{lip} \sim 0$ [114] and $C_o^{det} = 1/(2\,\mathrm{nm})$, where 2 nm is approximately the radius of a detergent micelle, after some algebra,

$$\frac{dE_{curv}}{dt} = 2\kappa \left( \frac{dA}{dt} \right) \left( 1 - \frac{A_o^2}{A^2} \right) (C_0^{det})^2 \tag{3.14}$$

This term is not constant over time. At the beginning of the expansion where $A_o \sim A$, it is $\sim 0$. However, when $A = 1.55 A_o$ at the onset of solubilization,

$$\begin{aligned} \frac{dE_{curv}}{dt} &= 2(8.5 \times 10^{-20}\,\mathrm{J})(37\,\mu\mathrm{m}^2/\mathrm{s})(1 - (A_o/1.55A_o)^2)(1/2\,\mathrm{nm})^2 \\ &= 9.3 \times 10^{-13}\,\mathrm{J/s} \end{aligned} \tag{3.15}$$

approaching the magnitude of $\frac{dE_{part}}{dt}$.

Finally, partitioning of detergents into lipid membranes is always accompanied by heat release or absorption [1]. Heat is either released or absorbed depending on the conditions of experiments.

As the consequence, Eq. (3.1) was dominated by $\frac{dE_{part}}{dt}$, $\frac{dE_{curv}}{dt}$ and absorbed or released heat because the other 3 terms had a much smaller magnitude. At the

commencement of the expansion in which $\frac{dE_{curv}}{dt}$ is $\sim 0$, $\frac{dE_{part}}{dt}$ must be counter-balanced by released heat with a positive sign to preserve the equality in Eq. (3.1). Therefore, heat was released during the expansion, namely the partitioning process was exothermic with a negative enthalpy. Due to this energy increment, the thermal energy or the temperature of the system increased. Presumably because the rate of detergent adsorption dominated over the desorption rate along the process, the partitioning of detergents continued. As more and more detergents partitioned into the bilayer, the magnitude of $\frac{dE_{curv}}{dt}$ came close to $\frac{dE_{part}}{dt}$. Hence, for preserving Eq. (3.1), the bilayer developed the curvature ($C \neq 0$) to reduce $E_{curv}$. Finally, the curvature was high enough and the bilayer dissolved into micelles.

We could take a further step to roughly estimate the energy barrier for detergents to partition into lipid bilayers, $E_a$, from the rate of expansion. Here, $E_a$ refers to the energy cost for a detergent to expose its hydrophobic part to the lipid headgroup layer when it inserts into the membrane. According to the Arrhenius rate equation,

$$\frac{dA}{dt} = (area\,per\,detergent) \times B \times exp(-E_a/kT) \tag{3.16}$$

$B$ is the pre-exponential factor or the collision frequency of detergents with an isolated bilayer. We modeled the collision frequency as the diffusion current of detergents (with a bulk concentration, $Q$, and a diffusion coefficient, $D$) to an absorbing circular disk of radius $R$ (radius of bilayers) [115], so

$$B = 4DQR = 4DQ\sqrt{A/\pi} \tag{3.17}$$

per second. From the Stokes-Einstein relation, a detergent molecule with a radius $\sim 1$ nm has a diffusion coefficient of $D \sim 200\,\mu\mathrm{m}^2/\mathrm{s}$ in water. Therefore,

$$\begin{aligned} \text{area per detergent} \times B &= (0.7\,\mathrm{nm}^2)(4)(200\,\mu\mathrm{m}^2/\mathrm{s})(1.8\,\mathrm{mM})\sqrt{5500\,\mu\mathrm{m}^2/\pi} \\ &= 25400\,\mu\mathrm{m}^2/\mathrm{s} \end{aligned} \tag{3.18}$$

For $\frac{dA}{dt} = 37\,\mu\mathrm{m}^2/\mathrm{s}$, $E_a = 6.5$ kT. The average energy barrier for the insertion of decyl maltoside into membranes is $5.9 \pm 1.4$ kT (n = 4). It is also important to note that we ignore the steric factor in the pre-exponential factor (that is only collisions

with the correct orientation will lead to partitioning of detergents). Under the absence of a long range attraction between detergents and bilayers, the steric factor is $\leq 1$, so $E_a$ reported here should be considered as the upper bound value.

For dodecyl maltoside, the maximum expansion of bilayers before the onset of solubilization was 30 ± 14 % and $E_a$ = 3.2 ± 1.9 kT (n=4). For CHAPS, it was 26 ± 1 % and 6.5 ± 0.5 kT (n=3). To close this section, it is intriguing to notice that for all of the three detergents tested here, the maximum expansion before solubilization is negatively correlated with $\frac{\frac{dA}{dt}}{A_o}$ with a correlation coefficient from -0.5 to -0.9. Qualitatively, this finding is reasonable because the faster the partitioning of detergents is, the higher is the possibility to create a local area enriched with detergents because they do not have sufficient time to mix homogeneously with lipids, thus dissolve that particular area faster. Quantitatively, from Eq. (3.1), $\frac{dE_{fric}}{dt}$ depends on $\left(\frac{dA}{dt}\right)^2$ while the remaining terms depend on $\frac{dA}{dt}$. As a consequence, $\frac{dE_{fric}}{dt}$ increases more than the other terms when $\frac{dA}{dt}$ gets larger. The system responses at the expense of $\frac{dE_{curv}}{dt}$ by lowering it (increase the curvature) for preserving Eq. (3.1). So bilayers dissolve faster and the maximum expansion drops.

### 3.3.2 CTAB

CTAB displayed a different solubilization pathway than the detergents in section (3.3.1). The process is depicted in Figure 3.8 (the movie M3-2 until $t$ = 124.6 s can be found at *http://www.youtube.com/watch?v=6_jTQgTsd_w&feature=plcp*). First, the bilayer expanded radially outward through a rolling motion similar to that discussed in section (3.3.1) when CTAB partitioned into its distal leaflet (image **a** to **e**). Accordingly, LR-PE accumulated at the edge (image **b**). In the subsequent images (image **c**), the outer zone appeared as its intensity was lower than the intensity of the inner zone (the original area of the bilayer). The dissolution and expansion proceeded until $t$ = 606 s (image **f**) and the bilayer was not completely dissolved.

As before, for the event shown in Figure 3.8, we plot the area of the bilayer, the average fluorescence intensity of images (which was multiplied by a factor of three to aid the reader's visualization), and the average fluorescence intensity of the inner and outer zone (as defined by the ROI labeled '1' and '2' in image **d**) as a function

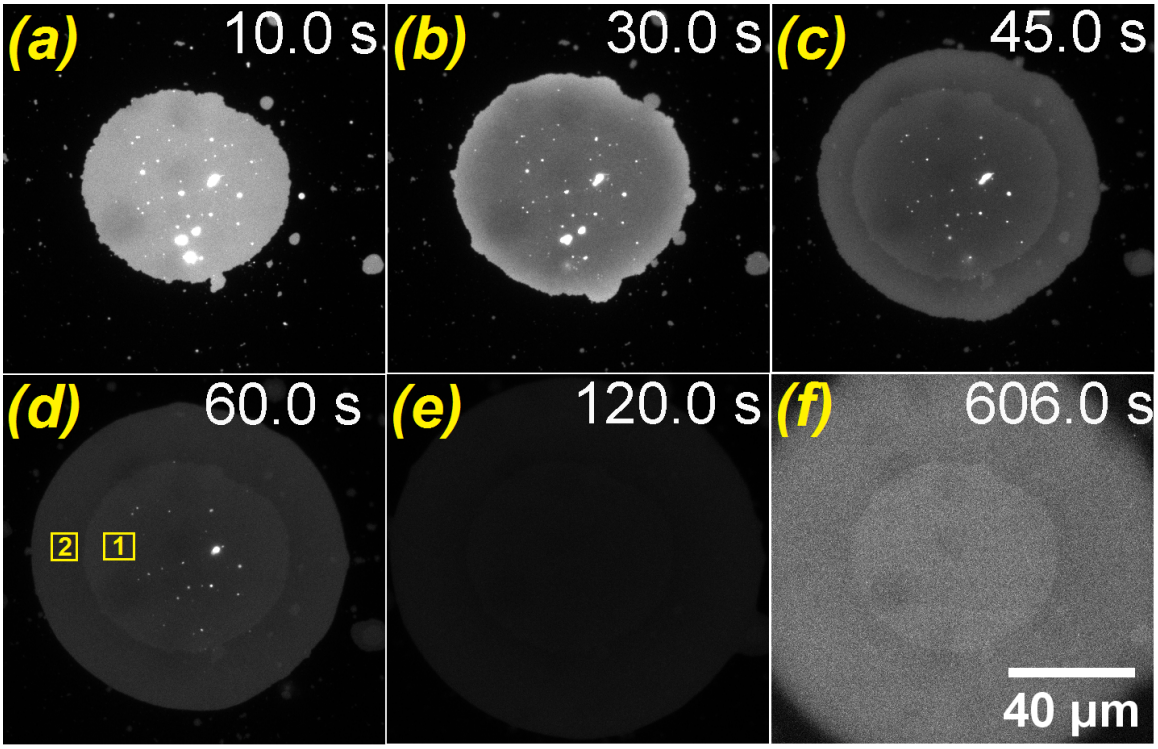


Figure 3.8: *Dissolution of a DOPC bilayer by 1 mM CTAB and the time series images of the process. All images are on the same contrast except for image* ***f*** *in which its contrast has been linearly enhanced. The movie M3-2 until* $t = 124.6$ *s can be found here.*

of time in Figure 3.9. The intensity trace revealed the distinction of solubilization pathway. Apart from a mild decrease over time before $t < 23$ s due to the bleaching of LR-PE, the intensity showed a noticeable drop at $t \sim 23$ s, concurrent with the initiation of the bilayer expansion. This implies CTAB began to solubilize the bilayer right after its partitioning. CTAB did not need to attain a critical lipid:detergent ratio (or a very low lipid:detergent ratio was required within the detection limit of this method) to solubilize the membrane. This was in stark contrast with the mode of action of the detergents in section (3.3.1) in which a critical detergent:lipid ratio was essential in inducing micellization. The solubilization through the direct uptake of lipids from the bilayer to detergent micelles can be excluded here, because this route apparently requires much higher energy and is usually related to the extraction of lipids from leaflets overpopulated with lipids and detergents [93, 97, 116]. We argue that solubilization must be correlated with partitioning of CTAB into the bilayer. Therefore, we propose four possible explanations: (1) CTAB might phase-separate

quickly into a detergent-enriched area [97], (2) the aggregation number of mixed CTAB-DOPC micelles is very low, (3) the curvature frustration induced by CTAB on distal leaflets is very high locally with just a few CTAB inclusion, or (4) CTAB dissociates from membranes very soon after the partitioning, and carry lipids bound to them away during the dissociation. So, a small number of CTAB is enough to start the solubilization.

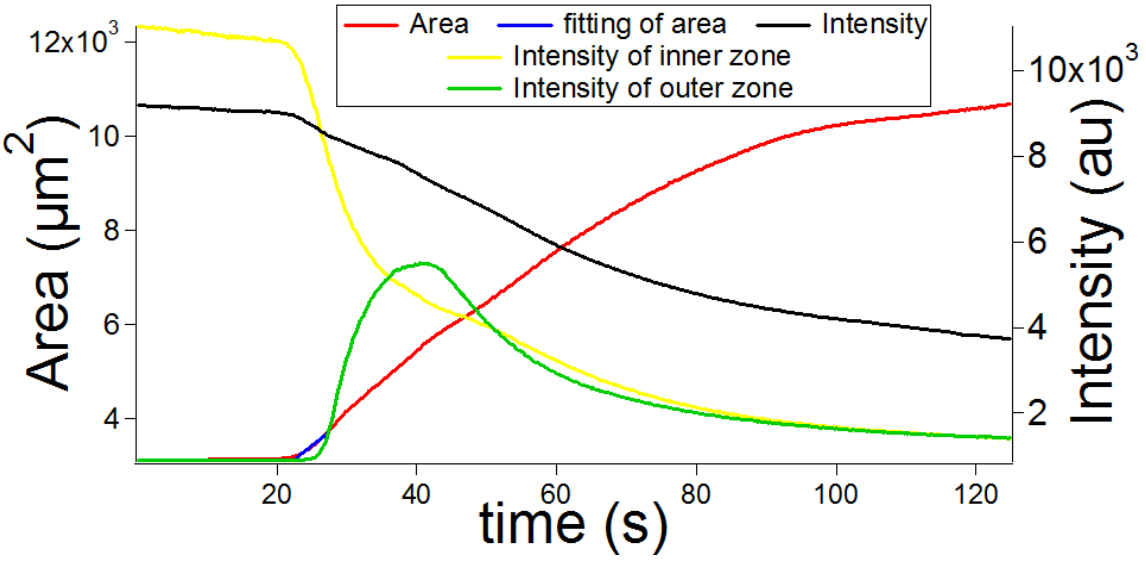


Figure 3.9: *The area of the bilayer, the fluorescence intensity of images, and the fluorescence intensity of the inner and outer zone are plotted as a function of time for images in Figure 3.8. The intensity of the inner and outer zone is the intensity of the ROI labeled '1' and '2' in image* ***d****. The intensity trace of the bilayer has been multiplied by a factor of 3 to aid reader's visualization.*

On one hand, the solubilization and the expansion of the bilayer continued after $t > 124.6$ s (the end of the graph in Figure 3.9). By that time, the bilayer was at least three times larger than the original bilayer and about 70% of the lipids had been dissolved as evident from the drop of intensity by a factor of three. On the other hand, the rate of solubilization and expansion slowed down considerably after $t > 80$ s. It is known that positively charged CTAB forms bilayers on negatively charged glass surfaces [117]. Therefore, formation of a CTAB bilayer on the uncovered glass surface around the lipid bilayer might slow down the expansion of the bilayer. Nevertheless, a linear fit from $t \sim 23$ to 28 s that accounted for the first 20% of the area expansion (compared with the original area) provided a $\frac{dA}{dt}$ of $114\,\mu\text{m}^2/\text{s}$.

The inner and outer zone appeared after $t > 45$ s (image **c** of Figure 3.8), indicating the proximal leaflet of the outer zone contained detergents. The intensity of the outer zone became lower than the inner zone's after $t > 50$ s (Figure 3.9), again suggesting that the outer zone was dissolved faster. Still, the distinction between the inner and the outer zone diminished after $t > 100$ s when their intensity traces overlapped (Figure 3.9 and image **e** and **f** in Figure 3.8). A tentative explanation is that after a significant amount of lipids in the inner zone were dissolved, the detergents could flip to the proximal leaflet of the inner zone relatively easily. Subsequently, the early presence of detergents in the proximal leaflet of the outer zone was no longer crucial in differentiating the solubilization of the inner and outer zone.

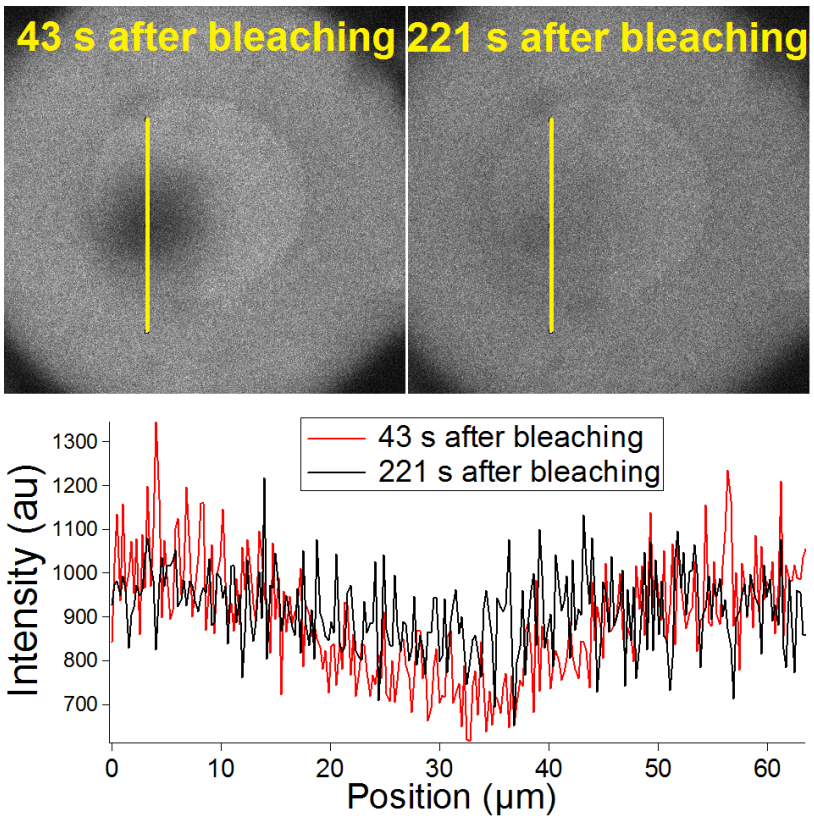


Figure 3.10: *A spot was bleached for the bilayer in Figure 3.8. The image taken 43s after bleaching the spot (upper left) and the fluorescence intensity profile along the yellow vertical line is shown (bottom graph). Another image taken 221 s after the bleaching (upper right) and its profile along the same line (bottom graph).*

The bilayer expanded by a factor of three after $t = 606$ s (image **f** of Figure 3.8), presumably because the lipids mixed with the adsorbed CTAB to form a continuous

mixed CTAB-DOPC bilayer. To show this was possible, a spot of diameter $\sim 26\,\mu$m was bleached. From the images taken 43 and 221 s after the bleaching (upper images of Figure 3.10), it is obvious that the fluorescence intensity of the bleached spot recovered when we inspect the fluorescence intensity profiles along the vertical yellow lines drawn across the spot (bottom graph of Figure 3.10). The intensity profile taken at $t = 43$ s shows a pronounced minimum due to the bleached spot which recovered to an almost constant intensity profile, indicating that the membrane was still a continuous bilayer.

Last but not least, by employing the Arrhenius rate equation as in section (3.3.1), we estimated that the energy barrier for CTAB to partition into lipid membranes within the first 20% expansion is 4.4 ± 0.9 kT from n = 4 measurements.

### 3.3.3 SDS

DOPC bilayers incubated with 9 mM of SDS typically exhibited the solubilization pathway in Figure 3.11 (the full movie M3-3 can be found at *http://www.youtube.com/watch?v=7AfBKZjklR4&feature=plcp*). As with the other detergents, partitioning of detergents into the bilayer led to a brighter edge (image **b**), which is characteristic of the rolling motion discussed earlier. In image **c**, micron-sized cylindrical micelles budded throughout the bilayer. The budding of cylindrical micelles was identified from a finger-like pattern emerging from the edge of the bilayer. The dissolution process from a bilayer to nano-sized (spherical) micelles was interceded by the formation of cylindrical micelles, which was not observed in the solubilization process induced by other detergents. The emergence of cylindrical micelles as an intermediate stage directly demonstrated the curvature frustration as the driving force for micellization. As more detergents inserted into the bilayer, the bilayer was dissolved into islands of micron-sized (cluster of bright spots within the bilayer in image **e**) before the bilayer was totally solubilized (image **f**).

In Figure 3.12 are the time evolution of the bilayer area, the average fluorescence intensity of images (which was multiplied by two to aid the reader's visualization) and the average fluorescence intensity of the inner and outer zone (ROI '1' and '2' in image **c**, which are very small in size) for the event shown in Figure 3.11. The bilayer started to expand at $t \sim 25$ s, with $\frac{dA}{dt}$ of $61\,\mu\text{m}^2/\text{s}$, until a notable drop in the intensity trace was recognized at $t \sim 30$ s, coincided with the budding of cylindrical micelles. As such, a critical lipid:detergent ratio is necessary for the dissolution of the

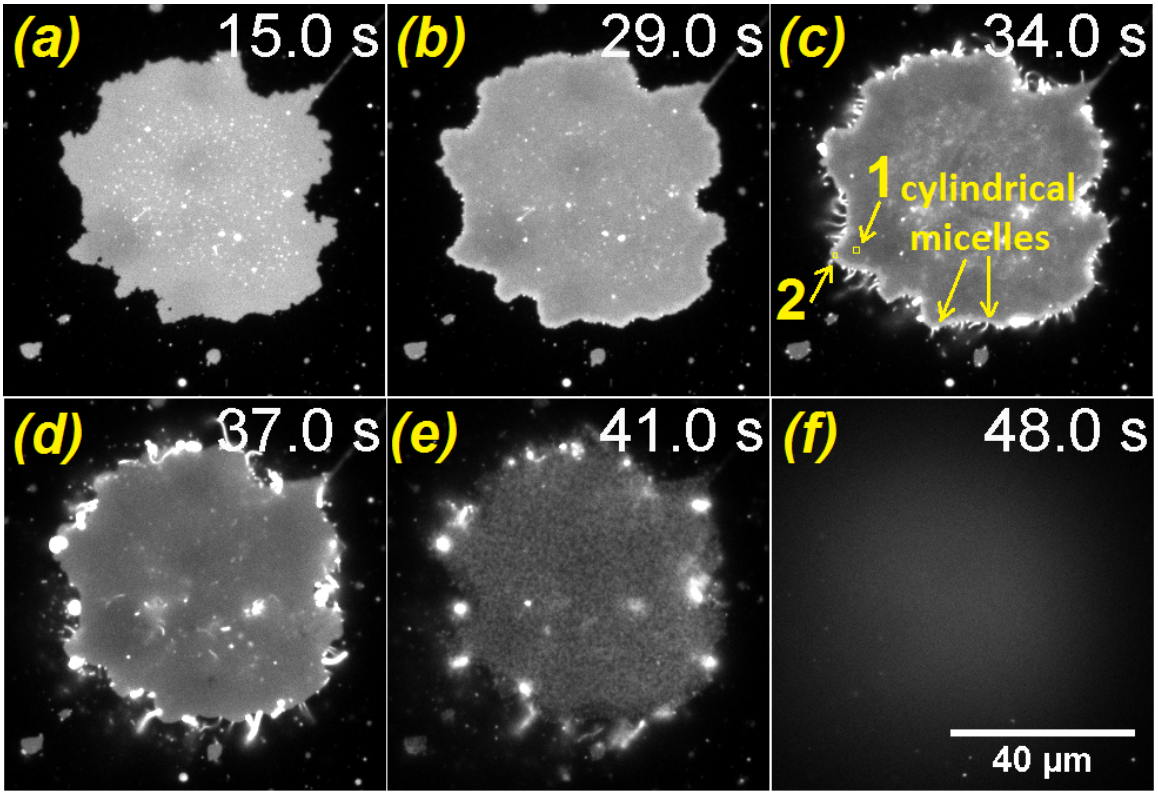


Figure 3.11: *Solubilization of a bilayer by 9 mM SDS and the time series images of the process. All images are on the same contrast. Cylindrical micelles were visualized at the edge of the bilayer (image* **c***). The full movie M3-3 can be found here.*

bilayer by SDS. Even though this is the case, the maximum expansion before the onset of solubilization was considerably smaller than that of observed for the detergents in section (3.3.1), at a value of 8 ± 3 % (n = 4). The bilayer continued to expand before another sharp drop in intensity was identified around $t \sim 40$ s. This sharp drop coincided with the dispersion of the membrane into islands in image **e** of Figure 3.11, indicating the dissolution was accelerated with the existence of bilayer islands. A potential justification is that when the bilayer was dissolved into islands, it exposed the edge that facilitated the translocation of detergents to its proximal leaflet, and therefore the bilayer was dissolved at a higher rate thereafter. The intensity declined to the background level after all the micelles diffused away after $t > 50$ s.

For SDS, we might presume that it did not partition into proximal leaflets of the outer zones due to the repulsion between its negatively charged headgroup and negatively charged glass surfaces. Here, the outer zone remained brighter than the

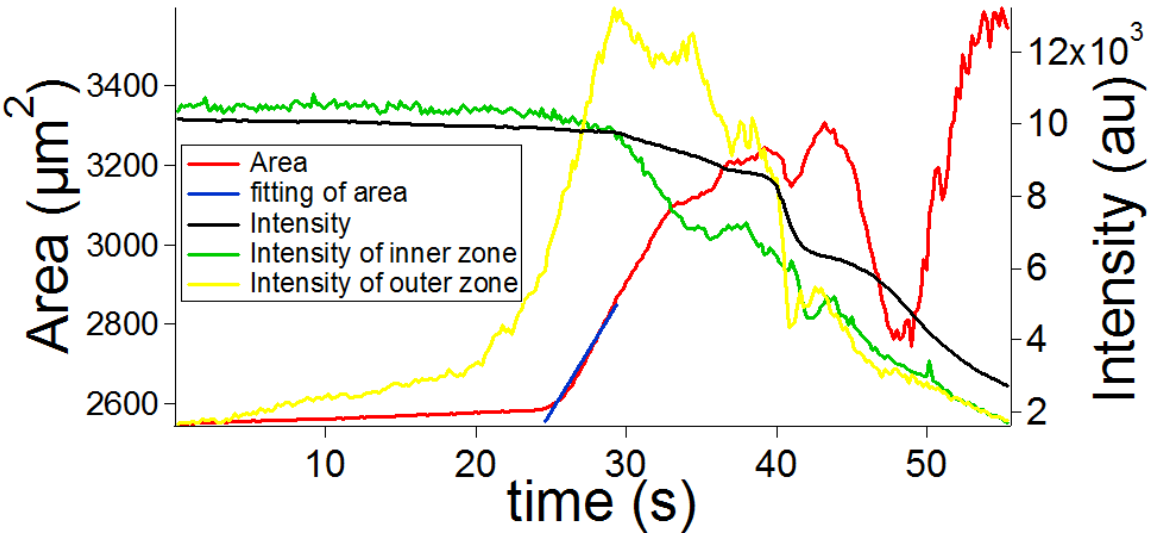


Figure 3.12: *The area of the bilayer, the fluorescence intensity of images (multiplied by two), and the fluorescence intensity of the inner and outer zone are plotted as a function of time for images in Figure 3.11. The intensity of the inner and outer zone is the intensity of the ROI labeled '1' and '2' in image* ***c***

inner zone for most of the dissolution process ($t$ from 30 to 40 s in Figure 3.12), due to the accumulation of LR-PE on the edge. LR-PE did not fade away easily by diffusion from the ROI chosen (or the edge), because the expansion was limited in size. So, it is neither straightforward to conclude that the outer zones dissolved faster than the inner zones, nor can we say SDS partitioned into proximal leaflets of the outer zones. Even so, what we can do is to evaluate the barrier of SDS insertion into bilayers, which was at 6.2 ± 0.8 kT (n = 4).

### 3.3.4 TritonX-100 and Tween20

Figure 3.13 shows the interactions of a bilayer with 0.24 mM of TritonX (the movie M3-4 until $t$ = 150 s can be found at *http://www.youtube.com/watch?v=I5jlHq4mUhg&feature=plcp*). The bilayer went through a similar process as upon exposure to CTAB, described in section (3.3.2), except that no inner or outer zone was detected along the process. To show this quantitatively, in Figure 3.14 we plot the fluorescence intensity along the yellow line in image **d** of Figure 3.13. At $t$ = 20 s, (image **a**), a drop in intensity is recognized at $r \sim 5$ $\mu$m due to the bilayer-glass boundary. When the bilayer expanded to the state

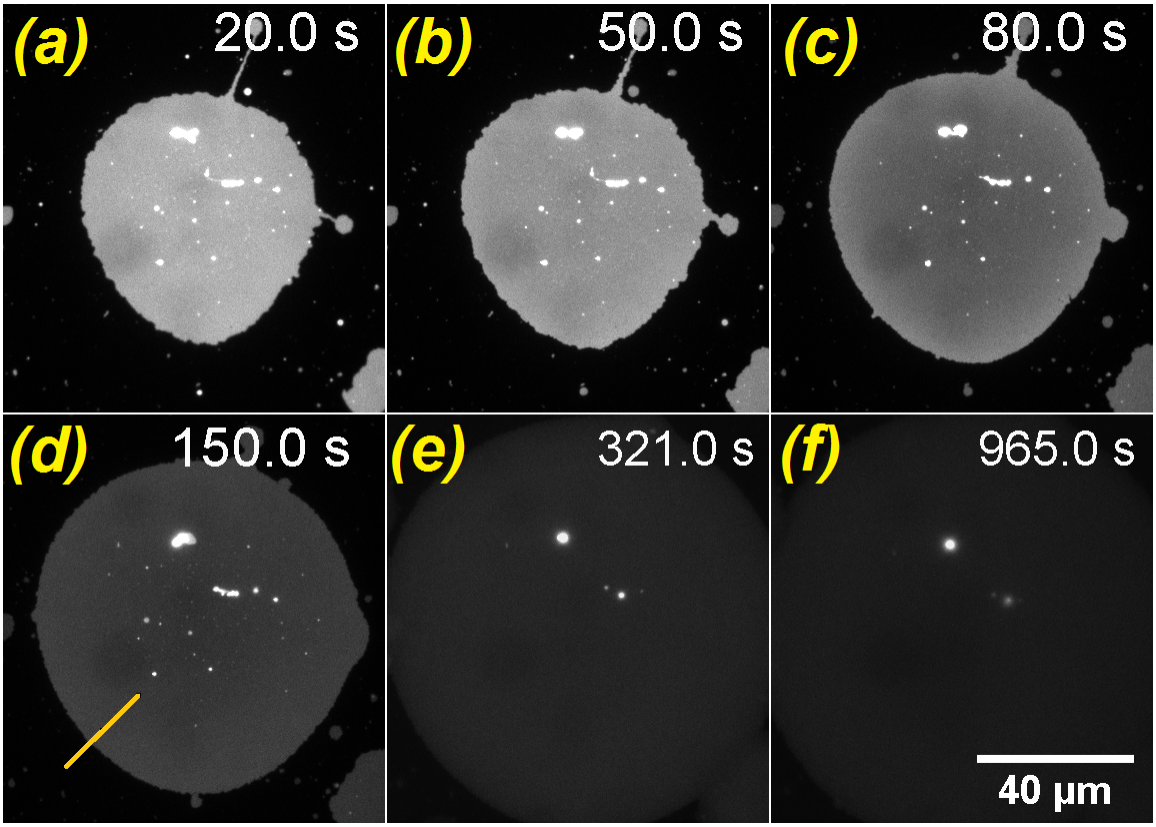


Figure 3.13: *Solubilization of a bilayer by 0.24 mM TritonX-100 and the time series images of the process. All images are on the same contrast except for image* ***e*** *and* ***f*** *in which their contrast has been linearly enhanced. No inner and outer zone was found throughout the event. The bilayer was not completely solubilized after 965 s (image* ***f****). The movie M3-4 until t = 150 s can be found here.*

shown in image **d** ($t = 120$ s), only one sharp drop in intensity was observed at $r \sim 17$ $\mu$m without a drop due to the inner-outer zone at the original bilayer-glass boundary. The absence of the outer and inner zone implies that it is unfavorable for both TritonX and Tween20 to partition into the proximal leaflets of the outer zones, perhaps due to the repulsive interaction between their headgroups (ethylene glycol) and glass. This is reasonable for Tween20 because its big headgroup (20 unit of ethylene glycol) will most probably be excluded from the restricted space between bilayers and glass.

In Figure 3.15, we plot the area of the bilayer, the average fluorescence intensity, and the time derivative of the intensity over time for the bilayer shown in Figure 3.13. The expansion started at $t \sim 40$ s. It was accompanied by a drop in the intensity at the same instant. The drop was characterized by a kink in the intensity trace or a

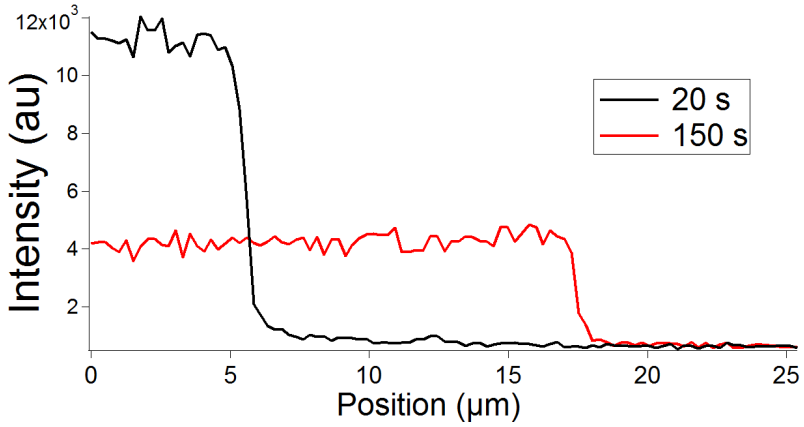


Figure 3.14: *The fluorescence intensity profile along the yellow line drawn in image* ***d*** *of Figure 3.13. The profile for image* ***a*** *(t = 20 s) and image* ***d*** *(t = 150 s) are shown to demonstrate the absence of the inner and outer zone.*

major discontinuity in the time derivative of the intensity that did not recover to the value at $t \sim 40$ s until the end of the graph. It shows that TritonX solubilized the bilayer as soon as it partitioned into the membrane, and a critical lipid:detergent ratio is not required for solubilization.

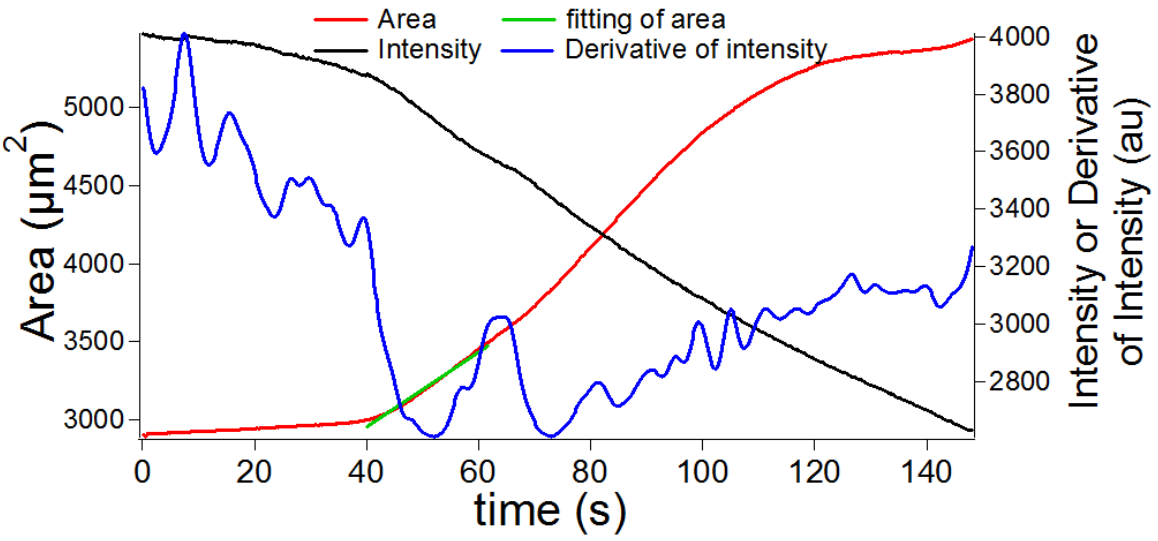


Figure 3.15: *The area of the bilayer, the fluorescence intensity and the time derivative of the intensity of images in Figure 3.13 are plotted as a function of time. The intensity showed a kink and the time derivative of the intensity shows a discontinuity at t = 40 s when solubilization started. During the first 20% expansion, the bilayer expanded at 24 $\mu m^2/s$.*

Both TritonX and Tween20 did not dissolve the bilayer entirely, even after 10 minutes or longer. For Tween20, bilayer area increased by 30 to 40% after tens of minutes. While for TritonX, bilayers enlarged by a factor of 2 to 4 in general, and a bleached spot in these bilayers recovered in tens of seconds, verifying that these bilayers were still continuous (data not shown). Lastly, for the initial 20% area expansion induced by TritonX, the energy barrier was 4.4 ± 0.9 kT (n = 5), and for the first 10% expansion due to Tween20, the barrier was 3.0 ± 2.4 kT (n = 5).

## 3.4 Discussion

In this chapter, we monitored the dissolution process of DOPC bilayer patches on glass by 7 distinct detergents with fluorescence microscopy. The novel and important findings from this work are:

- Different detergents solubilize bilayers in different pathways. As a general rule, partitioning of detergents increases the area of bilayers. Nonetheless, for decyl/dodecyl-maltoside, CHAPS and SDS, solubilization starts when the bilayers reach a critical lipid:detergent ratio, whereas such a critical ratio is not required for CTAB, TritonX and Tween20 where solubilization starts once they partition into the bilayers. After the onset of solubilization, it is possible for bilayers to expand their area. The detergents that do not require a critical lipid:detergent ratio to solubilize membranes violate the 3-stage model because this model assumes that a lamellar to micellar transition will only take place after a critical lipid:detergent ratio is reached. This observation was made possible when we measured the area of bilayers while simultaneously utilized the fluorescence intensity of images as the solubilization indicator. The variation in the solubilization pathways described here would be hidden in the other experimental methods mentioned in Introduction, since they are usually sensitive to only one or other parameter(s) of the dissolution process. For instance, light scattering is only sensitive to the sizes of mixed lipid-detergent vesicles but not to the onset of solubilization, and it is always assumed that solubilization starts when the vesicles reach their maximum sizes [118]. The pathway's discrepancy revealed here may shed light on the formation of detergent-resistant domains, in which TritonX is usually associated with [1, 119].

- Detergents on distal leaflets alone are sufficient to dissolve the inner zones of supported lipid bilayers. This was not anticipated because it has been generally assumed without rigorous proof that detergents need to be present in both leaflets to induce micellization [93].

- From the expansion dynamics of bilayers and Eq. (3.1), we quantitatively showed that curvature frustration of membranes provoked solubilization. Membranes curved into micelles when they acquired enough curvature energy to do so. This was particular evident for SDS when we observed cylindrical micelles directly budding from membranes. Therefore, for incorporating non-bilayer forming molecules into supported bilayers, this results shed light on balancing the values of adhesion energy, $\frac{dE_{adhe}}{dt}$, with curvature energy, $\frac{dE_{curv}}{dt}$. This can be achieved by using charged surfaces and oppositely charged bilayers, by controlling the ratio of bilayer forming molecules to non-bilayer forming molecules, or by using curved solid surfaces.

- Based on a simple diffusion model and the Arrhenius rate equation, we estimated the energy barrier for the partitioning of detergents into lipid bilayers is on the order of 3 to 7 kT per molecule. To the best of our knowledge, this is the first time this number is ever reported in the literature.

## 3.5 Conclusions

We solubilized isolated DOPC bilayers on glass by different detergents. Even though there are several reports on solubilization of supported lipid bilayers by detergents in the literature [119–121], none of them provides a detailed description of the solubilization pathways reported here. The results presented here should improve the understanding of surfactant-lipid membrane interactions, which in turn advance our knowledge in the field of biomembrane research and biosensing applications of supported membranes. In term of fabrication of mixed lipid-detergent bilayers, the results should also be useful. For instance, one would use detergents like decyl/dodecyl maltoside or CHAPS, which require a large critical detergent:lipid ratio in order to solubilize bilayers, instead of CTAB, TritonX-100 or Tween20, which dissolve bilayers upon partitioning, to fabricate mixed bilayers. Meanwhile, by tuning the adhesion energy between solid

surfaces and bilayers, non-bilayer forming molecules can be incorporated stably into planar bilayers for functioning of membranes.

# Chapter 4

# Partitioning of Organic Solvents into Supported Lipid Bilayers

## 4.1 Introduction

The self-assembly of materials depends critically on solvent environments. For example, phospholipids assemble into a lamellar bilayer phase in water, but exist as monomers in most of the organic solvents. The solvent environments also have significant impacts on protein folding, dispersion of emulsions, polymers, surfactants, synthesis of nanomaterials, and aggregations of particles. Therefore, if the interactions between supported bilayers and organic solvents are well understood, organic solvents can be used for manipulating the properties of supported membranes.

We investigated the interactions between organic solvents (methanol, ethanol, isopropanol, propanol, acetone and chloroform) and solid-supported lipid bilayers. For this aim, we prepared fluorescently-labeled DOPC bilayer patches supported on glass. These isolated patches were deposited through rupturing of giant unilamellar vesicles (GUVs) and were a few thousand square micrometers big. They can freely expand to uncovered glass surfaces once organic solvents partition into them. This area expansion was measured with fluorescence microscopy. By titration of the bilayers with increasing volume fractions of organic solvents, we measured the rate of area expansion, the maximum area expansion of the bilayers and the free energy of partitioning. Finally, we performed fluorescence video microscopy experiments to capture the adsorption and the desorption dynamics of organic solvents to and from lipid membranes.

## 4.2 Materials and Methods

### Materials

1,2-dioleoyl-sn-glycero-3-phosphocholine (DOPC) and 1,2-dioleoyl-sn-glycero-3-phospho ethanolamine-N-(lissamine rhodamine B sulfonyl) (ammonium salt) (LR-PE) were purchased from Avanti Polar Lipids (Alabaster, AL) and used as received. Ethanol was purchased from Pharmco Aaper (Brookfield, CT). Methanol, propan-2-ol (isopropanol), acetone and chloroform were purchased from Fisher Scientific (Pittsburgh, PA). Propan-1-ol (propanol) was purchased from Alfa Aesar (Ward Hill, MA). Number 1.5 thickness glass coverslips were purchased from Electron Microscopy Science (Hatfield, PA). All other chemicals were of HPLC grade and the ultrapure water was prepared in a Millipore (Billerica, MA) Milli-Q water purification device.

### Formation of GUVs and Supported Lipid Bilayers

GUVs and patches of lipid bilayers were formed by the methods discussed in Chapter 3.

### Fluorescence Microscopy

Fluorescence imaging was performed by using the fluorescence microscope as described in Chapter 3. For titration experiments, organic solvents at increasing volume fractions were injected into the chambers containing bilayers. Images were taken 5 minutes after the injection of organic solvents because the bilayers reached a new equilibrated area after 5 minutes. The values reported in the titration experiments were the average $\pm$ standard deviation of 3 to 4 independent measurements. For video recording, videos were made at 2 or 5 fps and recording of images was started a few seconds before the injection of organic solvents or rinsing of buffers.

### Fluorescence Recovery After Photobleaching (FRAP)

To verify that the fluorescence from the objects observed in the experiments was from fluid lipid bilayers, FRAP experiments were routinely performed as described in section (2.1.2) and the results were similar to the curve in Figure 2.3.

**Image Analysis**

ImageJ (National Institute of Health) was used for off-line image processing. To determine the area of bilayers, the images recorded were converted to binary images by setting a threshold intensity halfway between the average background and the average object intensity.

## 4.3 Results and Discussion

### 4.3.1 Titration with Organic Solvents

We deposited isolated DOPC bilayer patches of a few thousand square microns on glass surfaces. They were doped with a small amount of LR-PE so that when they were visualized under a fluorescence microscope, their area can be measured accurately. A typical fluorescence image of a representative bilayer is displayed in image **a** of Figure 4.1.

We titrated the bilayers that were under buffers initially with increasing volume fractions of organic solvents. These solvents are methanol, ethanol, isopropanol, propanol, acetone and chloroform. Apart from chloroform, which has a maximum solubility of 0.8%, the other solvents are miscible with water. When solvents partitioned into membranes, bilayers expanded to uncovered glass surfaces. It is illustrated in Figure 4.1. In this example, the bilayer was titrated with ethanol, with no ethanol in image **a**, to 15 and 30% of ethanol by volume in the bulk solution (image **b** and **c**). Its area increased accordingly when ethanol partitioned into its distal leaflet (leaflet facing the bulk solution, see next section). Eventually, when the bulk solution contained 50% of ethanol (image **d**), the bilayer dispersed into small islands and was almost dissolved.

We quantified the area change from the images and plot the area expansion of the bilayer, $\frac{A - A_o}{A_o}$, in which $A$ and $A_o$ are the area with and without ethanol, against the volume fractions of ethanol in the bulk. The data points (in black $\circ$) are shown in Figure 4.2. The area increased linearly with volume fractions of ethanol until the solution contained 30% of ethanol, in which it had expanded by $\sim 29\%$. A linear fit (–) up to 20% of ethanol shows that the bilayer expanded by 0.97% for every percent of ethanol added. Beyond 30% of ethanol, lipids in the bilayer were dissolved gradually and it was accompanied by an area drop. On average, for ethanol, bilayers expanded

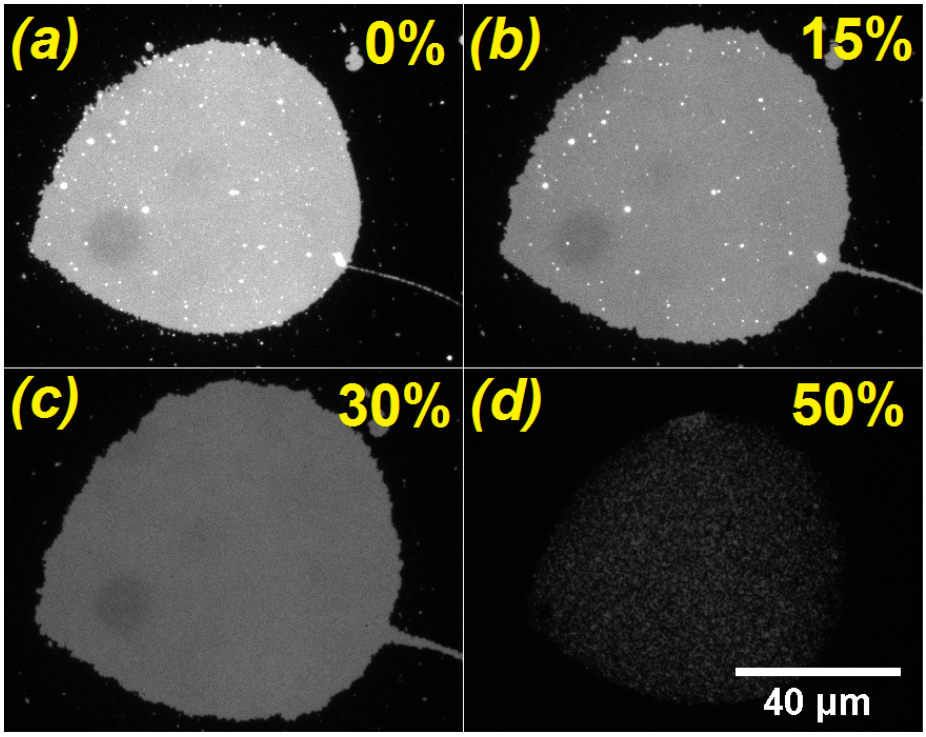


Figure 4.1: *The titration of a DOPC bilayer with increasing volume fractions of ethanol as indicated at the upper right corner of each image. The bilayer expanded as ethanol partitioned into it as shown from image* ***a*** *to* ***c****. The area was maximum at 30% of ethanol (image* ***c****) and any further adsorption dissolved the bilayer. At 50% ethanol (image* ***d****), the bilayer was almost dissolved.*

by 27.6 ± 2.8 % before the commencement of dissolution at 31.7 ± 2.9 % of ethanol, with an expansion rate of 0.94 ± 0.03.

The above experiments were repeated for methanol, isopropanol, propanol and acetone. The representative titration curve for each solvent is plotted in Figure 4.2. For methanol, the maximum expansion before the onset of solubilization was 13.5 ± 1.0 % and the solubilization was initiated at 36.3 ± 2.5 % of methanol with an expansion rate of 0.46 ± 0.03. For isopropanol, they were 38.2 ± 1.1 %, 23.3 ± 2.9 % and 1.77 ± 0.18, for propanol they were 71.4 ± 4.0 %, 21.7 ± 2.9 % and 3.34 ± 0.54, whereas for acetone they were 11.4 ± 2.4 %, 38.3 ± 2.9 % and 0.51 ± 0.07.

The maximum area expansion follows the order of acetone ∼ methanol < ethanol < isopropanol < propanol. For 1-alcohols in this study (methanol, ethanol and propanol), the maximum expansion increased by a factor of 2 to 2.6 for every additional $CH_2$ in the hydrocarbon chains of alcohols. It is known that all 3 alcohols mainly reside in

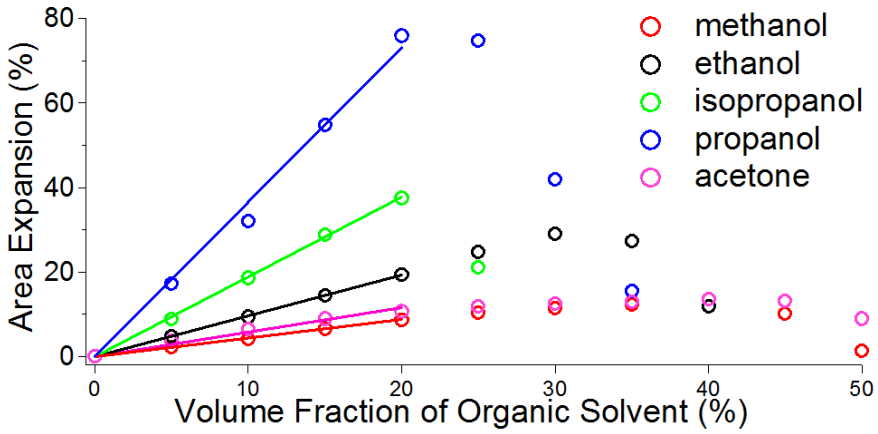


Figure 4.2: *The titration curves for different organic solvents. The area expansions are plotted against the volume fractions of solvents in the bulk solution (○) while linear fits are plotted in lines (–).*

the headgroup region of lipid bilayers, with the hydrocarbon chains pointing toward or insert into the hydrocarbon core of membranes [122–129]. Since the hydrocarbon chains of the alcohols are much shorter than the hydrocarbon chains of DOPC, partitioning of 1-alcohols induces void space in the hydrocarbon core of membranes. The alkyl chains of lipids would either become more disorder or form an interdigitation phase [124–126, 128, 130–132] to compensate for the expansion. The increase in the maximum expansion from methanol to propanol illustrates the significance of 1-alcohols' hydrocarbon chains in assisting the expansion. From a structural point of view, the longer the hydrocarbon chains of alcohols are, the deeper they partition into the hydrocarbon core of membranes, thus occupy more volume and create less void space in the hydrocarbon core. Less disordering of lipid chains is thus required to achieve the same area expansion. Besides, the alcohols with longer hydrocarbon chains will most probably shield the lipid chains better in a fully interdigitated phase (full interdigitation is a case in which the alcohols are directly in contact with the lipids in the opposite leaflet) [123, 128]. As a result, they allow a much larger area expansion before the packing frustration induces the structural breakdown of membranes. It is also remarkable to notice that the maximum area expansion of propanol was larger than its isomer, isopropanol. Propanol has the hydroxyl group at the terminal carbon atom whereas the hydroxyl of isopropanol is located on the central carbon atom. Thus it is hypothesized that isopropanol penetrates less into the membrane hydrocarbon core

if its hydroxyl is to stay within the lipid headgroups. Following the same argument, we suggest that acetone has the least ability to partition into the hydrocarbon core of membranes since its maximum area expansion was the least among the solvents tested.

It is imperative to show that the dissolution of lipid bilayers by organic solvents was due to the packing frustration as discussed in the previous paragraph, and was not provoked by the decrease of the solvent polarity when organic solvents were mixed with water. When the polarity of solvents is reduced, it is possible that lipids are dissolved in the solvents as monomers. To prove this was not the case, we calculate the Dimroth and Reichardt polarity index [133], $E_T^N$ ($0 < E_T^N < 1$, $E_T^N = 1$ for the most polar solvent, water, and $E_T^N = 0$ for the least polar solvent, tetramethylsilane), of the water-organic solvent mixtures when they induced the solubilization of lipid membranes. Since the water-methanol mixture provoked the dissolution at a volume ratio of 63.7:36.3, $E_T^N \sim 0.88$ [134]. While for a water-acetone mixture at a volume ratio of 61.7:38.3, $E_T^N < 0.82$ at the onset of dissolution. Hence, the polarity of solvents was not the crucial factor in solubilizing membranes since these 2 mixtures solubilized the membranes at a different hydrophobicity. It is further corroborated by the fact that in a mixture with a high percentage of organic solvents, organic solvent-lipid micelles are formed [130,131,135], demonstrating the importance of packing frustration in determining the onset of solubilization.

If the area of solvents in membranes is known, the maximum area expansion of lipid bilayers can be converted to the maximum binding ratio between organic solvents and lipids. When the area of DOPC bilayers were increased by $27.6 \pm 2.8$ % due to the partitioning of ethanol, the excess area must be covered by ethanol. Therefore, with an area per molecule of 72 and 18 Å$^2$ for DOPC [136] and ethanol [122] respectively, the molar ratio of ethanol in the mixed lipid-ethanol bilayers is

$$\begin{aligned} x_{ethanol}^{bilayer} &= \frac{n_{ethanol}^{bilayer}}{n_{ethanol}^{bilayer} + n_{lipid}^{bilayer}} \\ &= 0.524 \pm 0.026 \end{aligned} \tag{4.1}$$

in which $n$ is the number of molecules. Therefore, a maximum binding stoichiometry of lipid:ethanol $\sim$ 1:1 was achieved before any further adsorption of ethanol dissolved the membranes. With an area per molecule of 16 and 18 Å$^2$ for methanol and

propanol [122], their molar ratio in the bilayers are 0.378 ± 0.018 and 0.740 ± 0.010 respectively, below which the bilayers can maintain a lamellar phase.

As a next step, we used the titration curves in Figure 4.2 to deduce the partition coefficient or the free energy of partitioning of organic solvents from the bulk solution into the membranes. We change the volume fractions of organic solvents in the bulk solution to the molar ratio of organic solvents in the bulk solution,

$$x^{bulk}_{org.\,sol.} = \frac{n^{bulk}_{org.\,sol.}}{n^{bulk}_{org.\,sol.} + n^{bulk}_{water}} \tag{4.2}$$

and change the area expansion to the molar ratio of organic solvents in bilayers as in Eq. (4.1). The resulting curves with data points in dots (•) are displayed in Figure 4.3. The partition coefficient, $K$ is defined as

$$K = \frac{x^{bilayer}_{org.\,sol.}}{x^{bulk}_{org.\,sol.}} \tag{4.3}$$

in the limit of $x^{bulk/bilayer}_{org.\,sol.} \to 0$ [122, 137]. To derive these values from Figure 4.3, we fitted the curves before the onset of dissolution to an exponential function,

$$x^{bilayer}_{org.\,sol.} = b(1 - exp(-hx^{bulk}_{org.\,sol.})) \tag{4.4}$$

where $b$ and $h$ are fitting parameters. The corresponding fits are shown in Figure 4.3 in lines. The partition coefficients are interpolated from the slope of these fittings at $x^{bulk}_{org.\,sol.} = 0$, so $K = bh$. For methanol, $K = 4.95 \pm 0.30$, for ethanol, $K = 10.8 \pm 0.30$, for propanol, $K = 46.3 \pm 11.7$. The free energy of partitioning, $\Delta G = -kT(lnK)$. It follows that $\Delta G$ = -1.60 ± 0.06 kT for methanol, $\Delta G$ = -2.38 ± 0.03 kT for ethanol, $\Delta G$ = -3.82 ± 0.25 kT for propanol. A systematic increment for the magnitude of $K$ or $\Delta G$ from methanol, ethanol to propanol is evident. These values are comparable to the $K$ that were reported to be 9.2, 23.8, 99.1 [122] and 7.8, 16.6 and 49.3 [138]. It supports the conclusion that hydrocarbon chains of 1-alcohols partition into the hydrocarbon core of membranes because the partitioning of a longer hydrocarbon chain from water to a hydrocarbon phase would produce larger free energy of partitioning.

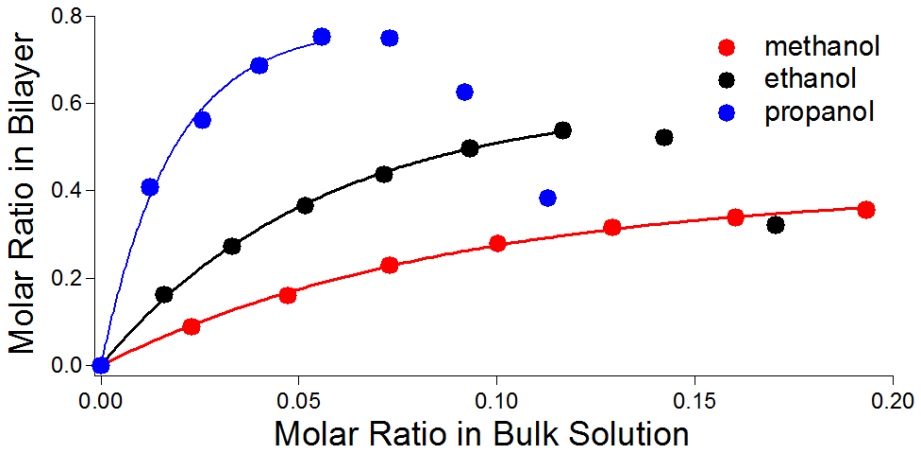


Figure 4.3: *Conversion of the titration curves in Figure 4.2 to the molar ratio of organic solvents in the bilayers and in the bulk (•). An exponential fit (–) was performed on each trace and the partition coefficients were interpolated from the fits by taking the slope at the origin.*

To verify the interpolation of titration curves did produce accurate values of $K$ and $\Delta G$, we repeated the experiments with low volume fractions of organic solvents ($< 2\%$, Figure 4.4). All the traces in Figure 4.4 (•), plotted as the molar ratio of solvents in bilayers against the bulk solution, were fitted to a linear function ($-$) passing through the origin. The slope of these linear functions is equal to $K$. The resulting $K$ are $5.68 \pm 3.53$, $17.85 \pm 7.81$, $50.40 \pm 13.08$ for methanol, ethanol, propanol respectively. These values are either close or within the error bars of the $K$ obtained from the preceding interpolation.

We are now in a position to compare the partition coefficients with the expansion rate of bilayers which follows the order of acetone $\sim$ methanol $<$ ethanol $<$ isopropanol $<$ propanol. For 1-alcohols, partition coefficients derived according to Eq. (4.3) can be correlated to the expansion rate of bilayers. Two quantities actually associated with each other with a correlation coefficient of $1.00 \pm 0.03$ for the partition coefficients derived from Figure 4.3 (data from reference [138] and [122] also correlates with the expansion rate with a correlation coefficient close to 1). Not only it illustrates the robustness of the bilayer expansion rate in evaluating the strength of interactions, it implies that the expansion rates are related to the partition coefficients based on Eq. (4.3) by a multiplication factor. Accordingly, if the expansion rate is in place of $K$ in the equation $\Delta G = -kT(lnK)$, $\Delta G$ obtained from this substitution differs

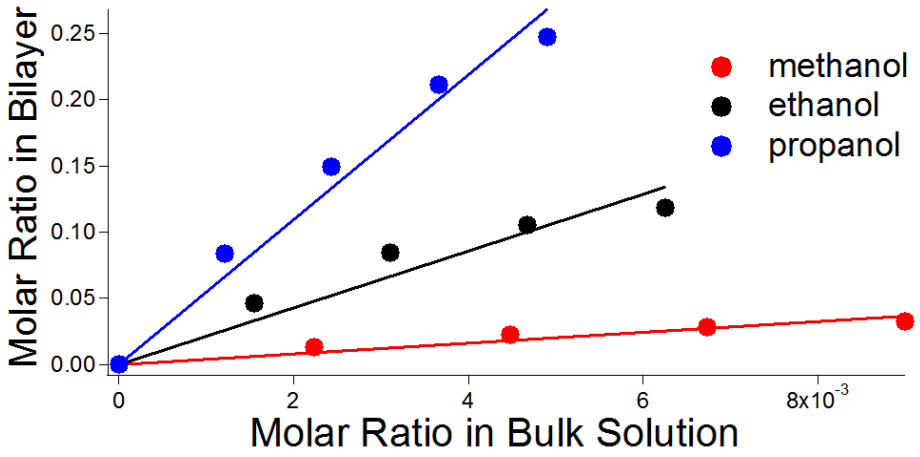


Figure 4.4: *The titration experiments were repeated for small volume fractions of organic solvents (•). The slope of the linear fits (–) is the partition coefficient.*

from $\Delta G$ defined by $K$ by an additive constant. This observation is in agreement with reference [137] where it was discovered that the free energy of partitioning varies by an overall additive constant when the definition of partition coefficients is different. Nevertheless, for comparing the strength of interactions between molecules and bilayers, $\Delta\Delta G$, which is the difference of free energy for 2 molecular species, can be assessed by using the expansion rate. Therefore, we propose to use the expansion rates in substitution for the partition coefficients to compare the strength of small molecule partitioning when the area of molecules in membranes is unknown. The proposed method is beneficial for supported membranes because the area expansion of membranes can be measured with fluorescence microscopy or AFM while the molar ratio of molecules in membranes is hard to be determined. So, we suggest that the partition coefficients of solvents into membranes follow the order of the expansion rates with acetone $\sim$ methanol $<$ ethanol $<$ isopropanol $<$ propanol. This order is justified by the same argument put forward for explaining the maximum area expansion previously, since a larger free energy is produced by a deeper penetration of solvents into hydrocarbon core of membranes. For instance, for propanol and isopropanol,

$$\begin{aligned}\Delta\Delta G &= \mathrm{kT} * \ln(\text{expansion rate of propanol}) \\ &\quad -\mathrm{kT} * \ln(\text{expansion rate of isopropanol}) \\ &= \mathrm{kT} * \ln(3.34) - \mathrm{kT} * \ln(1.77) \\ &= 0.63 * \mathrm{kT}\end{aligned} \tag{4.5}$$

Lastly, we did the titration with chloroform (data not shown). The maximum volume fraction of chloroform was limited to the solubility of chloroform in water. The area expansion rate of bilayers was 5.08 ± 1.03 and the maximum expansion within the limit of chloroform solubility was 2.5 ± 0.5 %. It is reasonable for chloroform to have the highest expansion rate among the solvents as it is the least polar solvent, and thus has the highest tendency to partition into membranes.

### 4.3.2 Partitioning Dynamics of Organic Solvents

We captured the partitioning dynamics of organic solvents into DOPC bilayer patches with fluorescence video microscopy. All the solvents exhibited identical dynamics and the situation depicted here applies to all solvents. The partitioning dynamics of ethanol into a DOPC bilayer, with 33.3% of ethanol in the bulk solution, is shown in Figure 4.5. This volume fraction of ethanol was slightly larger than the volume fraction of ethanol that started to solubilize the bilayers at 31.7 ± 2.9 %.

In Figure 4.5, a few representative images from the video are shown (The full movie M4-1 can be found at *http://www.youtube.com/watch?v=mybkjm2J3eQ&feature=plcp*). Initially, the bilayer was $\sim 4100\ \mu\mathrm{m}^2$ (image **a**). After $t > 6$ s, the ethanol began to partition into the bilayer and led to its area expansion until $t \sim 25$ s (image **b** and **c**). After $t > 25$ s, some lipids at its edge were dissolved and the bilayer shrank until a new equilibrated area was reached after $t > 40$ s (image **d**), presumably because the desorption rate of ethanol was close in magnitude to the adsorption rate at this surface concentration of ethanol. As a result of the lipid dissolution at the edge, the edge developed a fingering pattern and became rougher than before (image **d**).

During the expansion from $t = 6$ to 25 s, the edge was higher in fluorescence intensity than the bilayer's interior as observed in image **b** and **c**, due to the accumulation of LR-PE. To show this quantitatively, in Figure 4.6, we plot the fluorescence intensity along a yellow line drawn across the edge in image **b** of Figure 4.5. The fluorescence intensity along that line at $t = 0$ s showed a sharp drop at $r \sim 13\ \mu$m, due to the

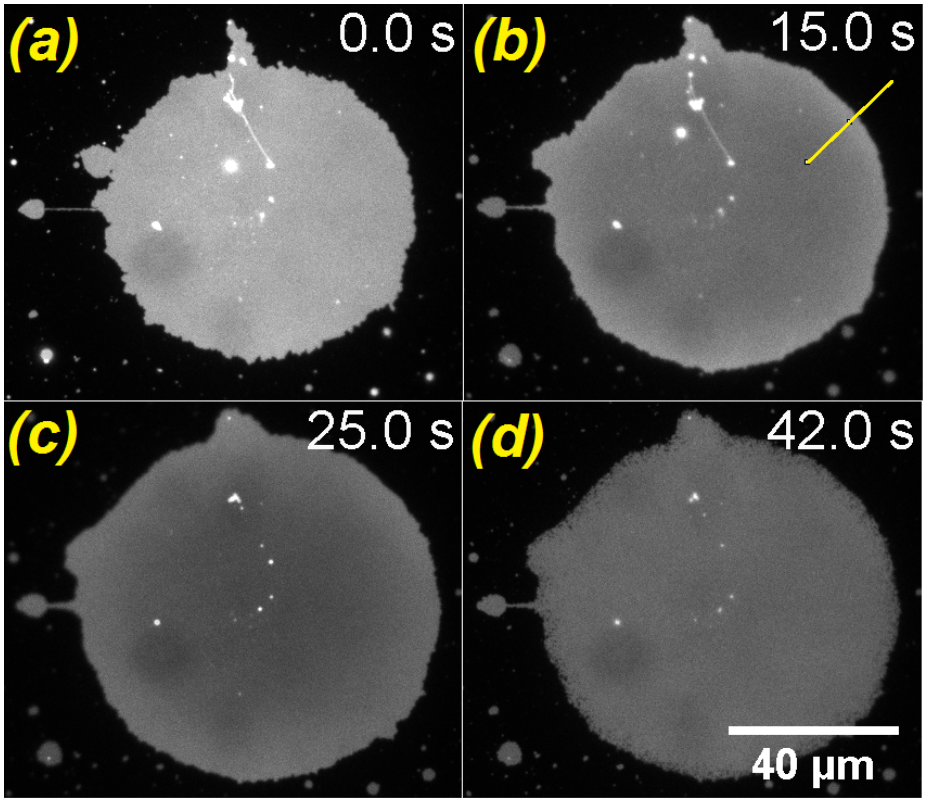


Figure 4.5: *The partitioning dynamics of ethanol into a DOPC bilayer, with 33.3% of ethanol in the bulk solution. The bilayer expanded from image* ***a*** *to* ***c*** *as ethanol partitioned into the membrane. The edge of the bilayer was brighter during the expansion (image* ***b*** *and* ***c****) and finally some of the lipids on the edge were dissolved and the bilayer shrank (image* ***d****). The full movie M4-1 can be found here.*

boundary of the bilayer and the uncovered glass surface. When the bilayer enlarged at $t = 15$ and 25 s (image **b** and **c**), this boundary was shifted to a larger $r$ at $\sim 15$ and 19 $\mu$m accordingly. Additionally, these 2 profiles were higher in the fluorescence intensity at the boundary than their interior (intensity at $r = 0$). It unmistakably confirms the density of LR-PE was higher on the edge during the area expansion. At $t$ = 42 s, since some of the lipids on the edge were dissolved, the boundary receded and the drop of intensity was located at a smaller $r$ compared with the drop of intensity at $t = 25$ s. The intensity at $r = 0$ diminished progressively as the bilayer expanded, because the density of LR-PE became smaller as the bilayer expanded and the the emission spectrum of LR-PE was blue-shifted when the fluorophores were in contact with organic solvents.

The accumulation of LR-PE on the edges of lipid bilayers is the signature of a

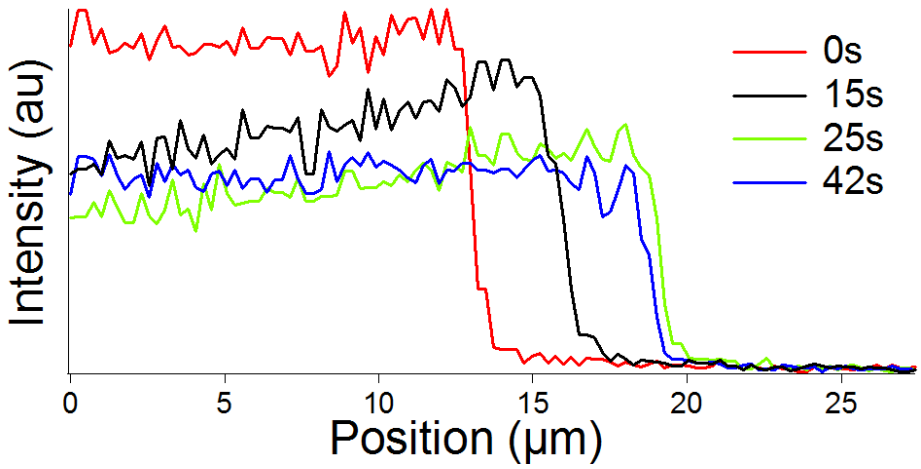


Figure 4.6: *The fluorescence intensity along the yellow line drawn in image* ***b*** *for images in Figure 4.5 to evaluate the evolution of the bilayer edge during the expansion.*

rolling motion as discussed in Chapter 3. Here, only the distal leaflets of the bilayers were exposed to organic solvents. As a result, the organic solvents partition into the distal leaflets but not the proximal leaflets. The distal leaflets, but not the proximal leaflets, expanded. The only way for this asymmetrical expansion to take place is through the rolling of the distal leaflets over the proximal leaflets. In this case, lipids in the proximal leaflets were stationary while lipids and adsorbed organic solvents in the distal leaflets moved radially outward and flipped into the proximal leaflets through the edges of the bilayers. Because it is unfavorable for LR-PE to reside in the proximal leaflets, presumably due to the steric and electrostatic repulsion between the headgroups and the glass surfaces, LRPE accumulated along the edges when they were pushed toward the edges by the rolling motion. They resisted the flipping into the proximal leaflets and led to the brighter edges as seen. It is also intriguing to note that if majority of the organic solvents were able to translocate to the proximal leaflets through the hydrocarbon core of membranes at a molecular time scale ($<$ seconds), then the expansion would not be asymmetrical and LR-PE would not accumulate along the edges. However, it was not the case and therefore we can safely conclude that the organic solvents we used here mainly locate on the headgroup region of the distal leaflets, as we claimed earlier.

To quantify the expansion process, we plot the area of the bilayer as a function of time in Figure 4.7. As described earlier, the bilayer expanded after $t > 6$ s and its area grew. The growth in area was approximately linear in time. The expansion came

to a halt with a maximum area of $\sim 5600\ \mu m^2$ at $t \sim 25$ s. A linear fit up to that point provides a $\frac{dA}{dt}$ of $87 \pm 1\ \mu m^2/s$. The bilayer had expanded by $\sim 37\%$ and it was more than the maximum area expansion of lipid-ethanol systems at 27.6% from the titration experiments. Therefore, the packing frustration induced the dissolution of lipids at the edge. The bilayer shrank from the edge and its area dropped to $\sim 5400\ \mu m^2$ at $t \sim 40$ s. After that, the area remained constant until $t \sim 80$ s. The final area expansion was $\sim 32\%$, close to the maximum area expansion of 27.6% from the titration experiments. The reduction of area always occurs first through the shrinkage of bilayers on the edges. A potential explanation would be because the edges were structurally weaker than the rest of the bilayers, since they might contain organic solvents in both the proximal and distal leaflets. As discovered in Chapter 3, the proximal leaflets within the original bilayers before the expansion were most probably in a gel phase. When the organic solvents flipped to the proximal leaflets from the distal leaflets, they may not mix with the lipids in the proximal leaflets within the original bilayers. It was possible that the proximal leaflets within the original bilayers were organic solvents free. Therefore, the bilayers near the edges were structurally perturbed more severely than the interior of bilayers and hence dissolved faster. It is unlikely that the dissolution was initiated near the edges to reduce the perimeter of the bilayers, which in turn reduced the energy associated with the bilayer line tension, because the perimeter of the bilayers increased (data not shown) as the edges became rougher upon dissolution.

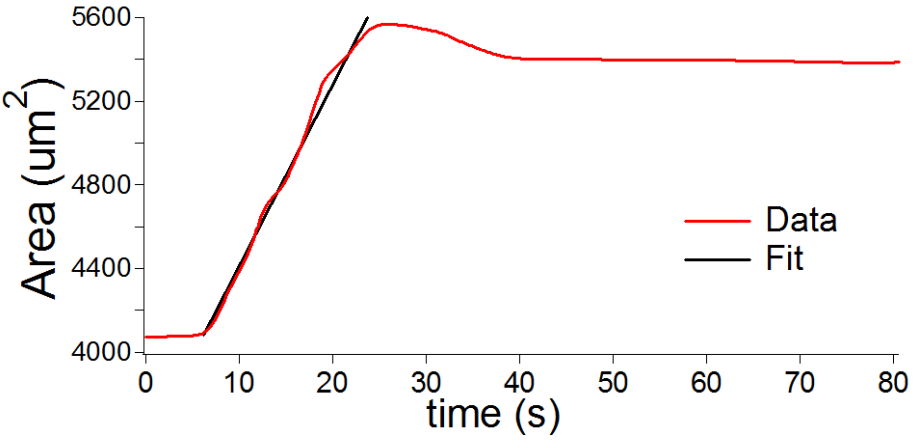


Figure 4.7: *The area of the bilayer in Figure 4-5 is plotted as a function of time. A linear fit up to the maximum size of the bilayer showed that* $\frac{dA}{dt} = 87 \pm 1\ \mu m^2/s$.

Similar to the expansion dynamics described in Chapter 3, during the expansion, the total energy of the system (bilayers + water + organic solvents), $E_{total}$, must be conserved. This implies its time derivative,

$$\frac{dE_{total}}{dt} = 0 = \frac{dE_{adhe}}{dt} + \frac{dE_{fric}}{dt} + \frac{dE_{edge}}{dt} + \frac{dE_{part}}{dt} + \frac{dE_{curv}}{dt} + released\,or\,absorbed\,heat \tag{4.6}$$

From Chapter 3, the adhesion energy was

$$\begin{aligned} \frac{dE_{adhe}}{dt} &= \gamma \frac{dA}{dt} \\ &= (-0.15\,\mathrm{mN/m}) \times (87\,\mu\mathrm{m}^2/\mathrm{s}) \\ &= -1.0 \times 10^{-14}\,\mathrm{J/s} \end{aligned} \tag{4.7}$$

The energy dissipated by friction was

$$\begin{aligned} \frac{dE_{fric}}{dt} &= \left(\frac{b}{8\pi}\right)\left(\frac{dA}{dt}\right)^2 \\ &= (10^8\,\mathrm{Ns/m^3}/8\pi)(87\,\mu\mathrm{m}^2/\mathrm{s})^2 \\ &= 3.0 \times 10^{-14}\,\mathrm{J/s} \end{aligned} \tag{4.8}$$

The line energy of the bilayer edge was

$$\begin{aligned} \frac{dE_{edge}}{dt} &= T \frac{dP}{dt} \\ &= (10\,\mathrm{pN})(1.5\,\mu\mathrm{m/s}) \\ &= 1.5 \times 10^{-17}\,\mathrm{J/s} \end{aligned} \tag{4.9}$$

$\frac{dP}{dt}$ is the change of the perimeter of the bilayer per unit time and is equal to 1.5 $\mu$m/s (data not shown).

The energy loss due to partitioning of ethanol was

$$\begin{aligned}\frac{dE_{part}}{dt} &= number\,of\,ethanol\,partitioned\,per\,unit\,time\,\times E_{part}^{molecule} \\ &= \left(\frac{dA}{dt}\right) \div (area\,per\,ethanol)\,\times\, E_{part}^{molecule} \\ &= (87\,\mu\mathrm{m}^2/\mathrm{s}) \div (0.18\,\mathrm{nm}^2)\,\times\,(-9.6\times10^{-21}\,\mathrm{J}) \\ &= -4.6\times10^{-12}\,\mathrm{J/s}\end{aligned} \tag{4.10}$$

where $E_{part}^{molecule}$ = -2.38 kT = $-9.6\times10^{-21}$ J is obtained from Section (4.3.1).

Similar to Chapter 3, the curvature energy of the planar bilayer,

$$E_{curv} = A\times\left(\left(\frac{1}{2}\right)\kappa(2C-2C_o)^2+\bar{\kappa}C^2\right) \tag{4.11}$$

requires special attention. To a good approximation, DOPC is a cylindrical molecule with a length $l$ ($\sim$ 15 Å) and a headgroup area $a_o$ (see Figure 4.8). Therefore, its volume is $la_o$. Upon partitioning of ethanol to the headgroup, the headgroup area becomes $a_o+\Delta a$. Therefore, the DOPC-ethanol complex no longer prefers a planar configuration and can be modeled as a cone-shaped molecule with a headgroup area $a_o+\Delta a$ (Figure 4.8). The complex favors a spherical micelle packing provided the spontaneous curvature of the complex is modeled as [110]

$$C_o \sim \frac{a_o+\Delta a}{3\times volume\,of\,the\,complex} \tag{4.12}$$

A DOPC molecule occupies a volume of 1300 Å$^3$ [136] while the volume of an ethanol is $\sim$ 100 Å$^3$ in its pure form. Consequently, with a maximum binding stoichiometry of $\sim$ 1:1 between DOPC and ethanol, we made an approximation that the volume of a DOPC-ethanol complex is almost equal to the volume of a DOPC $\sim la_o$. As a result, $C_o \sim \dfrac{a_o+\Delta a}{3la_o}$. By substituting $C_o$ into $E_{curv}$ and making use of the fact that $\dfrac{a_o+\Delta a}{a_o} = \dfrac{A}{A_o}$, we obtained

$$\frac{dE_{curv}}{dt} = \left(\frac{2}{3}\right)\kappa\left(\frac{dA}{dt}\right)\left(\frac{A}{lA_o}\right)^2 \tag{4.13}$$

This term was not constant over time. Since the area of the bilayer, $A$, grew linearly in time, $\frac{dE_{curv}}{dt}$ increased quadratically in time. At the beginning of the expansion where $A_o = A$, it was $\sim 2.2 \times 10^{-12}$ J/s with a $\frac{dA}{dt}$ of 87 $\mu$m$^2$/s. However, when $A = 1.365A_o$ in which the expansion was maximum, it became $4.1 \times 10^{-12}$ J/s, approaching the magnitude of $\frac{dE_{part}}{dt}$.

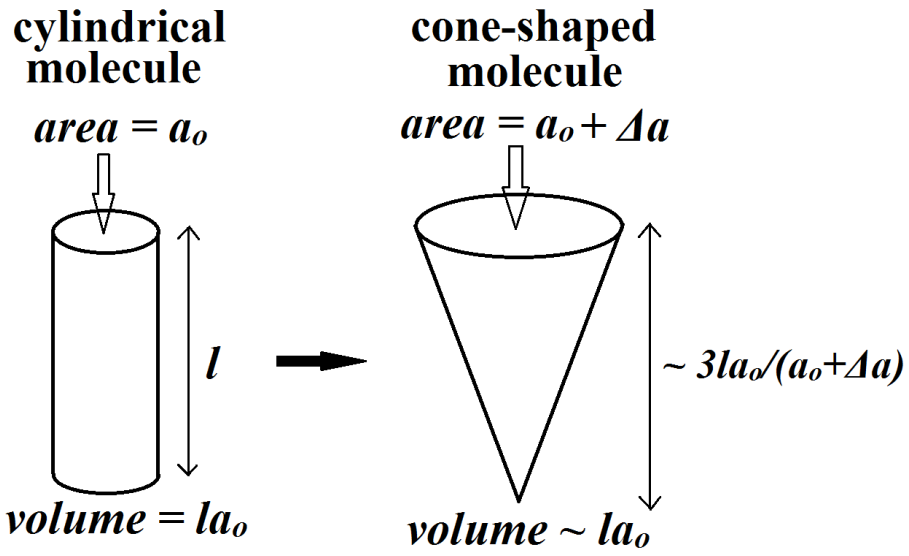


Figure 4.8: *The conversion of a cylindrical molecule such as DOPC into an inverted cone-shaped molecules upon the binding of organic solvents to the headgroup of DOPC. The inverted cone-shape molecule favors a speherical micelle instead of a planar bilayer if its spontaneous curvature* $C_o \sim \frac{a + a_o}{3la_o}$.

Finally, partitioning of organic solvents into lipid membranes is always accompanied by heat release or absorption [137]. Heat is either released or absorbed depending on the conditions of experiments.

As the consequence, Eq. (4.6) is dominated by $\frac{dE_{part}}{dt}$, $\frac{dE_{curv}}{dt}$ and the released or absorbed heat because the other 3 terms had a much smaller magnitude. Since $\frac{dE_{curv}}{dt}$ increased over time, at the commencement of the expansion, $\frac{dE_{part}}{dt}$ must be counter-balanced by released heat, which had a positive sign to preserve the equality in Eq. (4.6). Therefore, heat was released during the expansion, namely the partitioning process was exothermic with a negative enthalpy. Due to this energy increment, the thermal energy or the temperature of the system increased. At the same time,

the generated heat induced disordering of lipid's chains as discussed in the titration experiments. As more and more organic solvents partitioned into the bilayer, the magnitude of $\frac{dE_{curv}}{dt}$ approached $\frac{dE_{part}}{dt}$, and the bilayer developed the curvature ($C \neq 0$) to reduce $\frac{dE_{curv}}{dt}$ for persevering Eq. (4.6). Hence, some of the lipids on the edge curved into micelles. Finally, when the magnitude of $\frac{dE_{curv}}{dt}$ was even closer to the magnitude of $\frac{dE_{part}}{dt}$, the expansion had to cease to satisfy the equality of Eq. (4.6) with $\frac{dA}{dt} = 0$. The fact that $\frac{dE_{curv}}{dt}$ or packing frustration was critical in membrane solubilization was in accord with results in Section (4.3.1) in which the maximum area expansion was related to the penetration depth of solvents in membranes.

### 4.3.3 Desorption of Organic Solvents

To study the desorption of organic solvents from DOPC bilayers, we incubated the bilayers with 25% of ethanol in the bulk solution, which would expand the bilayers by $24.2 \pm 1.3$ %. Later we monitored the desorption of ethanol from the bilayers when the ethanol in the solution were rinsed away. The results are shown from Figure 4.9 to 4.12.

In Figure 4.9 are the time series images of the desorption process (the full movie M4-2 can be found at *http://www.youtube.com/watch?v=OhOd_UMQ6g8&feature=plcp*). When the ethanol was desorbed from the bilayer, the bilayer shrank from its edge and a fingering pattern emerged from the edge (image **b** to **d**), similar to the dissolution of lipids on the edges as discussed in Section (4.3.2). To depict this scenario precisely, a yellow line was drawn across the edge in image **b** and the corresponding fluorescence intensity along this line is plotted in Figure 4.10 for the images in Figure 4.9. At $t = 0$ s, the intensity along the line had a drop in intensity at $r \sim 12$ $\mu$m, which was due to the bilayer-glass boundary. The bilayer-glass boundary retreated to $r < 10$ $\mu$m at $t = 10$ and 15 s, verifying the shrinkage of the bilayer along the edge during the displacement of ethanol from the bilayer.

In addition to the shrinkage on the edge, multiple pores nucleated within the interior of the bilayer and grew in size (dark spots from image **b** to **d** in Figure 4.9). These pores stayed permanently and did not reseal. Therefore, there were at least 2 ways for the bilayer to reduce its area upon the desorption of ethanol (which was true

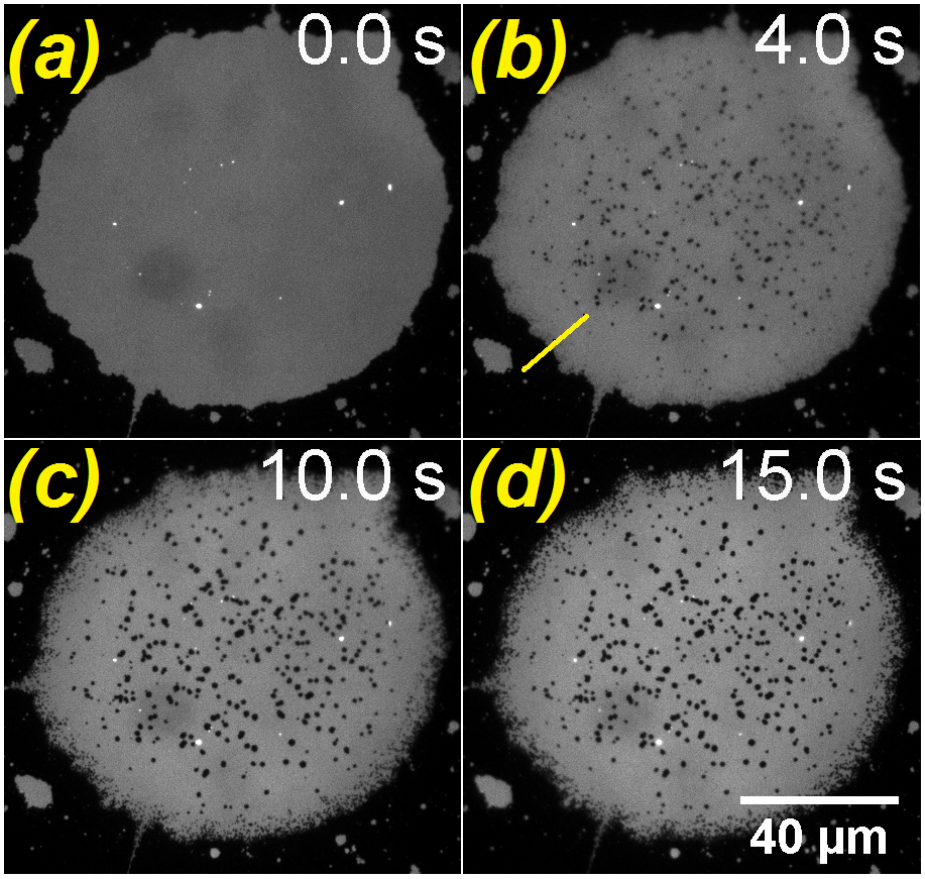


Figure 4.9: *The desorption of ethanol from the bilayer and the time series images of the process. The bilayer shrank from the bilayer edge and developed a fingering pattern (image* ***b*** *to* ***d****). At the same time, multiple pores of micron-sized were formed within the bilayer. The full movie M4-2 can be found here.*

for all the organic solvents tested here). It also means the area expansion and the area reduction of the bilayers did not follow a reversible pathway, namely the area reduction can be mediated along the bilayers edges or within their interior. When ethanol was released from distal leaflets of bilayers to the bulk solution, it created a corresponding vacancy in the bilayers. The tension rose as the lipid hydrocarbon chains were exposed to the aqueous phase. To relax the tension, the area per lipid in the distal leaflets needs to be reduced. Thus, lipids in proximal leaflets would need to flip to distal leaflets to maintain the same area between the proximal and distal leaflets. During the partitioning of organic solvents, the bilayers expanded through the rolling motion and lipids flipped from the distal to the proximal leaflets only through the edges of bilayer patches. This rolling motion can be reversed with the lipids flipped from the

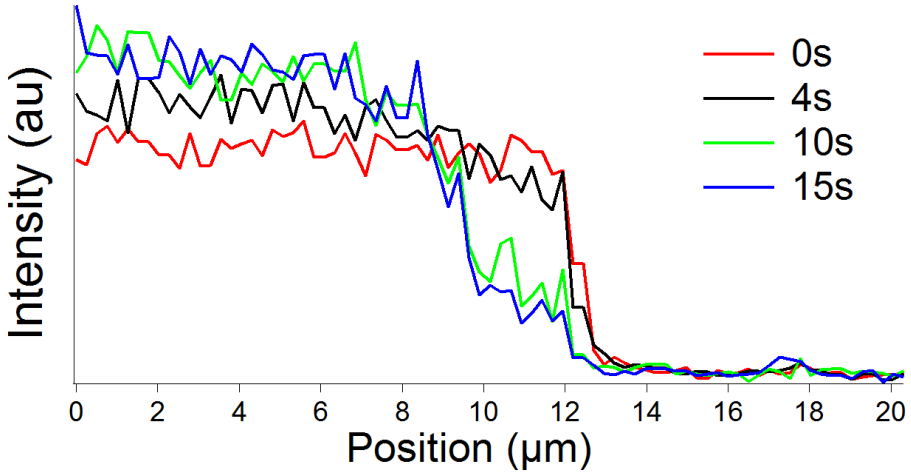


Figure 4.10: *The fluorescence intensity along the yellow line drawn in image* ***b*** *of Figure 4.9 to show the shrinkage of the bilayer on its edge.*

proximal to the distal leaflets through the edges again. Provided the expansion and the shrinkage were totally reversible, the bilayers will only shrink through the edges and no pores will be formed within the bilayers. However, it was not the case and the bilayers relaxed the tension following the desorption of organic solvents by the shrinkage on the bilayers edges and by the formation of pores. In Figure 4.11, the area of the bilayer and the pores are plotted with respect to time. A linear fit at the early stage of the desorption revealed that the area of the bilayer was reduced at a rate of $214.9 \pm 4.8$ $\mu m^2/s$ and the pores grew at a rate of $89.4 \pm 3.5$ $\mu m^2/s$. Therefore, the shrinkage of the bilayer edge took place at a rate of $214.9 - 89.4 = 125.5$ $\mu m^2/s$.

On the other hand, it is notable that the contour length of the bilayer edge increased during the desorption, due to the growth of the fingering pattern on the edge and the creation of multiple pores. The length of the bilayer edge (perimeter of bilayer patches + perimeter of the pores) is plotted in Figure 4.12. At the very beginning of the desorption process, the edge increased at a rate of $358.2 \pm 15.1$ $\mu m/s$ from a linear fit. This scenario was in contrary to a common belief that bilayer edges should be minimized in length to minimize the line energy of the edges. For instance, only a single pore was formed in a giant unilamellar vesicle under tension and resealed as the tension vanished [109]. In contrast with that case, multiple pores nucleated in the bilayer and increased the length of the bilayer edge. Resealing of the pores or the self-healing property of bilayers was not observed later at all (after $> 10$ minutes, data not shown). This discrepancy highlights the fact that edges of supported lipid

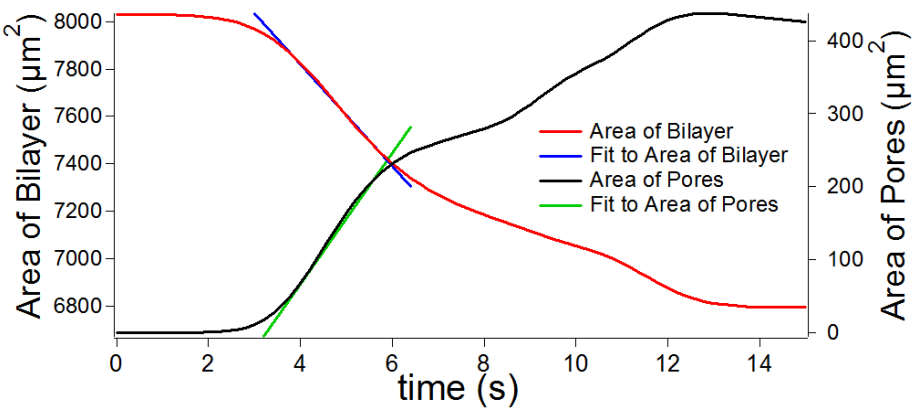


Figure 4.11: *The area of the bilayer and the pores within are plotted as a function of time for the event in Figure 4.9. From the fitting, the bilayer shrank at a rate of 214.9 ± 4.8 $\mu m^2/s$ and the pores grew at a rate of 89.4 ± 3.5 $\mu m^2/s$.*

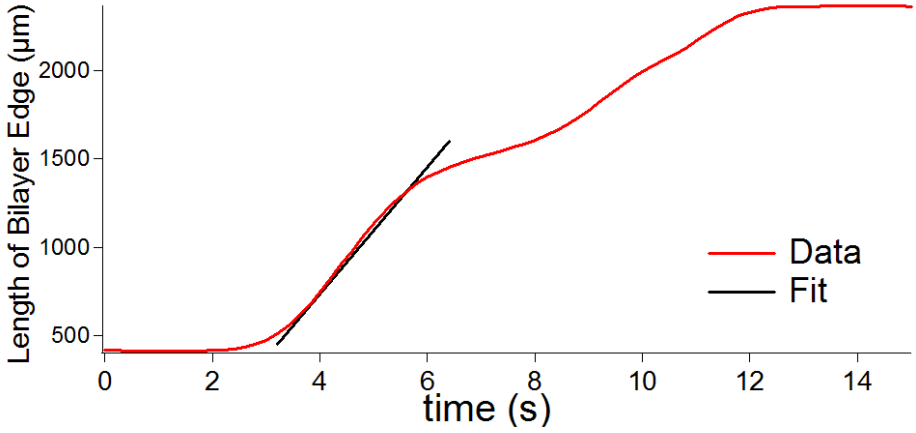


Figure 4.12: *The time evolution of the length of the bilayer edge (bilayer + pores) for the event in Figure 4.9. The growth was 358.2 ± 15.1 $\mu m/s$ from the fitting.*

bilayers behave differently with edges of lipid vesicles. We propose that it is due to non-fluid bilayer edges. As discussed in Chapter 3, proximal leaflets of supported bilayers were most probably in a gel phase since they did not allow the mixing of lipids with detergents. In conjunction with this finding, it was shown in a previous report that the edges of supported lipid bilayers were in an ordered phase [139], which was reasonable considering the property of proximal leaflets would definitely influence the edges. Following these observations, we strongly argue that due to the interactions between solid surfaces and bilayers, the bilayer edges are not fluid and thus their length does not need to be minimized. The suggestion is further supported as the

bilayers in image **a** of Figure 4.1, 4.5 and 4.9 were not perfectly circular (circularity $<$ 1) to shorten the exposed edges, because these edges were not fluid and cannot change the shape of the bilayers subsequently.

## 4.4 Conclusions

In a nutshell, we had characterized the interactions of organic solvents (methanol, ethanol, propanol, isopropanol, acetone and chloroform) with supported lipid bilayers on glass. We did the titration experiments to probe the area expansion of the bilayers due to the partitioning of organic solvents. We suggests the rate of bilayer expansions is a useful indicator for comparing the strength of solvent-membrane interactions, while the maximum area expansion correlates with the penetration depth of solvents into the hydrocarbon core of membranes. In addition, the maximum area expansion of bilayer patches was directly converted to the maximum binding stoichiometry between lipids and organic solvents. From the titration curves, we also deduced the partition coefficients and the free energy of partitioning. Partitioning and desorption dynamics of organic solvents were studied to elucidate the response of bilayers. The expansion of bilayers was accomplished with the rolling motion of distal leaflets over proximal leaflets. Together with the maximum area expansion in titration experiments, the expansion dynamics implied that curvature energy plays a dominant role in stability of bilayers. Moreover, desorption of organic solvents increased the length of exposed bilayer edges and left permanent pores inside the bilayers. Last but not least, to account for the growth of lipid bilayer edges and the absence of self-healing, it is suggested that the bilayer edges were not fluid. Despite the fact that supported lipid bilayers are popular nowadays both as models biomembranes and in technological applications, no systematic studies exist to decipher their stability and interactions with organic solvents. This work will be valuable in filling the gap and broaden the potential of supported membranes.

# Chapter 5

# Formation of sparsely-tethered Bilayer Lipid Membranes (stBLMs) with Vesicle Hemifusion*

## 5.1 Introduction

As mentioned in Chapter 3 and 4, proximal leaflets of glass supported lipid bilayers are most probably in a gel phase due to the adhesion between lipid headgroups and glass surfaces. As a consequence, incorporation of integral membrane proteins into supported lipid bilayers seems less promising since functionality of proteins would be severely distorted due to a higher than usual lateral pressure imposed by proximal leaflets.

To overcome this limitation, various supported membrane architectures are designed to decouple the effect of underlying solid substrates. For example, instead of supported on solid surfaces directly, thin layers of polymers are deposited in between solid surfaces and lipid bilayers. The thickness of polymer films can be tuned to be several nanometers to avoid a direct contact between proteins and substrates. However, the coverage of lipid bilayers on polymer films is usually incomplete and therefore are not electrically insulating to be considered as useful models to study the properties of incorporated ion channels.

*This method is historically called vesicle fusion instead of hemifusion. Nevertheless, from the data presented in Chapter 6, we suggest that hemifusion is a better term for this process. See Discussion of Chapter 6 for details.

Another highly promising candidate for membrane proteins incorporation is sparsely-tethered bilayer lipid membranes (stBLMs) (see Figure 1.3). Through thiol-gold bonds, some of the lipids (thiolated or tethering lipids) in proximal leaflets are tethered to underlying gold surfaces. The tethering lipids (WC14, FC16 and HC18) have 6 to 9 unit of ethylene glycol in between thiols and alkyl chains, which lift the membranes up from the gold surfaces for submembrane spaces of $\sim 2$ nm thick. If all the lipids in proximal leaflets are tethered, the proximal leaflets are densely packed by tethering lipids with no room for free lipids, and the submembrane spaces are non-hydrated with only $< 5\%$ of water by volume. To increase the hydration level in the submembrane spaces and space out the proximal leaflets for transmembrane proteins incorporation, tethering lipids are co-adsorbed with small spacer molecules ($\beta$-mercaptoethanol, $\beta$ME) at different ratios to the gold surfaces to control the lateral density of tethering lipids. Mixtures of tethering lipids and $\beta$ME lead to stBLMs with $> 50\%$ water in the submembrane spaces. The existence of 2 nm thick hydrated layers should avoid a direct contact of transmembrane proteins with solid supports, which would otherwise denature or impede functionality of proteins.

Previously, to form stBLMs, gold surfaces are co-absorbed with tethering lipids and spacer molecules to form hydrophobic (water contact angle from $\sim 80^\circ$ to $110^\circ$) mixed self-assembled monolayers (SAMs). Bilayers are completed subsequently with rapid solvent exchange (RSE) [23, 24]. In RSE, SAMs are incubated with lipids in organic solvents (usually ethanol) and the solutions are flushed with large amounts of aqueous buffer. Lipids precipitate on SAMs to form stBLMs. The resulting stBLMs are electically insulating (resistance $> 100$ k$\Omega$cm$^2$), fluid (diffusion coefficient of lipids $> 2$ $\mu$m$^2$/s) [60] and long term stable ($\sim$ days).

However, the major disadvantage of RSE is that it makes transmembrane proteins incorporation impossible because proteins denature in organic solvents. Therefore, to incorporate proteins which have transmembrane domains, the only way is to preform stBLMs with RSE, and then incubate the stBLMs with proteins of interest. This method works only for a certain number of proteins or peptides such as gramicidin, valinomycin and $\alpha$-hemolysin [35, 140]. Majority of transmembrane proteins are in detergent micelles to shield their hydrophobic domains from a direct contact with water. So, incubate stBLMs with proteins in detergent micelles will perturb the stBLMs because the detergents will eventually dissolve the membranes (Chapter 3).

One way to overcome this problem is to complete the bilayers with vesicle hemi-

fusion instead of RSE. In vesicle hemifusion, SAMs are incubated with lipid vesicles and the hydrophobicity of SAMs drives the rupturing of vesicles to complete the bilayers. Proteins reconstituted in vesicles are transported to stBLMs during the process. The method to incorporate transmembrane proteins into lipid vesicles is well-established. Therefore, vesicle hemifusion is preferred over RSE for proteins incorporation. Furthermore, regardless of initial orientations of proteins in lipid vesicles, the proteins incorporated into stBLMs with vesicle hemifusion are uni-directional because inner leaflets of vesicles have to be separated from outer leaflets during the process [17] (see Chapter 6). In addition, chemical compositions of stBLMs would be better controlled with vesicle hemifusion since it is unclear whether RSE preserves the chemical composition of lipids dissolved in organic solvents upon precipitation to mixed SAMs.

Vesicle hemifusion has been performed to form other tethered or hybrid bilayer systems on hydrophobic surfaces. In those cases, densely packed monolayers, which are very hydrophobic (water contact angle $\sim 110^{\circ}$), are used as the SAMs. However, densely packed SAMs make the transmembrane proteins incorporation impossible. In our case, mixed SAMs are used but they decrease the surface hydrophobicity to $< 90^{\circ}$ of water contact angle. Vesicle hemifusion on low hydrophobic surfaces is scarcely demonstrated if not none. Previously, mixed SAMs are formed with cholesterol anchors and spacer molecules [22]. The hydrophobicity or the water contact angle of the mixed SAMs was controlled by adjusting the ratio of cholesterol anchors to spacer molecules. However, mixed SAMs in that case phase separated into hydrophobic (cholesterol anchors) and hydrophilic (spacers) domains [141]. While in our case, with small spacer molecules like $\beta$ME, tethering lipids mix homogeneously with spacer molecules, creating homogeneous mixed SAMs with no phase separation [23, 141]. Therefore, even though vesicle hemifusion on mixed SAMs of different hydrophobicity had been investigated, it remains unclear whether or not vesicle hemifusion will also work for mixed SAMs with relatively low water contact angles, but with no phase separation, as in our case.

In this chapter, we investigated the formation of stBLMs through vesicle hemifusion. The formation of stBLMs with vesicle hemifusion was probed with Electrical Impedance Spectroscopy (EIS) and Neutron Reflectivity (NR). We varied the hydrophobicity of mixed SAMs systematically by varying the ratio of tethering lipids (FC16) to $\beta$ME on gold surfaces. We showed that successful formations of highly insulating stBLMs

with vesicle hemifusion depends critically on concentrations of lipid vesicles and on the hydrophobicity of mixed SAMs. We also compared stBLMs formed with RSE and with vesicle hemifusion. RSE produced more insulating stBLMs at low water contact angles ($< 90°$) but the difference diminished for mixed SAMs of high contact angles ($> 100°$). To demonstrate versatility of this method to form different membrane mimics, stBLMs were formed with negatively charged lipids and with E. coli polar lipids extract. A well-controlled formation of stBLMs with vesicle hemifusion, which facilitates protein incorporation and preserves chemical compositions, will improve the potential of stBLMs in both biomedical research and technological applications.

## 5.2 Materials and Methods

### Materials

1,2-diphytanoyl-sn-glycero-3-phosphocholine (DPhyPC), 1-palmitoyl-2-oleoyl-sn-glycero-3-phosphoethanolamine (POPE), 1-palmitoyl-2-oleoyl-sn-glycero-3-phospho-(1'-rac-glycerol) (sodium salt) (POPG) and E. coli Polar Lipid Extract were purchased from Avanti Polar Lipids (Alabaster, AL) and used as received. Silicon wafers (100) were purchased from Silicon Quest International (Santa Clara, CA). $\beta$-mercaptoethanol ($\beta$ME) was purchased from Sigma Aldrich (St. Louis, MO). FC16 was synthesized according to a previous protocol [24]. All other chemicals were of HPLC grade and the ultrapure water was prepared in a Millipore (Billerica, MA) Milli-Q water purification device.

### Formation of Self-Assembly Monolayers (SAMs)

Silicon wafers were sputtered with $\sim$ 2 nm thick of chromium adlayers, followed by another layers of gold ($\sim$ 50 nm for EIS and $\sim$ 13 nm for NR), by using a high energy magnetron (ATC Orion, AJA International, North Scituate, MA). Upon breaking the vacuum of magnetron, gold-coated wafers were immediately transferred to an ethanolic solution of FC16:$\beta$ME mixture, at a total concentration of 0.2 mM but with varying ratios of FC16 and $\beta$ME. The wafers were left incubated in the FC16:$\beta$ME solution overnight to form mixed SAMs.

### Vesicle Hemifusion and Rapid Solvent Exchange (RSE)

Lipids of desired compositions were dissolved in chloroform at 25 mg/ml. The chloroform was evaporated under a vacuum for forming dry lipid films. Subsequently, lipids were further dissolved in pentane and dried under the vacuum again for at least a few hours to remove residual organic solvents. After this, dry lipid films were resuspended in aqueous buffers and sonicated to form microns size multilamellar lipid vesicles (MLV). To further reduce the size and lamellarity of vesicles, MLVs were extruded through polycarbonate membranes (usually with a pore size of 100 nm, Avanti Polar Lipids, Alabaster, AL) for at least 11 times. The resulting vesicles were large unilamellar vesicles (LUVs) of $\sim$ 100 nm in diameter. Mixed SAMs were incubated with LUVs under different conditions to complete the bilayers through vesicle hemifusion. LUVs were used within a few days after the preparation.

Rapid solvent exchange (RSE) was performed by incubating mixed SAMs with 10 mg/ml of desired lipid compositions in ethanol. Later, lipids in ethanol were flushed with large amounts of aqueous buffers so that lipids precipitated to the SAM surfaces to complete the bilayers.

### Electrical Impedance Spectroscopy (EIS)

Impedance measurements were performed as described in Section (2.2.2). The resulting impedance spectra were fitted to an equivalent circuit in Figure 2.7 to extract the values of constant phase element (CPE) and resistances of stBLMs.

### Neutron Reflectivity (NR)

NR measurements were performed at NG1 reflectometer at the NIST Center for Neutron Research (NCNR). Silicon substrates for stBLMs were assembled in a neutron wet cell and reflectivity was measured from $Q_z = 0.01$ to 0.3 $\text{Å}^{-1}$. The measurements for each solvent contrast typically took $\sim$ 6 hours for collecting sufficient statistics. The box model fitting was then carried out by GA_REFL [23], which is developed at NCNR.

## 5.3 Results and Discussion

### 5.3.1 Comparison between Vesicle Hemifusion and RSE on SAMs of Low Hydrophobicity

Previously, stBLMs on mixed SAMs of low hydrophobicity (water contact angle $< 90°$) were formed with RSE instead of vesicle hemifusion. It is because mixed SAMs with high ratio of $\beta$ME to FC16 are not hydrophobic enough to rupture closed-shell lipid vesicles [142], while RSE can most probably bypass this barrier by transferring lipids to SAM surfaces as monomers or micelles during the solvent exchange process [135]. For example, it was found that instead of forming planar membranes, vesicles only absorbed to mixed SAMs having a water contact angle of $\sim 70°$ [143]. To demonstrate feasibility of vesicle hemifusion to form complete stBLMs on SAMs of low hydrophobicity, FC16:$\beta$ME = 3:7 SAMs (water contact angle $\sim 80°$ [24], and the ratio of FC16:$\beta$ME refers to the ratio of FC16:$\beta$ME in the ethanolic solution that was used to form mixed SAMs) were prepared. The SAMs were incubated with 5 mg/ml of DPhyPC vesicles for 1 hour before the excess vesicles were rinsed away. As a comparison, stBLMs were also formed with RSE on these SAMs. The typical impedance spectra of DPhyPC stBLMs formed with both vesicle hemifusion and RSE are shown in Figure 5.1. The stBLM formed with vesicle hemifusion had a resistance, $R_{stBLM} = 35 \pm 1$ k$\Omega$cm$^2$, $CPE_{stBLM} = 1.13 \pm 0.18$ $\mu$Fcm$^{-2}$s$^{\alpha-1}$ and $\alpha = 0.963 \pm 0.002$ from the equivalent circuit fitting. For RSE, $R_{stBLM} = 437 \pm 2$ k$\Omega$cm$^2$, $CPE_{stBLM} = 1.33 \pm 0.13$ $\mu$Fcm$^{-2}$s$^{\alpha-1}$ and $\alpha = 0.936 \pm 0.002$. With a $CPE_{stBLM} \sim$ capacitance $\sim 1.1$ to $1.3$ $\mu$Fcm$^{-2}$s$^{\alpha-1}$, which is a typical capacitance for lipid bilayers, it is concluded that a complete stBLM is formed with vesicle hemifusion. Nevertheless, the stBLM formed with RSE showed a resistance that was one order of magnitude larger than vesicle hemifusion. It demonstrates the importance of hydrophobicity in forming an insulating stBLM with vesicle hemifusion. Even though stBLMs formed with vesicle hemifusion and RSE showed a huge difference in their resistances, their structures were minimally different, as the insulating property is very sensitive to the presence of small water-filled pores in the membranes as discussed in Section (2.2.1) [23] (see also the result of NR).

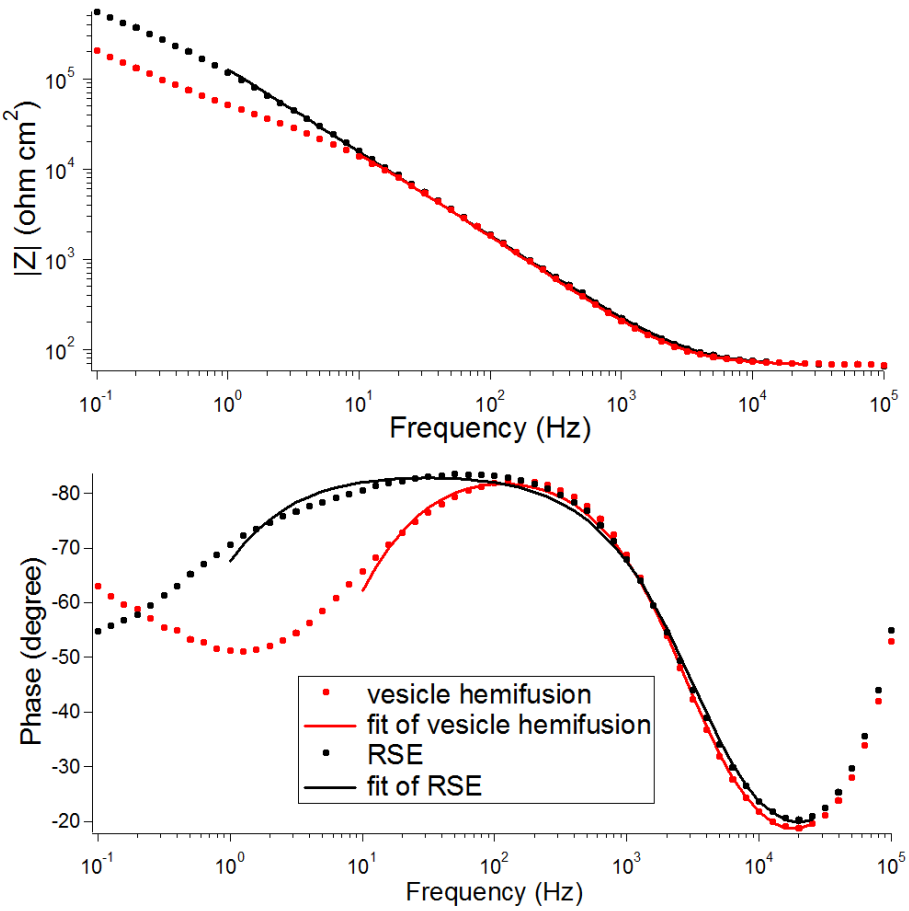


Figure 5.1: *The impedance spectra of DPhyPC stBLMs formed with vesicle hemifusion or RSE on SAMs of low hydrophobicity (FC16:$\beta$ME = 3:7).*

### 5.3.2 The Effect of SAM Hydrophobicity on Vesicle Hemifusion

As verified in the previous section, RSE was far more superior in forming highly insulating stBLMs on surfaces of low hydrophobicity compared with vesicle hemifusion. The most probable reason was because these SAM surfaces were not sufficient hydrophobic to rupture the lipid vesicles, and therefore there were slightly less lipids deposited on the SAMs in comparison with RSE. To bypass this problem, we prepared SAMs with higher ratios of FC16 to increase the surface hydrophobicity. The vesicle hemifusion was carried out by using the FC16:$\beta$ME = 3:7, 4:6 and 5:5 SAMs (water contact angle $\sim$ 80°, 90° and 105° respectively [24]). The formation of DPhyPC stBLMs was characterized by impedance measurements and the impedance spectra,

together with the corresponding equivalent circuit fittings are shown in Figure 5.2. The fitting parameters of the equivalent circuit are also shown in Table 5.1.

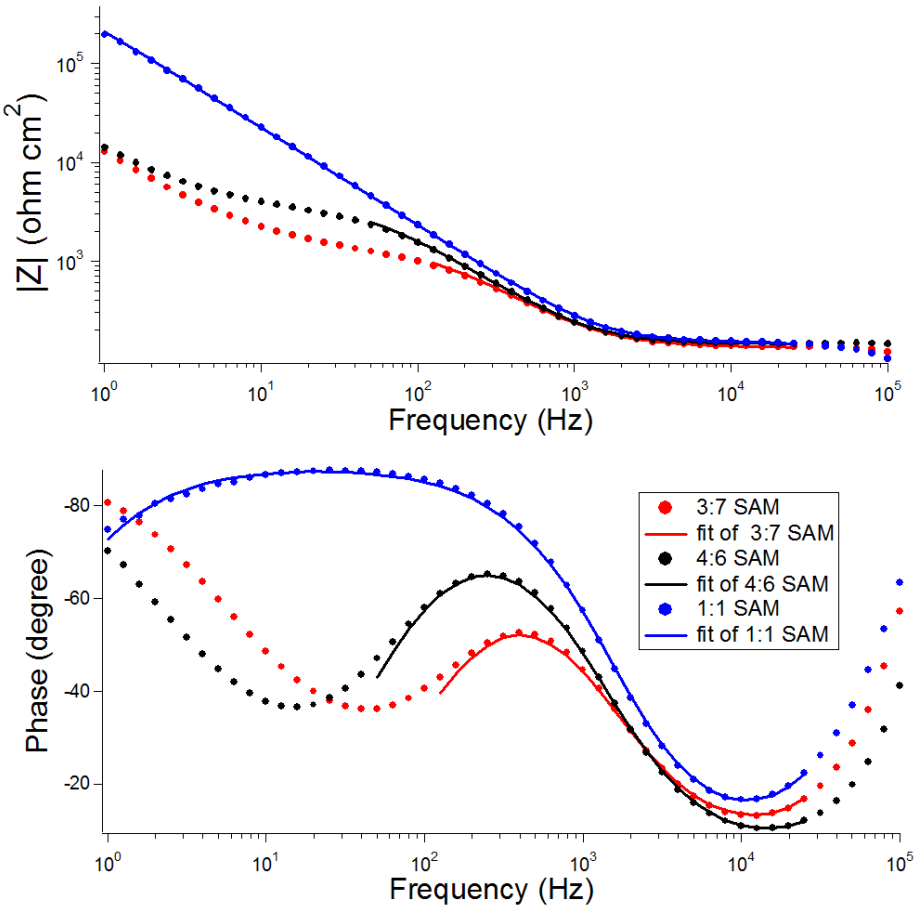


Figure 5.2: *The impedance spectra and the fittings for DPhyPC stBLMs formed on FC16:βME = 3:7, 4:6 and 5:5 SAMs with vesicle hemifusion.*

| | $CPE_{stBLM}(\mu\text{Fcm}^{-2}\text{s}^{\alpha-1})$ | $\alpha$ | $R_{stBLM}(\text{k}\Omega\text{cm}^2)$ |
|---|---|---|---|
| 3:7 SAM | 1.58 ± 0.08 | 0.939 ± 0.005 | 1.3 ± 0.0 |
| 4:6 SAM | 1.15 ± 0.03 | 0.968 ± 0.003 | 3.6 ± 0.1 |
| 5:5 SAM | 0.74 ± 0.00 | 0.989 ± 0.001 | 746 ± 21 |

Table 5.1: *Fitting parameters of the equivalent circuit for DPhyPC stBLMs on SAMs of different hydrophobicity.*

From the fittings, it is clear that stBLMs became more insulating as the SAMs were more hydrophobic. It illustrates the importance of surface hydrophobicity in rupturing vesicles or the importance of densely packed SAMs in producing stBLMs

with high resistances. Since the resistances of stBLMs increased by more than 2 orders of magnitude from 3:7 and 4:6 SAMs to 1:1 SAMs, 1:1 SAMs are a better choice to form stBLMs with vesicle hemifusion from an electrical viewpoint.

### 5.3.3 The Effect of Vesicle Concentrations on Vesicle Hemifusion

To further optimize vesicle hemifusion as an alternative to form stBLMs, we investigated the influence of lipid vesicle concentrations on the electrical properties of stBLMs. FC16:$\beta$ME = 1:1 SAMs were incubated with 0.1, 0.5, 1 and 10 mg/ml of DPhyPC vesicles for 1 hour to form stBLMs with vesicle hemifusion. stBLMs were also formed with RSE for comparison. The resulting impedance spectra are shown in Figure 5.3 and the fitting parameters are summarized in Table 5.2. Under all conditions, even if the concentrations of vesicles varied by 2 orders of magnitude, stBLMs have a $CPE_{stBLM}$ of 0.75 to 0.83 $\mu$Fcm$^{-2}$s$^{-1}$, which did not show a significant difference. However, for stBLMs formed with 1 and 10 mg/ml of vesicles through vesicle hemifusion, the resistances were $\sim$ 6 M$\Omega$cm$^2$. While the resistance dropped to $\sim$ 4 M$\Omega$cm$^2$ for 0.5 mg/ml of vesicles and further dropped by 2 orders of magnitude to 74 k$\Omega$cm$^2$ for 0.1 mg/ml of vesicles. This data showed the insulating property of stBLMs critically depends on the concentration of lipid vesicles used during hemifusion [144, 145]. According to the literature, to form hybrid or tethered bilayer membranes on densely packed SAMs (water contact angle $> 110^\circ$) with vesicle hemifusion, usually only $<$ 0.1 mg/ml of vesicles are used. However, these concentrations are not optimal to form well-insulating stBLMs on mixed SAMs of lower hydrophobicity here. From the data, we could identify 1 mg/ml of vesicles as the optimum concentration for vesicle hemifusion, since below this concentration the resistances start to drop, while above this concentration the resistances do not really increase significantly. In term of protein incorporation with vesicle hemifusion, preparing 1 mg/ml of proteoliposomes is also feasible and does not require too much materials. Besides, at this surface hydrophobicity, vesicle hemifusion formed stBLMs which were as insulating as RSE ($R_{stBLM} \sim 8$ M$\Omega$cm$^2$), indicating FC16:$\beta$ME = 1:1 SAMs are ideal SAMs for vesicle hemifusion if highly insulating stBLMs are desired.

Even though resistances of stBLMs critically depends on the concentrations of vesicles, their structure should still be similar since resistances of membranes are very

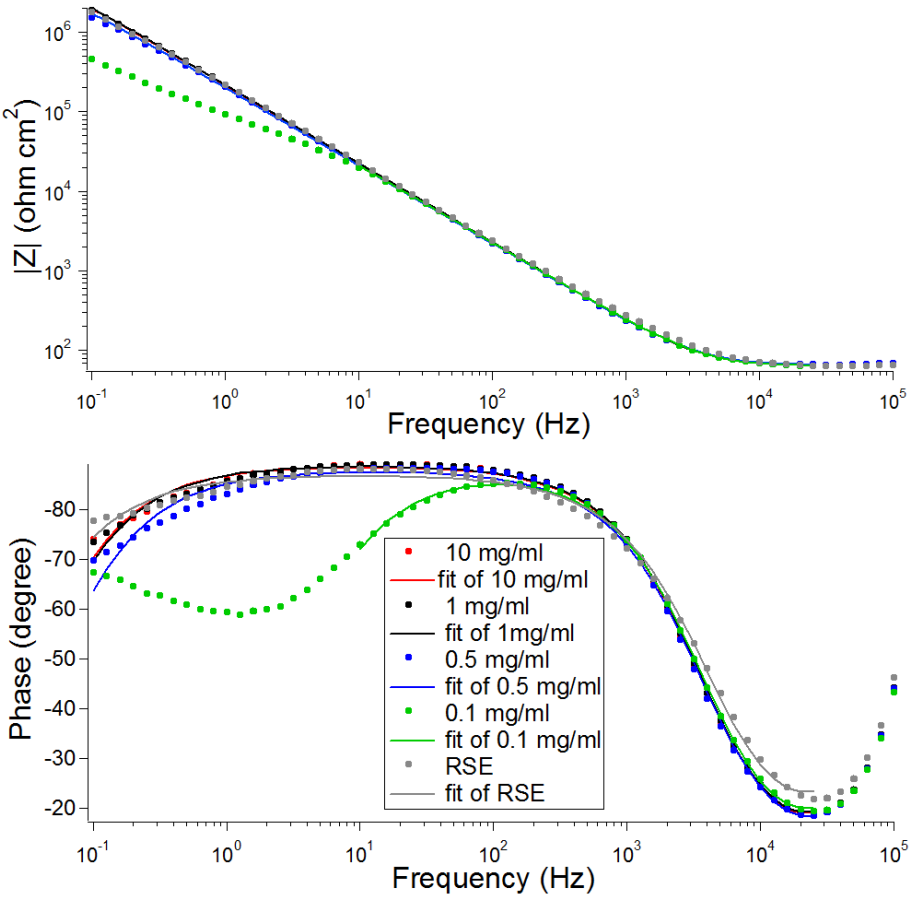


Figure 5.3: *The vesicle hemifusion was performed with different concentrations of DPhyPC vesicles on 1:1 SAMs. RSE was also carried out as a comparison.*

| | $CPE_{stBLM}(\mu\text{Fcm}^{-2}\text{s}^{\alpha-1})$ | $\alpha$ | $R_{stBLM}(\text{M}\Omega\text{cm}^2)$ |
|---|---|---|---|
| 0.1 mg/ml | 0.80 ± 0.01 | 0.981 ± 0.001 | 0.074 ± 0.000 |
| 0.5 mg/ml | 0.83 ± 0.01 | 0.977 ± 0.001 | 4.1 ± 0.2 |
| 1 mg/ml | 0.75 ± 0.00 | 0.988 ± 0.001 | 6.0 ± 0.2 |
| 10 mg/ml | 0.76 ± 0.00 | 0.987 ± 0.009 | 6.2 ± 0.2 |
| RSE | 0.80 ± 0.01 | 0.966 ± 0.001 | 8.6 ± 0.6 |

Table 5.2: *Fitting parameters of the equivalent circuit are shown as a function of vesicle concentrations and RSE.*

sensitive to existence of pores (see the NR results). To explain the concentration dependence of vesicle hemifusion, we suggest that when a vesicle hemifuses with a bare hydrophobic SAM surface, the lipid monolayer does not form a densely packed domain on the SAM surface. Instead, it tends to cover the SAM surface as much as possible

and therefore the monolayer is stretched (unpublished data) [146, 147]. The stretched monolayer protects the SAM surface from further hemifusion of vesicles or hemifusion becomes less likely to happen on these spots. When a relatively high concentration of vesicles was used (> 1 mg/ml), vesicles hemifuse with the bare SAM very quickly and cover the entire SAM in a minimum amount of time (less than a few minutes, data not shown), before the densely packed monolayer has the chance or space to be stretched into a loosely packed monolayer. As a result, vesicle hemifusion relies on the arrival rate or concentration of vesicles at the very beginning of the process to form highly insulating stBLMs in the end.

### 5.3.4 The Effect of Calcium on the Formation of Negatively-Charged POPE:POPG = 3:1 stBLMs

To demonstrate versatility of vesicle hemifusion for forming stBLMs of different chemical compositions, we hemifused vesicles of POPE:POPG = 3:1 (by weight) to SAMs. This particular composition was chosen because it is a mimic of E. coli membranes. As opposed to zwitterionic DPhyPC we used earlier in this study, POPG is negatively charged. Therefore, strong electrostatic repulsion existed and it was discovered that the presence of calcium facilitates the formation of stBLMs through vesicle hemifusion [141]. In this case, POPE:POPG = 3:1 vesicles were prepared in 150 mM NaCl buffer with and without 4 mM of calcium chloride. FC16:$\beta$ME = 3:7 SAMs were incubated with 1 mg/ml of vesicles for 2 hours before the excess vesicles were rinsed away with buffer without calcium. Impedance measurements were performed and the resulting impedance spectra are shown in Figure 5.4. Without calcium, no electrically insulating stBLMs were formed at all since the resulting spectrum was a typical spectrum for a SAM instead of a stBLM. While under the presence of 4 mM calcium during hemifusion, a stBLM of $R_{stBLM} = 6.0 \pm 0.2$ k$\Omega$cm$^2$, $CPE_{stBLM}$ = $0.85 \pm 0.02$ $\mu$Fcm$^{-2}$s$^{-1}$ and $\alpha = 0.967 \pm 0.003$ was formed. The functions of calcium are at least 2-fold in this case: (1) they shield negatively charged lipids from each other by decreasing the Debye length; (2) they bridge headgroups of negatively charged lipids together during hemifusion [148]. For lipid vesicles directly fuse on hydrophilic surfaces, usually calcium is needed to overcome the repulsion of negatively charged vesicles with negatively charged solid surfaces [30]. However, for hemifusion of vesicles on hydrophobic surfaces, this is unlikely to happen. Therefore, the function

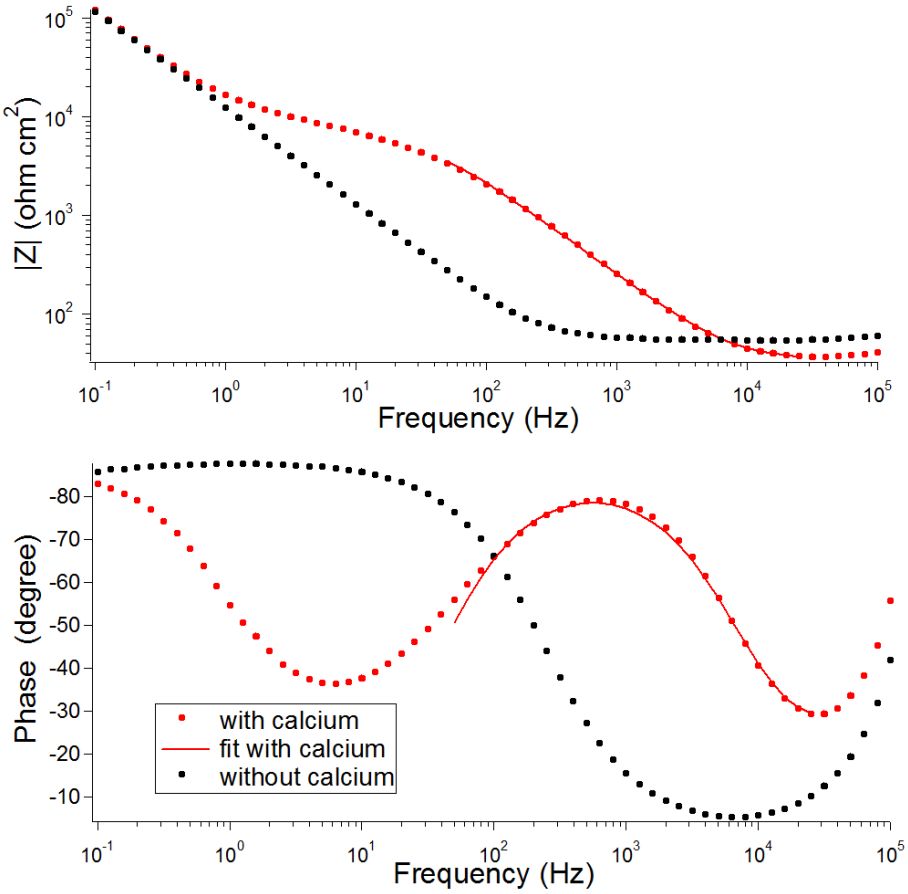


Figure 5.4: *The formation of POPE:POPG = 3:1 stBLMs with and without calcium during hemifusion.*

of calcium should be the following. Firstly, vesicles hemifuse to hydrophobic SAMs to form loosely packed stBLMs as discussed previously and calcium plays a minimal role in this process. Later, vesicles further hemifuse to these loosely packed stBLMs until densely packed and insulating stBLMs are formed [146, 147]. It is at this point that calcium plays a role because the loosely packed stBLMs are now negatively charged with PG in them. Calcium can either be used to overcome the electrostatic repulsion between the vesicles and the loosely packed stBLMs or bridges the PG headgroups from both the vesicles and the stBLMs during hemifusion. For example, with 4 mM of $CaCl_2$, the Debye length decreases from 7.8 Å (in 150 mM NaCl) to 6.1 Å (in 150 mM NaCl + 4 mM of $CaCl_2$) [110]. A 20% decrease in Debye length and the ability of calcium to bridge the headgroups of negatively charged lipids are crucial to produce insulating stBLMs. Finally, the structure of a POPE:POPG =3:1 stBLM was also

probed with NR and is discussed in the following section.

### 5.3.5 The Effect of High Concentrations of Monovalent Salt in forming E. coli Polar Extract stBLMs

Instead of using POPE:POPG as the mimic of E. coli membranes, vesicle hemifusion can be used to form stBLMs directly from E. coli polar extract vesicles. E. coli polar extract has a composition of PE:PG:cardiolipin = 67:23.2:9.8 by weight. PG is singly negatively charged while cardiolipin is doubly negatively charged. Therefore, the charge density of E. coli polar extract is larger than POPE:POPG = 3:1 membranes. As discussed in the previous section, calcium promotes hemifusion of negatively charged vesicles. However, even a few mM of calcium induce aggregations of negatively charged vesicles. To avoid this, instead of calcium, high concentrations of monovalent salt can be used to overcome the electrostatic repulsion. In this case, E. coli polar extract vesicles were prepared in 100 mM (Debye length 9.6 Å) or 500 mM (Debye length 4.3 Å) of KCl. These vesicles were hemifused to FC16:$\beta$ME = 1:1 SAMs and impedance measurements were taken in 100 mM KCl later. The resulting impedance spectra are shown in Figure 5.5. The stBLM formed under 500 mM KCl had $R_{stBLM} = 1.7 \pm 0.0$ M$\Omega$cm$^2$, $CPE_{stBLM} = 0.67 \pm 0.00$ $\mu$Fcm$^{-2}$s$^{\alpha-1}$ and $\alpha = 0.997 \pm 0.001$, while the stBLM formed under 100 mM KCl has $R_{stBLM} = 61 \pm 1$ k$\Omega$cm$^2$, $CPE_{stBLM} = 0.71 \pm 0.01$ $\mu$Fcm$^{-2}$s$^{\alpha-1}$ and $\alpha = 0.973 \pm 0.001$. A difference in membrane resistances by about a factor of $\sim 30$ demonstrates the significance of ionic strength in hemifusing negatively charged vesicles to SAMs. Theoretically, one can decrease the Debye length indefinitely to screen the charges of vesicles by increasing the concentration of monovalent salt before the saturation of the salt is reached, leaving the short range repulsive hydration force ($\sim$ 1 nm) [110] as the only barrier for hemifusion. So, with high salt concentrations, insulating stBLMs are formed with vesicle hemifusion even with highly charged vesicles.

### 5.3.6 Structure of stBLMs studied by Neutron Reflectivity (NR)

To investigate structural properties of stBLMs formed with vesicle hemifusion, NR was performed on DPhyPC stBLMs formed on a FC16:$\beta$ME = 3:7 and 1:1 SAM, and

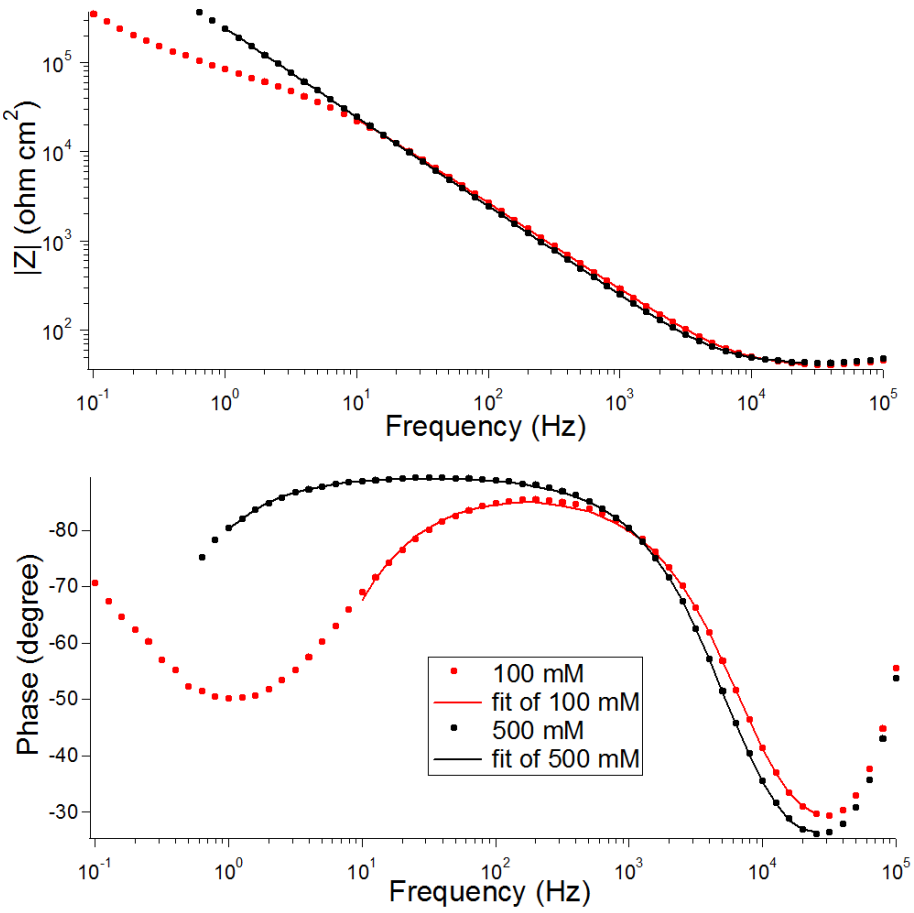


Figure 5.5: *The formation of E. coli stBLMs with either 100 or 500 mM of monovalent salt.*

a POPE:POPG = 3:1 stBLM on a 3:7 SAM. Reflectivity was modeled with the box model as described in Section (2.3). The model consisted of a semi-infinite silicon layer, followed by a layer of silicon oxide, a layer of chromium, a layer of gold, a layer of submembrane space, a layer of proximal leaflet's alkyl chains, a layer of distal leaflet's alkyl chains, a layer of lipid headgroups and finally another layer of semi-finite solvents. In this model, the thickness of the proximal leaflet's alkyl chains was constrained to be the same as the thickness of the distal leaflet's alkyl chains. The structural properties of these stBLMs, obtained from the fitting, are summarized in Table 5.3.

For the DPhyPC stBLM on a 3:7 SAM, the reflectivity curves and the best-fit neutron scattering length density profiles (nSLD) are shown in Figure 5.6 and 5.7 respectively. To further evaluate the robustness of the model and the uncertainties of the fitting parameters, we employed a Monte Carlo resampling method in generating

| | DPhyPC on 1:1 SAM | DPhyPC on 3:7 SAM | POPE:POPG = 3:7 |
|---|---|---|---|
| Thickness of submembrane space, $d_{sub}$ (Å) | 21.7 ± 0.5 | 19.8 ± 0.5 | 20.1 ± 0.7 |
| Volume fraction of water in submembrane space | 0.44 ± 0.01 | 0.51 ± 0.02 | 0.38 ± 0.01 |
| Thickness of distal/ proximal leaflet, $d_{lipid}$ (Å) | 16.1 ± 0.3 | 15.3 ± 0.18 | 14.8 ± 0.4 |
| Volume fraction of proximal leaflet | 0.987 ± 0.018 | 0.994 ± 0.012 | 0.970 ± 0.026 |
| Volume fraction of distal leaflet | 0.986 ± 0.011 | 0.999 ± 0.002 | 0.991 ± 0.013 |
| nSLD of alkyl chain, $\rho_{CH}$ (Å$^{-2}$) | (-3.51 ± 0.31) $\times 10^{-7}$ | (-3.13 ± 0.35) $\times 10^{-7}$ | (-1.33 ± 0.48) $\times 10^{-7}$ |

Table 5.3: *Fitting parameters of the box model to the reflectivity curves are shown for the stBLMs formed with vesicle hemifusion. The uncertainties are the standard deviations of the distributions obtained from 1000 iterations of Monte Carlo resampling.*

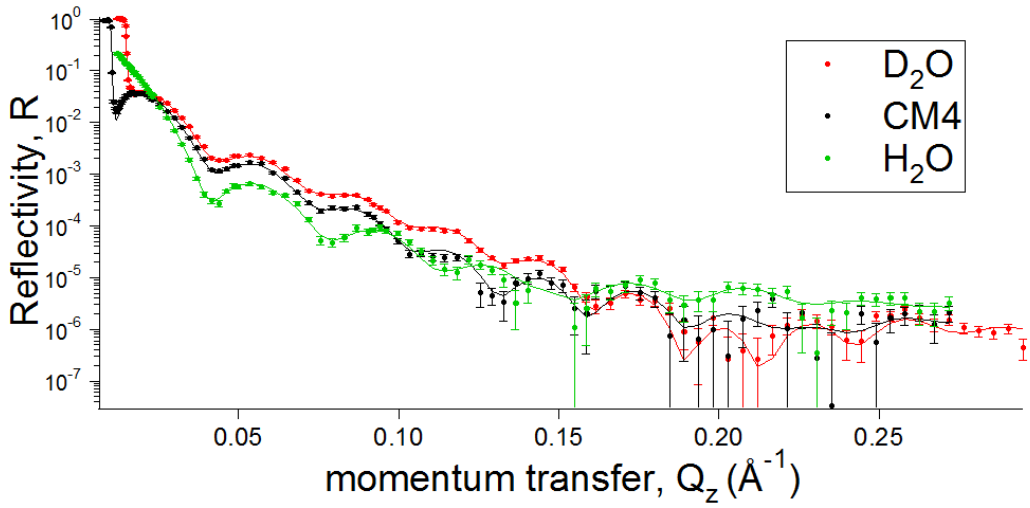


Figure 5.6: *The reflectivity curves for a DPhyPC stBLM on a FC16:βME = 3:7 SAM and the corresponding best-fits to the box model in 3 different solvent contrasts.*

1000 synthetic curves and fitted these curves to the same model as described in Section (2.3). This led to 1000 nSLD profiles and 1000 values for each fitting parameter. The resulting overlaid nSLD profiles from this resampling approach are displayed in Figure 5.8, 5.9 and 5.10 for the stBLM in $D_2O$, CM4 and $H_2O$. The shades of gray in these figures show the frequency a particular nSLD value was hit at a particular position

by the resampling method. Also shown in Figure 5.11 are the distributions of 6 fitting parameters, which are pertinent to the lipid membrane, generated by the same method. It is evident from Figure 5.7 that a complete bilayer was formed with vesicle hemifusion because the solvents were excluded from the hydrocarbon core, as indicated by the overlapping of the nSLD profiles near the distal and proximal leaflet of the stBLM (at the distance of $\sim$ 200 Å), which would otherwise show distinct nSLD with distinct solvents. Also in Figure 5.8 to 5.10, the nSLD profiles show narrow widths at the same distance for the distal leaflet, illustrating the nSLD variation in this layer is marginal. Hence, in Figure 5.11, the distribution of the volume fraction of both the proximal and distal leaflet are highly inclined toward a value of 1, corroborating the fact that the solvents were almost totally excluded from the hydrocarbon core of the membrane (volume fraction of the solvent + volume fraction of the alkyl chain = 1). The total alkyl chains (distal + proximal leaflet) thickness is $\sim$ 3 nm, which is a typical thickness of a lipid bilayer.

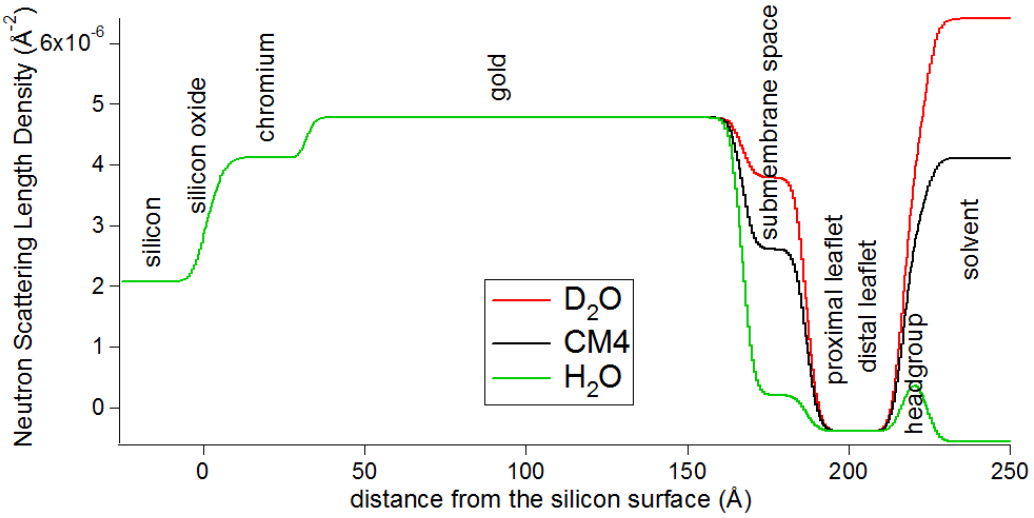


Figure 5.7: *The best-fit nSLD profiles obtained from the box model fitting to the reflectivity curves in Figure 5.6.*

While for the DPhyPC on the 1:1 SAM (the reflectivity curves and the best-fit nSLD profiles are shown in Figure 2.9 and 2.10), the volume fraction of the alkyl chain of the proximal and distal leaflet were 0.987 $\pm$ 0.018 and 0.986 $\pm$ 0.011, which unmistakably showed the formation of a defect free bilayer. Due to a less densely packed proximal leaflet of the 3:7 SAM compared with the 1:1 SAM, the hydration level in the 3:7 SAM was higher (0.51 $\pm$ 0.02 vs 0.44 $\pm$ 0.01). In addition, presumably

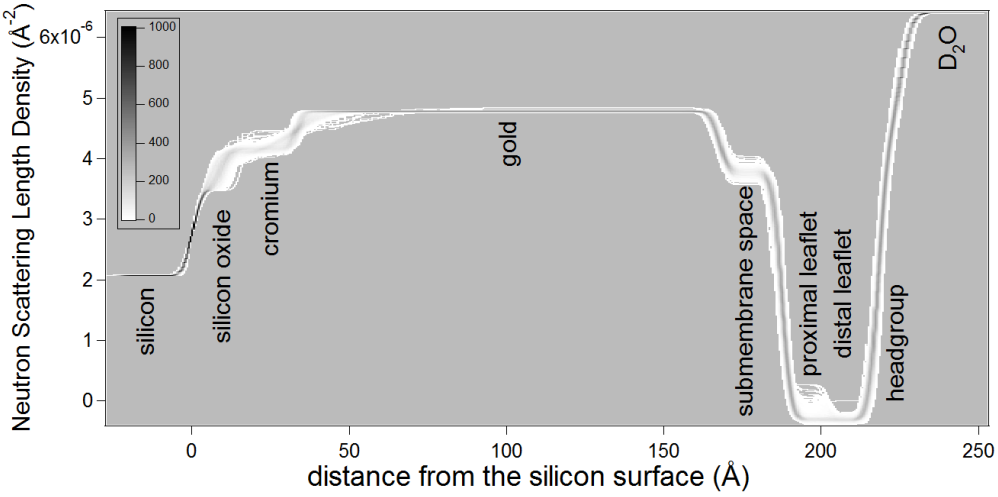


Figure 5.8: *The 1000 overlaid nSLD profiles obtained from the Monte Carlo resampling for the stBLM in Figure 5.6 in $D_2O$.*

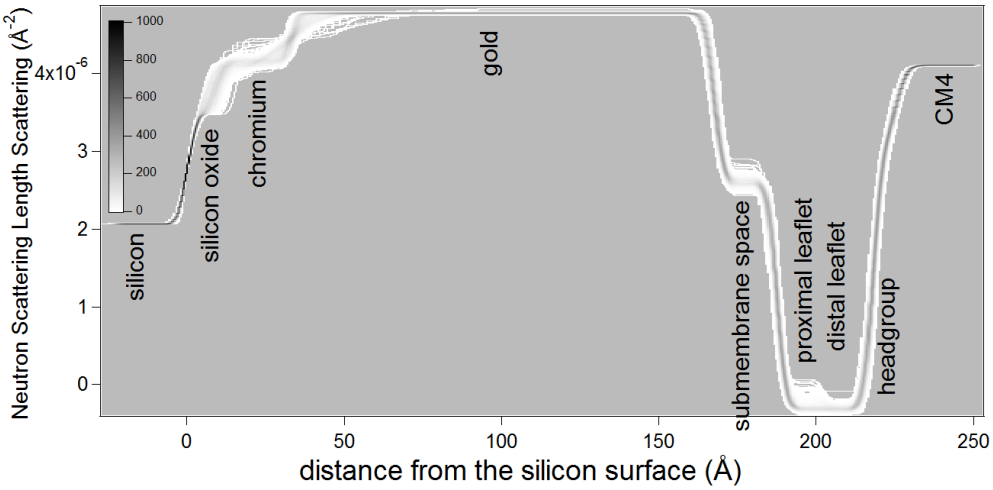


Figure 5.9: *The 1000 overlaid nSLD profiles obtained from the Monte Carlo resampling for the stBLM in Figure 5.6 in CM4.*

because tethering lipids (or the proximal leaflet) have a larger tilt angle with respect to membrane normal when they are loosely packed, DPhyPC on the 3:7 SAM has a thinner alkyl chain for the proximal and distal leaflet (15.3 ± 0.18 vs 16.1 ± 0.3 Å) and a thinner submembrane space (19.8 ± 0.5 vs 21.7 ± 0.5 Å) than DPhyPC on the 1:1 SAM.

The nSLD of the lipid alkyl chain, $\rho_{CH}$ are (-3.51 ± 0.31) x $10^{-7}$ Å$^{-2}$ (1:1 SAM) and (-3.13 ± 0.35) x $10^{-7}$ Å$^{-2}$ (3:7 SAM). Since in the box model, we constrainted

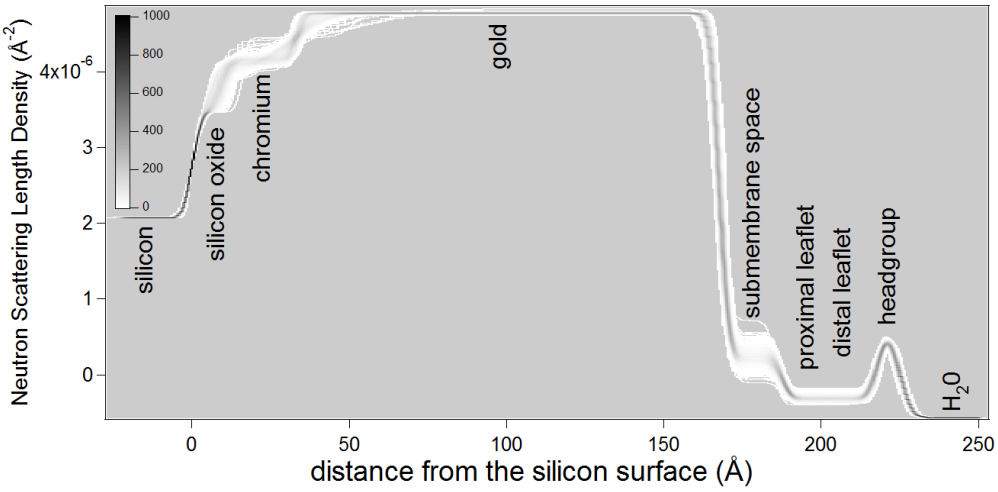


Figure 5.10: *The 1000 overlaid nSLD profiles obtained from the Monte Carlo resampling for the stBLM in Figure 5.6 in $H_2O$.*

the $\rho_{CH}$ to be the same for both the proximal and distal leaflet, the reported $\rho_{CH}$ here is considered as the average $\rho_{CH}$ for both leaflets. By using the average scattering length of diphytanoyl and dipalmitoyl (alkyl chain of FC16) chain of -3.58 x $10^{-4}$ Å, the area per lipid is 64.1 ± 6 Å$^2$ (1:1 SAM) and 72.0 ± 9.2 Å$^2$ (3:7 SAM) respectively. These values are comparable to the area per lipid in liposomes or multistacks of fully hydrated lipid bilayers. For example, the area per lipid for DPhyPC is 80 Å$^2$ [149,150], while the area per lipid for DPPC is 64 Å$^2$ in the fluid phase. Therefore, it should be expected that the area per lipid for a DPhyPC stBLM lies between 64 to 80 Å$^2$, which is true in these cases. An increase of ∼ 8 Å$^2$ on the area per lipid also reflects a denser packed alkyl chain for the 1:1 SAM compared with the 3:7 SAM.

Hydrated submembrane spaces are needed to incorporate transmembrane proteins or facilitate ion transport across supported membranes [69, 140]. With 2 nm thick submembrane spaces of ∼ 50% water, stBLMs are a better candidate for these purposes than other supported membranes. The DPhyPC stBLM on the 3:7 SAM has 7% more water in the submembrane space compared with the DPhyPC on the 1:1 SAM. However, the resistance of DPhyPC on the 3:7 SAM is only tens of kΩcm$^2$, whereas DPhyPC on the 1:1 SAM is ∼ MΩcm$^2$. So if highly insulating membranes are required, 1:1 SAMs can be used to incorporate proteins through vesicle hemifusion.

Regardless of vesicle hemifusion or RSE, the structure of DPhyPC formed on the 3:7 SAM showed no significant differences [24]. Both stBLMs have approximately the

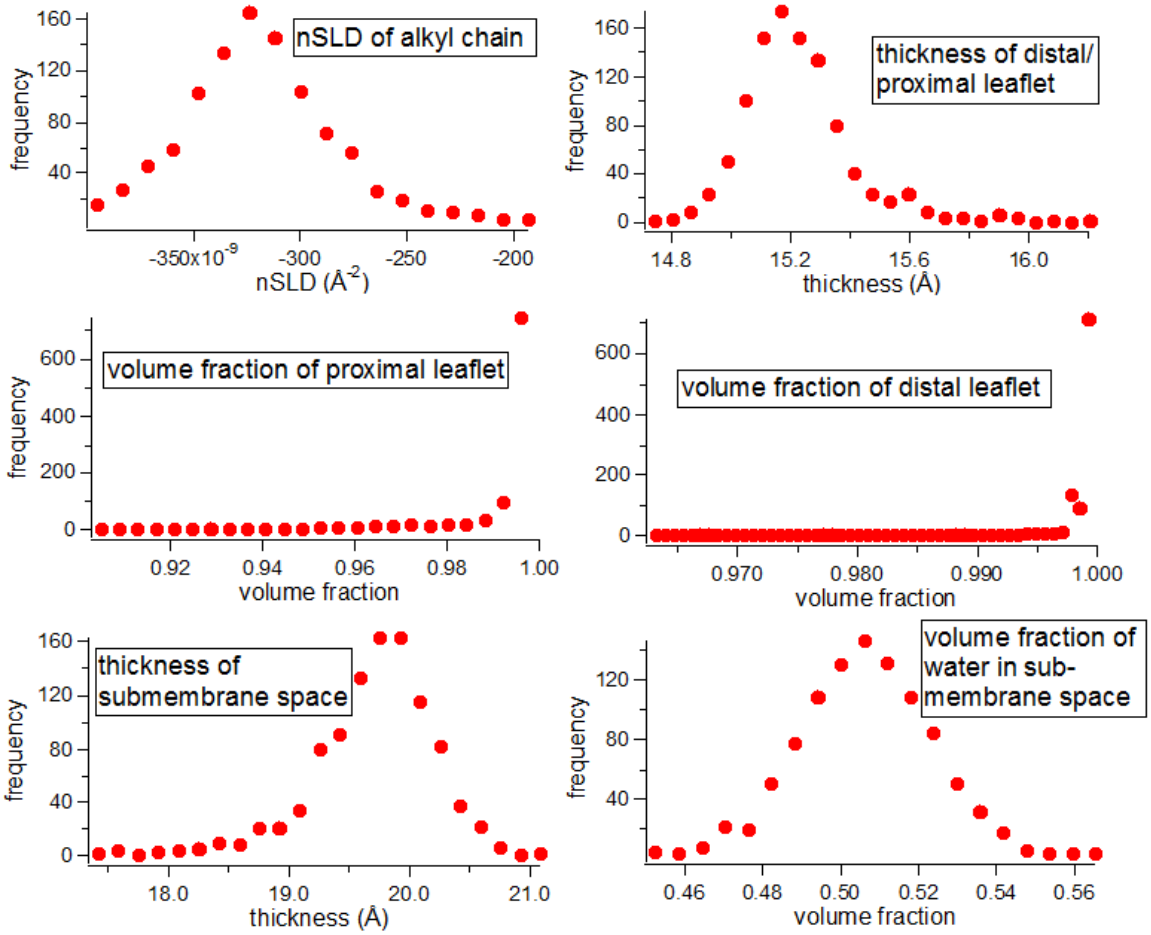


Figure 5.11: *The distributions of the fitting parameters obtained from Monte Carlo resampling for the stBLM in Figure 5.6.*

same structure in terms of alkyl chain thickness and hydration levels in submembrane spaces, indicating the final structure of stBLMs does not rely on the formation process. Nevertheless, the resistances of stBLMs on 3:7 SAMs, formed with vesicle hemifusion, are much lower than stBLMs formed with RSE (Figure 5.1). This order of magnitude difference in resistance values, which reflects the presence of small pores in stBLMs ($<<$ 1%), is beyond the detection limit of NR [23]. Therefore, impedance measurements supplement NR in detecting presence of small defects in stBLMs.

Finally, for the POPE:POPG = 3:1 stBLM on a 3:7 SAM, in which the vesicle hemifusion was done under the presence of 1 mM of calcium to promote the hemifusion of negatively charged lipids, the resulting stBLM has a total alkyl chain thickness of 29.6 $\pm$ 0.8 Å and a volume fraction of alkyl chain $\sim$ 1. This result proved the

capability of vesicle hemifusion to form complete stBLMs with charged lipids. It also supports the impedance measurements that complete POPE:POPG stBLMs can be formed under the presence of calcium.

## 5.4 Conclusions

In this chapter, we have characterized the formation of stBLMs with vesicle hemifusion systematically by using EIS and NR. The critical parameters, which are decisive in forming insulating or complete stBLMs, for example surface hydrophobicity, vesicle concentrations, the presencce of calcium and high concentration of salt, were revealed. When SAMs are of low hydrophobicity, even though high concentrations of lipid vesicles are sufficient in forming complete stBLMs as validated by impedance and NR measurements, the resistances of the membranes are still less superior in comparison with stBLMs formed with RSE. However, when the hydrophobicity of the SAMs is raised, the distinction between the hemifusion and RSE diminishes, while still maintaining highly hydrated submembrane spaces. Moreover, calcium and high concentrations of monovalent salt are crucial in assisting the hemifusion of negatively charged vesicles. With these results, vesicle hemifusion will serve as an alternative to RSE for reconstituting integral membrane proteins and for controlling the chemical compositions of stBLMs precisely.

# Chapter 6

# The Mechanism of Vesicle Hemifusion with Planar Hydrophobic Surfaces*

## 6.1 Introduction

In Chapter 5, we formed stBLMs by incubating mixed SAMs with lipid vesicles. In fact, incubating surfaces of interest with lipid vesicles is a common method in preparing solid supported lipid membranes [11]. Lipid bilayers are deposited on hydrophilic surfaces such as glass, mica and silicon dioxide from lipid vesicles [30]; whereas lipid monolayers are deposited on hydrophobic surfaces from lipid vesicles [21,22,36]. For the former process, different kinds of experiments have been done to monitor the vesicles rupturing or fusion on hydrophilic surfaces, and an absorption to rupturing pathway for bilayer deposition has been identified at a single vesicle level [30, 32, 33, 152–156].

For supported lipid monolayers on hydrophobic surfaces, self-assembled monolayers (SAMs) are first formed on solid surfaces such as gold or silicon dioxide. SAMs expose their alkyl chains away from the surfaces and make the surfaces hydrophobic. Later SAMs are incubated with lipid vesicles for deposition of lipid monolayers to complete the bilayers. Even though vesicle hemifusion on hydrophobic surfaces has been monitored in situ by using different surface sensitive techniques such as Surface Plasmon Resonance (SPR), Quartz Crystal Microbalance (QCM), Atomic

*The materials of this chapter has been published in reference [151].

Force Microscopy (AFM), fluorescence intensity measurement, Electrical Impedance Spectroscopy (EIS) and x-ray reflectivity [21, 22, 36, 144–147, 152, 154, 157], most of these methods only probed the lipid deposition globally, namely the overall deposition of lipid materials to surfaces. How does a single vesicle reorganize on the surfaces is beyond the scope of these methods and a complete picture is still missing. In this chapter, we fill the gap for these methods by providing the reorganization pathway of vesicles on surfaces at a single vesicle level.

On the other hand, it is well known that Langmuir monolayers can be deposited at the air-water interface by spreading of lipid vesicles from the water subphase [158]. The transformation from bilayers to monolayers at hydrophobic surfaces and at the air-water interface may be two sides of the same coin. The results in this work are valuable in explaining the spreading of lipid vesicles at the air-water interface as well.

In this work, we prepared octadecyltrichlorosilane (OTS) SAMs on glass surfaces (alkylated glass). We injected fluorescently labeled DOPC giant unilamellar vesicles (GUVs) on top of these alkylated glass and performed fluorescence imaging at 19 fps ($\sim$ 53 ms temporal resolution) to capture the reorganization of GUVs upon hitting the hydrophobic surfaces to form hybrid bilayer lipid membranes. Fluorescence imaging was done at 2 different focal planes, namely at the glass-water interface and the equatorial plane of GUVs, to supplement the information obtained from each other. In one of the experiments, fluorophores on outer leaflets of GUVs were quenched to probe the movement of inner leaflets during the reorganization. Based on the results, we put forward a model on how closed-shell bilayers are transformed to surface monolayers at an unprecedented detail.

## 6.2 Materials and Methods

### Materials

1,2-dioleoyl-sn-glycero-3-phosphocholine (DOPC), 1,2-dioleoyl-sn-glycero-3-phosphoethanolamine-N-(lissamine rhodamine B sulfonyl) (ammonium salt) (LR-PE) and 1,2-dipalmitoyl-sn-glycero-3-phosphoethanolamine-N-(7-nitro-2-1,3-benzoxadiazol-4-yl) (ammonium salt) (NBD-PE) were purchased from Avanti Polar Lipids (Alabaster, AL) and used as received. Number 1.5 thickness glass coverslips were purchased from Electron Microscopy Science (Hatfield, PA). Octadecyltrichlorosilane (OTS) and sodium

dithionite were purchased from Fisher Scientific (Pittsburgh, PA). All other chemicals were of HPLC grade and the ultrapure water was prepared in a Millipore (Billerica, MA) Milli-Q water purification device.

### Preparation of OTS SAMs

Glass coverslips were sonicated in hydrogen peroxide:sulfuric acid = 1:4 v/v solution ("Piranha solution") for 10 minutes, followed by rinsing with copious amounts of water and were dried under a stream of nitrogen gas. They were then immediately immersed in 4 mM OTS in dodecane to form SAMs. After overnight incubation, the alkylated glass was sonicated in chloroform to remove any non-specific adsorption. The water contact angle of the SAMs was 105° to 110°. The alkylated glass was assembled into Sykes-Moore chambers for imaging.

### Formation of Giant Unilamellar Vesicles (GUVs)

GUVs were formed with the gentle hydration method as in Chapter 3 and 4. DOPC was mixed with 1wt.% of LR-PE or NBD-PE (molar ratio of 160:1 or 110:1, respectively). Before fluorescence imaging, GUVs were diluted with a buffer solution of 95 mM NaCl + 10 mM HEPES at pH $\sim$ 7, which is approximately isosmotic with 200 mM sucrose solution, to a final concentration of 0.00125 to 0.01 mg/ml.

### Selective Quenching of Fluorophores on the Outer Leaflet

The method reported by McIntyre and Sleight [159] was used to selectively quench NBD-PE on outer leaflets of GUVs. 200 $\mu$l of labeled GUVs solution was mixed with 4 $\mu$l of freshly prepared 1 M sodium dithionite + 1 M Tris for 10 minutes, followed by a 10-fold dilution to prevent further quenching. GUVs were then immediately used for fluorescence imaging. Fluorescence intensity measurements showed that the treatment with dithionite reduced the NBD fluorescence by $\sim$ 45%, consistent with the assumption that only the NBD on the outer leaflets were quenched.

### Fluorescence Microscopy

The details of fluorescence imaging were similar with the conditions in Chapter 3 and 4. Image recording was carried out at 19 fps. We performed two different sets of

experiments. In the first experiment, the image plane was set at the glass-membrane-water interface to visualize the hemifusion of GUVs and the spreading of monolayers on the substrates. In the second experiment, the microscope was focused on the equatorial plane of GUVs. In both cases, the small depth of field ($\sim$ 900 nm) of the high-NA objective provides an excellent optical sectioning ability in the axial direction, therefore enabling us to image the respective planes with minimal background fluorescence signals from out-of-focus planes. Except for NBD quenching experiments, GUVs were routinely labeled with LR-PE.

#### Fluorescence Recovery After Photobleaching (FRAP)

FRAP was performed according to the protocol in Chapter 3 and 4 to measure diffusion coefficients of LR-PE in hybrid bilayer lipid membranes and to verify the fluorescence observed was indeed originated from membranes.

#### Image Analysis

To determine the area of hemifusion zones, images recorded were converted to binary images by setting a threshold intensity of (average background + average object) $\div$ 2 by using ImageJ or by using a standard method implemented in *Matlab* [160]. To determine the intensity distributions within the hemifusion zones, the normalized angular averages of the intensities of circles concentric about the contact point were calculated as a function of radial distance with the 'Radial Profile' or 'Radial Profile Extended' plugins in ImageJ. Radial derivatives of these radial profiles were calculated and peaks in the derivatives were used to identify the boundaries between inner and outer zones and between outer zones and backgrounds.

## 6.3 Results

### 6.3.1 Imaging at Glass-Water Interfaces

In this case, fluorescence imaging was performed at glass-water interfaces. Hemifusion between GUVs and SAM surfaces occurred at these interfaces and lipid monolayers were deposited from GUVs to surfaces. A hemifusion event is showed in Figure 6.1 (the full movie M6-1 can be found at

*http://www.youtube.com/watch?v=aUN1eG6Ku7w&feature=plcp*). There are 4 main features from this movie and will be discussed in the following paragraphs.

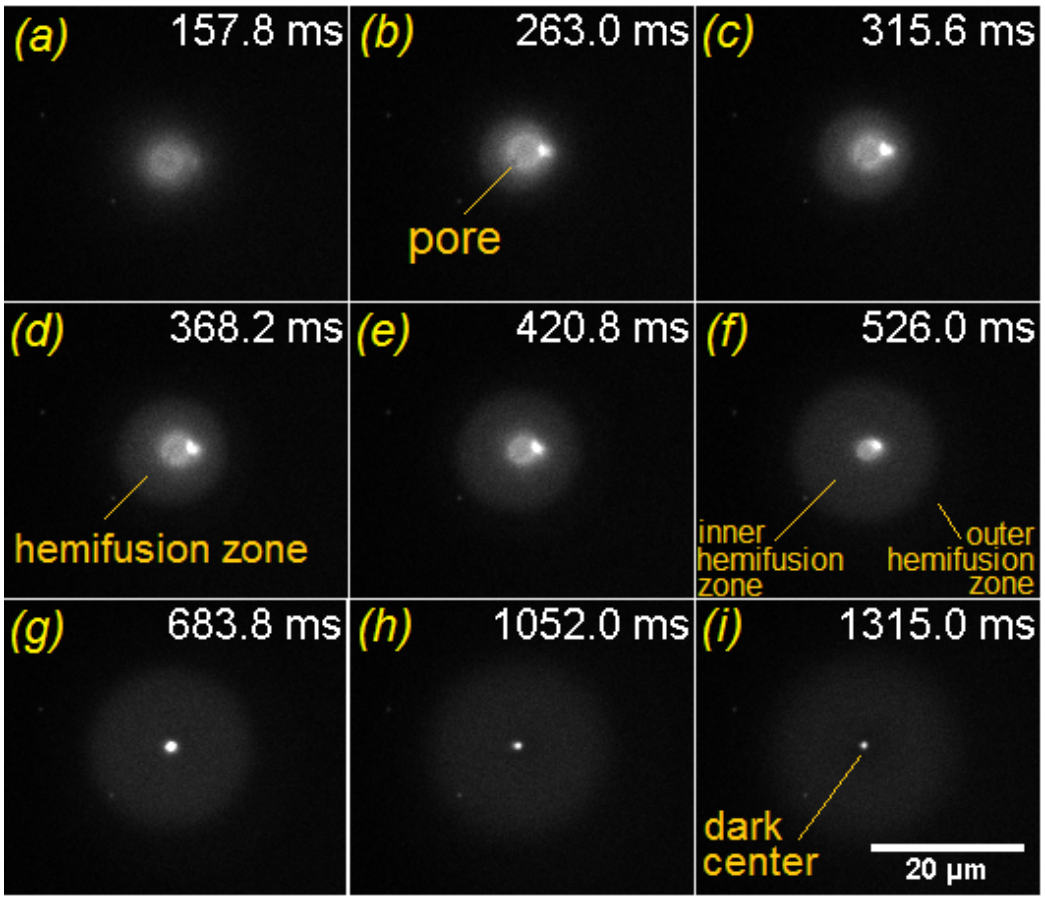


Figure 6.1: *The hemifusion between a GUV and a SAM was captured at the glass-water interface. The full movie M6-1 can be found here.*

(A) At the beginning of the event, a GUV with a radius, $\rho \sim 4$ $\mu$m, drifted into the focal plane and made a contact with the surface. Image **a** of Figure 6.1 showed the GUV was immobilized on the SAM shortly before the hemifusion started. Because the focal plane was at the bottom of the GUV at this moment, this and subsequent images were affected by the stray light emitted from the remaining part of the GUV that was slightly out of focus. Therefore, the initial deposition of lipid materials on the surface was hard to determine because of the stray light. Nevertheless, when the hemifusion commenced, a lipid monolayer was deposited from the GUV to the surface. The circular lipid monolayer expanded

radially outward from the contact site and we call the monolayer-covered area as hemifusion zone (image **d**). In image **d**, the hemifusion zone was considerable larger than the stray light region and was hence clearly visible. Following the initiation of the hemifusion, the radial expansion of the monolayer proceeded until the entire GUV hemifused with the surface (image **d** to image **i**) and the process completed within $\sim 1$ s.

At first sight, one can only recognized a single circular hemifusion zone. However, a careful inspection of the images revealed that there was another dark outer hemifusion zone that haloed the bright inner hemifusion zone (image **f** of Figure 6.1). This dark outer zone expanded together with the bright inner zone as an annulus with a width of $\sim 5$ $\mu$m. To show this observation quantitatively, a radial profile was produced from the center of hemifusion zones. For image **f**, the resulting radial profile and its (negative) radial derivative are shown in Figure 6.2. Apart from a drop in intensity at $r \sim 9$ $\mu$m, which occurred at the boundary between the inner and the outer zone, a 'tail' was observed between $r \sim 10$ and 15 $\mu$m, that showed a higher intensity than the background ($r > 15$ $\mu$m) and decreased gradually to the background level with growing $r$. Provided the intensity drop across a boundary can be modeled as an error function, the corresponding derivative across the boundary would show a peak. Hence, peaks in the derivative trace implied where these boundaries were located. Two peaks in the derivative trace were identified by this procedure and their locations are marked with dashed vertical lines in Figure 6.2. These peaks are attributed to the boundaries between the inner and the outer hemifusion zone, and between the outer hemifusion zone and the background, respectively.

The intensity trace in Figure 6.2 also provides an estimate of the relative lipid density in the two zones since the fluorescence intensity is proportional to the lipid density. After the background subtraction, the average fluorescence intensity in the outer zone was $\sim 10\%$ of that in the inner zone, indicating the lipid density of the outer zone was only 10% of the inner zone's.

(B) Image **b** and **c** in Figure 6.1 showed a single, small dark spot (diameter $\sim 500$ nm) near the center of the hemifusion zone. It was a hemifusion pore that allowed the expulsion of GUV contents and the transfer of lipids from the inner to the outer leaflet during the monolayer deposition process. It became too small to be

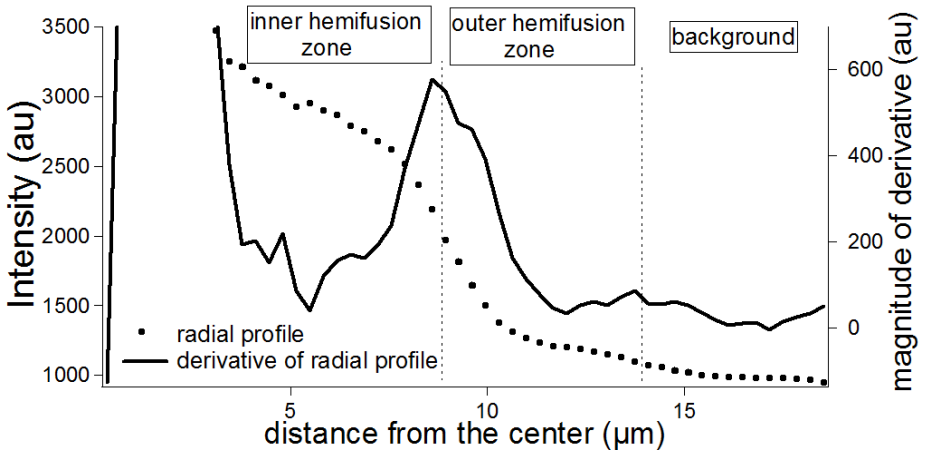


Figure 6.2: *The radial profile and the corresponding radial derivative are shown for image* ***f*** *in Figure 6.1. The peaks in the derivative trace, which were marked with dashed vertical lines, were used to identify the boundary between the inner and the outer hemifusion zone, and the boundary between the outer hemifusion zone and the background.*

imaged by the fluorescence microscope after image **c**. Imaging at the equatorial plane of GUVs would characterize the pore formation better.

(C) At the end of the hemifusion process, the center of the hemifusion zone was darker than the deposited monolayer surrounding it. Figure 6.3 shows a contrast-enhanced version of image **i** in Figure 6.1. Apart from a highly fluorescent particle that was deposited near the center, a decrease in the fluorescence intensity around the center of the deposited monolayer is quite obvious. To evaluate the darkening of the center, a yellow vertical line was drawn across the center by avoiding the highly fluorescent particle and the intensity distribution along this line is displayed in Figure 6.3. The trace shows a reduced fluorescence intensity from 10 to 16 $\mu$m. At the LR-PE concentration used ($< 1$ mol%), we do not anticipate self-quenching of fluorophores and therefore assume the intensity is proportional to the concentration of LR-PE. Therefore, this observation proposes that the center of the hemifusion zone was depleted of lipids at the end of the hemifusion.

(D) The time course of the monolayer deposition is plotted in Figure 6.4. Initially, the fluorescence from the GUV outshone the intensity of the deposited monolayer ($t < 200$ ms). Image analysis yielded a constant area of $\sim 50$ $\mu$m$^2$ during this period of time. However, in image **c** of Figure 6.1 ($t > 200$ ms) and onward,

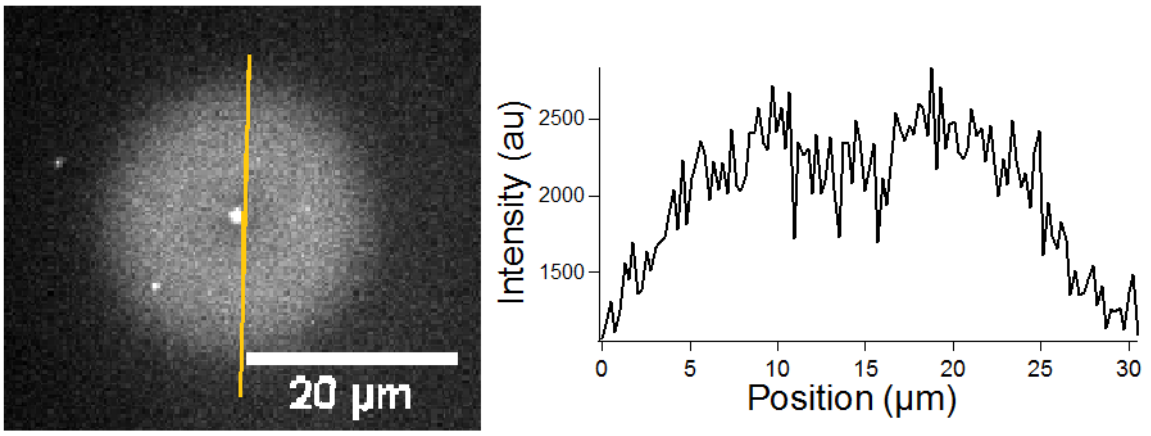


Figure 6.3: *On the left is the contrast enhanced version of image* ***i*** *in Figure 6.1. A yellow vertical line is drawn across the center of the hemifusion zone and the intensity along this line is plotted on the right to show the darkening of the center at the end of the hemifusion.*

the area of the hemifusion zone has grown considerably beyond the size of the background fluorescence of the GUV, and therefore its area can be determined accurately. Figure 6.4 shows a steep initial rise of the hemifusion zone that started to level off (image **g** and beyond) when the area of the deposited monolayer reached the combined area of the two GUV monolayer leaflets, $A_{GUV} \sim 400$ $\mu$m$^2$. In this region, the average linear growth or the expansion coefficient, $\frac{dA}{dt}$, of the hemifusion zone was 710 $\pm$ 32 $\mu$m$^2$/s. The expansion slowed down significantly after all the GUV lipids have been deposited ($A > 400$ $\mu$m$^2$), but did not completely come to a halt because lipids at the periphery of the hemifusion zone spread further out into the area devoid of lipids by diffusion.

A second GUV hemifusion event, which showed more clearly the pore formation and the existence of the inner and outer hemifusion zone, is shown in Figure 6.5 (the full movie M6-2 can be found at *http://www.youtube.com/watch?v=40eyFRtSFd0&feature=plcp*). The size of the GUV was twice larger than the GUV in Figure 6.1 ($\rho \sim 8$ $\mu$m). Hemifusion proceeded as described earlier, but the increased GUV volume led a larger hemifusion pore (image **b** to **f** of Figure 6.5), which was at its maximum size in image **b** and shrank in the later images. Moreover, lipid vesicles that were initially trapped inside the hemifusing GUV were expelled with the aqueous content through the hemifusion pore (image **d**

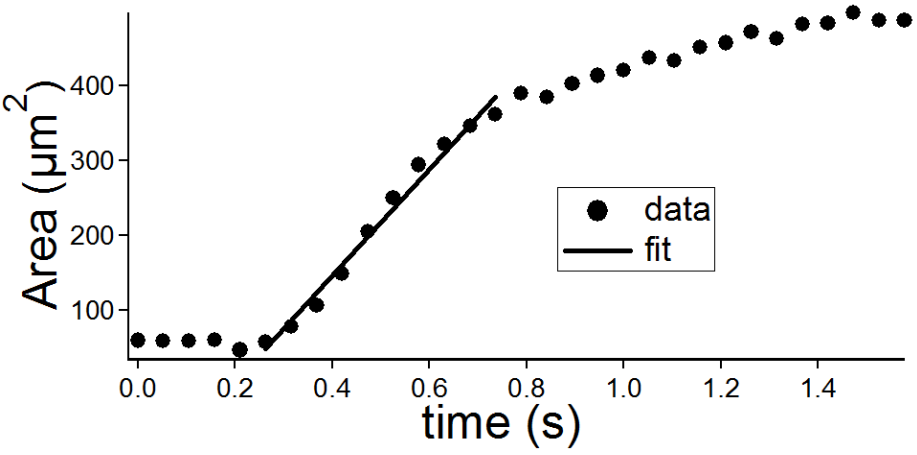


Figure 6.4: *The area growth of the hemifusion zone is plotted as a function of time and the intermediate of the expansion was fitted to a linear function to yield a* $\frac{dA}{dt}$ *of* $710 \pm 32\ \mu m^2/s$.

to **f**). As the vesicles and water were expelled, the GUV was pushed in the opposite direction. In Figure 6.6, we plot the radial profile and its radial derivative for image **i** in Figure 6.5. The existence of 2 peaks in the derivative trace confirmed the presence of two hemifusion zones, in which the inner hemifusion zone was confined to $r < 17$ $\mu$m and the outer hemifusion zone was from $r \sim 17$ to 25 $\mu$m. Additionally, in Figure 6.7, the area of the hemifusion zone is plotted as a function of time and a linear fit shows that $\frac{dA}{dt} = 1100 \pm 14\ \mu\text{m}^2/\text{s}$.

### 6.3.2 Imaging at Equatorial Planes of GUVs

The hemifusion event in Figure 6.8 (the full movie M6-3 can be found at *http://www.youtube.com/watch?v=2_uNW97J2_c&feature=plcp*) was carried out by focusing at the equator of the GUV during the hemifusion. Initially, the GUV appeared as a circular ring that was the optical section of the GUV at its equator. In addition, the GUV contained encapsulated vesicles in which one of them was also dissected by the focal plane (image **a**). At the starting point of the hemifusion, the encapsulated vesicle that was dissected by the focal plane drifted out of focus (image **c**), was expelled from the GUV (image **d**), and then drifted back into the focal plane again (images **e** and **f**). The expulsion process completed in about 3 frames ($\sim$ 160 ms). After the expulsion, the GUV contracted toward the SAM, as indicated by size reduction of

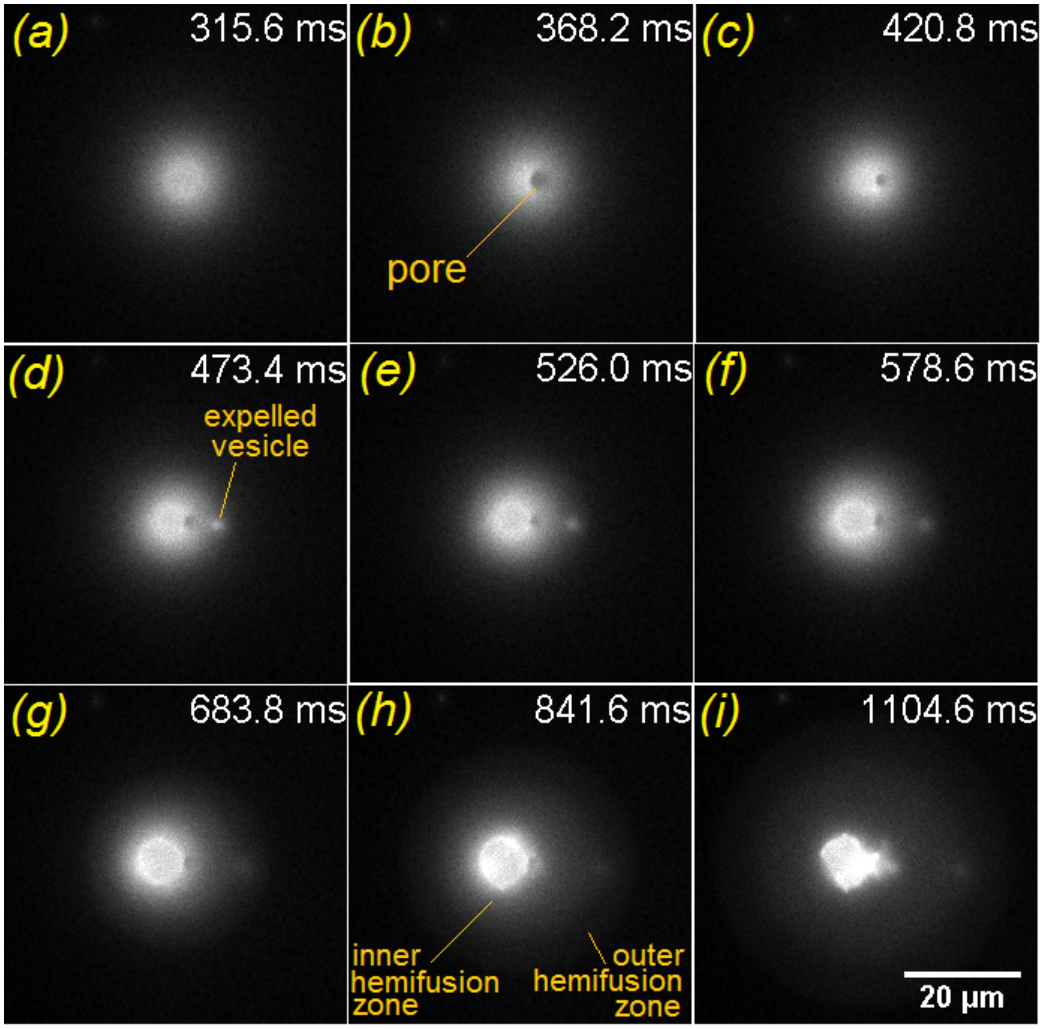


Figure 6.5: *The hemifusion of a GUV with a SAM that clearly shows the formation of a pore (image* ***b****) and the presence of the inner and outer hemifusion zone (image* ***h****). The full movie M6-2 can be found here.*

the GUV optical section. Concurrently, an out of focus hemifusion zone expanded radially outward from the contact site between the GUV and the surface.

The direct observation of the expulsion of encapsulated vesicles unmistakably proved the formation of a hemifusion pore at the early stage of the hemifusion. Moreover, it supported that the pore was formed close to the membrane contact site because the expelled vesicle, which drifted out of focus during the expulsion, reappeared in the focal plane again. Would the pore be located above the focal plane, which was farther away from the glass surface, the expelled vesicle would simply drift

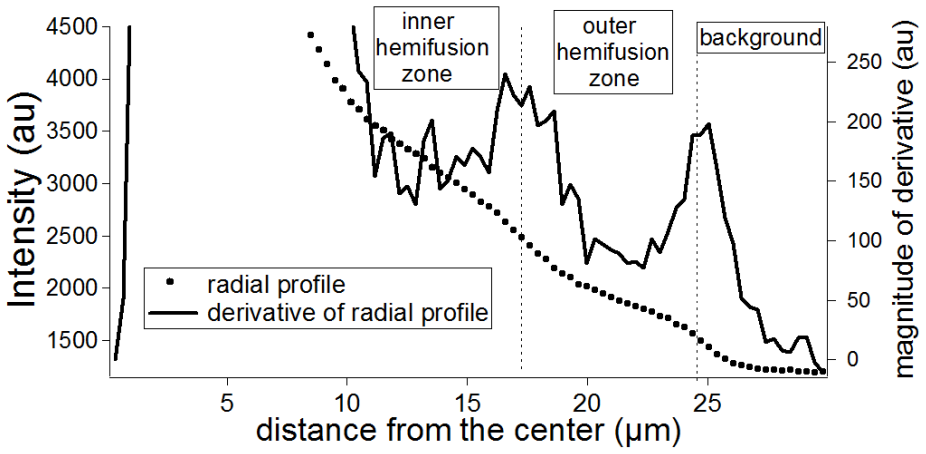


Figure 6.6: *The radial profile and the derivative for image* ***i*** *in Figure 6.5.*

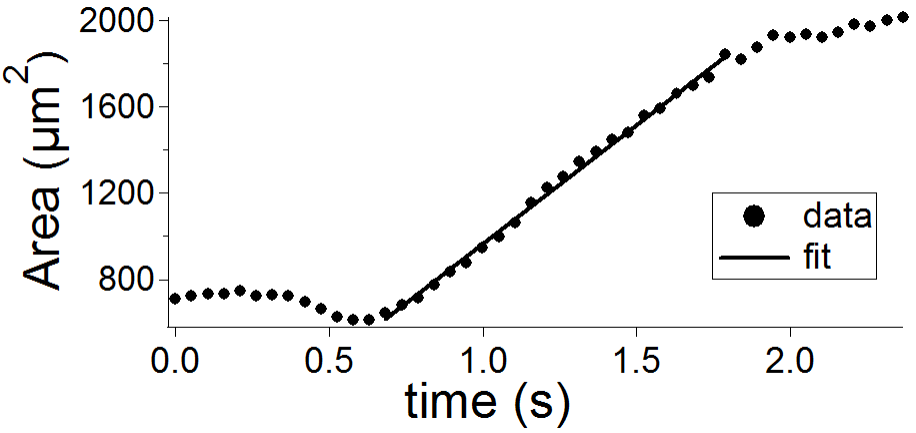


Figure 6.7: *The growth of the hemifusion zone for the event in Figure 6.5.*

away and was less likely to reappear in the images at a later time.

In events where we were able to follow the simultaneous expulsion of multiple encapsulated vesicles, we observed that these vesicles always ejected toward the same direction, suggesting that there was only one pore formed during the hemifusion. For instance, in Figure 6.9 (the full movie M6-4 can be found at *http://www.youtube.com/watch?v=PnzReroRA04&feature=plcp*), multiple encapsulated vesicles were expelled toward a single direction (arrow in image **c**) and appeared out of focus, corroborating our statement in this paragraph. The formation of a single pore is consistent with an earlier result [109], as it costs less energy to form a single pore instead of multiple pores with the same combined area.

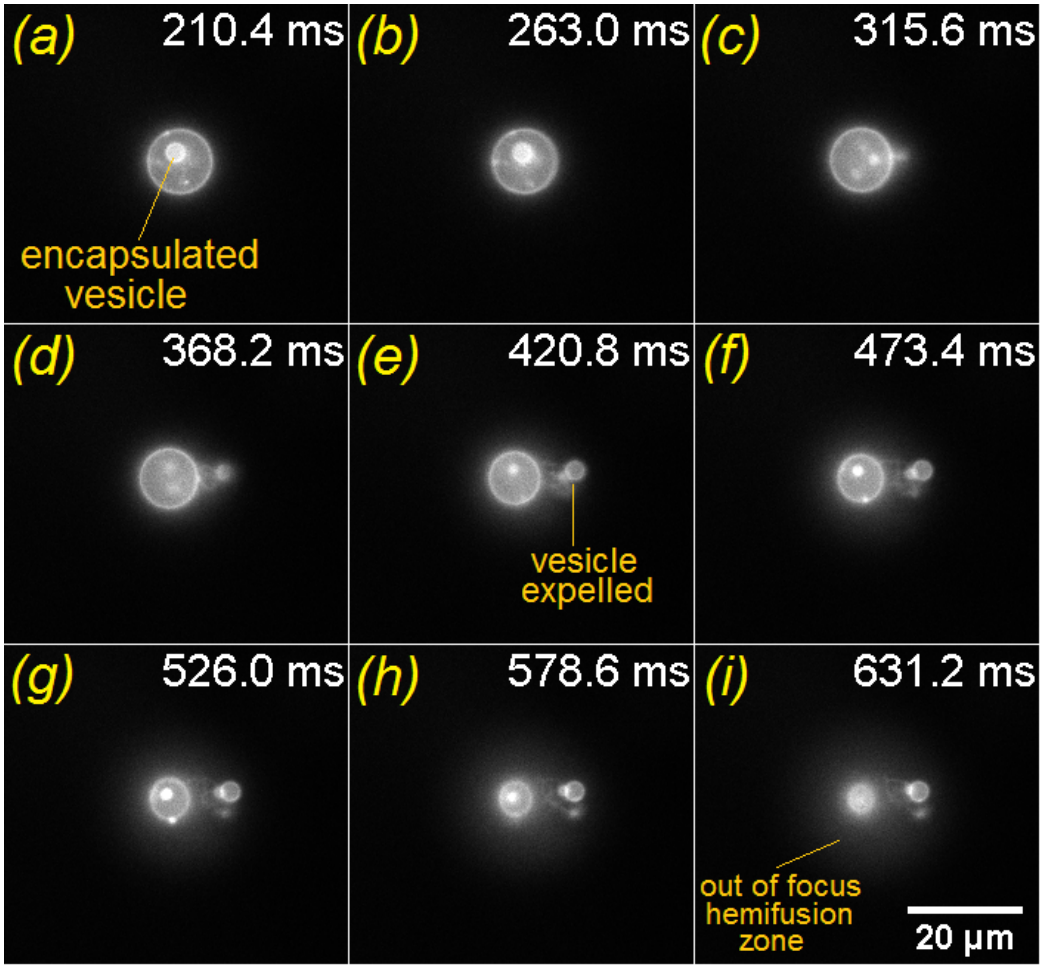


Figure 6.8: *An encapsulated vesicle that was in focus initially (image* ***a****) was expelled and drifted out of focus during the expulsion, supporting the formation of a pore near the membrane contact site. The full movie M6-3 can be found here.*

### 6.3.3 Imaging with Fluorophores on Outer Leaflets of GUVs Quenched

NBD-PE labeled GUVs were treated with sodium dithionite as described to permanently quench the NBD on outer leaflets of GUVs and images were obtained by focusing at the glass-water interface. We showed a typical hemifusion event recorded under this condition in Figure 6.10 (the full movie M6-5 can be found at *http://www.youtube.com/watch?v=9yqWBr7Fqec&feature=plcp*). The hemifusion of the inner leaflet of the GUV proceeded as described for Figure 6.1 and 6.5, except that no outer hemifusion zone was observed. Initially, a GUV ($\rho \sim 4.5$ $\mu$m) approached

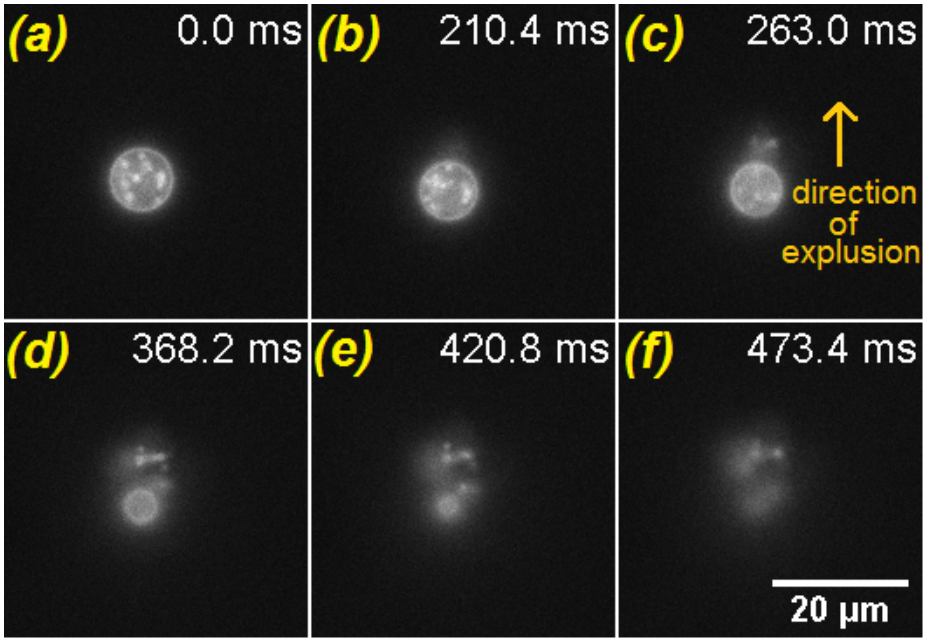


Figure 6.9: *The formation of a single pore is validated in this hemifusion event in which multiple encapsulated vesicles were expelled toward the same direction (arrow in image* **c***). The full movie M6-4 can be found here.*

the surface where it was immobilized (image **a** of Figure 6.10). A nearly circular hemifusion zone expanded from the membrane contact site (images **b** to **e**). Eventually, the center of the hemifusion zone became darker in the end (image **f**, and its contrast has been linearly enhanced). In distinction with hemifusion events where both the GUV leaflets were labeled, only the inner hemifusion zone was detected with this labeling scheme. Accordingly, in Figure 6.11, which is the radial profile for image **d** in Figure 6.10, only one drop in intensity is seen around $r \sim 11$ $\mu$m. Thus, on the same graph, only one peak is identified as the boundary between the inner hemifusion zone and the background in the derivative trace. It directly pinpoints a fact that the outer hemifusion zones consist of lipids from outer leaflets of GUVs solely. Finally, in this event, the area of the deposited monolayer increased at a $\frac{dA}{dt}$ of $738 \pm 29$ $\mu$m$^2$/s from a linear fit to the area growth in Figure 6.12.

### 6.3.4 Fluorescence Recovery After Photobleaching (FRAP)

To verify the hemifusion of GUVs did form fluid hybrid bilayer membranes, FRAP was routinely performed as quality control experiments. In Figure 6.13 is a typical

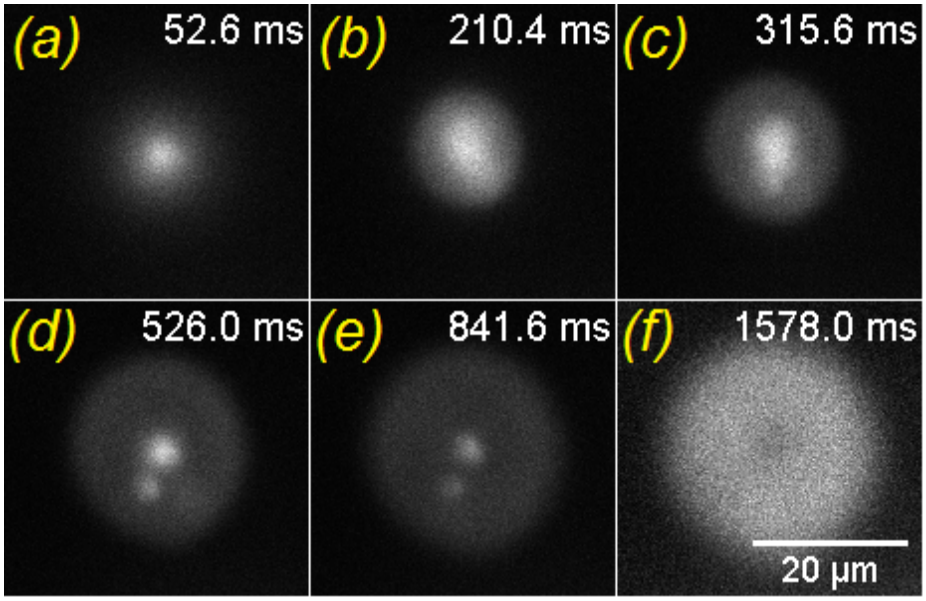


Figure 6.10: *A hemifusion event in which fluorophores on the outer leaflet of the GUV were quenched. The hemifusion occurred without the presence of the outer hemifusion zone. The contrast of image* ***f*** *has been linearly enhanced. The full movie M6-5 can be found here.*

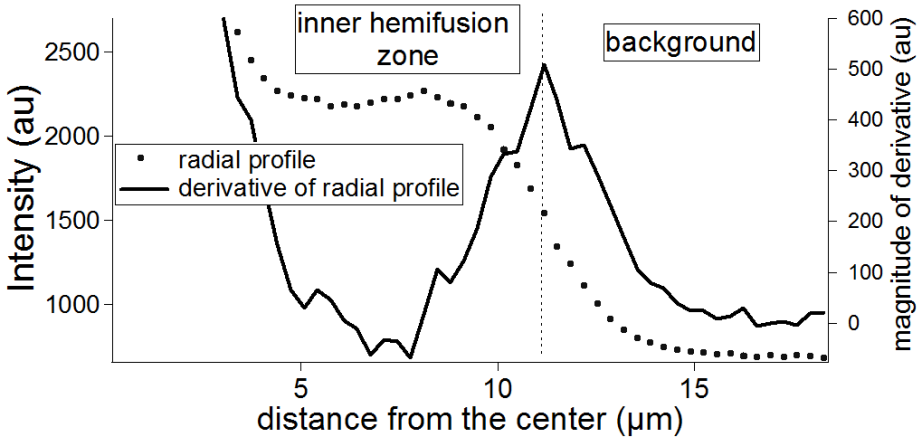


Figure 6.11: *The radial profile and the derivative for image* ***d*** *of Figure 6.10.*

FRAP recovery curve of a DOPC hybrid bilayer. From the fitting, lipids diffused a rate of 2.12 $\pm$ 0.05 $\mu m^2/s$.

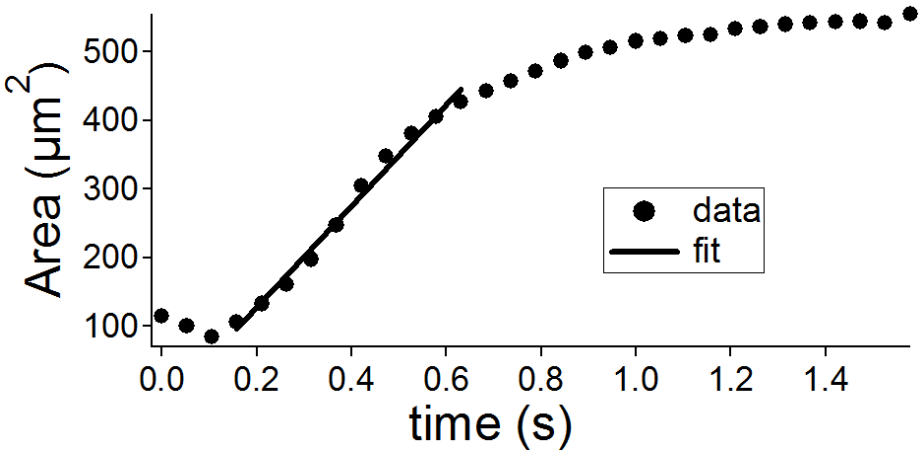


Figure 6.12: *The area growth of the hemifusion zone in Figure 6.10.*

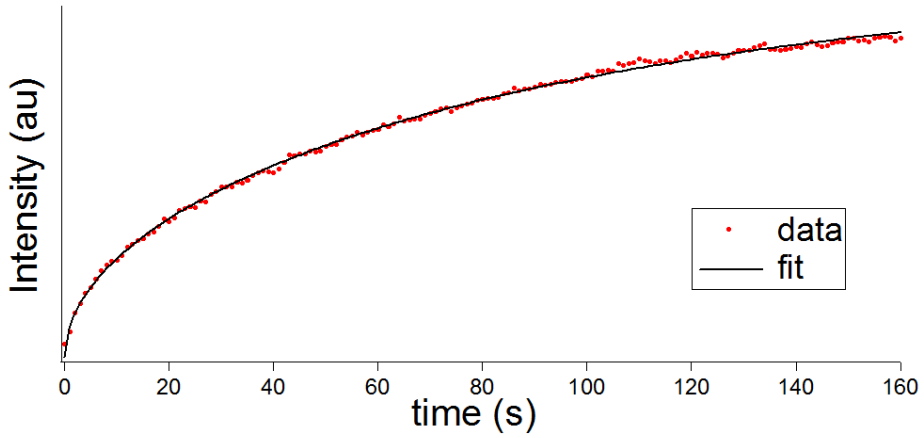


Figure 6.13: *A FRAP recovery curve for a hybrid bilayer formed with the hemifusion of GUVs. The diffusion coefficient was 2.12 ± 0.05 $\mu m^2/s$.*

## 6.4 Discussion

The observations presented above suggest the following scenario and is schematically depicted in Figure 6.14. After encountering a hydrophobic surface, presumably due to the unfavorable interaction between lipid headgroups and the hydrophobic surface, the outer leaflet of the GUV at the contact point breaks apart and forms a structure which we shall call as the hemifusion diaphragm (highlighted in the ellipse of Figure 6.14(A) and its size has been exaggerated with respect to the GUV) [161]. Lipids in the outer leaflet (colored in red) are transferred to the SAM surface through the hemifusion diaphragm as indicated by the arrows. The deposited monolayer forms

the outer hemifusion zone as observed and expands radially outward from the contact site. The lipid density in the outer hemifusion zone is low as verified by the results in Figure 6.1 and 6.5 because the transfer of lipids to the surface at this stage cannot happen without stretching the outer leaflet.

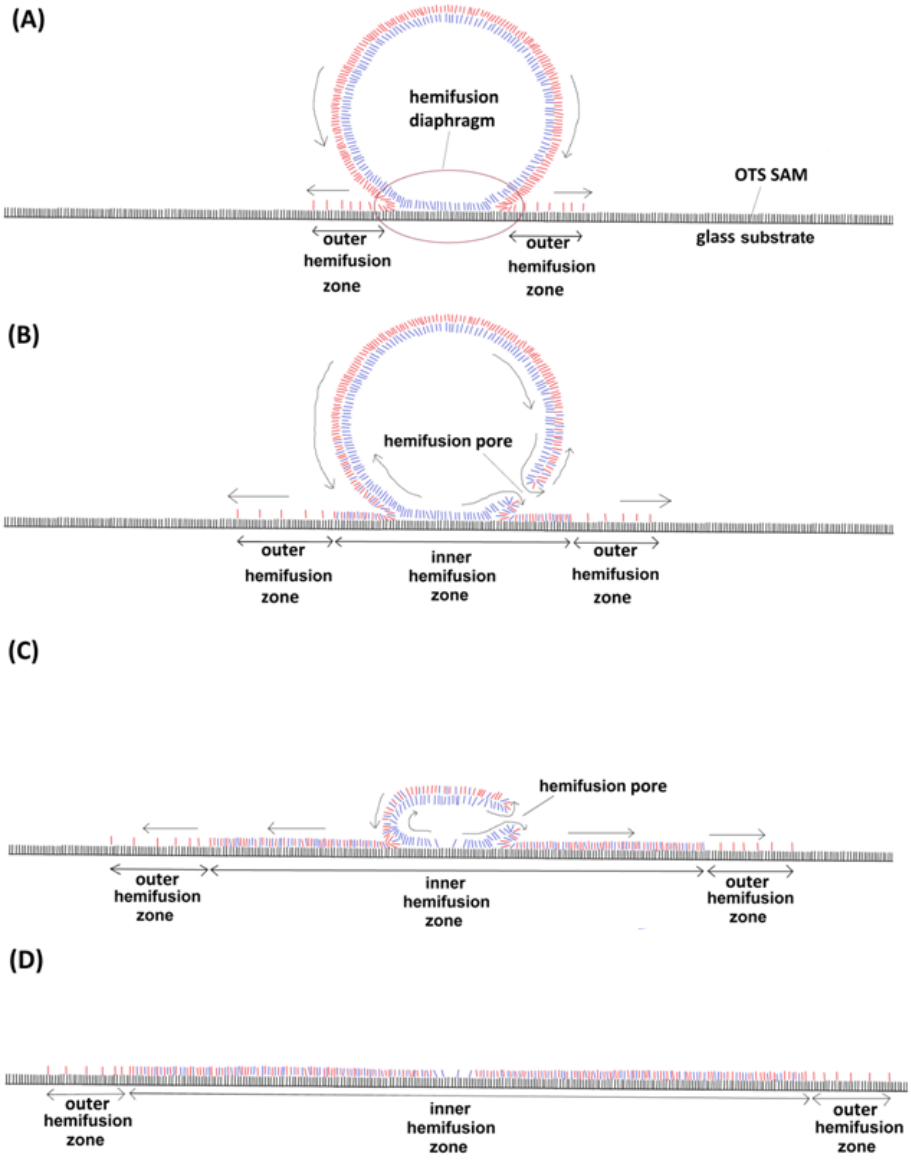


Figure 6.14: *The schematic model of the hemifusion between a GUV and an OTS SAM. Lipids in the outer leaflet originally are colored in red whereas lipids in the inner leaflet originally are colored in blue.*

As more and more lipids are transferred from the outer leaflet to the outer

hemifusion zone, the outer leaflet is stretched even more. This raises the tension of the outer leaflet until it is large enough to rupture the GUV. Hence, a hemifusion pore is formed near the contact site as drawn in Figure 6.14(B). The hemifusion pore establishes a mechanism for the lipid transfer between the outer and inner leaflet and the expulsion of the contents encapsulated in the GUV. As a result, lipids in the inner leaflet (colored in blue) flip to the outer leaflet through the pore, and are further transferred to the SAM surface. At this point, the movement of lipids to the surface is unrestricted anymore since the transfer is no longer held back by the stretching of the GUV. Consequently, the transfer of lipids from both leaflets leads to an inner hemifusion zone that is densely packed with lipids. This explanation is compatible with the presence of an inner zone, which is high in fluorescence intensity, and an outer zone, which is low in fluorescence intensity and comprised exclusively of lipids from the outer leaflet. This effect is illustrated in Figure 6.14(B) such that the outer zone consists of a dilute lipid monolayer and these lipids are colored in red to demonstrate that they are the original outer leaflet's lipids, while the inner zone is a densely packed monolayer with a mixture of red and blue lipids to show they are the lipids from both leaflets of the GUV. Driven by surface hydrophobicity, together with the outer hemifusion zone, the inner hemifusion zone expand radially outward from the contact site as indicated by the arrows.

Additionally, we can estimate the tension of the GUV to form a hemifusion pore from the area of the outer hemifusion zone. For example, in Figure 6.1, a GUV of 4 $\mu$m in radius had an outer zone which is about 5 $\mu$m larger than the inner zone in radius. Besides, the lipid density of the outer zone was only $\sim$ 10% of the lipid density in the inner zone. Therefore, about $0.1 \times \pi(5\,\mu\text{m})^2 \sim 8\,\mu\text{m}^2$ of lipids has been extracted to the outer hemifusion zone from the GUV with an original area of $4\pi(4\,\mu\text{m})^2 \sim 200\,\mu\text{m}^2$ right before the formation of the pore. For the remaining lipids on the outer leaflet to cover the same area of $200\,\mu\text{m}^2$, these lipids must be stretched to have an area which was $\sim 8\,\mu\text{m}^2 \div 200\,\mu\text{m}^2 \sim 4\%$ larger than before. For a lipid bilayer, the surface tension, $\tau$, is related to the stretching modulus of a lipid bilayer, $K_a$, through the relation $\tau = K_a \dfrac{\Delta A}{A}$, in which $\Delta A$ and $A$ are the area change and the original area of the lipid bilayer respectively [110]. Likewise, for a monolayer, $\tau = \dfrac{K_a}{2}\dfrac{\Delta A}{A}$. In this case, $\dfrac{\Delta A}{A} = 0.04$ and $K_a \sim 200$ mN/m. From the relationship, the surface tension of the outer leaflet right before the formation of the pore was $\sim 4$ mN/m. Surface tension of this value is known to rupture a GUV [162]. Furthermore,

from the extent of the outer hemifusion zone and the initial expansion dynamics, we estimate that the formation of the pore occurred $\sim \pi(5\,\mu\text{m})^2 \div 710\,\mu\text{m}^2/\text{s} \sim 0.1$ s after the formation of the hemifusion diaphragm.

It is intriguing that hemifusion pores are always formed near GUV-SAM contact sites. Since the speed of sound in a lipid monolayer is on the order of 200 m/s [163], tension should be uniformly distributed across the entire outer leaflets (< microseconds) between the formation of the hemifusion diaphragms and the pores ($\sim 0.1$ s from the previous paragraph). So, the pore formation near the contact sites suggests that the area close to the contact sites is the area where the lipid bilayer structure is already strongly perturbed, which may due to the largest flow speed of outer leaflet lipids to preserve the flux of lipids at all radial distances (see $\frac{dE_{fric}}{dt}$ of Section 3.3.1).

The expulsion of aqueous contents from GUVs also occurs through the pores during the hemifusion, as evident from the events in Figure 6.8 and 6.9. The pores are the largest at the very beginning of their formation, and contract later since less volume is being expelled per unit time because GUVs lose their surface area linearly. We also argue that there is only one pore formed during the hemifusion as the perimeter of pores is a high-energy line, which should be minimized in length.

As the hemifusion continues, more lipids are transferred to the surface and the hemifusion zone spreads out as in Figure 6.14(C). Simultaneously, the GUV shrinks at the contact site. The inner leaflet of the GUV is pulled radially outward at the end of the expansion and leaves a center with reduced lipid density in Figure 6.14(D). Lastly, hemifusion completes when all the lipids have been deposited to the SAM surface.

The hemifusion to bare SAM surfaces and to loosely packed hybrid bilayers proceeds through the same pathway as described. This is in accord with the results reported previously as lipid monolayers do not form domains on hydrophobic surfaces [146, 147]. Instead, they tend to cover the surfaces as much as possible to shield the surfaces from a direct contact with water. Therefore, GUVs hemifuse to bare SAMs and form loosely packed hybrid bilayers first. Subsequently, hemifusion takes place on these loosely packed hybrid bilayers until densely packed hybrid bilayers are created.

Historically, deposition of lipid monolayers to hydrophobic surfaces from lipid vesicles is termed fusion. However, from the results obtained, we prefer to call this process hemifusion, as hemifusion is defined as the mixing of proximal leaflets between 2 opposing vesicles with their distal leaflets remain separated [161]. In our case, proximal leaflets of hybrid bilayers (OTS SAM) are covalently bound to glass surfaces

and can not undergo any reorganization. Therefore, hemifusion is a more appropriate term to describe the deposition of materials from vesicles to hydrophobic surfaces.

Similar to the quantitative treatment as presented in Chapter 3 and 4, the expansion dynamics of lipid monolayers would give us important information. Again, we require that the total energy of the system is conserved and therefore

$$\frac{dE_{surf}}{dt} + \frac{dE_{fric}}{dt} + \frac{dE_{expul}}{dt} = \frac{dE_{total}}{dt} = 0 \tag{6.1}$$

during the expansion of the hemifusion zones.

$\frac{dE_{surf}}{dt}$ is the energy loss when hydrophobic OTS SAM surfaces are covered by lipid monolayers to shield them from water. From Chapter 3 or 4,

$$\begin{aligned} \frac{dE_{surf}}{dt} &= -\gamma \frac{dA}{dt} \\ &= -2\pi\gamma R \frac{dR}{dt} \\ &= -2\pi\gamma R v(R) \end{aligned} \tag{6.2}$$

in which $A$ and $R$ are the area and the radius of hemifusion zones so $A = \pi R^2$, $v(R) = \frac{dR}{dt}$ and $\gamma$ is the surface energy of OTS SAMs in water.

$\frac{dE_{fric}}{dt}$ is the friction experienced by lipid monolayers when they slide on SAM surfaces. This scenario is depicted in Figure 3.7 by assuming the surface is covered by a circular ring of a lipid monolayer from $r = \epsilon$ to $R$. Identical with the situation portrayed in Chapter 3 and 4,

$$\begin{aligned} \frac{dE_{fric}^{unit\,area}}{dt} &= bv(r)\frac{dr}{dt} \\ &= bv^2(r) \end{aligned} \tag{6.3}$$

To conserve the flux of lipids at different $r$, it is required that $v(r) = v(R)\frac{R}{r}$. Substituting this relationship into $\frac{dE_{fric}^{unit\,area}}{dt}$, one gets

$$\frac{dE_{fric}^{unit\,area}}{dt} = bv^2(R)\frac{R^2}{r^2} \tag{6.4}$$

By integrating the previous expression over the entire area of the circular ring,

$$\begin{aligned}\frac{dE_{fric}}{dt} &= \int_{\epsilon}^{R} bv^2(R)\frac{R^2}{r^2}\,2\pi r\,dr \\ &= 2\pi bR^2\left(\frac{dR}{dt}\right)^2 ln\left(\frac{R}{\epsilon}\right)\end{aligned} \tag{6.5}$$

In this case, $\epsilon$ is the radius of the hemifusion diaphragms, namely the radial distance from the origin of the hemifusion zones in which lipids are transferred from GUVs to SAMs. $b \sim 10^8\,\mathrm{Nsm}^{-3}$ is the friction coefficient between lipid monolayers and hydrocarbon chains of underlying OTS SAMs. Since $v(R) = \dfrac{dA}{dt} \div 2\pi R$, by ignoring the term $ln\left(\dfrac{R}{\epsilon}\right)$ (which is $> 1$), the magnitude of

$$\begin{aligned}\frac{dE_{fric}}{dt} &\sim \frac{b}{2\pi}\left(\frac{dA}{dt}\right)^2 \\ &\sim \frac{10^8\,\mathrm{Nsm}^{-3}}{2\pi}(700\,\mu\mathrm{m}^2/\mathrm{s})^2 \\ &\sim 10^{-11}\,\mathrm{J/s}\end{aligned} \tag{6.6}$$

for the event in Figure 6.1.

$\dfrac{dE_{expul}}{dt}$ is the energy dissipated due to the expulsion of GUV contents in a low Reynold number environment. Its magnitude scales with $\eta RV^2$, in which $\eta$ is the viscosity of water, $R$ is the radius of pores and $V \sim 200\,\mu$m/s is the speed of expelled vesicles obtained from the event in Figure 6.8. Hence, we find $\dfrac{dE_{expul}}{dt} \sim 10^{-16}\,$J/s.

In Eq. (6.1), $\dfrac{dE_{surf}}{dt}$ has a different sign with respect to $\dfrac{dE_{fric}}{dt}$ and $\dfrac{dE_{expul}}{dt}$. Also, as a consequence of $\dfrac{dE_{fric}}{dt} \gg \dfrac{dE_{expul}}{dt}$, $\dfrac{dE_{fric}}{dt} + \dfrac{dE_{expul}}{dt} \sim \dfrac{dE_{fric}}{dt}$. As such, it follows that $\dfrac{dE_{surf}}{dt} + \dfrac{dE_{fric}}{dt} = 0$.

By using the functional form of $\dfrac{dE_{surf}}{dt}$ and $\dfrac{dE_{fric}}{dt}$, Eq. (6.1) reduces to

$$2\pi bR^2v^2(R)ln\left(\frac{R}{\epsilon}\right) = 2\pi\gamma Rv(R) \tag{6.7}$$

Upon substituting $v(R) = \dfrac{dR}{dt}$ and rearranging,

$$\frac{dR}{dt} = \frac{\gamma}{bRln(R/\epsilon)} \tag{6.8}$$

Integrating the preceding equation with respect to $R$ and $t$,

$$\begin{aligned} \gamma t &= b\int_{\epsilon}^{R} R'ln(R'/\epsilon)dR' \\ &= \frac{b}{2}\left(R^2ln\frac{R}{\epsilon\sqrt{e}} + \frac{\epsilon^2}{2}\right) \\ &\sim \frac{bR^2}{2}ln\frac{R}{\epsilon\sqrt{e}} \end{aligned} \tag{6.9}$$

where we have made the approximation that the radius of the hemifusion zone, $R$, is much larger than the radius of the hemifusion diaphragm, $\epsilon$, to get the last expression.

Finally, the area of the hemifusion zone,

$$A = \pi R^2 = \frac{2\pi\gamma}{bln(R/\epsilon\sqrt{e})}t \tag{6.10}$$

Therefore, the area growth of the hemifusion zone approximately scales with time with an expansion rate,

$$\frac{dA}{dt} = \frac{2\pi\gamma}{bln(R/\epsilon\sqrt{e})} \tag{6.11}$$

The linear growth in area is similar in nature to the spreading of lipid films on surfaces as revealed by earlier works [41, 42, 164].

The exact value of $\epsilon$ is unknown from images taken. Nonetheless, its value must be smaller than the size of the pores observed in Figure 6.1 and 6.5 and fortunately, the value of $ln(R/\epsilon\sqrt{e})$ only changes by a factor of 2 even if the value of $R/\epsilon$ changes by

an order of magnitude. As a result, it is not a bad choice to make an assumption that on average $R/\epsilon \sim 10$ during the expansion. For instance, the average $R$ for the event in Figure 6.1 was $\sim 5$ $\mu$m and the pore was $< 500$ nm. Accordingly, $\frac{dA}{dt} \sim 1.1\frac{\pi\gamma}{b}$. The average $\frac{dA}{dt}$ for $n = 22$ observations is $970 \pm 430\,\mu\text{m}^2/\text{s}$. Hence, with this value of $\frac{dA}{dt}$, the surface energy of OTS SAMs, $\gamma$, is equal to 30 mN/m. This value is comparable to the surface tension of hydrocarbon-water interfaces at 40 to 50 mN/m [110], thus demonstrating the essential role of surface hydrophobicity in driving the spreading of lipid monolayers on SAM surfaces.

## 6.5 Conclusions

In this chapter, we have imaged the reorganization of GUVs on OTS SAMs to complete the bilayers at a single vesicle level. Visualization of individual hemifusion events leads us to construct a model for the process, which captures all the features unveiled in these events. This is the first time the transformation of closed shell lipid bilayers to surface monolayers is being explored. Even though the work was driven originally by the motivation to understand the formation of supported lipid monolayers from lipid vesicles, the mechanistic insights gained here for the complex vesicle-surface interactions should shed light on the reorganization of vesicles during membrane fusion, and further improve the design of lipid vesicles as a carrier in drug delivery.

# Chapter 7

# *In vitro* Assay for Membrane Tethering by GRASP Proteins

## 7.1 Introduction

The Golgi apparatus is one of the most conspicuous organelles in metazoan cells with important functions in post-translational processing of proteins synthesized in the endoplasmic reticulum. Its basic building block is a cisternal which is a flattened membrane bounded compartment. Cisternae stack together to form ministacks, and ministacks are further linked laterally on the rim of cisternae to form the characteristic ribbon structure of the Golgi apparatus. The ribbon structure is regulated by cells for its function and its inheritance. How the cells control this highly organized internal structure is one of the most intriguing questions in cell biology.

Two closely related membrane-associated proteins, GRASP65 [165] and GRASP55 [166] (Golgi Reassembly And Stacking Protein with a molecular weight of 65 and 55 kDa respectively), have been localized on the *cis* and medial Golgi cisternae respectively [165, 166]. They are essential in stacking of cisternae to form ministacks or tethering of Golgi ministacks to form the characteristic ribbon-like stucture [167]. Both GRASP proteins contain two PDZ domains and an internal ligand sequence as evident from the crystal structure of GRASP55 (Figure 7.1) [168]. In cells, the internal ligand of the first protein binds to the first PDZ domain of the second protein located on an opposing membrane, dimerize *in trans* to tether two membranes, and this process has been shown to be regulated during mitosis by CDK1 and PLK1

kinases [169]. Even though functionality of these proteins has been tested *in vivo* on both the Golgi apparatus and on mitochondrial membranes [170–173], an *in vitro* demonstration of this reaction using purified GRASP proteins alone is still lacking. So far, the only cell free demonstration of the tethering activity by GRASP proteins was performed with the crosslinking of Dyna beads [172, 173]. However, localization of GRASP to polystyrene surfaces may affect the proper functioning of proteins, making the studies less than physiologically relevant.

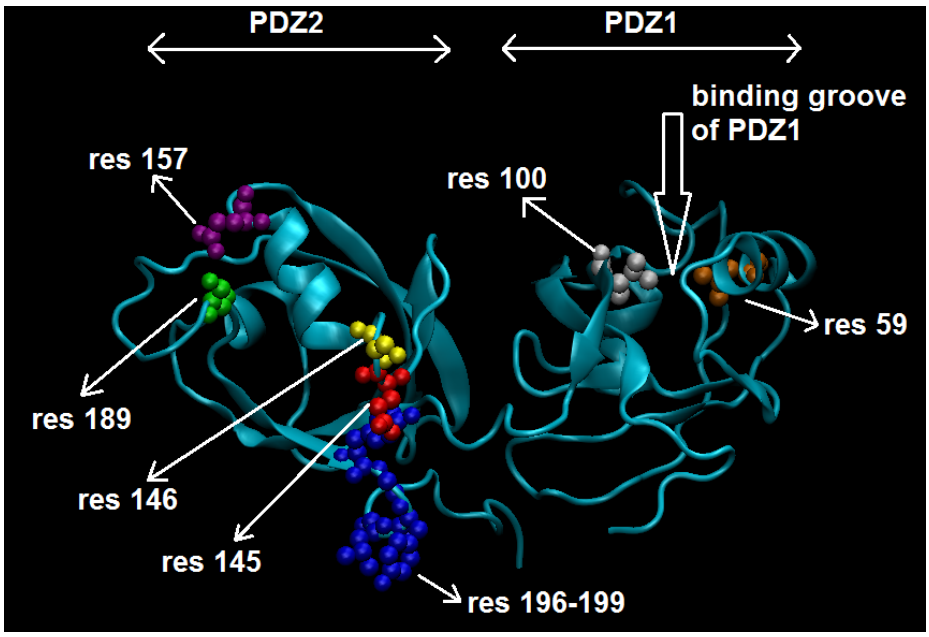


Figure 7.1: *The crystal structure of GRASP55 from its 7th to 208th residue (PDB code: 3RLE). GRASP contains PDZ1 and PDZ2 and an internal ligand. Functional residues of the protein are highlighted with different colors.*

To investigate functionality of GRASP55 *in vitro*, we developed a fluorescence microscopy based assay by using lipid vesicles and sparsely-tethered bilayer lipid membranes (stBLMs) to quantify the tethering capability of purified GRASP proteins. In cells, GRASP65 is recruited to Golgi by GM130 whereas GRASP55 is by golgin45 [171]. In our assay, we established an anchoring scheme for truncated GRASP55 by using bacterially myristoylated proteins with a C-terminal hexahistidine tag, which can bind to lipids functionalized with NTA-nickel on their headgroups (NTA-nickel lipids) in both stBLMs and vesicles. The vesicles, but not the stBLMS, were doped with a low concentration of fluorescently-labelled lipids. Hence, by taking fluorescence images at the interfaces of stBLMs, the quantity of tethered vesicles, which is the indicator of

GRASP55 tethering ability, was inferred directly from fluorescence intensity of the images.

Employing this assay, we show that GRASP55 can, indeed, tether membranes on its own *in vitro*. We then go on to test other key findings regarding the regulation of this process as seen in cells with mutants of GRASP55 to establish this as a functional and physiologically relevant assay. Lastly, from preliminary analysis of neutron reflectivity data, we resolved the orientation of GRASP55 on stBLMs, which is consistent with the results of the assay.

## 7.2 Materials and Methods

### Materials

1,2-dioleoyl-sn-glycero-3-phosphocholine (DOPC), 1,2-dioleoyl-sn-glycero-3- phosphoethanolamine (DOPE), 1,2-dioleoyl-sn-glycero-3-phospho-L-serine (sodium salt) (DOPS), L-$\alpha$-phosphatidylinositol (Liver, Bovine) (sodium salt) (Liver PI), cholesterol (ovine wool), Sphingomyelin (Brain, Porcine), 1,2-dioleoyl-sn-glycero-3-phospho- ethanolamine-N-(lissamine rhodamine B sulfonyl) (ammonium salt) (LR-PE) and 1,2-dioleoyl-sn-glycero-3-[(N-(5-amino-1-carboxypentyl)iminodiacetic-acid)succinyl] (nickel salt) (NTA-nickel lipids) were purchased from Avanti Polar Lipids (Alabaster, AL) and used as received. Number 1.5 thickness glass coverslips were purchased from Electron Microscopy Science (Hatfield, PA) while the microscope glass slides were purchased from Fisher Scientific (Pittsburgh, PA). All other chemicals were of HPLC grade and the ultrapure water was prepared in a Millipore (Billerica, MA) Milli-Q water purification device.

### Formation of sparsely-tethered Bilayer Lipid Membranes (stBLMs)

stBLMs were formed as described in Chapter 5. In brief, $\sim$ 2 nm of chromium adlayers were first sputtered either on number 1.5 glass coverslips (for fluorescence microscopy) or microscope glass slides (for Surface Plasmon Resonance). For fluorescence microscopy experiment, the coverslips were further sputtered with $\sim$ 6 nm of gold, which made the gold-coated coverslips optically transparent. For Surface Plasmon Resonance (SPR) experiments, the glass slides were further sputtered with $\sim$ 45 nm of gold for excitations of surface plasmon. Gold-coated coverslips/slides were

immersed in an ethanolic solution consisted of 30% of HC18 and 70% of $\beta$ME, at a total concentration of 0.2 mM, to form mixed self-assembled monolayers (SAMs). Rapid solvent exchange or vesicle hemifusion were used to complete the formation of stBLMs of desired membrane compositions from the SAMs.

### Preparation of Lipid Vesicles

Lipid vesicles were prepared with the extrusion method as described in Chapter 5. Dry lipid films were rehydrated and sonicated in 50 mM potassium phosphate buffer at pH $\sim$ 7.45. To control the size of vesicles, vesicle suspensions were extruded through 2 polycarbonate membranes with pore sizes of 200 nm, 100 nm or 30 nm, at least 18 times. The sizes of vesicles were checked by dynamic light scattering (Malvern Zetasizer Nano ZS, UK). Vesicles with 100 nm extrusion were used throughout the experiments unless otherwise stated. For DOPC vesicles used for the formation of stBLMs through vesicle hemifusion, 0, 0.74 or 2.2 mol % of NTA-nickel lipids (vs total lipids) were incorporated into the vesicles. Fluorescently-labeled lipids, LR-PE, were mixed with vesicles at a molar percentage of 0.125%.

### Protein Purification

GRASP55 was cloned into the pRSET-B vector by PCR amplification into the EcoRI site. Subsequently, the N-terminal His tag was deleted by a PCR loop-out procedure and a 10 amino acid linker (ASSRSGGSGA) followed by a hexahistidine sequence was inserted after residue 208, followed by a stop codon to create GRASP55(1-208)-ASSRSGGSGA-HHHHHH. The His-GRASP55(1-208) construct was made by PCR deletion of the His tag from GRASP55(1-208)-ASSRSGGSGA-His and reintroduction immediately before the starting methionine. Protein induction was done as described previously [171]. Myristoylation was achieved by co-expression of the myristoyl transferase and myristic acid addition during the induction as described previously [171] to make the Myr-GRASP55(2-208)-ASSRSGGSGA-His proteins (referred as 'wild type' proteins). The mutation was induced by PCR mutagenesis using the Quickchange procedure (Stratagene).

### Surface Plasmon Resonance (SPR)

The details of SPR measurements are described in Chapter 2. In brief, $\triangle pixel$ of SPR minimum positions is used to quantify the binding of His-tagged GRASP55 to stBLMs incorporated with NTA-nickel lipids. stBLMs were incubated with increasing concentrations of proteins sequentially. The final $\triangle pixel$ as a function of protein concentrations is fitted to the Langmuir adsorption equation to extract the binding constant of His-tagged proteins with stBLMs. The exact concentrations of proteins were measured with Bradford assay.

### Fluorescence Microscopy

stBLMs on gold-coated glass coverslips were assembled in Sykes-Moore chambers. 1.2 $\mu M$ of proteins and 0.01 mg/ml of fluorescently-labeled vesicles were injected into the chambers. The solutions were mixed occasionally and stBLMs were incubated with proteins and vesicles for 1, 3 or 5 hours before the excess proteins and vesicles in the bulk solutions were rinsed away. Afterwards the chambers were transferred to a Carl Zeiss Axiovert 200M inverted microscope. The fluorescence images of vesicles tethered to stBLMs were taken similar to the conditions in Chapter 3 and 4. The image acquisition parameters were chosen to minimize the number of saturated pixels in images. For each sample, at least 12 images (100 x 100 $\mu$m$^2$ per image) chosen at random positions were taken. After the background subtraction, the fluorescence intensity of these images was used to quantify the tethering activity of proteins. For Fluorescence Recovery After Photobleaching (FRAP) experiments, a spot of $\sim$ 26 $\mu$m was bleached by the excitation light at its highest intensity and the recovery of the bleached spot was monitored after the bleaching.

### Student T-test and p-value

In order to compare the tethering ability of proteins (or mutants) under various circumstances, Student T-test was carried out and p-values were reported [174]. When p-values $< 0.05$, the results are statistically significant and if p-values $< 0.01$, the results are highly statistically significant.

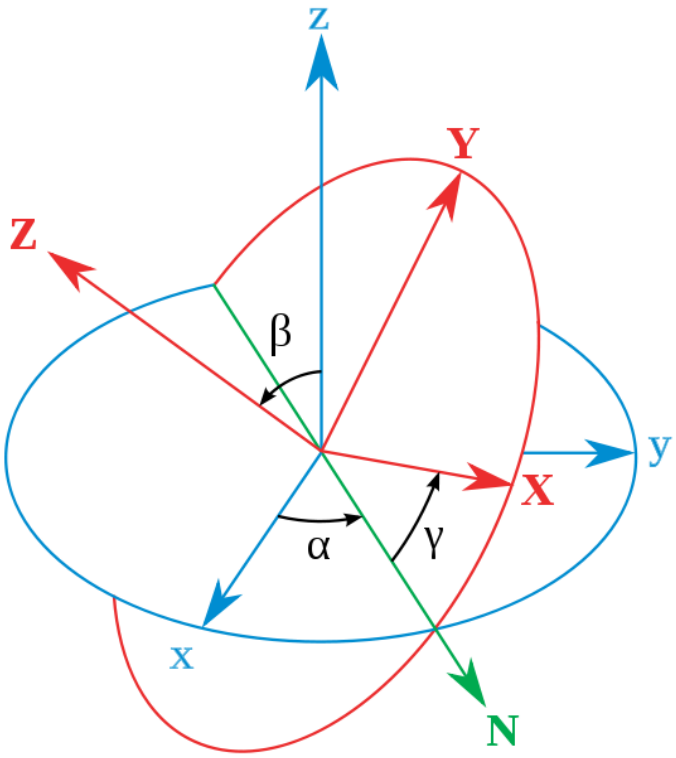


Figure 7.2: *3 Euler angles, $\alpha$, $\beta$ and $\gamma$ are used to describe the orientation of proteins on membranes. The membranes are located on the x-y plane so the resulting nSLD profile along the z-axis is $\alpha$ invariant.*

### Neutron Reflectivity (NR)

NR measurements were performed at NG7 reflectometer at the NIST Center for Neutron Research (NCNR). The silicon substrates for stBLMs were assembled in a neutron wet cell and reflectivity was measured from $Q_z = 0.01$ to 0.25 Å$^{-1}$. A stBLM with a molar ratio of DOPC:NTA-nickel lipid = 9:1 was formed with vesicle hemifusion. NR was first performed with the stBLM in $D_2O$ and $H_2O$. Later the measurements were performed with 1.2 $\mu$M of Myr-GRASP(2-208)-ASSRSGGSGA-HHHHHH in the bulk solution. Finally, the proteins were rinsed away and measurements were again carried out with $D_2O$ and $H_2O$. Data was fitted by using the continuous distribution (CD) model for the stBLM and a monotonic Hermite spline for the proteins. The protein nSLD profile is constrained to be single-peaked. From the protein nSLD profile, its orientation is determined through fittings of the crystal structure of GRASP55(7-208) (PDB code: 3RLE). The orientation of protein is described by 3 Euler angles, $\alpha$, $\beta$ and $\gamma$ (Figure 7.2). Since membranes are located on the x-y plane, the rotation along

z-axis or $\alpha$ is irrelevant as the nSLD profile of a protein along the z-direction is $\alpha$ invariant. Therefore, by varying the values of $\beta$ (0 to 180°), $\gamma$ (0 to 360°), the location of the GRASP55 crystal structure along z-axis and the protein surface density, the resulting nSLD profiles were calculated by using a grid spacing of 0.5 $\mathring{A}$, which is further convoluted with a Gaussian function of a width 2.5 $\mathring{A}$ to account for the surface roughness of stBLMs. This set of nSLD profiles were compared with the experimental nSLD profile to determine the best-fit orientation.

## 7.3 Results

### 7.3.1 Binding of His-tagged GRASP55 to stBLMs incorporated with NTA-nickel Lipids

The very first step of the assay was to confirm the recruitment of truncated wild type proteins, Myr-GRASP55(2-208)-ASSRSGGSGA-HHHHHH, which are His-tagged at the C-terminal and myristoylated at the N-terminal, to stBLMs by NTA-nickel lipids. For this aim, DOPC stBLMs were incorporated with 1 mol% of NTA-nickel lipids and the stBLMs were incubated with increasing concentrations of proteins. From SPR measurements, the $\triangle pixel$ of minimum positions after the protein injection was monitored and the result is shown in Figure 7.3.

As shown in Figure 7.3, every time a higher concentration of proteins was injected, the SPR minimum shifted up to a higher pixel value and the $\triangle pixel$ values almost came to a new equilibrium after about tens of minutes. With increasing concentrations (0 to 5.34 $\mu$M), more and more proteins were bound to the surface of the stBLM as indicated by the increasing $\triangle pixel$. The kinetic of $\triangle pixel$ for each concentration was fitted to a single exponential function to extract the final $\triangle pixel$ as $t \to \infty$ (not shown). Consequently, the final $\triangle pixel$ is plotted as a function of protein concentrations in Figure 7.4 and it is fitted to the Langmuir adsorption equation. From the fitting, a binding constant of 0.32 $\pm$ 0.09 $\mu$M and a $\triangle pixel_{max}$ of 25.4 $\pm$ 2.5 pixels are obtained. This binding constant is comparable to the binding constant between His-tagged proteins and NTA-nickel lipids as reported in the literature [175, 176], suggesting a dominant role of His-NTA-nickel chelation in recruiting proteins to membranes. A $\triangle pixel_{max}$ of 25.4 pixels corresponds to a 2.13 Å of dry protein layer that completely covers the surface of stBLMs. Assuming the thickness of GRASP55 on membranes to

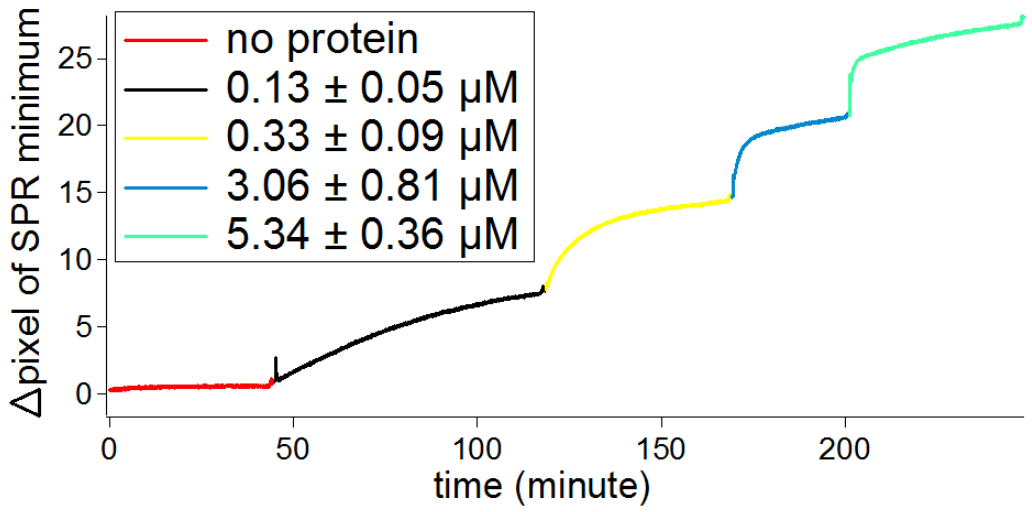


Figure 7.3: *The DOPC stBLM incorporated with 1 mol% of NTA-nickel lipids was incubated with increasing concentrations of proteins. The △pixel of the SPR minimum (vertical axis) was monitored as a function of time (horizontal axis).*

be $\sim$ 4 nm, this $\triangle pixel_{max}$ proposes that the proteins cover about (2.13 Å) $\div$ (4 nm) x 100% = 5.3% of the stBLM surface.

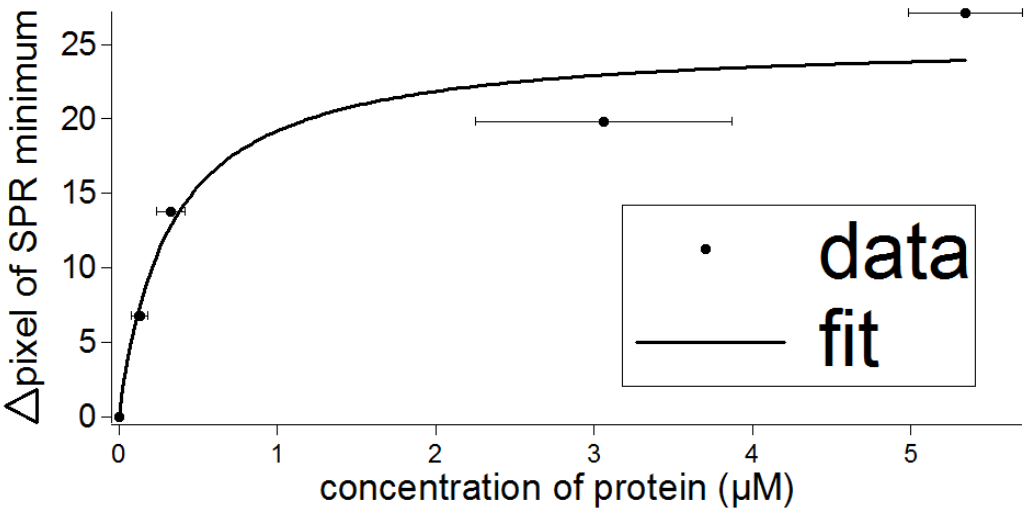


Figure 7.4: *The final △pixel for the stBLM in Figure 7.3 is plotted as a function of protein concentrations and it is fitted to the Langmuir adsorption equation.*

As a control for non-specific protein recruitment to stBLMs, we also studied the binding of His-tagged GRASP55 proteins to DOPC stBLMs without NTA-nickel lipids. From the result shown in Figure 7.5, only a marginal amount of proteins ($<$ 2 pixels)

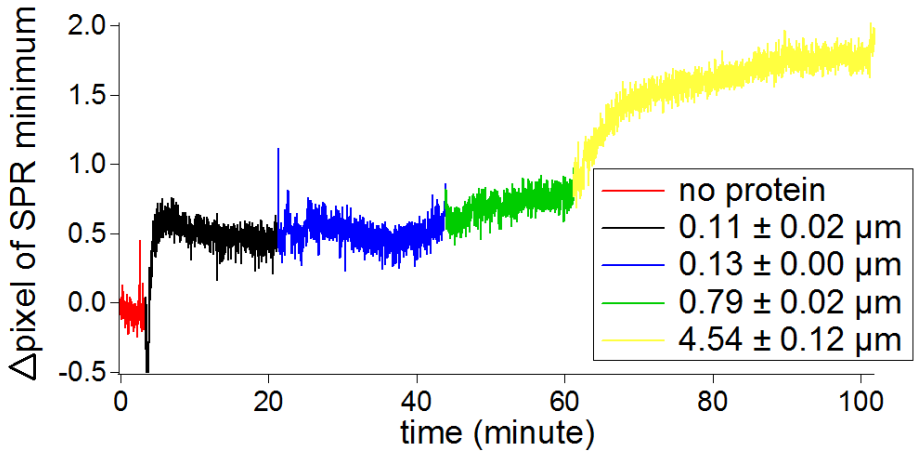


Figure 7.5: *The non-specific binding of GRASP55 to a DOPC stBLM without NTA-nickel lipids.*

were non-specifically absorbed to the stBLM even with the highest concentration of proteins tested. This implies that the myristic acid on the N-terminal is not enough to recruit GRASP55 to membranes by itself. This experiment confirms that we have a control over the association of GRASP55 with stBLMs by using NTA-nickel lipids, which is crucial for the fluorescence microscopy based assay discussed in the following sections.

### 7.3.2 Tethering of Vesicles to stBLMs by GRASP55

After establishing the anchoring scheme for GRASP55, we examined the ability of GRASP55 in membrane tethering. In these experiments, DOPC vesicles (extruded with 100 nm of polycarbonate membranes and with a size distribution of 84.5 ± 28.4 nm from dynamic light scattering) and DOPC stBLMs were incorporated with NTA-nickel lipids. The stBLMs were incubated with 1.2 $\mu$M of wild type proteins and 0.01 mg/ml of fluorescently-labeled vesicles simultaneously for 3 hours before the excess proteins and vesicles in the bulk solution were rinsed away. Fluorescence images of tethered vesicles on stBLMs were taken and the fluorescence intensity of these images was measured to quantitatively evaluate the tethering activity of GRASP55 *in vitro*.

For example, as seen in the image on the left of Figure 7.6, only a few low intensity spots are detected after the stBLM was incubated with vesicles (both with 2.2 mol% of NTA-nickel lipids), but without GRASP55 proteins. These spots were most likely

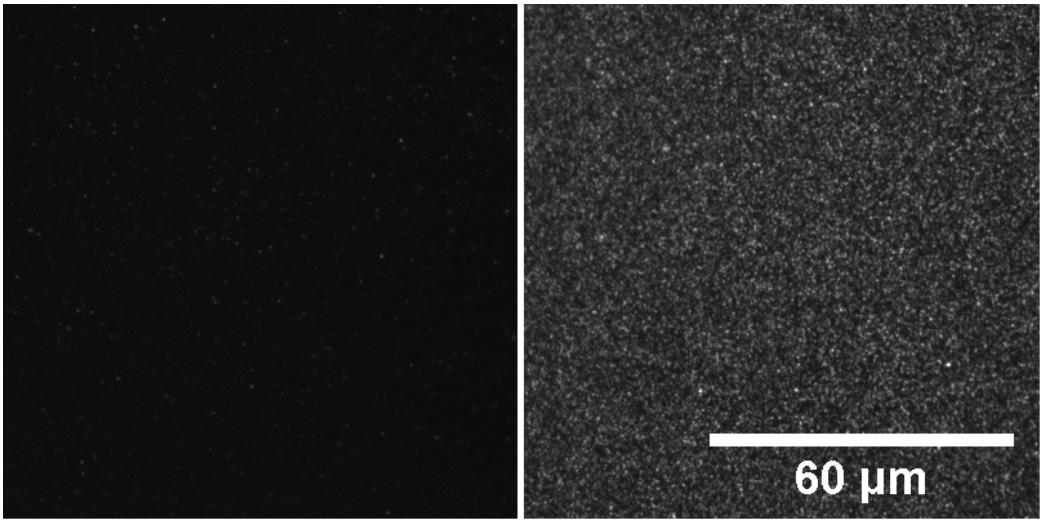


Figure 7.6: *The fluorescence image on the left was taken after the DOPC stBLM (2.2 mol% of NTA-nickel lipids) was incubated with DOPC vesicles (2.2 mol% of NTA-nickel lipids) for 3 hours, while the image on the right was taken with additional GRASP55 in the incubation. Both images are in the same contrast.*

due to non-specifically adsorbed vesicles on the stBLM. In contrast, a representative image on the right was imaged under identical membrane conditions, except with 1.2 $\mu$M of GRASP55 included in the incubation. Under this condition, a multitude of bright fluorescent spots are observed, indicating vesicles were tethered on the stBLM.

These experiments were repeated with varying molar ratios of NTA-nickel lipids: 0 or 2.2 mol% in vesicles and 0, 0.74 or 2.2 mol% in stBLMs, with or without the proteins included in the incubation. The fluorescence intensity of images in each circumstance is summarized in Figure 7.7. As expected, only a minimum amount of vesicles were tethered/absorbed to stBLMs when proteins were absent or when NTA-nickel lipids were not incorporated into vesicles (the first and second bar in Figure 7.7, both of which $< 100$ a.u.). However, when proteins were included in the assay, the number of tethered vesicles increased with NTA-nickel lipid concentrations in stBLMs as measured by an increment in the overall fluorescence intensity up to $\sim$ 1800 a.u. (the fourth and the fifth bar). Interestingly, a low level of tethering was also observed in the 3rd bar ($\sim$ 400 a.u.) when only vesicles, but not stBLMs, contained NTA-nickel lipids. We attribute this minor increase to the fact that vesicles that were non-specifically absorbed to stBLMs further tethered vesicles to them through GRASP55. Thus, the fluorescence intensity of tethered vesicles in this condition was

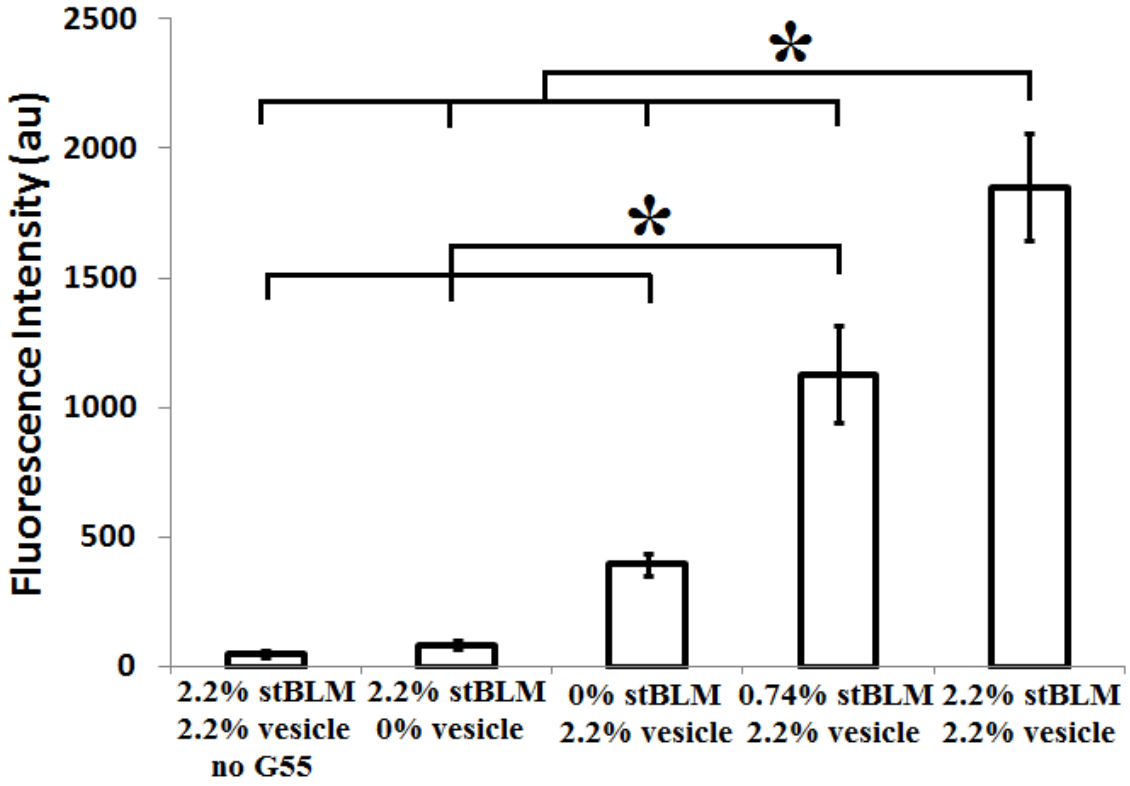


Figure 7.7: *The fluorescence intensity of tethered DOPC vesicles to DOPC stBLMs incorporated with different amounts of NTA-nickel lipids in vesicles and stBLMs (indicated at the bottom of each bar). Except for the first bar, wild type GRASP55 was used in these assays. Each bar is the average ± standard error for at least n = 3 samples. ⋆ indicates the 1-tailed p-value between 2 bars is < 0.01.*

higher than the background intensity in the first and second bar. In fact, at the end of the 3 hours incubation, vesicle aggregates on the order of tens of microns were detected in the bulk solution. Therefore, this result suggests that there were multilayers of vesicles tethered to stBLMs in the fourth and fifth bar, as the first layer of tethered vesicles provided the surfaces of reaction for the tethering to take place subsequently. In short, the data in this figure unambiguously validates that GRASP55 is sufficient and necessary for membrane tethering.

In addition, to prove the tethering of vesicles to stBLMs was actually mediated by the recruitment of GRASP55 to membranes exclusively, we incubated the vesicle-stBLM systems in the fifth bar of Figure 7.7 with 200 mM of imidazole to release the His-tagged GRASP55 from the membranes. The treatment of imidazole reduced

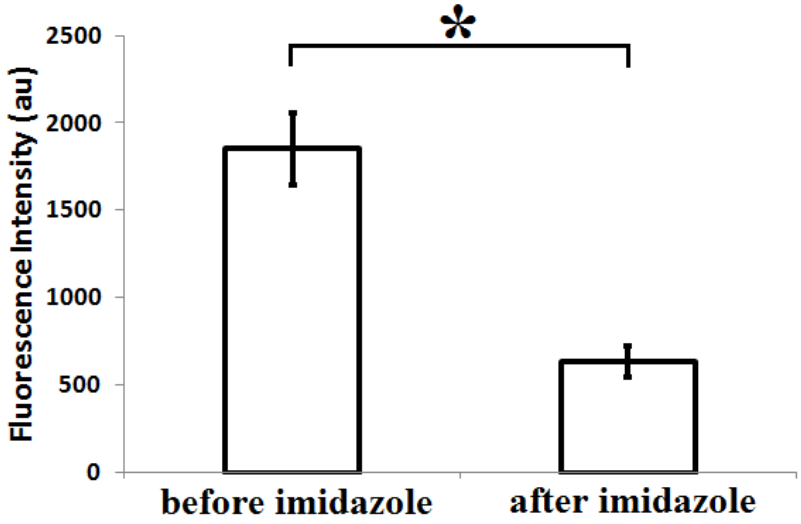


Figure 7.8: *The reduction of fluorescence intensity after the treatment with 200 mM of imidazole for the fifth bar in Figure 7.7. Each bar is the average ± standard error for at least n = 3 samples. ⋆ indicates the 1-tailed p-value between 2 bars is < 0.01.*

the fluorescence intensity by a factor of 3, from $\sim$ 1800 a.u. to $\sim$ 600 a.u. (Figure 7.8), indicating tethered vesicles were released from stBLMs following the unbinding of GRASP55.

As tethered vesicles were confined to planar surfaces, it was easy to study the mobility of the vesicles with Fluorescence Recovery After Photobleaching (FRAP). In these measurements, a spot was bleached and the recovery was monitored. In Figure 7.9 are the images of the bleached spot taken 0 (on the top left) and 27 minutes (top right) after the bleaching of DOPC vesicles tethered to a DOPC stBLM (both with 2.2 mol% of NTA-nickel lipids) by GRASP55. Radial profiles are calculated for the images from the center of the bleached spot and are shown at the bottom of the figure. In that graph, both radial profiles highly overlap with each other and can be modeled as a step function with a boundary near $r \sim 12$ $\mu$m, which is the boundary of the bleached spot. The image taken 27 minutes after the bleaching shows no signs of recovery compared with the image taken right after the bleaching, and hence the vesicles were immobilized on the surface following the tethering. It is not completely unanticipated, since there are reports in the literature that showed the immobilization of vesicles upon tethering to supported lipid membranes [47, 177] or the diffusion of vesicles is considerably reduced with multi-tethers [178].

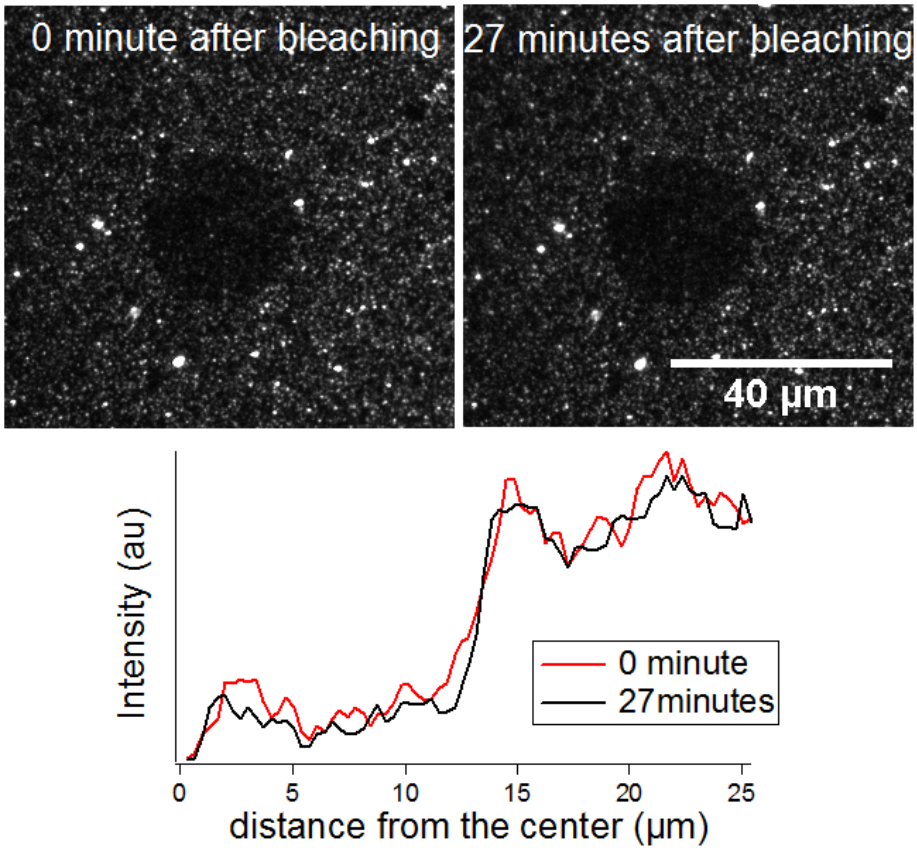


Figure 7.9: *The images of a bleached spot taken 0 or 27 minutes after the bleaching. The graph at the bottom is the radial profile from the center of the bleached spot for both images.*

To sort out the influence of incubation time, the experiments for the fifth bar of Figure 7.7 (2.2 mol% NTA-nickel lipids in both vesicles and stBLM) were repeated for 1 and 5 hours of incubation before the excess vesicles and proteins were rinsed away. The resulting fluorescence intensity as a function of incubation time is displayed in Figure 7.10. 1 hour of incubation clearly generated less tethered vesicles as its intensity was only one third of the intensity of 3 and 5 hours incubation. With increasing incubation time, the number of tethered vesicles leveled off after 3 hours as its intensity was close to the intensity of 5 hours incubation and they are not statistically different (1-tailed p-value $> 0.05$). As a result, an equilibrium was reached in term of vesicle tethering to stBLMs after 3 hours and this incubation time is optimum for this assay.

Another parameter that affected the outcomes of the assay is sizes of vesicles. For instance, on one hand, the absence of GRASP unlinked the Golgi ribbon structure

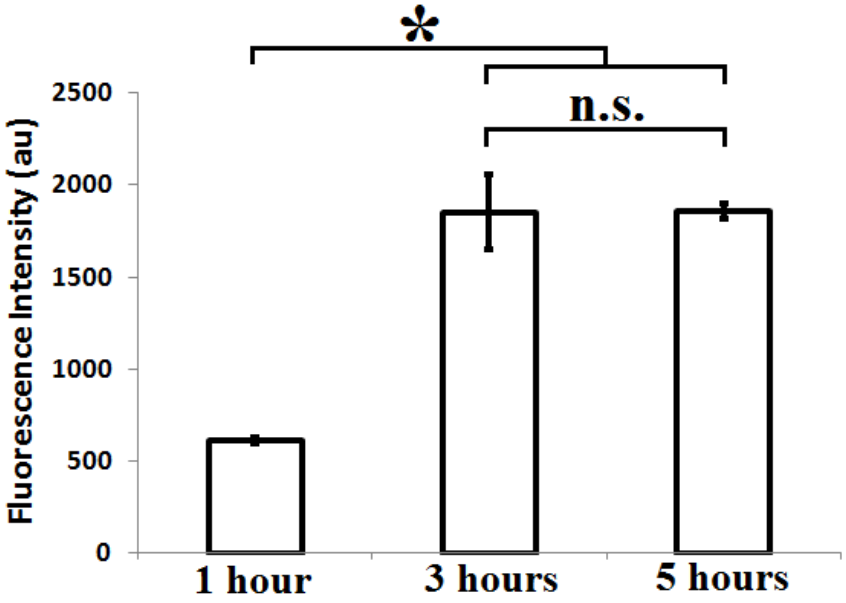


Figure 7.10: *The fluorescence intensity of tethered vesicles as a function of incubation time. Each bar is the average ± standard error for at least n = 3 samples. ⋆ indicates the 1-tailed p-value between 2 bars is < 0.01 and n.s. indicates the difference is not statistically significant with a p-value > 0.05.*

into isolated ministacks [167, 170]. So it implies that GRASP is either localized or only functional at the rims of Golgi cisternae, which are highly curved. On the other hand, due to the interactions between vesicles and stBLMs, the system might prefer vesicles of certain sizes over the others [179]. It prompted us to examine the effect of vesicle' diameters in this assay. For this goal, DOPC vesicles incorporated with 2.2 mol% of NTA-nickel lipids were extruded with polycarbonate membranes of 30, 100 and 200 nm. The extrusion produced mono-disperse vesicles with a size distribution of 45.1 ± 13.5, 84.5 ± 28.4 and 125.3 ± 49.1 nm (average ± standard deviation of the distribution) respectively, as measured by dynamic light scattering. Together with 1.2 $\mu$M of GRASP55, the vesicles were incubated with DOPC stBLMs incorporated with 2.2 mol% of NTA-nickel lipids for 3 hours.

We show the results for these experiments in Figure 7.11. The vesicles with a diameter $\sim$ 45 nm ($<$ 300 a.u.) were not tethered to stBLMs as efficient as the vesicles of 84.5 and 125.3 nm, both of which $\sim$ 1900 a.u. Besides, with a plateau that was reached for vesicles larger than 84.5 nm (with 100 nm extrusion), vesicles with 100 nm extrusion would be the best candidate in this assay for maximizing the signal

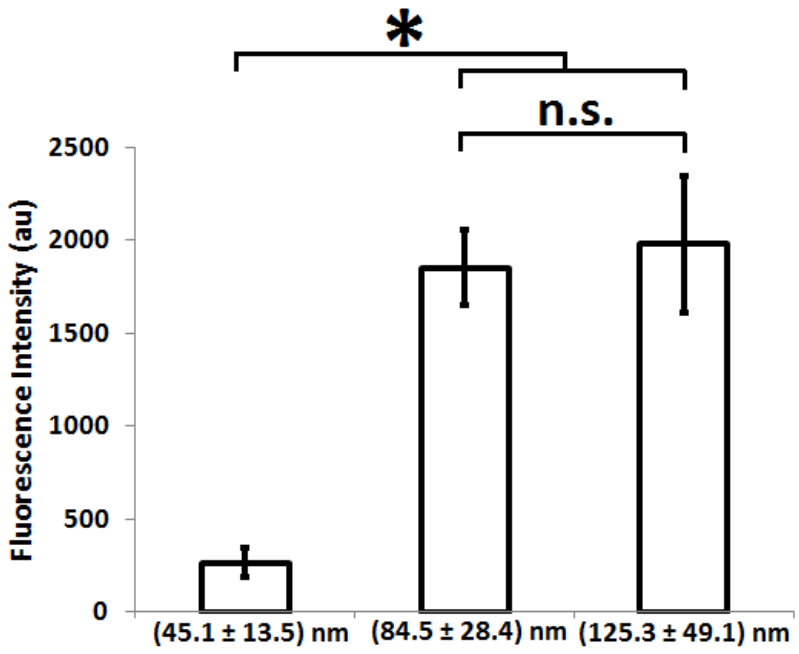


Figure 7.11: *The dependence of tethering on diameters of vesicles. Each bar is the average ± standard error for at least n = 3 samples. ⋆ indicates the 2-tailed p-value between 2 bars is < 0.05 and n.s. indicates the difference is not statistically significant with a p-value > 0.05.*

of tethered vesicles, as the extrusion with polycarbonate membranes of large pore sizes can compromise the lamellarity of vesicles, and thus the fluorescence intensity no longer truly reflects the number of tethered vesicles if they are multilamellar.

In our case, the dependence of tethering on sizes of vesicles can be qualitatively explained by a simple model developed recently [179]. First, since a large vesicle in close proximity with a planar membrane has more area accessible for multi-tethering to take place compared with a small vesicle, this assay favors large vesicles in term of tethering. Second, except for the dimerization energy of proteins, the interactions between vesicles and planar membranes involve the electrostatic, van der Waals and hydration force between two opposing membranes. For DOPC which is zwitterionic, no electrostatic interactions exist between vesicles and stBLMs. Assuming the thickness of tethers between vesicles and stBLMs is on the order of $\delta = 4$ nm, the repulsive hydration energy between a vesicle and an infinitely large stBLM, $U_H$, is [179]

$$U_H = \pi B \lambda_H^2 D * exp\left(\frac{-\delta}{\lambda_H}\right) \tag{7.1}$$

in which $D$ is the diameter of the vesicle, $B = 10^{10}$ Pa and $\lambda_H = 0.193$ nm are two phenomenological constants. Therefore

$$U_H = 1.17 \times 10^{-18}\, D \tag{7.2}$$

The van der Waals attraction energy, $U_v$, under the identical condition is

$$U_v = -\frac{A_H}{6}\left[\frac{D}{2}\left(\frac{1}{2t+\delta} - \frac{1}{t+\delta} + \frac{1}{\delta}\right) - ln\left[\frac{\delta(\delta+2t)}{(\delta+t)^2}\right]\right] \tag{7.3}$$

where $t = 4$ nm is the thickness of a lipid bilayer and $A_H$ is the Hamaker constant given by

$$A_H = 2\kappa\delta A_0 * exp(-2\kappa\delta) \; + \; A_1 \tag{7.4}$$

$\kappa$ is the inverse of Debye length $= 0.736$ nm$^{-1}$ for 50 mM of salt buffer, $A_0 = A_1 = 3.5 \times 10^{-21}$ J. It follows that $A_H = 3.56 \times 10^{-21}$ J. By substituting this value into $U_v$,

$$U_v = (-6.17 \times 10^{-14}\, D \; + \; constant) \tag{7.5}$$

It is obvious that $\mid U_v \mid \gg \mid U_H \mid$. By ignoring the dimerization energy, the total energy to tether a vesicle to a planar membrane is $U_{total} \approx U_v$. This is as expected since the tethers ($\delta$) are not small enough for the hydration to play a role.

In equilibrium, the number of tethered vesicles is governed by the Boltzmann distribution. As a consequence, the tethering activity follows the distribution

$$exp\left(\frac{-U_{total}}{kT}\right) \sim exp\left(\frac{-U_v}{kT}\right) \sim exp\left(\frac{constant \times D}{kT}\right) \tag{7.6}$$

namely the number of tethered vesicles increases with the diameter of vesicles. The data in Figure 7.11 is justified by this physical argument and GRASP does not localize or functional at membranes of high curvature in this *in vitro* environment, otherwise the vesicles of 45.1 nm would show the highest tethering activity among the vesicles tested.

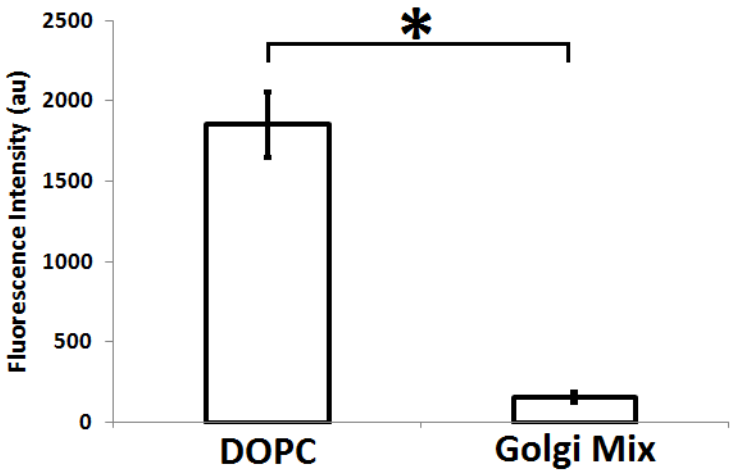


Figure 7.12: *The comparison between DOPC and Golgi mix membranes.* $\star$ *indicates the 2-tailed p-value between 2 bars is* $< 0.01$.

To create a more physiologically relevant environment for GRASP, the assay was performed with Golgi mix membranes. stBLMs and vesicles (100 nm extrusion) were prepared according to a molar composition of DOPC:DOPE:Liver PI:DOPS:cholesterol: Brain Sphingomyelin = 43:19:10:5:16:7 and were incubated with GRASP55 to investigate the effect of membrane compositions on tethering activity. The results for both the Golgi mix and DOPC membranes are presented in Figure 7.12. In the bar chart, the tethering was lowered by a factor of 10 when DOPC was replaced by Golgi mix. It is noticeable that Golgi mix membranes contain 15 mol% of negatively charged lipids (Liver PI and DOPS). As such, the vesicles need to overcome the electrostatic repulsion to be tethered to stBLMs. Again, the model that is used to explain the dependence of vesicle' sizes is employed here. For Golgi mix, an extra electrostatic energy, $U_E$, of the form

$$U_E = \frac{\epsilon\epsilon_o D}{8}\left[2\Psi\Psi_C * ln\left(\frac{1+exp(-\kappa\delta)}{1-exp(-\kappa\delta)}\right) + (\Psi^2+\Psi_C^2) * ln(1-exp(-\kappa\delta))\right] \quad (7.7)$$

is required for a vesicle to be tethered to a stBLM compared with DOPC [179]. In this expression, $\epsilon$ and $\epsilon_o$ are the permittivity of vacuum and the dielectric constant of water. Additionally,

$$\Psi = \frac{q\chi}{A_{lipid}\epsilon\epsilon_o\kappa} \quad (7.8)$$

and

$$\Psi_C = \frac{q\chi D^2}{2A_{lipid}D\epsilon\epsilon_o\left(1+\frac{\kappa D}{2}\right)} \tag{7.9}$$

are the surface potential of an infinite large Golgi mix stBLM and a vesicle with a diameter D [180] respectively. With an area per lipid $A_{lipid}$ of 70 Å$^2$, an electronic unit charge $q$ and $\chi = 0.15$, the molar fraction of charged lipids in the membrane,

$$U_E = 3.34 \times 10^{-21}\,\mathrm{J} \tag{7.10}$$

Similarly, the tendency for a Golgi mix vesicle to be tethered to a Golgi mix stBLM should only be $exp\left(-\frac{U_E}{kT}\right) \sim 0.4$ of DOPC according to the Boltzmann distribution. The prediction is higher than the experimental result in which the tethering activity was reduced by a factor of 10. However, considering this model only takes the interactions of a vesicle with a planar membrane into account, and neglects the interactions between adjacent vesicles, which would otherwise increase the electrostatic repulsion, the physics behind the reduction of tethering due to the electrostatic repulsion is reasonable.

### 7.3.3 The Effect of GRASP55 Mutants on Tethering Activity

To elucidate the properties of GRASP at a molecular level, the assay was carried out with mutants of GRASP55. The residues that are hypothesized to play a role in dimerization are either mutated or deleted. The summary of the results, performed with DOPC vesicles and stBLMs incorporated with 2.2 mol% of NTA-nickel lipids, is presented in Figure 7.13, with the intensity of wild type proteins shown in the first bar for comparison.

Based on the crystal structure of GRASP55 in Figure 7.1 [168], it is conceived that residue 196 to 199 (highlighted in blue in Figure 7.1) constitute the ligand that binds to the binding pocket of PDZ1. It is shown in image **A** of Figure 7.14 where the internal ligand perfectly fits into the pocket of PDZ1. This hypotheses was confirmed by an mitochondrial tethering assay. In that assay, while the wild type full length GRASP55 was able to cluster mitochondria when it was targeted to mitochondrial membranes,

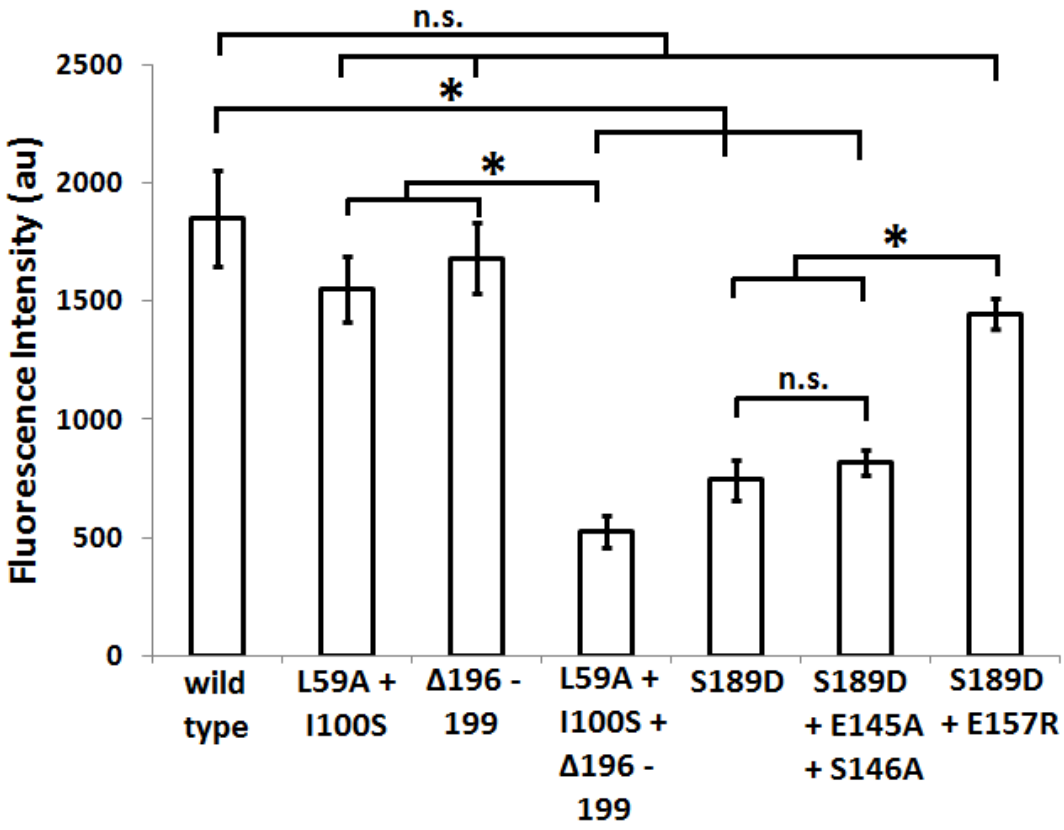


Figure 7.13: *The tethering activity of GRASP55 mutants. Each bar is the average ± standard error for at least n = 3 samples. ⋆ indicates the 1-tailed p-value between 2 bars is < 0.01 and n.s. indicates the difference is not statistically significant with a p-value > 0.05.*

the proteins with the internal ligands deleted (Δ196-199) and the proteins with the two most hydrophobic residues within the binding pocket of PDZ1 mutated (L59A + I100S, highlighted in Figure 7.1 in orange and gray) failed to cluster mitochondria [168]. Therefore, we tested this observation *in vitro* and the tethering activity of these mutants is shown in the second and the third bar. The fluorescence intensity of tethered vesicles was only reduced slightly compared with wild type proteins and the differences are not statistically significant (1-tailed p-values > 0.05). These results are in strike contrast with the mitochondrial assay. Nevertheless, when the internal ligands were deleted simultaneously with the mutation of PDZ1 (L59A + I100S + Δ196-199), the fourth bar showed a significant reduction of tethering activity to about 500 a.u. It illustrates both the internal ligands and PDZ1 take part in the

dimerization. We attribute the discrepancy of this assay with the mitochondrial assay to the sensitivity of assay. For example, if either Δ196-199 or L59A + I100S decreases the dimerization constant of GRASP55, and hence the tethering activity, then L59A + I100S + Δ196-199 should further decrease the dimerization constant. Unfortunately, we do not know the exact relationship between the dimerization constant with the number of tethered vesicles in this assay and the clustering of mitochondria. The number of dimers needed to tether a vesicle to stBLMs can vary from the dimers needed to tether two mitochondria. As an example, out of hundreds of bound proteins on a vesicle, it is reported that only one tether is required for the vesicle to be tethered to supported membranes [181, 182], whereas it might be harder to tether mitochondria membranes due to a crowded membrane environment. As such, there is no surprise that two assays investigated the tethering ability of GRASP at different range of the dimerization constant, in addition to distinctive sensitivity and saturation.

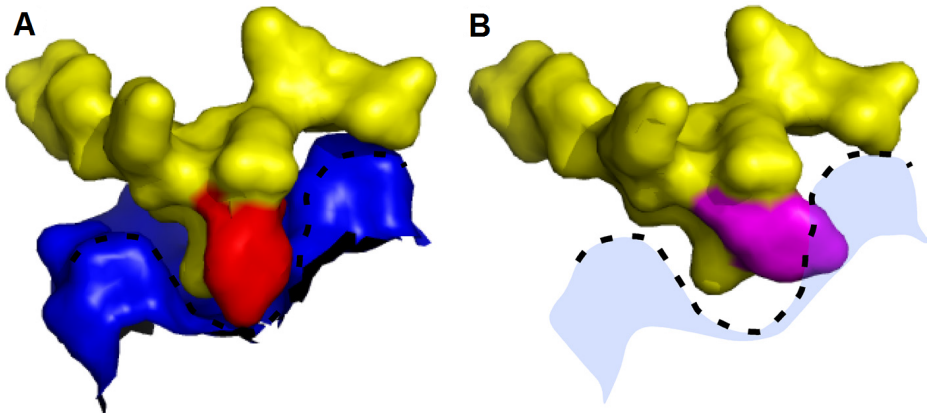


Figure 7.14: *The binding of the internal ligand to the binding pocket of PDZ1. Image* ***A*** *is the crystal structure of wild type proteins while image* ***B*** *is the crystal structure of S189D. The ligand is shown in yellow whereas the binding pocket of PDZ1 is shown in blue. The red and pink residue is Tyr-198 and its conformation is perturbed in S189D and no longer fits perfectly into the pocket. The image is adapted from reference [3].*

During mitosis, GRASP65 is phospharylated on serine-189 and leads to unlinking of Golgi ribbon structure [3]. Based on the crystal structure of GRASP55 phosphomimic, S189D [3], mutation from serine to aspartic acid allosterically induces a conformational change on the internal ligand. Tyr-198, which is one of the residues that forms the ligand, does not match perfectly into the PDZ1 binding pocket due to the mutation (image **B** in Figure 7.14). Therefore, in the mitochondrial assay, S189D was not able to cluster mitochondria [3]. The effect of S189D was also tested in this stBLM-vesicle

assay and the result was shown in the fifth bar of Figure 7.13. Only less than half of the fluorescence intensity was recorded for S189D in comparison with wide type proteins, consistent with the picture provided by the crystal structure and the mitochondrial assay.

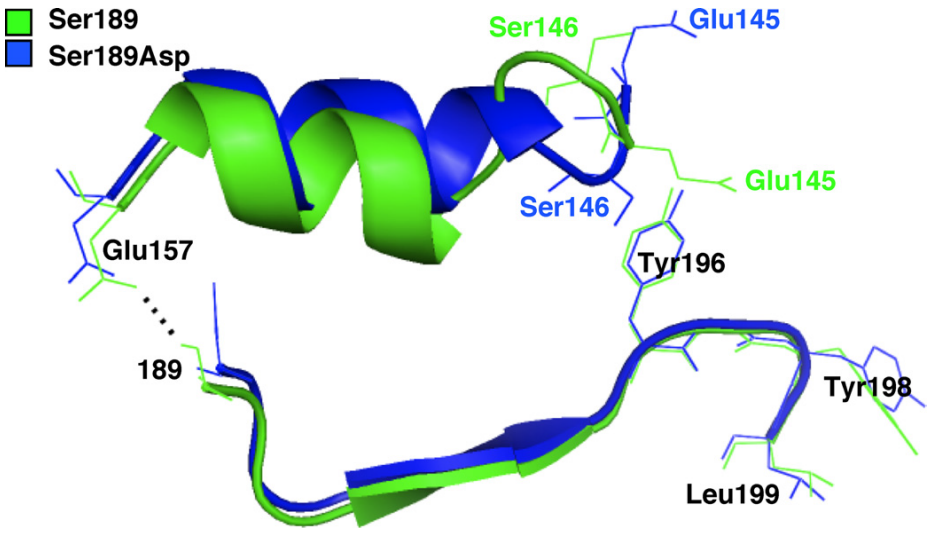


Figure 7.15: *The crystal structure of wild type proteins (in green) and S189D (in blue) are overlaid to show the effect of S189D that allosterically changes the conformation of Glu-145, Ser-145, Tyr-198. The image is adapted from reference [3].*

Two schemes are envisaged to rescue the tethering activity of S189D according to a comparison between the wild type and the S189D crystal structure (Figure 7.15). Glu-145 and Ser-146, which are located adjacent to the internal ligand, are flipped in S189D, and regulate the conformation of Tyr-198. Additionally, a polar contact between Ser-189 and Glu-157 in the wild type structure is broken in S189D. To compensate for the impaired tethering of S189D, 2 mutated constructs were devised. In the first construct, the charged Glu-145 and the polar Ser-146 were both mutated with a hydrophobic residue alanine (S189D + E145A + S146A, the sixth bar in Figure 7.13) to reverse the flipping of the residues. In the second construct, to restore the contact between negatively charged Asp-189 (S189D) with Glu-157 which is also negatively-charged, Glu-157 was replaced with positively-charged Arg-157 (S189D + E157R in the seventh bar of Figure 7.13). Even though both constructs re-established the tethering in the mitochondrial assay (reference [3] and results in preparation for publication), only the second construct was able to offset the phosphoinhibition of S189D in this assay. In contrast with S189D + E145A + S146A that did not

demonstrate a variation with respect to S189D, the tethered vesicles grew by a factor of two for S189D + E157R. In fact, the tethering ability of S189D + E157R was comparable to wild type proteins with a 2-tailed p-value of $> 0.05$. Disagreement observed for S189D + E145A + S146A in this and the mitochondrial assay reveal distinctive features of 2 assays in studying functionality of proteins.

### 7.3.4 The Effect of Membrane Anchors on Tethering

The tethering mediated by GRASP55 requires a correct orientation of proteins on membranes. The coordination between the internal ligands and the binding pockets of PDZ1 on opposing membranes facilitates dimerization *in trans*. For instance, the clustering of mitochondria highly depended on the anchoring scheme of GRASP65 on membranes. The dually anchored GRASP65 on both the C- and N-terminal clustered mitochondria while singly anchored GRASP65 on only either C- or N-terminal failed to do so [171]. A potential justification is that when the proteins are dually anchored on membranes, their orientation is fixed in such a way to assist *trans* pairing of proteins on opposing membranes as schematically illustrated in Figure 7-16 (see also Section (7.3.6)). When they are only singly anchored, they possess the freedom to rotate and flip on membranes. As a result, they might pair up with proteins on the same membranes and thus dimerize *in cis*. To examine the consequence of membrane anchors, apart from the wild type proteins which are dually anchored through myristoyl groups at the N-terminal and histidine tags on the C-terminal, 2 singly anchored GRASP55 were prepared. They were proteins with the exclusion of myristoyl groups at the N-terminal ('His at C-term') and proteins with the histidine tags moved from the C- to the N-terminal ('His at N-term'). The tethering of DOPC vesicles to DOPC stBLMs by these constructs are presented in Figure 7.16.

The results in Figure 7.16 clearly indicate the singly anchored proteins (the second and third bar) were not able to tether vesicles as efficient as the dually anchored proteins (the first bar). Although the tethering activity of singly anchored proteins was weakened, they were still able to dimerize *in trans* ($\sim$ 1000 a.u.) since the intensity was still much higher than the background ($<$ 100 a.u. in Figure 7.7). Therefore, it is suggested that some of the singly anchored proteins formed *trans*-pairs and some of the proteins formed *cis*-pairs in this assay.

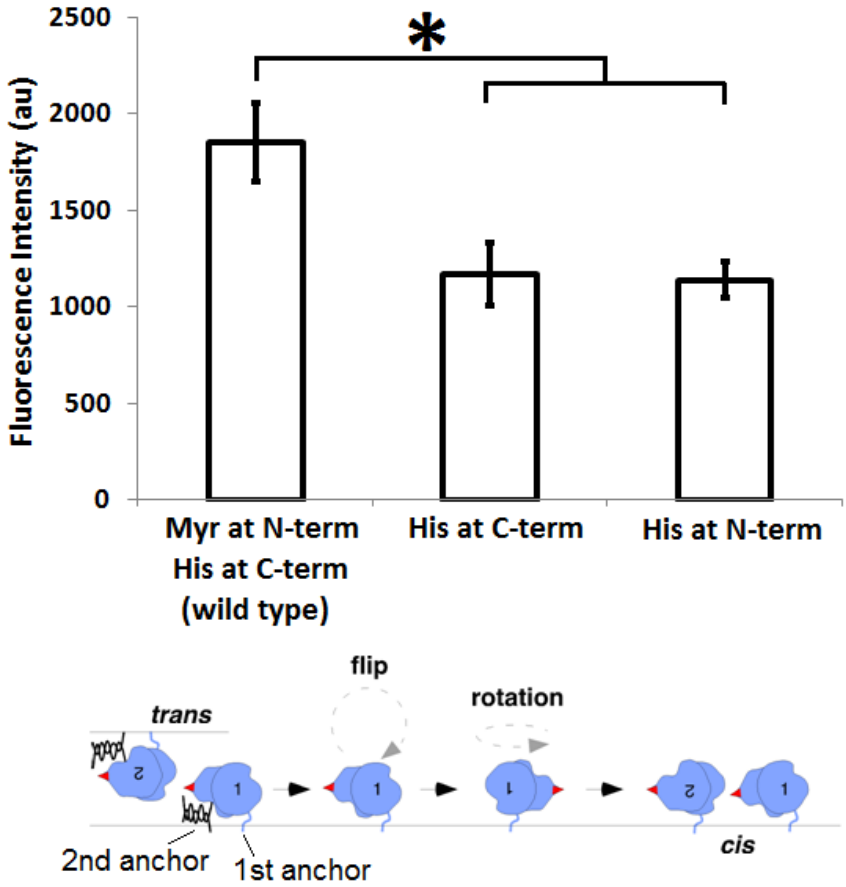


Figure 7.16: *The effect of membrane anchors on tethering. Except for the proteins in the first bar which were dually anchored, the proteins in the second and third bar were only singly anchored to membranes through the histidine tag at the C- or N-terminal. Each bar is the average ± standard error for at least n = 3 samples. ⋆ indicates the 1-tailed p-value between 2 bars is < 0.01. The figure at the bottom is the schematic diagram of dually and singly anchored proteins. When a protein is dually anchored on the left, its orientation favors dimerization in trans and thus tethers opposing membranes together. When it is only singly anchored, it is able to flip and rotate as illustrated on the right to form a cis-pair with the second protein on the same membrane.*

### 7.3.5 Tethering by GRASP65

As the last experiment in this assay, the tethering activity of GRASP65 was studied. The GRASP domain of GRASP65 from the 1st to the 255th residue was used as the construct. It was also myristoylated at the N-terminal and was His-tagged at the C-terminal to be recruited to membranes. The result, together with the wild

type GRASP55 as a comparison, is shown in Figure 7.17. The number of tethered vesicles by GRASP65 is close to GRASP55, demonstrating the functionality of GRASP domain of both GRASP65 and GRASP55 in membrane tethering.

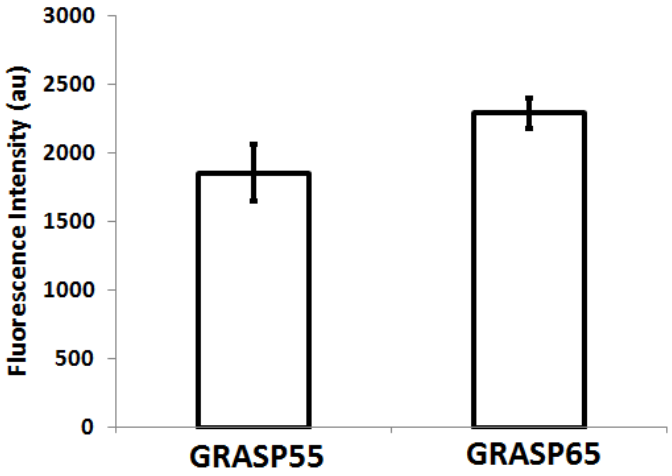


Figure 7.17: *Tethering of DOPC vesicles to DOPC stBLMS mediated by GRASP65. Each bar is the average ± standard error for at least n = 3 samples.*

### 7.3.6 Orientation of GRASP55 on stBLMs

To figure out the orientation of wild type GRASP55 on stBLMs, neutron reflectivity was performed. Reflectivity curves obtained under $H_2O$, with and without bound GRASP55 on a stBLM, are shown in Figure 7.18. A clear difference in the reflectivity from $Q_z = 0.04$ to 0.08 $Å^{-1}$ is observed due to an extra protein layer on the surface of the stBLM. The reflectivity curves were then subjected to continuous distribution (CD) model fittings to recover the corresponding nSLD profiles as shown in the inset of Figure 7.18. An additional protein layer was identified at $z \sim 300$ $Å$ in the nSLD profile.

In Figure 7.19, a detailed area profile from the CD model fitting is display. Each (sub)molecular component is represented by a peak that is the sum of two error functions as discussed in Chapter 2. These peaks are $\beta$ME, PEG of tethering lipids, glycerol backbone of tethering lipids, PC and NTA-nickel headgroups of the proximal and distal leaflet, and the methyl group and $CH_2$ alkyl chains of both leaflets. Moreover, the area profile of bound proteins is found from $z \sim 60$ to 140 Å. For illustration,

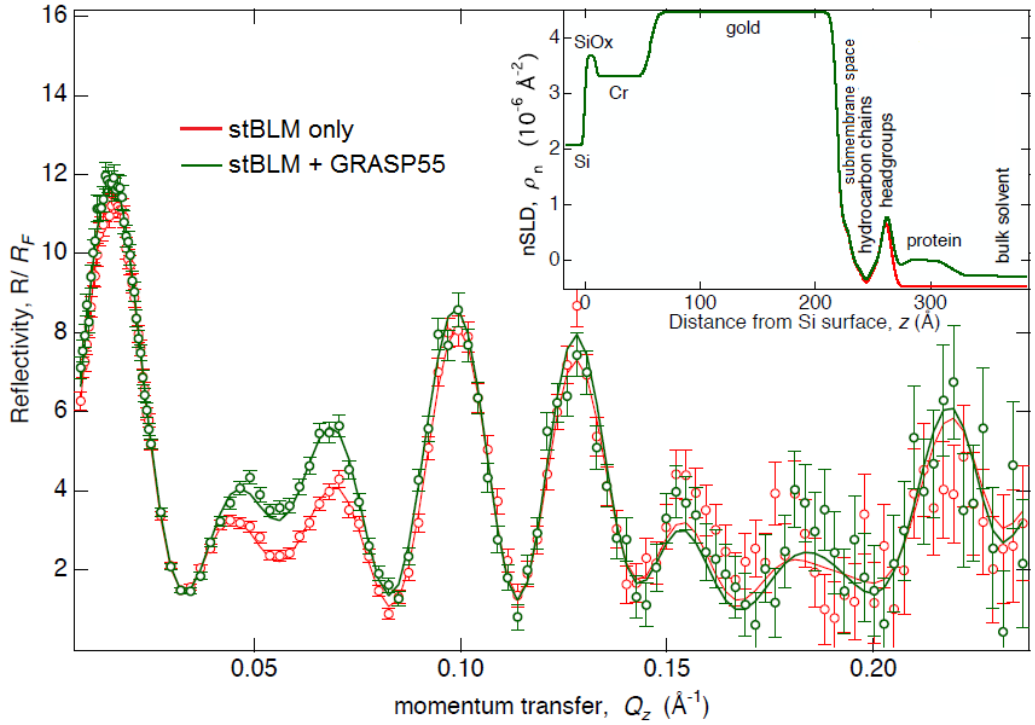


Figure 7.18: *The normalized reflectivity curves, recorded under $H_2O$, are shown for a neat stBLM and after GRASP55 was bound to its surface. In the inset are the nSLD profiles for both curves retrieved from CD model fittings.*

the area profile of the GRASP55 crystal structure, rotated to ($\beta$, $\gamma$) = (40°, 160°), is presented on the same graph.

The area profile of bound proteins is utilized to sort out the orientation of proteins. For this purpose, the crystal structure of GRASP55(7-208) was used. Even though there are 5 and 16 missing residues at the N- and C-terminal compared with the proteins in the experiment, the preliminary analysis using the crystal structure is a good starting point for further refinements. The crystal structure was translated along z-direction and rotated in $\beta$ and $\gamma$ to produce a set of area or nSLD profiles along the z-axis. $\chi^2$ between this set of profiles with the experimental profile in Figure 7.19 was calculated to evaluate the goodness of fit.

In a fit where $\beta$ was constrained to be less than 90°, the resulting $\chi^2$ is plotted as a function of $\beta$ and $\gamma$ in Figure 7.20. Two local minima are recognized in that plot near ($\beta$, $\gamma$) = (48°, 154°) and (50°, 273°) with their narrow confidence interval shown in contours of different colors. Their respective $\chi^2$ are 1.09 and 1.64. Consequently,

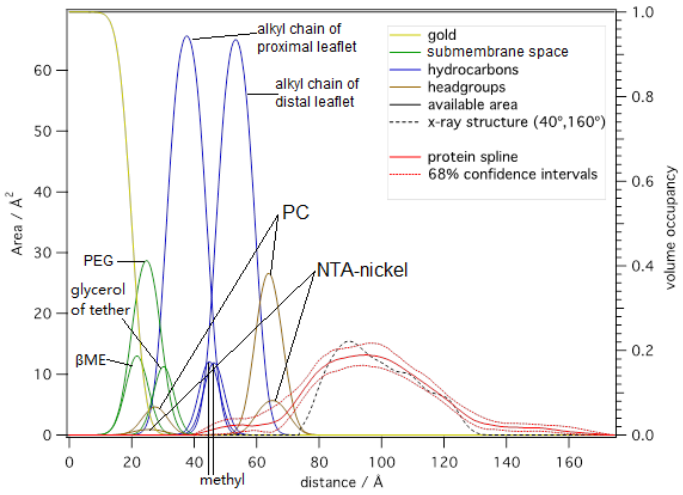


Figure 7.19: *The area profile of the stBLM and bound GRASP55 from CD model fitting. The uncertainty of the protein's area profile is shown as the 68% confidence interval. The area profile of the crystal structure rotated to a value of (β, γ) = (40°, 160°) is shown for illustration.*

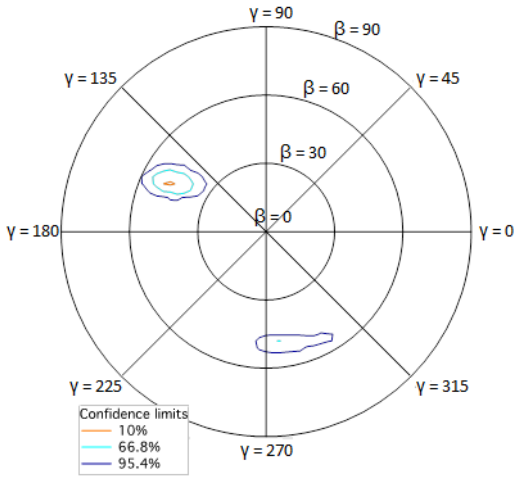


Figure 7.20: *The $\chi^2$ plot for (β, γ). 2 local minima are found at (48°, 154°) and (50°, 273°) and their confidence interval is shown with contours of different colors.*

(48°, 154°) is the current best-fit orientation.

To visualize the best-fit orientation, the crystal structure is rotated to (50°, 155°) in Figure 7.21. In this figure, the membrane is located at the bottom of the figure and is parallel to the x-y plane. The N-terminal colored in red is situated close to the membrane surface while the C-terminal colored in yellow is 10 to 15 Å away from the

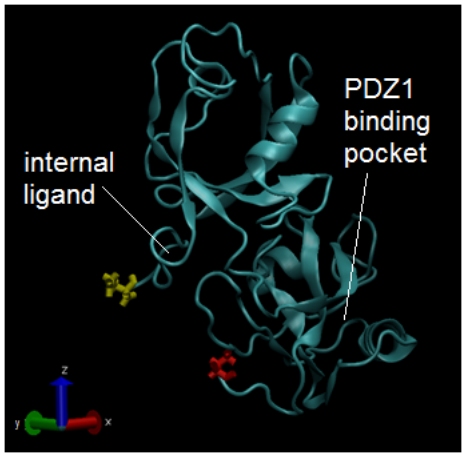


Figure 7.21: *The best-fit orientation with ($\beta$, $\gamma$) $\sim$ (50°, 155°). The membrane is located on the x-y plane at the bottom of the figure. The N-terminal is colored in red and the C-terminal is colored in yellow.*

membrane. Considering there are 16 missing residues at the C-terminal, a distance of 10 to 15 Å from the membrane is reasonable. Most importantly, the internal ligand and the binding pocket of PDZ are both exposed toward bulk water phase. They are not buried toward the membrane surface which would otherwise impede their participation in dimerization. This finding is in accord with the mutation study in the fluorescence microscopy based assay.

## 7.4 Discussion

The main objective of this work is to study the functionality of GRASP55 in an *in vitro* environment. For this aim, we set up an anchoring scheme for GRASP55 to be recruited to lipid membranes through the chelation of His-tags with NTA-nickel lipids. The binding of GRASP55 to stBLMs was verified by SPR measurements. Following this, an assay, in which stBLMs were incubated simultaneously with fluorescently-labeled lipid vesicles and GRASP55, was designed. The fluorescence images of tethered vesicles were recorded on the stBLM interfaces and the intensity of images was employed as the indicator of GRASP55 tethering activity.

The assay provides a neat and simple method to examine the functionality of proteins. Based on our study, vesicles were only tethered to stBLMs if and only if GRASP55 was recruited to both stBLMs and vesicles, and this relied on the

concentration of NTA-nickel lipids incorporated into membranes (Figure 7.7). This result proves that the GRASP domain is sufficient and necessary to tether vesicles to stBLMs. Furthermore, we suggest that there were multilayer of vesicles on stBLM surfaces, where GRASP55 tethered the second layer of vesicles to the first layer, subsequently tethered the third layer to the second layer and so forth.

A few parameters were investigated to optimize the assay. They were the incubation time, the sizes of vesicles and the membrane compositions (Figure 7.10 to 7.12). The conditions that maximized the number of tethered vesicles were used throughout the assay. Besides, to explain the dependence of the assay on these parameters, we considered the interactions between vesicles and stBLMs to be the key factors. The van der Waals, hydration and electrostatic energy are involved to tether vesicles in close proximity with stBLMs. Therefore, these interactions determine which conditions are favored according to the Boltzmann distribution. The implication of this observation is particular intriguing in the case of DOPC against Golgi mix membranes. At first thought, Golgi mix membranes that provide a more native environment for GRASP should be the natural choice for this assay. However, due to the electrostatic repulsion between vesicles and stBLMs of like charges, the number of tethered vesicles was extremely low compared with DOPC, and thus was not the most advantageous system to be used. It exemplifies the importance of fine-tuning the physical parameters in the assay to optimize the outcomes.

Next, from the mutation study of GRASP55, we identified the functioning residues that participate in dimerization (Figure 7.13). An internal ligand from the 196th to 199th residue and PDZ1 were recognized to play a role in tethering. No effects were observed when the ligand was deleted or when the PDZ1 was mutated separately, inconsistent with the mitochondrial assay. The tethering was only lowered when the ligand was deleted and when the PDZ1 was mutated concurrently. A word of caution is expressed on the anomaly of two assays since they might have distinct sensitivity and saturation, and response to different range of the dimerization constant. Single molecule experiments can be performed in the future to reveal the disparity of two assays. The tethering was also perturbed by the phosphomimic, S189D, which regulates the dimerization allosterically, but was compensated by an corresponding mutation of E157R by restoring an electrostatic contact between 2 residues.

Furthermore, in Figure 7.16, the influence of membrane anchors was explored. It was discovered that the tethering was higher for dually anchored proteins compared

with singly anchored proteins. It implies the protein' orientation is anchor-dependent and the internal ligand and PDZ1 might be orientated on membranes to favor dimerization *in trans* if the proteins are dually anchored.

Finally, we performed NR measurements on GRASP55 bound to a stBLM (Figure 7.18 to 7.21). From the preliminary analysis, the proteins exposed the internal ligands and PDZ1 binding pockets toward the aqueous phase. Since the proteins that we used in NR experiments contained extra residues at both terminals compared with the GRASP55 crystal structure employed in data fitting, a molecular dynamics simulation will be carried out to find out the configuration of the extra residues. Equipped with a full length protein configuration from the simulation, a full and detailed examination will confirm or readjust the current best-fit orientation. Nevertheless, the present NR result is encouraging as it is consistent with the picture that the ligands and pockets are essential in tethering.

The *in vitro* platform we established in this study is an instance where supported membranes are used in molecular biology study. In general, despite the popularity of supported membranes in the field of chemistry and engineering, most of the research aims to exploit the potential of supported membranes in biosensing and technological applications and the promise of supported membranes in molecular biology is yet to come. Although there are a few cases of vesicles tethering on supported membranes, these studies employed the well known biotin-streptavidin/avidin/neutravidin binding [47, 179] or DNA [181, 183] as the tethers and so were not biologically relevant.

One of the most versatile aspects of this assay lies in the fact that it is now straightforward to study the properties and interactions of proteins involved in membrane tethering with a single assay. Instead of histidine tags, by incorporating binding partners of GRASP55 and GRASP65, golgin45 and GM130 respectively, to supported membranes, the binding constants of GRASP55-golgin45 and GRASP65-GM130 can be measured with SPR and the corresponding mutation study would elucidate the molecular mechanism of binding. The subsequent vesicles tethering measurements are performed within the same assay. Supplemented with surface sensitive methods such as AFM (probing the lateral organization of membrane-protein systems), x-ray and neutron reflection (determine the orientation of proteins), and single particle tracking of fluorescently-labeled proteins or vesicles (measuring the binding stoichiometry), supported membranes open up an avenue for uncovering molecular mechanisms with a reductionist system. Additionally, the core parameters of the assay, for instance

membrane compositions and surface density of proteins, can be tweaked to optimize the signal of a specific phenomenon.

## 7.5 Conclusions

In summary, we have developed a stBLMs and lipid vesicles based *in vitro* assay to study the functionality of GRASP55 in membrane tethering. We corroborated previous results that GRASP domain is essential in tethering. The internal ligands and binding pockets are directed toward the aqueous phase to take part in dimerization from the preliminary neutron reflectivity analysis. This functional assay is an illustration of using supported membranes in molecular biology studies. We foresee the extensive applications of supported membranes in this field because of their potential both as a high throughput screening platform and as a system for single molecule study, which are realized by the use of surface sensitive techniques to examine their interactions with biomolecules.

# Bibliography


[1] H. Heerklotz, *Quarterly Reviews of Biophysics* **41**, 205 (2008).

[2] P. Shekhar, H. Nanda, M. Losche, F. Heinrich, *Journal of Applied Physics* **110**, 102216 (2011).

[3] S. T. Truschel, M. Zhang, C. Bachert, M. R. Macbeth, A. D. Linstedt, *The Journal of Biological Chemistry* **287**, 19870 (2012).

[4] G. Valincius, *et al.*, *Biophysical Journal* **95**, 4845 (2008).

[5] P. Mueller, D. O. Rudin, H. T. TIien, W. C. Wescott, *Nature* **194**, 979 (1962).

[6] M. Montal, P. Meuller, *Proceedings of the National Academy of Sciences* **69**, 3561 (1972).

[7] D. Lasic, *Trends in Biotechnology* **16**, 307 (1998).

[8] M. Schalke, M. Lösche, *Advances in Colloid and Interface Science* **88**, 243 (2000).

[9] M. Lösche, *Current Topics in Membranes* **52**, 117 (2002).

[10] V. von Tscharner, H. M. McConnell, *Biophysical Journal* **36**, 421 (1981).

[11] A. A. Brian, H. M. McConnell, *Proceedings of the National Academy of Sciences* **81**, 6159 (1984).

[12] L. K. Tamm, H. M. McConnell, *Biophysical Journal* **47**, 105 (1985).

[13] E. Sackmann, *Science* **271**, 43 (1996).

[14] I. Czolkos, A. Jesorka, O. Orwar, *Soft Matter* **7**, 4562 (2011).

[15] I. K. Vockenroth, *et al.*, *Biointerphases* **3**, FA68 (2008).

[16] E. T. Castellana, P. S. Cremer, *Surface Science Reports* **61**, 429 (2006).

[17] V. Kiessling, M. K. Domanska, D. Murray, C. Wan, L. K. Tamm, *Wiley Encyclopedia of Chemical Biology* (2008), pp. 411–422.

[18] I. Gözen, A. Jesorka, *Analytical Chemistry* **84**, 822 (2012).

[19] H. Lang, C. Duschl, H. Vogel, *Langmuir* **10**, 197 (1994).

[20] B. A. Cornell, *et al.*, *Nature* **387**, 580 (1997).

[21] S. Lingler, I. Rubinstein, W. Knoll, A. Offenhäusser, *Langmuir* **13**, 7085 (1997).

[22] L. M. Williams, *et al.*, *Langmuir* **13**, 751 (1997).

[23] D. J. McGillivray, *et al.*, *Biointerphases* **2**, 21 (2007).

[24] F. Heinrich, *et al.*, *Langmuir* **25**, 4219 (2009).

[25] V. Atanasov, *et al.*, *Biophysical Journal* **89**, 1780 (2005).

[26] A. L. Plant, *Langmuir* **9**, 2764 (1993).

[27] A. L. Plant, M. Gueguetchkeri, W. Yap, *Biophysical Journal* **67**, 1126 (1994).

[28] M. Wagner, L. Tamm, *Biophysical Journal* **79**, 1400 (2000).

[29] M. Tanaka, E. Sackmann, *Nature* **437**, 656 (2005).

[30] R. P. Richter, R. Bérat, A. R. Brisson, *Langmuir* **22**, 3497 (2006).

[31] a. a. Brian, H. M. McConnell, *Proceedings of the National Academy of Sciences* **81**, 6159 (1984).

[32] C. Hamai, P. S. Cremer, S. M. Musser, *Biophysical Journal* **92**, 1988 (2007).

[33] K. L. Weirich, J. N. Israelachvili, D. K. Fygenson, *Biophysical Journal* **98**, 85 (2010).

[34] O. Sandre, L. Moreaux, F. Brochard-Wyart, *Proceedings of the National Academy of Sciences* **96**, 10591 (1999).

[35] D. J. McGillivray, *et al.*, *Biophysical Journal* **96**, 1547 (2009).

[36] E. Kalb, S. Frey, L. K. Tamm, *Biochimica et Biophysica Acta (BBA) - Biomembranes* **1103**, 307 (1992).

[37] J. W. Lichtman, J.-A. Conchello, *Nature Methods* **2**, 910 (2005).

[38] F. Lanni, H. E. Keller, *Imaging Neurons: A Laboratory Manual*, R. Yuste, A. Konnerth, F. Lanni, eds. (Cold Spring Harbor Labroratory, 2000), chap. 1, pp. 1.1–1.72, first edn.

[39] T. Baumgart, S. T. Hess, W. W. Webb, *Nature* **425**, 821 (2003).

[40] S. L. Veatch, S. L. Keller, *Biophysical Journal* **85**, 3074 (2003).

[41] J. Raedler, H. Strey, E. Sackmann, *Langmuir* **11**, 4539 (1995).

[42] B. Sanii, A. N. Parikh, *Soft Matter* **3**, 974 (2007).

[43] P. Jönsson, J. P. Beech, J. O. Tegenfeldt, F. Höök, *Journal of the American Chemical Society* **131**, 5294 (2009).

[44] I. Czolkos, J. Guan, O. Orwar, A. Jesorka, *Soft Matter* **7**, 6926 (2011).

[45] H. Nabika, T. Sumida, K. Murakoshi, *Current Drug Discovery Technologies* **8**, 301 (2011).

[46] J. D. Knight, M. G. Lerner, J. G. Marcano-Velázquez, R. W. Pastor, J. J. Falke, *Biophysical Journal* **99**, 2879 (2010).

[47] E. Boukobza, A. Sonnenfeld, G. Haran, *The Journal of Physical Chemistry B* **105**, 12165 (2001).

[48] C. Yoshina-Ishii, S. G. Boxer, *Journal of the American Chemical Society* **125**, 3696 (2003).

[49] D. Stamou, C. Duschl, E. Delamarche, H. Vogel, *Angewandte Chemie International Edition in English* **115**, 5738 (2003).

[50] A. H. Kunding, M. W. Mortensen, S. M. Christensen, D. Stamou, *Biophysical Journal* **95**, 1176 (2008).

[51] M. J. Saxton, K. Jacobson, *Annual Review of Biophysics and Biomolecular Structure* **26**, 373 (1997).

[52] D. Axelrod, D. E. Koppel, J. Schlessinger, E. Elson, W. W. Webb, *Biophysical Journal* **16**, 1055 (1976).

[53] E. Wu, K. Jacobson, D. Papahadjopoulos, *Biochemistry* **16**, 3936 (1977).

[54] J. Yguerabide, J. A. Schmidt, E. E. Yguerabide, *Biophysical Journal* **40**, 69 (1982).

[55] D. M. Soumpasis, *Biophysical Journal* **41**, 95 (1983).

[56] B. L. Sprague, R. L. Pego, D. A. Stavreva, J. G. McNally, *Biophysical Journal* **86**, 3473 (2004).

[57] D. Magde, E. Elson, W. Webb, *Physical Review Letters* **29**, 705 (1972).

[58] R. Rigler, U. Mets, J. Widengren, P. Kask, *European Biophysics Journal* **22**, 169 (1993).

[59] H. Qian, M. P. Sheetz, E. L. Elson, *Biophysical Journal* **60**, 910 (1991).

[60] S. Shenoy, *et al.*, *Soft Matter* **6**, 1263 (2010).

[61] L. Guo, *et al.*, *Chemphyschem* **9**, 721 (2008).

[62] E. Barsoukov, J. R. Macdonald, eds., *Impedance Spectroscopy: Theory, Experiment, and Applications* (John Wiley & Sons, 2005), second edn.

[63] H. Coster, T. Chilcott, A. Coster, *Bioelectrochemistry and Bioenergetics* **40**, 79 (1996).

[64] G. Wiegand, N. Arribas-Layton, H. Hillebrandt, E. Sackmann, P. Wagner, *The Journal of Physical Chemistry B* **106**, 4245 (2002).

[65] L. Becucci, M. R. Moncelli, R. Naumann, R. Guidelli, *Journal of the American Chemical Society* **127**, 13316 (2005).

[66] J. W. F. Robertson, *et al.*, *The Journal of Physical Chemistry B* **112**, 10475 (2008).

[67] J. Lin, M. Merzlyakov, K. Hristova, P. C. Searson, *Biointerphases* **3**, FA33 (2008).

[68] A. J. Bard, L. R. Faulkner, *Electrochemical Methods: Fundamentals and Applications* (John Wiley & Sons, 2000), second edn.

[69] G. Krishna, J. Schulte, B. A. Cornell, R. J. Pace, P. D. Osman, *Langmuir* **19**, 2294 (2003).

[70] L. J. Jeuken, R. J. Bushby, S. D. Evans, *Electrochemistry Communications* **9**, 610 (2007).

[71] G. Krishna, *et al.*, *Langmuir* **17**, 4858 (2001).

[72] P. Nelson, *Biological Physics: Energy, Information, Life* (W. H. Freeman and Company, 2008), first edn.

[73] J. Fitter, T. Gutberlet, J. Katsaras, eds., *Neutron Scattering in Biology* (Springer, 2006).

[74] D. Vaknin, K. Kjaer, J. Als-Nielsen, M. Lösche, *Biophysical Journal* **59**, 1325 (1991).

[75] H. Nanda, *et al.*, *Biophysical Journal* **99**, 2516 (2010).

[76] J. Fitter, T. Gutberlet, J. Katsaras, eds., *Neutron Scattering in Biology: Techniques and Applications* (Springer, 2006), first edn.

[77] L. Kalé, *et al.*, *Journal of Computational Physics* **151**, 283 (1999).

[78] J. Homola, *Analytical and Bioanalytical Chemistry* **377**, 528 (2003).

[79] J. Homola, S. S. Yee, G. Gauglitz, *Sensors and Actuators B: Chemical* **54**, 3 (1999).

[80] R. B. Schasfoort, A. J. Tudos, eds., *Handbook of Surface Plasmon Resonance* (RSC Publishing, 2008), first edn.

[81] J. Homola, *Chemical reviews* **108**, 462 (2008).

[82] L. S. Jung, C. T. Campbell, T. M. Chinowsky, M. N. Mar, S. S. Yee, *Langmuir* **14**, 5636 (1998).

[83] M. Kyoung, E. D. Sheets, *Biophysical Journal* **95**, 5789 (2008).

[84] H. Fischer, I. Polikarpov, A. F. Craievich, *Protein Science* **13**, 2825 (2004).

[85] S. Shenoy, *et al.*, *Plos One* **7**, e32591 (2012).

[86] A. Helenius, K. Simons, *Biochimica et Biophysica Acta (BBA) - Biomembranes* **415**, 29 (1975).

[87] D. Lichtenberg, R. J. Robson, E. A. Dennis, *Biochimica et Biophysica Acta (BBA) - Reviews on Biomembranes* **737**, 285 (1983).

[88] D. D. Lasic, *The Biochemical Journal* **256**, 1 (1988).

[89] J. Lasch, *Biochimica et Biophysica Acta (BBA) - Biomembranes* **1241**, 269 (1995).

[90] M. Almgren, *Biochimica et Biophysica Acta (BBA) - Biomembranes* **1508**, 146 (2000).

[91] H. Heerklotz, J. Seelig, *Biochimica et Biophysica Acta (BBA) - Biomembranes* **1508**, 69 (2000).

[92] M. Ollivon, S. Lesieur, C. Grabielle-Madelmont, M. Paternostre, *Biochimica et Biophysica Acta (BBA) - Biomembranes* **1508**, 34 (2000).

[93] M. le Maire, P. Champeil, J. V. Mø ller, *Biochimica et Biophysica Acta (BBA) - Biomembranes* **1508**, 86 (2000).

[94] J.-L. Rigaud, M. Chami, O. Lambert, D. Levy, J.-L. Ranck, *Biochimica et Biophysica Acta (BBA) - Biomembranes* **1508**, 112 (2000).

[95] R. M. Garavito, S. Ferguson-Miller, *The Journal of Biological Chemistry* **276**, 32403 (2001).

[96] A. M. Seddon, P. Curnow, P. J. Booth, *Biochimica et Biophysica Acta (BBA) - Biomembranes* **1666**, 105 (2004).

[97] M. Nazari, M. Kurdi, H. Heerklotz, *Biophysical Journal* **102**, 498 (2012).

[98] F. Nomura, *et al.*, *Proceedings of the National Academy of Sciences* **98**, 2340 (2001).

[99] G. Staneva, M. Seigneuret, K. Koumanov, G. Trugnan, M. I. Angelova, *Chemistry and Physics of Lipids* **136**, 55 (2005).

[100] T. P. Sudbrack, N. L. Archilha, R. Itri, K. A. Riske, *The Journal of Physical Chemistry B* **115**, 269 (2011).

[101] K. Akashi, H. Miyata, H. Itoh, K. Kinositajr, *Biophysical Journal* **71**, 3242 (1996).

[102] S. Manley, V. Gordon, *Current Protocols in Cell Biology* **40**, 1 (2008).

[103] S. Massari, R. Colonna, E. Folena, *Biochimica et Biophysica Acta (BBA) - Biomembranes* **940**, 149 (1988).

[104] H. Schönherr, J. M. Johnson, P. Lenz, C. W. Frank, S. G. Boxer, *Langmuir* **20**, 11600 (2004).

[105] G. H. Zan, C. Tan, M. Deserno, F. Lanni, M. Lösche, *Soft Matter* **8**, 10877 (2012).

[106] R. Merkel, E. Sackmann, E. Evans, *J Phys France* **50**, 1535 (1989).

[107] E. Evans, a. Yeung, *Chemistry and Physics of Lipids* **73**, 39 (1994).

[108] R. M. Raphael, R. E. Waugh, *Biophysical Journal* **71**, 1374 (1996).

[109] E. Karatekin, *et al.*, *Biophysical Journal* **84**, 1734 (2003).

[110] J. N. Israelachvili, *Intermolecular and surface forces* (Academic Press, 1991), second edn.

[111] W. Rawicz, K. C. Olbrich, T. McIntosh, D. Needham, E. Evans, *Biophysical Journal* **79**, 328 (2000).

[112] C. Hamai, T. Yang, S. Kataoka, P. S. Cremer, S. M. Musser, *Biophysical Journal* **90**, 1241 (2006).

[113] D. Andelman, M. Kozlov, *Europhysics Letters* **25**, 231 (1994).

[114] J. Zimmerberg, M. M. Kozlov, *Nature Reviews Molecular Cell Biology* **7**, 9 (2006).

[115] H. C. Berg, *Random Walks in Biology* (1993).

[116] U. Kragh-Hansen, M. le Maire, J. V. Mø ller, *Biophysical Journal* **75**, 2932 (1998).

[117] J. L. Parker, V. V. Yaminsky, P. M. Claesson, *The Journal of Physical Chemistry* **97**, 7706 (1993).

[118] O. Lambert, D. Levy, J. L. Ranck, G. Leblanc, J. L. Rigaud, *Biophysical Journal* **74**, 918 (1998).

[119] A. E. Garner, D. A. Smith, N. M. Hooper, *Biophysical Journal* **94**, 1326 (2008).

[120] V. N. Ngassam, M. C. Howland, A. Sapuri-Butti, N. Rosidi, A. N. Parikh, *Soft Matter* **8**, 3734 (2012).

[121] S. Morandat, K. El Kirat, *Colloids and Surfaces B: Biointerfaces* **55**, 179 (2007).

[122] H. V. Ly, M. L. Longo, *Biophysical Journal* **87**, 1013 (2004).

[123] M. Kranenburg, M. Vlaar, B. Smit, *Biophysical Journal* **87**, 1596 (2004).

[124] L. Löbbecke, G. Cevc, *Biochimica et Biophysica Acta (BBA) - Biomembranes* **1237**, 59 (1995).

[125] M. Patra, *et al.*, *Biophysical Journal* **90**, 1121 (2006).

[126] J. A. Barry, K. Gawrisch, *Biochemistry* **33**, 8082 (1994).

[127] S. E. Feller, C. A. Brown, D. T. Nizza, K. Gawrisch, *Biophysical Journal* **82**, 1396 (2002).

[128] T. Adachi, H. Takahashi, K. Ohki, I. Hatta, *Biophysical Journal* **68**, 1850 (1995).

[129] A. N. Dickey, R. Faller, *Biophysical Journal* **92**, 2366 (2007).

[130] U. Vierl, L. Löbbecke, N. Nagel, G. Cevc, *Biophysical Journal* **67**, 1067 (1994).

[131] A. A. Gurtovenko, J. Anwar, *The Journal of Physical Chemistry B* **113**, 1983 (2009).

[132] J. Mou, J. Yang, C. Huang, Z. Shao, *Biochemistry* **33**, 9981 (1994).

[133] C. Reichardt, *Chemical Reviews* **94**, 2319 (1994).

[134] T. M. Krygowski, P. K. Wrona, U. Zielkowska, C. Reichardt, *Tetrahedron* **41**, 4519 (1985).

[135] A. O. Hohner, M. P. C. David, J. O. Rädler, *Biointerphases* **5**, 1 (2010).

[136] J. Nagle, S. Tristram-Nagle, *Biochimica et Biophysica Acta (BBA) - Biomembranes* **1469**, 159 (2000).

[137] E. S. Rowe, F. Zhang, T. W. Leung, J. S. Parr, P. T. Guy, *Biochemistry* **37**, 2430 (1998).

[138] J. M. Diamond, Y. Katz, *The Journal of Membrane Biology* **17**, 121 (1974).

[139] A. M. Smith, M. Vinchurkar, N. Gronbech-Jensen, A. N. Parikh, *Journal of the American Chemical Society* **132**, 9320 (2010).

[140] J. K. R. Kendall, *et al.*, *Chemphyschem* **11**, 2191 (2010).

[141] L. J. Jeuken, *et al.*, *Sensors and Actuators B: Chemical* **124**, 501 (2007).

[142] V. I. Silin, *et al.*, *Journal of the American Chemical Society* **124**, 14676 (2002).

[143] T. Baumgart, *et al.*, *Journal of Colloid and Interface Science* **258**, 298 (2003).

[144] J. Hubbard, V. Silin, A. Plant, *Biophysical Chemistry* **75**, 163 (1998).

[145] L. Williams, *et al.*, *Supramolecular Science* **4**, 513 (1997).

[146] J. T. Woodward, C. W. Meuse, *Journal of Colloid and Interface Science* **334**, 139 (2009).

[147] S. T. Wang, M. Fukuto, L. Yang, *Physical Review E* **77**, 1 (2008).

[148] J. Wilschut, N. Düzgüne, R. Fraley, D. Papahadjopoulos, *Biochemistry* **19**, 6011 (1980).

[149] S. Tristram-Nagle, *et al.*, *Chemistry and Physics of Lipids* **163**, 630 (2010).

[150] N. Kučerka, M.-P. Nieh, J. Katsaras, *Biochimica et Biophysica Acta (BBA) - Biomembranes* **1808**, 2761 (2011).

[151] G. H. Zan, C. Tan, M. Deserno, F. Lanni, M. Lösche, *Soft Matter* **8**, 10877 (2012).

[152] C. A. Keller, B. Kasemo, *Biophysical Journal* **75**, 1397 (1998).

[153] J. M. Johnson, T. Ha, S. Chu, S. G. Boxer, *Biophysical Journal* **83**, 3371 (2002).

[154] J. Jass, T. Tjärnhage, G. Puu, *Biophysical Journal* **79**, 3153 (2000).

[155] R. Richter, A. Mukhopadhyay, A. Brisson, *Biophysical Journal* **85**, 3035 (2003).

[156] T. H. Anderson, *et al.*, *Langmuir* **25**, 6997 (2009).

[157] I. K. Vockenroth, C. Rossi, M. R. Shah, I. Köper, *Biointerphases* **4**, 19 (2009).

[158] C. Joseph-Aiguier, *Biochimica et Biophysica Acta (BBA) - Biomembranes* **507**, 62 (1978).

[159] J. C. McIntyre, R. G. Sleight, *Biochemistry* **30**, 11819 (1991).

[160] J. Selinummi, J. Seppälä, O. Yli-Harja, J. Puhakka, *BioTechniques* **39**, 859 (2005).

[161] L. V. Chernomordik, M. M. Kozlov, *Nature Structural & Molecular Biology* **15**, 675 (2008).

[162] E. Evans, V. Heinrich, F. Ludwig, W. Rawicz, *Biophysical Journal* **85**, 2342 (2003).

[163] J. Griesbauer, A. Wixforth, M. F. Schneider, *Biophysical Journal* **97**, 2710 (2009).

[164] I. Czolkos, Y. Erkan, P. Dommersnes, A. Jesorka, O. Orwar, *Nano Letters* **7**, 1980 (2007).

[165] F. A. Barr, M. Puype, J. Vandekerckhove, G. Warren, *Cell* **91**, 253 (1997).

[166] J. Shorter, *et al.*, *The EMBO Journal* **18**, 4949 (1999).

[167] M. A. Puthenveedu, C. Bachert, S. Puri, F. Lanni, A. D. Linstedt, *Nature Cell Biology* **8**, 238 (2006).

[168] S. T. Truschel, *et al.*, *The Journal of Biological Chemistry* **286**, 20125 (2011).

[169] D. Sengupta, A. D. Linstedt, *The Journal of Biological Chemistry* **285**, 39994 (2010).

[170] T. Feinstein, A. Linstedt, *Molecular Biology of the Cell* **19**, 2696 (2008).

[171] C. Bachert, A. D. Linstedt, *The Journal of Biological Chemistry* **285**, 16294 (2010).

[172] Y. Wang, J. Seemann, M. Pypaert, J. Shorter, G. Warren, *The EMBO Journal* **22**, 3279 (2003).

[173] Y. Wang, A. Satoh, G. Warren, *The Journal of Biological Chemistry* **280**, 4921 (2005).

[174] G. Cumming, F. Fidler, D. L. Vaux, *The Journal of Cell Biology* **177**, 7 (2007).

[175] J. A. Nye, J. T. Groves, *Langmuir* **24**, 4145 (2008).

[176] E. Gizeli, J. Glad, *Analytical Chemistry* **76**, 3995 (2004).

[177] M. Bally, *et al.*, *Physical Review Letters* **107**, 188103 (2011).

[178] B. van Lengerich, R. J. Rawle, S. G. Boxer, *Langmuir* **26**, 8666 (2010).

[179] A. H. Kunding, *et al.*, *Biophysical Journal* **101**, 2693 (2011).

[180] W. C. K. Poon, D. Andelman, eds., *Soft Condensed Matter Physics in Molecular and Cell Biology* (Taylor & Francis, 2006), first edn.

[181] C. Yoshina-Ishii, *et al.*, *Langmuir* **22**, 5682 (2006).

[182] M. E. Bowen, K. Weninger, A. T. Brunger, S. Chu, *Biophysical Journal* **87**, 3569 (2004).

[183] J. J. Benkoski, F. Höök, *The Journal of Physical Chemistry B* **109**, 9773 (2005).